The Prediction of Wrinkle Formation in Non-crimp Fabrics during Double Diaphragm Forming

By

Fei Yu

MSc.

Thesis submitted to the University of Nottingham for the degree of Doctor of Philosophy

October 2021

Abstract

Liquid composite moulding (LCM) processes are an economical alternative to autoclave-cured prepreg, as intermediate material forms are less expensive, capital equipment costs are lower and cycle times are shorter. LCM is suitable for producing aerospace quality components, but the process chain is dependent on a separate preforming process to convert 2D fibre formats into complex 3D shapes prior to moulding. Preforming is difficult to automate to ensure defect-free architectures, as multiple plies are often formed at the same time according to predefined forming loads and constraints. Corrections to the draping direction, force and sequence can be easily refined during manual hand layup, as the laminator works on one ply at a time. Corrections to the forming sequence cannot be easily made during automated forming, therefore numerical models are required during the design phase to refine process parameters to ensure that defects do not evolve.

This thesis seeks to develop a robust simulation methodology for modelling the forming behaviour of biaxial fabrics, in order to enable effective identification of forming related defects and assist in process design for improving the quality of preforms. Research has been conducted in three main areas:

(I) Material characterisation and model development.

A macroscale constitutive model has been developed to simulate the forming behaviour of biaxial fabrics, based on an explicit finite element scheme, incorporating the effects of bending stiffness to predict wrinkling. Cantilever tests were employed to characterise the bending behaviours of a twill-weave woven fabric and a non-crimp fabric (NCF) with pillar stitches, providing linear (a constant rigidity) and nonlinear bending stiffness models to represent the fabric materials. Experimental and numerical studies have shown that the bending behaviour of the fabrics is nonlinear, which is dependent on the fibre curvature along the bending direction. Forming simulations using a constant bending stiffness from the standard cantilever test (BS EN ISO 9073-7; 1998) produced unrealistic predictions for fabric bending and wrinkling behaviours, while the nonlinear model produced more accurate forming induced wrinkle patterns compared to the experimental data. The nodal distance between the deformed fabric mesh and the tool surface was identified to be a suitable method to locate areas containing out-of-plane defects, using the principal curvature to further isolate wrinkles from areas of fabric bridging (poor conformity).

(II) Multi-resolution modelling approach for defect identification.

A multi-resolution modelling strategy was developed for determining forming induced defects in large-scale DDF components, using a macroscopic global-to-local sub-modelling technique. The fabric constitutive model developed in Stage (I) above was used for predicting macro-scale defects (i.e. wrinkling and bridging defects at the ply level) during double diaphragm forming (DDF) of a generic geometry comprising local changes in cross-sectional shape. Comparisons between simulations and experimental results confirmed the accuracy of the forming model, but the runtime of the full-scale shell-element model was found to be impractical. Therefore, a multi-resolution modelling strategy was developed to improve the overall computational efficiency. Areas containing potential defects were initially determined by a full-scale global simulation using a coarse membrane-element mesh (element edge length of ~5mm). Results with higher resolution (wrinkle amplitude of ~1mm) and more realistic shapes were subsequently obtained by local sub modelling, using higher order shell-element meshes, based on boundary conditions derived from the global simulation.

The applied methodology enabled an 87% saving in the runtime compared to the high fidelity full-scale shell-element model for the same geometry, with the length of wrinkles and area of fabric bridging predicted within 10% compared to experimental data. These reductions will become more significant as the overall length scale is increased for components produced by DDF, as defects will tend to be within more localised regions.

(III) Defect formation and mitigation during multi-ply NCF forming.

Forming experiments and simulations were performed to investigate the mechanism of wrinkling in multi-layered NCF plies during DDF. Simulation results indicate that in-plane fibre compression, caused by dissimilar shear deformation between adjacent plies, can lead to out-of-plane wrinkles, where the wrinkle length is a function of the relative fibre angle at the ply-ply contact interface. The most severe wrinkles occurred when the inter-ply angle was 45° for a multi-ply biaxial NCF preform. Numerical and experimental studies have shown that out-of-plane wrinkles are sensitive to the friction resistance between NCF plies and therefore lubricating the fibres can minimise wrinkling defects caused by dissimilar inter-ply deformation.

In summary, results from the first part of the thesis (Chapter 3 and Chapter 4) demonstrate the importance of incorporating a curvature-dependent bending behaviour into fabric constitutive modelling for correctly predicting forming behaviour of bi-axial fabrics. The multi-resolution forming simulation strategy (Chapter 5) extends the capability of the proposed fabric model to

predict macroscale defects in large structures more efficiently. The study on multi-ply fabric forming (Chapter 6) provides further understanding about the effect of inter-ply sliding on ply wrinkling, enabling a feasible solution for wrinkle mitigation. The results from this work can be directly extended for industrial application to improve the performance of composite structures made via fabric preforms.

Acknowledgements

Contents

Chapter 1   Introduction

1.1   Background

Advanced composites, such as carbon fibre reinforced polymers (CFRPs), have been widely used in the aerospace and automotive sectors, driven by the increasing demand for fuel economy and environmental benefits. The use of CFRPs for commercial aircraft design can typically offer 10 – 30% reduction in structural weight compared to an aluminium baseline [1], which is of great importance for minimising fuel consumption and maximising payload. It is reported that replacing conventional aluminium-based structures in aircrafts with lightweight composite materials can lead up to 20% reduction in CO_2 emission during their lifetime [2].

The Boeing 787 Dreamliner, launched in 2013, marked an important milestone in aircraft production, achieving up to 50% of the structure made by lightweight composites [3]. The Airbus A350 XWB, launched in the same year, contained 53% composites by weight [4]. Whilst prepreg-based composites suit current production rates for wide-body aircrafts (i.e. 10-14 per month per OEM (Original Equipment Manufacturer)), there is an increasing demand for narrow-bodied single aisle aircrafts and therefore more efficient materials and processes are required. Airbus is therefore seeking to switch the traditional time- and labour-intensive hand layup prepreg components on A320 to those made through faster automated processes, such as resin transfer moulding (RTM) or vacuum infusion, with the aim to increase production rate towards 100 per month [5]. In addition to the reduction in weight, replacing metal components with composites provides aircraft structures with outstanding corrosion resistance [6] and fatigue performance [7]. In the automotive industry, lightweight composites are also finding their way into wider applications for road vehicles due to the stringent regulations on carbon emissions. The launch of the BMW i3 was a successful innovation in using CFRPs for the main structure (i.e. passenger cell) of a road vehicle [8], with a target production volume of 35,000 vehicles per annum. To achieve higher fuel efficiency and lower carbon emission, CFRP components have also been used on mainstream vehicles, such as the Audi A8 and BMW 7-Series [9, 10]. Recent advancements in hybrid composite moulding enable functional elements of dissimilar materials to be integrated to offer higher structural performance and better bonding quality compared to traditional joining methods [5, 11]. Structures containing multiple components can therefore be

produced directly by in-mould forming and assembling [5, 12], which enables shorter cycle times and reduced part counts [13].

The total demand for CFRPs is expected to exceed 190,000 tons by 2050 [14], but the wider application of composites to commercial areas is still restricted by the long manufacturing cycle times, high raw material and labour costs. The autoclave moulding method has been traditionally developed for manufacturing aerospace-grade composites using prepregs, but the annual production volume is typically below 1,000 parts per annum (ppa) primarily due to the slow ramp rates used during the heat-curing process and the high capital cost of the equipment. This method is generally impractical to fulfil the production volume expected by the automotive industry, i.e. 10-200,000ppa depending on the performance expectation. Moreover, using prepregs is not cost-effective due to their high material price compared to dry fabrics and limited shelf life (up to six months at room temperature). As the use of composites increases for primary structures within the airframe of commercial aircraft, reducing capital investment and labour cost is becoming a crucial factor for manufacturing these next-generation aerospace composites.

Manufacturing techniques such as resin transfer moulding (RTM) and its variants (e.g. high-pressure RTM and vacuum assisted RTM) utilise vacuum and pressure to assist resin flow into the pre-consolidated reinforcements, constrained by a heated closed mould. RTM is more suitable for producing net-shaped components and the capital investment is reported to be 75% lower than for autoclave cured components of a similar size. [15]. An automated preforming step is typically required for RTM to convert flat carbon fibre reinforcements into complex 3D shapes prior to liquid moulding at the required rate, in order to reduce the production time compared to hand layup. However, due to the large deformation required during forming, defects such as wrinkles, bridging and fibre misalignment (See Figure 1.1) can be generated within the fabric blank, which can degrade the mechanical performance of the final composite parts by up to 40% [16].

Figure 1.1 Typical modes of forming induced defects in a composite seat back.

It is therefore important to ensure the quality of preforms is maximised by avoiding defects during the forming stage. In this thesis, a fabric constitutive model is developed to facilitate process simulations to enable process refinement, based on an explicit finite element scheme. This tool is used to overcome the challenges associated with forming large-scale components, in which defects occur due to the local variation in geometry and interactions between the fibre reinforcement plies. This work specifically focuses on reducing the computational time required for simulating the forming behaviour of non-crimp fabrics for large-scale components.

1.2   Theme definition

This work aims to provide robust simulation tools and process improvements to enable composite components to be designed and manufactured from fabric preforms more efficiently and with more confidence. Double diaphragm forming (DDF) is the main focus for this research as it is capable of producing large-scale components without similar sized presses or autoclaves.

Fabric wrinkling and bridging at the macroscale are the primary defect modes that occur due to the DDF process. Whilst the out-of-plane bending resistance of the fabric is orders of magnitude lower than the in-plane stiffness in the principal fibre directions, realistic predictions for the location, number and size of macroscale defects requires suitable fabric bending properties to be incorporated. This is because fabric wrinkling is essentially caused by ply buckling, which is related to the out-of-plane fabric bending stiffness. The first part of the thesis (Chapter 3 and Chapter 4) focuses on developing a novel macro-scale modelling approach considering fabric bending stiffness to predict the formation of defects at the macro-scale, enabling the explicit shape of wrinkles and bridging to be modelled with sufficient accuracy. Different approaches for incorporating the effects of the fabric bending stiffness into the forming simulation are characterised, with the results compared to guide the selection of a suitable modelling framework.

High mesh densities are typically required to capture critical wrinkles with low amplitude (~1-2 mm), but this inevitably leads to an impractical increase in computation time, preventing wider adoption of these tools within industry. For DDF simulations in particular, highly non-linear materials and complex ply-ply interactions can lead to impractical runtimes for large structures (e.g. > 10m in length), even when using high performance cluster computing. However, large scale components such as aerospace wing spars and ribs generally only exhibit a moderate variation in surface curvature along their length. Defects in this case are usually concentrated around small local regions with doubly-curved features, with the rest of the component being free of forming related defects. The second part of this thesis (Chapter 5) is therefore driven by the need for an efficient modelling approach to identify process-induced defects at sufficient resolution for local critical regions of large components. This will be achieved by a multi-resolution analysis utilising the efficiency of a membrane-element-based model and the accuracy of a shell-element-based model.

Whilst the deformation mechanisms of fabric reinforcements are relatively well understood, there is uncertainty about how defects form during DDF, particularly for multi-layered non-crimp fabric plies. In the last part of the thesis (Chapter 6), forming experiments and simulations will be conducted to understand the effects of inter-ply sliding during multi-ply fabric forming, with the aim to guide process design for defect control.

In summary, outcomes of this research will enable the prediction and evaluation of manufacturing related defects for non-crimp fabrics during DDF, enabling effective solutions to be developed to improve the quality of preforms in future designs.

1.3   Outline of thesis

The outline of the thesis follows the research objective presented in Section 1.2. Research activities are carried out as follows:

Chapter 2 reviews the state-of-the-art in fabric forming research, with the emphasis on 2D fabrics. The procedure of Resin Transfer Moulding (RTM) is briefly reviewed to understand the importance of fabric preforming stage within the manufacturing chain. Typical processes for producing fabric preforms are compared to understand the primary modes of forming-induced defects. The fibre architectures of commonly used 2D fabrics are reviewed to understand the deformation mechanism during fabric forming. Existing fabric characterisation methods are reviewed to support constitutive modelling, to understand the capability and limitation of each method. Research on process simulation for defect identification and mitigation are discussed to understand the gaps in the current knowledge and challenges in process improvement.

In Chapter 3, a macro-scale constitutive model for simulating the forming behaviour of biaxial fabrics is developed and validated. By incorporating the nonlinear bending contribution into a non-orthogonal constitutive model for biaxial fabrics, the model enables fibre rotation and fibre-orientation-dependent bending behaviour to be considered in the simulation framework. Cantilever tests are employed to characterise the bending behaviour of fabrics, providing input parameters for simulating the realistic wrinkling behaviour of fabrics. The model is validated for a biaxial woven fabric and a non-crimp fabric (NCF). Finally, the effects of fabric wrinkling and stitch failure on the in-plane shear behaviour of the NCF during bias extension test are discussed.

In Chapter 4, the developed fabric model is used to simulate the wrinkling behaviour of biaxial fabrics during press tool forming, in order to understand the influence of fabric bending stiffness on wrinkle prediction. Simulation results from different bending models are compared to demonstrate the suitability of using the curvature-dependent bending model for process simulation. A new methodology is developed to locate and quantitatively evaluate the severity of fabric wrinkles, based on the nodal distance between in the fabric ply and the tool surface. The principal curvature of the wrinkle can also be extracted from the FE simulation results, which enables wrinkles to be distinguished from fabric bridging.

In Chapter 5, a global-to-local modelling strategy is presented based on the Abaqus in-built sub modelling module to predict the formation of macro-scale defects in the biaxial NCF during Double Diaphragm Forming (DDF). A full-scale simulation using a coarse membrane-

element mesh is employed to determine areas with potential defects based on high shear strain and poor fabric-tool conformity, providing boundary conditions for the subsequent sub modelling. The sub models were constructed using high-fidelity shell-element meshes to explicitly predict the shape of defects at the macro-scale. This multi-resolution modelling approach is validated against experimental data and a corresponding reference simulation, to demonstrate the precision and potential run-time saving for modelling large components.

In Chapter 6, the effect of inter-ply sliding on the formation of wrinkling defects is investigated for multi-ply NCF preforms during the DDF process. Numerical simulations are performed to investigate the influence of the ply layup sequence and the coefficient of interfacial friction, assisting in process refinement to control the severity of defects. The feasibility of interfacial lubrication for mitigating defects induced by dissimilar shear deformation of plies is investigated by experiments and simulations.

Conclusions are drawn in Chapter 7 to summarise the primary discoveries for this research and to provide guidelines for process analysis and design.

The resulting publications are presented in Appendix A.

Chapter 2   Literature review

2.1   Introduction

In this chapter, a brief introduction to composite preforming is presented, including a review of different reinforcements and forming processes to understand the forming behaviour of fabrics and the cause of forming related defects. Different approaches and apparatuses are compared to understand their capabilities for characterising the mechanical properties of fabrics. State-of-the-art techniques for fabric forming simulation are reviewed to understand the current challenges in fabric material modelling and defect prediction. A series of candidate solutions for defect mitigation are summarised to give an overview of the up-to-date progress on improving fabric formability towards defect-free preforms. In order to fill in the gaps in the current knowledge, the primary themes are identified in the field of composites preforming, with the aim to improve simulation capabilities for defect prediction and explore feasible solutions for defect mitigation.

2.2   Fabric reinforced composites

2.2.1   Production procedure

Fabric reinforced composites can be manufactured by the well-established resin transfer moulding (RTM) technology, which includes a number of variants, such as vacuum-assisted RTM, RTM Light and compression RTM. This technology enable composite components to be made with lower capital investment compared to autoclave curing prepregs. A typical RTM process chain consists of three stages, i.e. 1) ply stack preparation, 2) preforming and 3) resin injection & curing, as illustrated in Figure 2.1. Each blank ply is initially cut from a fabric roll into a 2D flat format and then stacked according to a specific layup sequence. Subsequently, a forming operation is performed to convert the 2D ply stack into the expected 3D geometry. Prior to forming, a small amount (4~6% wt) of thermoset or thermoplastic binder is often added to the fabric [17, 18]. The preform is heated to melt/soften the thermoset or thermoplastic binder, which then consolidates the preform to maintain the formed shape after cooling. The preforms are subsequently trimmed and then transferred to a heated matched RTM tool located in a press. Low viscosity resin is injected and the component is left to cure once the tool is fully filled. Finally, the consolidated component can be demoulded from the tool for final trimming.
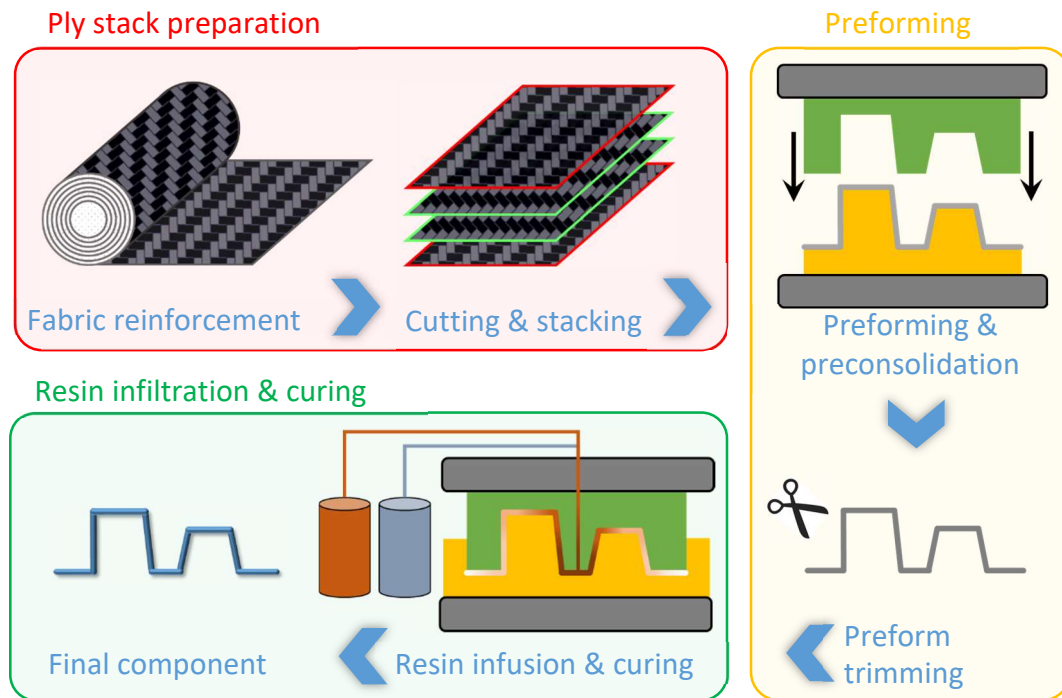
Figure 2.1: Process chain of resin transfer moulding (RTM) for production of fabric reinforced composites.

According to the Takt time of each process step, the fabric preforming step is the slowest and can create a bottle-neck in the process chain [19]. Employing automated fabric forming operations can significantly reduce the overall cycle time of the RTM process, but defects in the form of wrinkles or bridging are more likely to occur due to reduced control of the fabric during the draping process. It was reported that the compressive strength and stiffness of a coupon-level composite component can be reduced by up to 70% due to the occurrence of wrinkling defects [20]. For complex geometries, fabric bridging can occur over the concave areas of the tool, causing large areas of poor conformity between the preform and the tool [21]. Therefore, a big challenge in automated forming is to design and control the process to ensure defect-free preforms, particularly for components with complex geometries. Understanding the forming behaviour of fabrics and the formation mechanisms of critical defects is of great importance to improve the overall product quality. Compared with costly trial and error, process simulation offers a cost-efficient way to predict the location and severity of manufacturing defects, which can facilitate process design for feasible solutions prior to manufacturing. In addition, the predicted variation of the fibre orientation due to forming can be supplied as input data for downstream modelling, such as resin infusion simulations or to inform structural analyses.

2.2.2   Fabric reinforcements

Fabric reinforcements are structured materials, which encompass a wide range of fibre architectures, from woven and non-crimp fabrics to 3D fabrics [22]. The focus of the current work is on 2D fabrics, including woven fabrics and biaxial non-crimp fabrics (NCF), as they are widely available from a number of commercial suppliers and possess good formability for the ease of manufacturing composite components with complex 3D features [23, 24]. Modern automated manufacturing techniques such as weaving and knitting have already been industrialised to ensure affordable and sufficient material supply of 2D fabric blanks for high volume production. Biaxial NCFs are the main interest of this thesis as they can offer higher tensile and flexural stiffness in finished components compared to woven composites, due to straighter fibres with less crimp, while a twill-weave fabric is used in the current work to help validate the developed numerical model.

2D woven fabrics are typically constructed by interlacing warp and weft yarns, as shown in Figure 2.2. Due to the gaps between undulating yarns, woven fabrics are capable of undergoing large in-plane shear deformation during preforming. The plain weave pattern (see Figure 2.2(a)) exhibits the highest level of interlacement, resulting in a relatively stable fibre architecture, while the satin weave pattern (e.g. a 4 harness satin pattern in Figure 2.2(c)) is the most formable pattern for woven fabrics. The stability and formability of the twill weave pattern (see Figure 2.2(b)) sits in between the plain weave and satin weave patterns.

The stability and formability of the fabric is also dependent on the yarn size (tow size for carbon fabrics). When yarn spacing is fixed, yarns of larger width (containing more individual filaments) typically lead to smaller gaps in the woven architecture, leading to lower locking angles as the yarns get compacted at lower shear angles [25]. An increase in yarn thickness can also reduce the gap width and simultaneously increase the level of yarn undulation, leading to lower formability and earlier "shear locking" for woven fabrics. Conversely, an increase in yarn size can lead to less crossover points per unit area of fabric, reducing the required shear force due to the reduction in friction at the crossover-interactions [25].
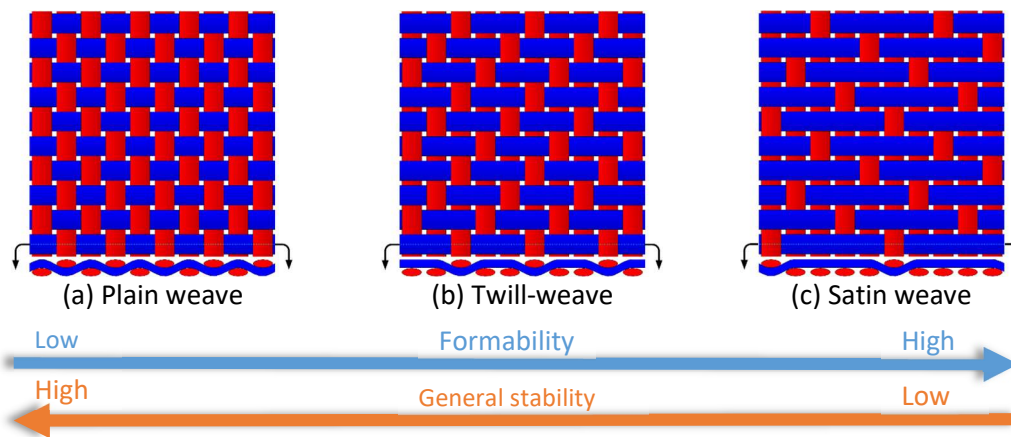
Figure 2.2: Yarn architecture of typical woven fabrics. Red yarns represent the warp and blue yarns represent the weft.

Non-crimp fabrics (NCF) are produced by assembling a single or multiple unidirectional (UD) fibre layer(s) via stitching, knitting, sewing or chemical bonding [26]. Compared to the interlaced fibre architecture of woven fabrics, the crimp-free fibres in NCFs leads to increased use of the fibre modulus and strength for composites. UD NCFs provide maximum flexibility for laminate design as the fibre orientation of each layer can be independently placed, but fibre gapping and local in-plane waviness are likely to occur during the preforming stage due to the low integrity in the transverse direction [27]. Tri-axial (e.g. 0°/90°/0° or 0°/±45°) or quad axial (0°/90°/±45°) NCFs offers better integrity during processing and can improve the overall production rate by minimising the individual number of NCF plies to be laid down onto the mould [28]. However, compared to biaxial NCFs, fibres in tri-axial or quad-axial NCFs are subject to more constraints due to higher inter-tow friction, which can cause larger out-of-plane wrinkles [29].

Biaxial NCFs are constructed by stitching two layers of UD fibres, typically oriented at 0°/90° or ±45°, offering a balance in terms of formability and productivity [26, 29]. Due to the constraining effect of the stitches, the formability of biaxial NCFs in relation to the shear deformation is strongly related to the stitch pattern. Biaxial NCFs comprising a pillar stitch pattern (Figure 2.3(a)) typically exhibit asymmetric shear behaviour as the stitches only reinforce the fabric resistance in one direction [30, 31], whereas the in-plane shear behaviour of an NCF comprising a tricot stitch pattern (Figure 2.3(b)) is more symmetrical and therefore not direction dependent [32]. Moreover, the formability of NCFs is also dependent on the mechanical properties of the stitch material, the stitch gauge (number of stitches per unit fabric width) and the stitch length (distance between two stitches in stitching direction).
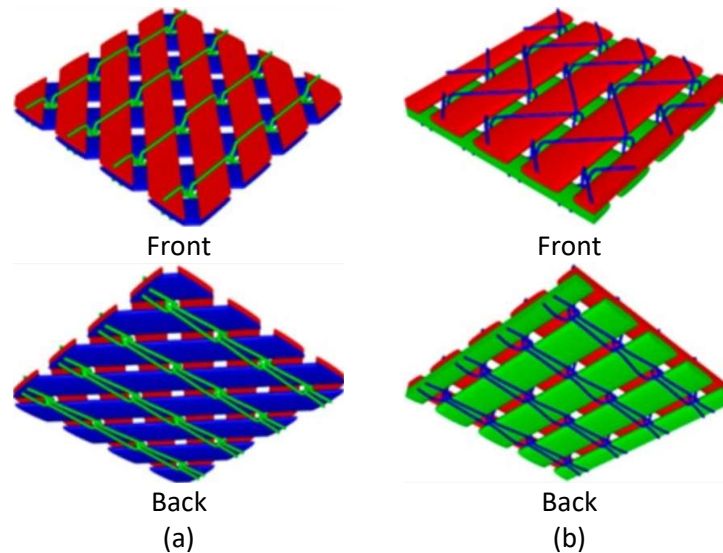
Figure 2.3: Mesoscale architectures of biaxial non-crimp fabrics with (a) pillar and (b) tricot stitching pattern. [32]

2.3   Fabric forming

2.3.1   Typical forming processes

The primary goal of any fabric forming process is to convert flat 2D fabric plies into complex 3D shapes according to the geometry of the target component. Hand draping has been historically employed to produce fabric preforms for complex geometries. However, the production rate is extremely low (<1,000 ppa) as the operator is only able to handle one ply or tape at a time and the shaping of the reinforcement has to be conducted at the same time as the lamination. In addition, the quality of the preform highly depends on the experience and working conditions of the operator, which can dramatically reduce the repeatability and therefore production quality for high-volume production. Manual labour should therefore be minimised to improve productivity and to avoid unintentional flaws introduced by the laminator. Collaborative robots have recently been combined with human operations to improve the quality and repeatability of preforming, but the reported reduction in cycle time is insignificant compared to hand layup [33].Therefore, there is a need for automated processes that can convert a stack of fabric plies into 3D complex shapes through a single operation, in order to ensure medium- or high-volume production with constant product quality.

Matched tool forming and diaphragm forming are commonly used to produce 3D preforms from flat stacks of fabric plies. The complexity of the target geometry, the required cycle time (hence expected production rate) and the necessary capital investment all need to be

considered when selecting a preforming process for a certain component. While both matched tool forming and diaphragm forming can be used for producing thermoset or thermoplastic composites directly [34, 35], the current work will focus on using these processes to produce dry preforms for liquid moulding processes.

2.3.1.1   Matched tool forming

The matched tool forming process typically employs a hydraulic press to apply a forming force via a matched pair of tools, creating the target geometry. As shown in Figure 2.4, the mould halves are opened and initially prepared with release agent to aid demoulding at the end of the process. A stack of fabric plies containing binder are positioned between the mould halves and a blank holder is employed to clamp the fabric blank around the edge of the cavity. The male half of the mould then moves towards the female half according to a specific stroke length to form the flat blank into a 3D shape. Meanwhile, the preform is heated to activate the binder material. Finally, the mould reopens after curing or cooling, depending on the binder material, and the preform is released for trimming. In addition to material property, forming temperature, blank holder force, interfacial friction, and forming sequence are some key process parameters controlling the quality of preforms.

This procedure was automated by BMW to produce high-quality preforms for the Body In White (BIW) of the i3 model, which enabled a daily output of 70 vehicles [36]. Whilst press-based matched-tool forming is capable of medium-volumes (20,000+ parts per annum per mould), the size of the component is limited by the dimension of the hydraulic press. For example, one of the world's largest presses for composites manufacturing is the 3600 ton high-rate Schuler press at the National Composites Centre (NCC), UK. However, its capability for producing large structures is limited by the dimension of the clamping surface (i.e. 3.6 m × 2.4 m) [37]. Typically, press-based forming is suitable for components of moderate dimensions (i.e. less than 2.0 m in length), but is impractical for large-scale components (> 10 m), such as wind turbine blades or aerospace wing spars.
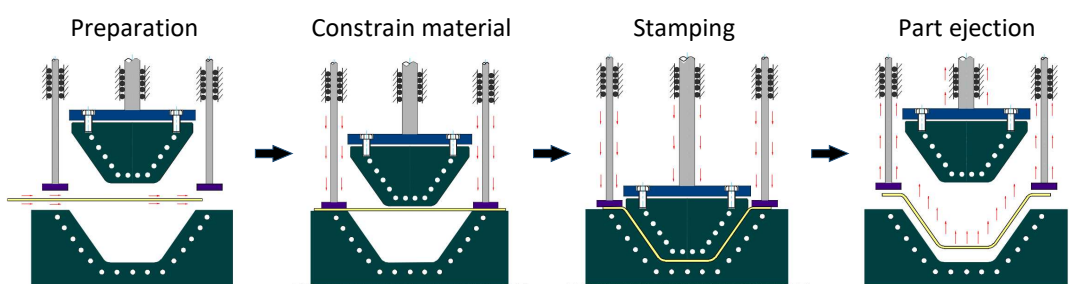
Figure 2.4: Typical matched tool forming process. [38]

2.3.1.2   Diaphragm forming

Diaphragm Forming is a scalable preforming process that uses vacuum-only generated forces to form fabric plies, enabling large composite structures to be manufactured without using oversized hydraulic presses or autoclaves [39-41]. Whilst the size of the diaphragm increases with the scale of the part, costs for setting up the fabric-diaphragm arrangement and incorporating a vacuum pump are typically much lower than the capital equipment costs for presses or autoclaves of a similar size. However, large diaphragm arrangements (10m+ preforms) can lead to difficulties in process automation, therefore additional handling equipment maybe required to facilitate this.

The process has been typically used to directly manufacture composites using thermoplastic [41-43] or thermoset prepregs [44-47], as well as binder-stabilised dry fabric preforms for liquid moulding [21, 48-50]. There are two diaphragm forming options, i.e. using either one diaphragm (Single Diaphragm Forming, SDF) or two diaphragms (Double Diaphragm Forming, DDF). In DDF, fabric plies are sandwiched between two deformable diaphragms, enabling the full ply stack to be formed in one operation. The SDF process is similar to DDF but without the lower diaphragm contacting the tool, which offers more process flexibility to form multi-layered preforms sequentially, but defects are easier to occur in SDF due to the lack of constraint from the lower diaphragm [50].

The DDF process is the main interest in this thesis. As shown in Figure 2.5, the process employs two layers of highly deformable elastomeric film (diaphragms) to apply the forming forces to the fabric stack with binder powders. The fabric plies are sandwiched between the deformable films, which are evacuated of air to provide some clamping force to help reduce out-of-plane fabric bucking [51, 52] compared to single diaphragm forming. The diaphragms are constrained around the perimeter by a picture frame, which is subsequently lowered to bring the diaphragm/fabric assembly into contact with a rigid male tool. A pressure differential is created between the lower diaphragm and the tool, which is used to deep-draw the diaphragm arrangement over the tool. The preform is then held in position and heated to activate the binder. Once the system has cooled, the lower vacuum is released to allow the preform to be removed from the tool. The process can be easily automated to produce repeatable net-shape preforms, but the formation of defects is highly dependent on the complexity of the component and the ply stacking sequence, which can limit the practical use of the process. The DDF process was successfully used by GKN Aerospace to

produce 14 m long aircraft wing spars, using prepreg-based layups, enabling the production time to be reduced to 24 hours compared to eight days for conventional hand layup [53].

| Preparation | Draping | Vacuuming | Part ejection |
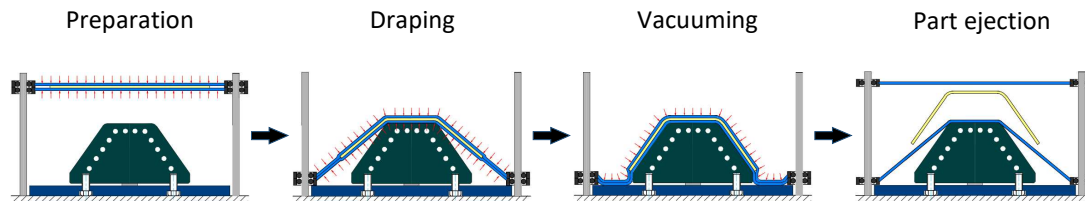
Figure 2.5: Typical double diaphragm forming (DDF) process. [38]

2.3.2   Introduction to forming deformation mechanisms

In general, the deformation mechanisms that occur during fabric forming are governed by the material behaviour of the fabric reinforcement and complex interactions at the interface between contacting materials. While the deformation of fabrics is complicated and related to the fibre architecture at the mesoscale, it can be primarily characterised by three basic deformation modes at the macro-scale; 1) in-plane shear, 2) in-plane tension, and 3) out-of-plane bending.

The *shear behaviour* of a fabric is the primary deformation mechanism experienced during forming. The in-plane shear force of 2D woven fabrics is mainly derived from the rotation and compaction of the primary yarns, while the shear resistance of NCFs is highly dependent on the stitch pattern [54, 55].

The *tensile behaviour* of a fabric depends on the level of crimp in the primary yarns, as the stiffness is nonlinear at low strains in the fibre direction and linear at higher strains as the yarns straighten, which is particularly relevant for woven fabrics [55].

The *bending behaviour* of a fabric is different to that of an ordinary continuum, since the fabric reinforcement is made up of fibres assembled via weaving or stitching, therefore relative movement is possible between fibres as the fabric bends [56]. Thus, the bending stiffness of fabrics cannot be directly derived from the axial modulus of fibres based on the classic plate and shell theory [57].

It is well documented that fabric-fabric and fabric-tool interactions can significantly influence the occurrence of forming related defects, especially when forming multi-layered fabric reinforcements [45, 46, 58, 59]. Similarly, the forming mechanisms of prepregs are of the same nature as dry fabrics because resin is melted during forming and does not change the

primary deformation modes [57], although the temperature-dependent viscosity derived from the melted resin adds additional complexity in the mechanical response of prepregs.

2.3.2.1   In-plane shear

In-plane shear is generally considered to be the dominant deformation mechanism for forming 2D fabric blanks into complex 3D shapes [55]. The in-plane shear modulus is orders of magnitude lower than the axial fibre modulus, due to the relatively weak assembly provided by interweaving (woven fabrics) or stitching (NCFs).

Figure 2.6 plots a typical shear force versus shear angle relationship between the warp and weft yarns of a woven fabric. Initially, the rotation of the interlaced yarns is restricted by the friction between fibres and the strain in the yarns is negligible [60], which results in a low shear force until the yarns start to compact laterally. Following a further increase in shear deformation, the shear force increases dramatically as a result of yarn compaction, which can lead to out-of-plane wrinkles if constraints are not applied [61, 62]. The critical shear angle, also referred to as the "locking angle", corresponds to the onset of fabric wrinkling [21, 63-66]. For woven fabrics, in-plane tension in the yarns can result in transverse compression to neighbouring yarns, increasing the frictional force between fibres [60]. As a result, the fabric exhibits a higher in-plane shear resistance when yarns are in tension [67]. Similarly, shear-locking-related wrinkling can be delayed by applying tension to the fibres to prevent out-of-plane buckling [67]. A recent study has shown that allowing more intra-yarn shear can delay the "shear locking" angle for woven fabrics, which could be a potential way to delay fabric wrinkling in forming processes [68]. For balanced woven fabrics, the magnitude of the shear force is independent of the shear direction, therefore shear tests are only required in one direction for characterising the shear resistance.
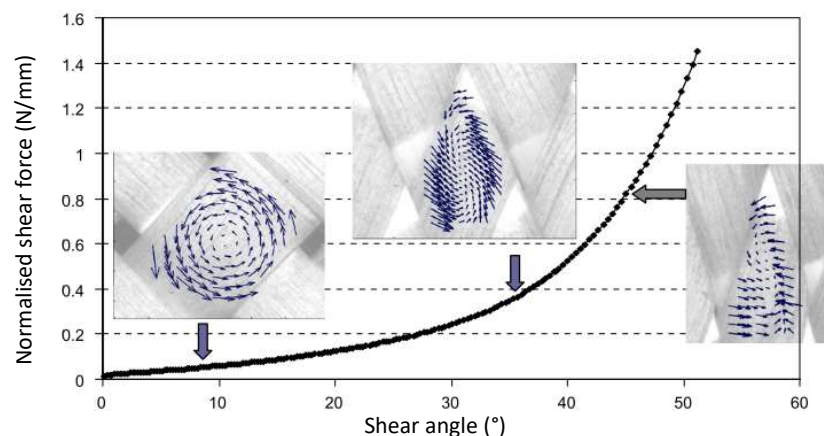
Figure 2.6: In-plane shear curve of the plain weave fabric. [60]

In addition to the primary reinforcement yarns, additional intra-ply stitches in NCFs constrain the relative rotation of the yarns and therefore the in-plane shear behaviour is dependent on the stitch pattern and orientation relative to the primary yarns. Biaxial NCFs often have two yarns orientated at ±45° or 0°/90°, assembled by either tricot or pillar stitches. As shown in Figure 2.7(a), when 0°/90° fibres are assembled by stitches following a tricot pattern running along the fibre direction, the NCF can be assumed to exhibit a symmetrical in-plane shear behaviour because the stitches are always subject to shear deformation regardless of the shear direction [32, 69, 70].

The ±45° NCFs with stitches along 0° directions (pillar stitches) often experience an asymmetric shear behaviour due to the contribution of the stitch in the two shear directions (see Figure 2.7(b)) [30, 70, 71]. In this case, the in-plane shear resistance of NCFs are typically characterised in relation to the deformation status of the stitches, i.e. positive shear or negative shear, corresponding to tension or compression of the stitches respectively. As shown in Figure 2.8 (a), when a biaxial NCF with a pillar stitch pattern is subjected to positive shear, the shear force increases linearly to a peak value until stitches start to fail. The shear force then drops significantly as a result of the progressive failure of the stitches, but increases again due to the yarn compaction at larger shear angles. The in-plane shear force curve for the negative shear direction is similar in shape to the curve for a woven fabric, as the shear resistance is primarily provided by the inter-yarn friction and compaction.
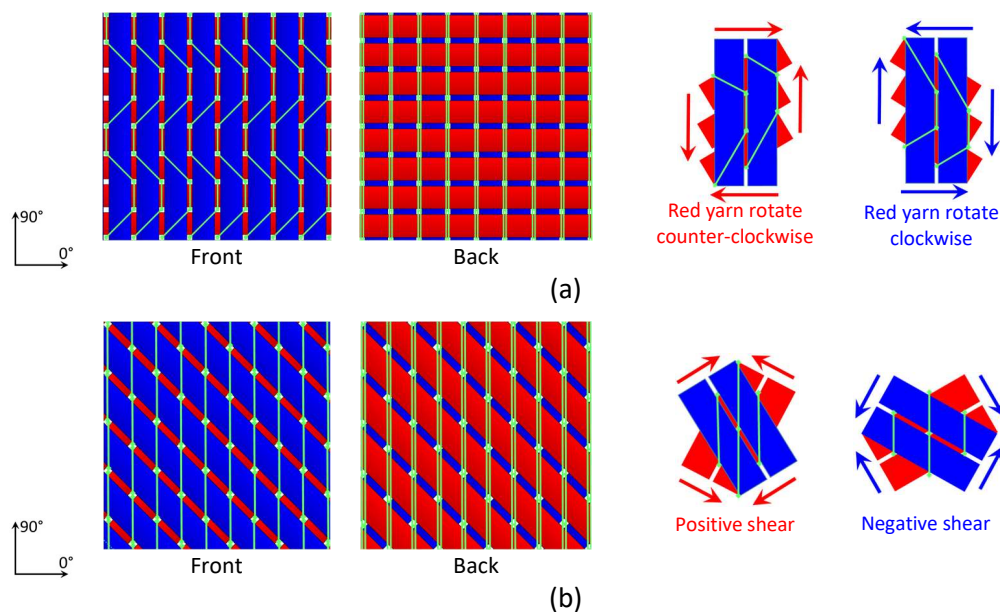
Figure 2.7: Schematics of stitch patterns and shear deformations for typical biaxial NCFs (a) a 0°/90° NCF with tricot stitches along 0° yarn direction and (b) a +45°/-45° NCF with pillar stitches along 0° direction. Green lines denote stitches.
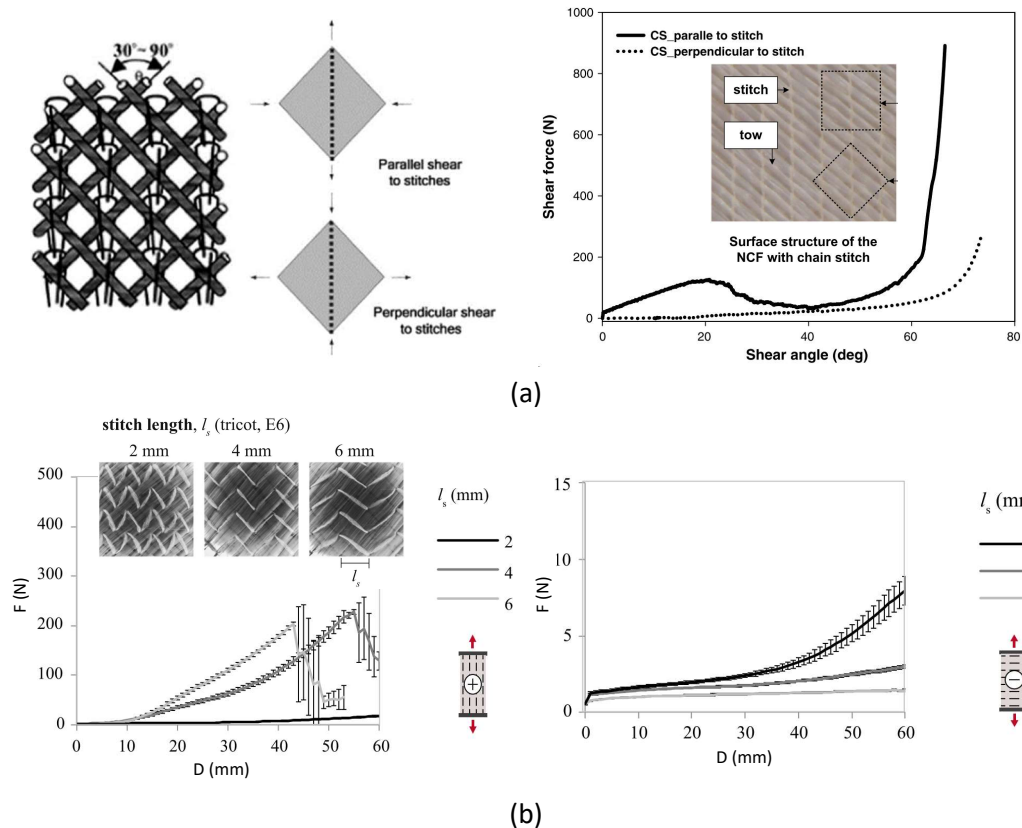
Figure 2.8: Typical in-plane shear resistance curves for ±45° NCFs with (a) pillar [31] and (b) tricot [72] stitching patterns.

The in-plane shear resistance of NCFs is also dependent on the stitching parameters. Krieger et al. [72] have compared the shear behaviours of biaxial NCFs (±45°) produced using the same tow material and areal weight but with different tricot stitching parameters. As shown in Figure 2.8(b), the shear resistance in the positive shear direction is generally higher than in the negative shear direction, indicating asymmetric shear behaviour. However, the increase in shear force under positive shear is dependent on the stitch gauge length. Experimental results show that the shear resistance under positive shear increases with increasing stitch gauge length, while the shear resistance under negative shear increases as the stitch length decreases (see Figure 2.8(b)).

2.3.2.2   In-plane tension

The axial tensile stiffness in each fibre direction is typically much higher in magnitude than the stiffness associated with the other forming deformation modes (i.e. bending and shear). Whilst the formability of a fabric is not directly related to the axial elongation of the fibres, the applied tensile load along the fibre direction accounts for the majority of the strain

energy during forming [73, 74] and areas of high tensile stress have been found to correlate well with the location of fabric bridging for complex tool geometries [21].

As shown in Figure 2.9(a), the tensile behaviour of woven fabrics is derived from the structural deformation of straightening undulating yarns [55, 74], which can lead to a nonlinear force-strain relationship in the warp or weft directions at small loads [73, 75], as shown in Figure 2.9(b). This nonlinearity was reported to be dependent on the level of yarn undulation, as larger degrees of initial crimp require larger tensile strains to eliminate it [75]. The modulus becomes linear after the yarn is fully stretched at larger strains, as shown in Figure 2.9(b). However, the tensile behaviour exhibits a biaxial phenomenon, since the level of yarn crimp reduces as the yarns straighten in the transverse direction, as shown in Figure 2.9(b).

(a)   (b)
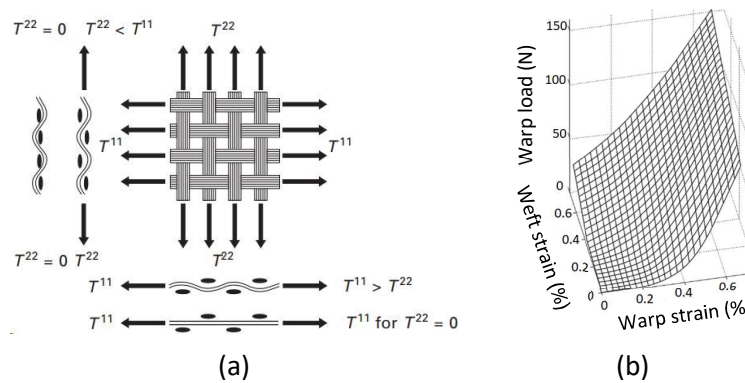
Figure 2.9: (a) Tensile interactions for a balanced plain weave fabric due to fibre interlacing; (b) biaxial tensile behaviour for a balanced plain weave fabric. [55]

Whilst the fibres in NCF plies are initially almost straight and are not interlaced, the tensile behaviour was also found to be initially nonlinear during tensile loading [54], as shown in Figure 2.10. This possibly occurs due to the original waviness or misalignment of fibres in plies [54], which indicates that fibres require pre-straightening before taking up the full tensile load. However, for the purpose of forming simulations, the axial modulus along the fibres is often assumed to be linear for computational efficiency without significantly comprising precision [38, 73].
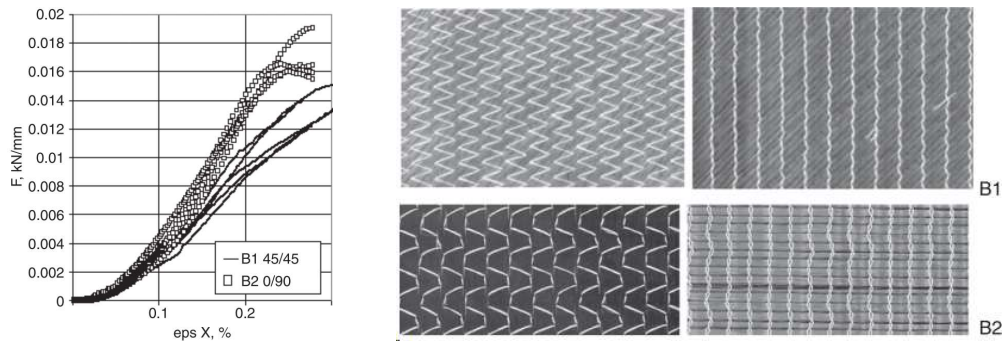
Figure 2.10: Tensile behaviour of two non-crimp fabrics B1 and B2 with different stitch patterns. [54]

2.3.2.3   Out-of-plane bending

The out-of-plane bending deformation of fabrics is another important forming mechanism as it enables curved components to be formed without damaging the fibres. Although fibres within the fabric are considered to be quasi-inextensible with high in-plane stiffness, the bending stiffness of fabric material is generally much lower than the value derived from the in-plane modulus of in fibre directions [57, 76, 77]. According to experimental results [56], a stack of fibres can undergo a bending deflection almost identical to a single fibre when inter-fibre slippage is not constrained (see Figure 2.11). Whereas stacked fibres typically exhibit a much higher bending resistance when constraints are imposed at the interface, such as through-thickness stitches (Figure 2.12). This indicates that the weak bending stiffness of fabrics is due to insufficient constraints on inter-fibre slippage during bending deformation. Additionally, the bending behaviour of fabrics in off-yarn direction can be lower than the on-yarn directions [78-80], indicating that the bending behaviour is orientation dependent.

| (a) | (b) | (c) |
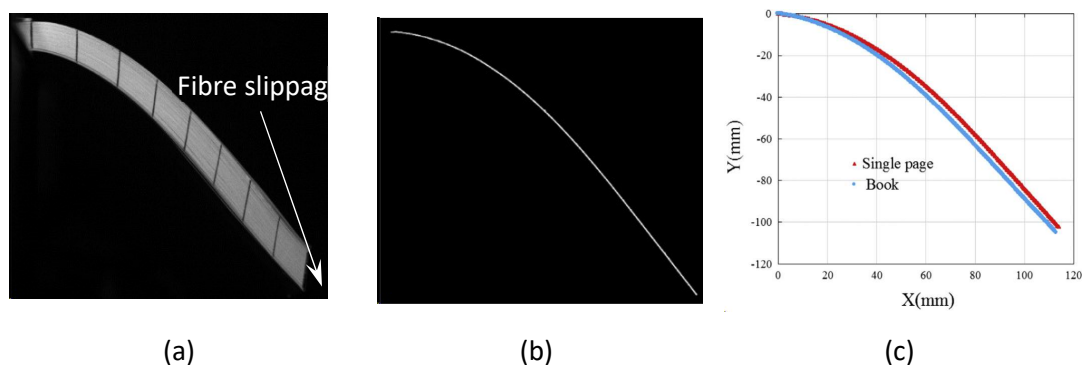
Figure 2.11: Cantilever bending: (a) global parallel fibre layers, (b) single fibre and (c) comparison of the mid-plane deflections. [56]

(a)　　　　　　　　　　(b)　　　　　　　　　　(c)
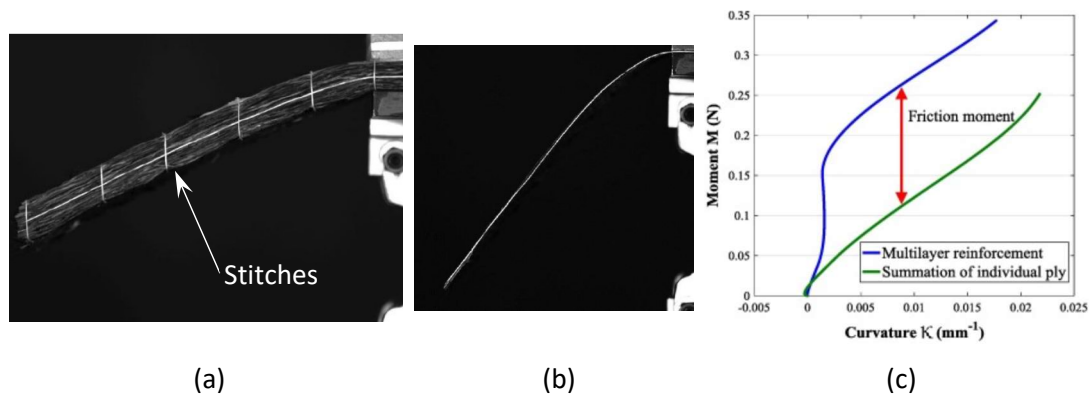
Figure 2.12: Cantilever bending: (a) multilayer reinforcements with stitches, (b) single fibre and (c) comparison of moment (per unit specimen width) vs curvature curves between multi-layer and single-layer reinforcements. [56]

The bending behaviour of fabric is related to the architecture of the yarns at the mesoscale. As shown in Figure 2.13(b), the yarn architecture is symmetric about the mid-plane for a balanced woven fabric, therefore the bending behaviour is independent of the bending direction (i.e. the direction of bending moment).
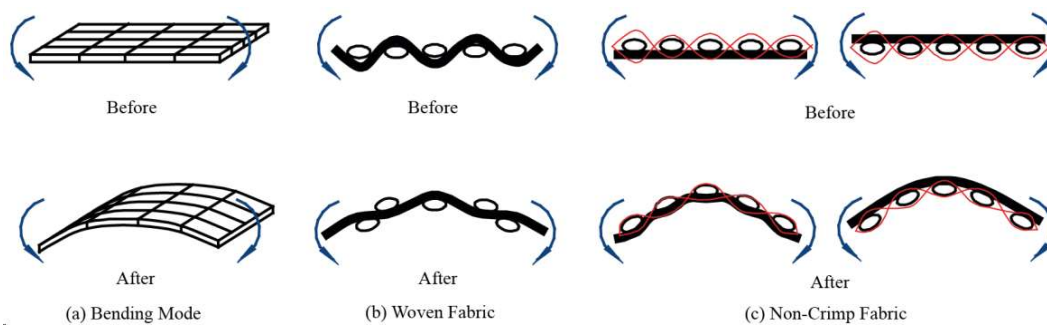
Figure 2.13: Out-of-plane bending mode and mechanisms for woven fabric and NCF respectively. [38]

For NCFs, stitches can provide some out-of-plane constraints on fibre slippage, and the bending moment is primarily carried by the yarns parallel to the deflection, as shown in Figure 2.13(c). Consequently, the bending behaviour of NCFs is dependent on the bending direction [81], due to the asymmetric fibre architecture in the through-thickness direction.

Although a linear bending moment-curvature relation has been typically adopted in the literature to describe the bending behaviour of fabrics at the macroscale, nonlinear bending resistance has commonly been observed in experiments for various fabrics [82-85]. As shown in Figure 2.14, fabrics tend to have a large bending stiffness under small bending deformation,

but the behaviour becomes non-linear and the bending stiffness decreases as the bending curvature increases due to slippage and buckling of fibres.
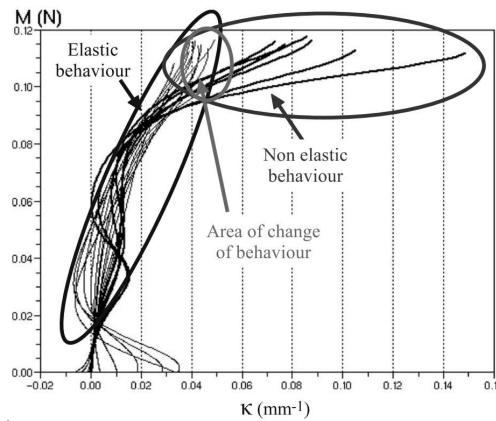
Figure 2.14: A typical nonlinear bending moment-curvature relation for a woven fabric. [82]

Hysteresis has also been reported for fabric bending behaviour during loading and unloading scenarios [86], corresponding to a quasi-plastic behaviour [87], which can be attributed to irreversible energy dissipation caused by inter-fibre friction [88]. This inelastic property may dominate the forming behaviour of fabrics if the punch displacement is reversed, however its influence is considered to be negligible on the forming deformation at the macro-scale when the punch displacement is monotonic [89]. The focus of the current work is therefore on the nonlinear elastic bending behaviour of fabrics.

2.3.2.4   Friction

The interfacial friction behaviour plays an important role in transferring loads from forming tools to the materials during the process [74]. The dynamic friction coefficient between the woven fabric and the aluminium tool surface is almost independent of the fibre orientation at the contact interface, while the inter-ply friction coefficient is much higher than the tool-fabric friction due to the compaction of yarns [90]. The fabric-tool friction coefficient typically decreases as the applied normal pressure increase, since the fabric surface becomes flattened as it is pressed against the tool [74, 91]. The inter-ply frictional behaviour is reported to be dependent on the relative fibre orientation between adjacent fabric plies, as yarns perpendicular to the sliding direction can provide some resistance to inter-ply movement [90, 92]. Moreover, the level of in-plane shear can change the surface topography of the fabric, therefore modifying the inter-ply friction behaviour [90]. The inter-ply frictional resistance for prepregs was reported to be a function of the forming rate and temperature, due to the influence on the viscosity of the resin [46, 93]. The inter-ply friction behaviour is

critical for forming multi-layered fabric plies with different orientations because incompatible shear deformation can be restricted by the frictional force and hence lead to wrinkling defects [94].

2.3.3   Forming related defects

Forming related defects can significantly reduce the mechanical performance of the final composite products. Defects at the macro-scale, such as out-of-plane wrinkles, introduced during the preforming stage can lead to fibre misalignment and resin-rich zones in the cured composite component [95, 96]. Fibre waviness at the macro-scale for example, can lead to significant reductions in both Young's modulus and compressive strength of unidirectional laminates (up to 70 % dependent on the severity of waviness) [20]. Therefore, it is important to understand the mechanisms behind the formation of these defects in relation to the corresponding forming process. In addition, robust methods are required to characterise the severity of these defects, in order to validate simulations reliably. Both macro and meso scale defects can be found in the preform produced by matched tool forming, while preforms produced by DDF are more sensitive to macro-scale defects due to the limited forming force available from the vacuum pressure and the lack of constraining force during material draw-in.

2.3.3.1   Defect mechanisms in matched tool forming

Commonly observed defect modes during matched tool forming are listed in Table 2.1, along with the primary formation mechanisms and applicable materials. Yarns move towards each other as the fabric shears in-plane, causing macro-scale (out-of-plane) wrinkles when local fabric buckling occurs due to excessive lateral yarn compaction [62] or stretching of stitches [72]. Therefore, the shear angle has been widely adopted in simulations to indicate the occurrence of "over-shear" induced wrinkling defects. However, wrinkles can also be found in regions where the shear angle is below the typical locking angle, therefore high shear regions do not always correspond to wrinkles [97]. This indicates that the wrinkling behaviour is a result of a global mechanical phenomenon dependent on the tensile, in-plane shear and most importantly out-of-plane bending behaviours. The overall wrinkle severity is also related to the complexity of the tool geometry because the fabric requires larger shear deformation to conform to sharp corners [98].

Table 2.1: Typical defect modes in matched tool forming.

Defect mode	Phenomena		Mechanism	Applicable materials
Macro-scale wrinkling			Fabric over shear Local compression	
Mesoscale wrinkling (out-of-plane & in-plane fibre buckling)	Out-of-plane buckling	In-plane buckling	fibre compression	NCF & Woven fabric
Fibre laddering			Transvers tension Contact friction	
Stitch damage	Stitch sliding	Stitch failure	Stitch failure	NCF only

Mesoscale wrinkling occurs in the fabric preform when yarns are subjected to longitudinal compression. These mesoscale wrinkles are either in the form of out-of-plane yarn buckles when the out-of-plane constraint is insufficient from the blank holder, or in-plane waviness when the blank holder force (BHF) is too high locally, causing the material to shear irregularly. This in-plane fibre buckling can be mitigated by adjusting the distribution of the BHF to provide axial tension in the yarns as required [31]. For a biaxial NCF with a pillar stitch pattern, through-thickness compression of the stitches in the negative shear regions were found to have less constraint on the fabric compared to straightened stitches under tension in the positive shear regions [98]. Therefore negative shear regions are more likely to develop mesoscale wrinkles for this type of fabric architecture, whereas tensile strain in stitches can provide some resistance to in-plane buckling of the fibres leading to out-of-plane wrinkling [98].

Excessive friction between plies or at the tool surface can damage the structural integrity of fabrics, leading to fibre laddering (i.e. transverse spreading of fibres) [90]. This type of defect is often found near sharp edges of the tool where fabric gets dragged by the tool-fabric frictional force. This defect mode is less likely to occur in regions where some shear
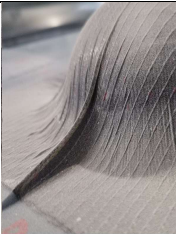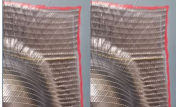
deformation has occurred, as shear-induced yarn compaction increase the stability of interlaced yarns [90].

Stitch damage is a unique defect mode for NCFs, typically in the forms of stitch failure and excessive stitch sliding. Due to the failure of stitches, the mesoscale architecture tends to become unstable and additional defects occur in the form of in-plane waviness and laddering.

2.3.3.2   Defect mechanisms in diaphragm forming

Surface defects including wrinkling and bridging (See Table 2.2), are more likely to occur [21, 40, 99, 100] in diaphragm forming, since the out-of-plane constraint to the ply stack is much less than for matched-tool forming. When forming NCF plies over double curved geometries, the formation of wrinkles was found to directly correlate with the level of shear deformation, giving an indication of the severity of yarn compaction [21]. This shear locking behaviour is dependent on the mesoscale architecture of the fabric. A biaxial non-crimp fabric (NCF) with a pillar stitch pattern was reported to be more prone to positive shear related wrinkling [101] compared to a comparable woven fabric with lower shear resistance, which enables more in-plane shear deformation prior to shear locking [100]. In addition to fabric over shear, fabric plies can bridge over the concave region of the tool due to insufficient slippage between the diaphragm and the tool, causing compressive strains perpendicular to the bridging path to trigger wrinkles [21]. This type of bridging related wrinkles is more relevant to the tool geometry and can occur in regions with insignificant shear deformation [100].

Table 2.2: Typical defect modes in diaphragm forming.

Defect mode	Phenomena	Mechanism	Applicable materials
Macro-scale wrinkling		Fabric over shear Local compression	NCF & Woven fabric
Fabric bridging		Insufficient material-tool slippage	

The initial orientation of the fabric blank with respect to the tool position can influence the local bending direction of yarns relative to the tool features, leading to different wrinkle patterns around doubly-curved surfaces [100]. Inter-ply slippage can occur when forming a stack of UD prepreg plies, as each ply within the layup exhibits different deformability in

relation to the tool geometry. This relative ply sliding can be constrained by the frictional resistance at the contact interface, which can lead to compressive forces in the fibre directions and therefore unwanted ply buckling at the macro-scale [47, 94].

Fabric bridging, also known as the poor fabric-tool conformity, is another commonly observed defect during diaphragm forming. It usually occurs in the deep concave areas of the tool where the material draw-in is prevented by the large diaphragm-tool friction [21]. For fabric prepregs, the bridging distance can be dependent on the forming rate, as the friction behaviour of prepregs is rate dependent due to the viscosity of the resin. Since the fibres in the bridged area are typically in tension, tensile strains along the fibres can be used to locate potential bridging defects from forming simulation results.

2.3.3.3   Defect measurement

Quantitative assessment of the quality of preforms relies on good characterisation data of forming related defects. A range of metrology methods have been used to capture and digitise defects in fabric preforms, supporting the validation of computational models. The main drawback of these techniques is that they only capture the effects of the defect at the outermost surfaces, therefore it can often be difficult to establish the root cause of a defect if it was initiated within a sub-surface ply.

The scattering effect of a slit laser light was successfully used to quantitatively characterise the wrinkling level of a NCF preform produced by a hemispherical tool [31]. However, it is difficult to obtain a 3D representation of wrinkles over the surface of the preform using this technique. Coordinate-measuring machines (CMM) can be used to measure the geometry of defects by sensing discrete points on the surface using a probe. This method was successfully used to retrieve the distribution of shear deformation of a consolidated preform [30]. However, the measuring process is time-consuming for complex 3D surfaces containing defects and the maximum achievable resolution is too low to capture small-scale defects.

There are also a range of commercially available techniques that can offer more straightforward measuring procedures and more robust data. Harrison et al. [80, 102] used digital image correlation (DIC) to measure shear deformation and out-of-plane wrinkles for woven fabrics during bias-extension tests. This technique was used by Viisainen et al. [98] to monitor the development of wrinkles during forming NCFs using different geometries. Carbon fabrics have to be pre-treated before DIC testing to provide a non-reflective surface, covered by a high contrast, random speckle pattern. Graphite powder sprays can be used to remove the reflection of carbon fibres and viscous white paint can be used to produce the

speckle pattern on the fabric surface, but it is possible that this may affect the mechanical properties of the fabric. The speckle pattern is also liable to degradation due to yarn rotation and sliding, causing problems with pattern-tracking. The Apodius 3D Vision System is able to map the surface texture of fabrics onto the 3D geometry of the preform by integrating a laser scanner with a camera censor, enabling effective detection of in-plane yarn misalignment [103].

2.4   Material characterisation

The mechanical properties of fabric reinforcements should be characterised to evaluate their formability and also to supply input data for process modelling and design. Only non-standard testing methods are typically available to characterise the mechanical properties of unconsolidated fabrics [104]. Numerical process simulations have been widely used to reduce the cost of design-for-manufacture, by predicting the location and severity of manufacturing defects instead of experimental trial and error [57, 105]. Furthermore, the change in fibre orientation due to the forming process can be predicted and used to facilitate downstream modelling of the resin infusion process and to determine the structural performance of the final component.

2.4.1   In-plane tension

2D woven fabrics can exhibit an initial non-linear stiffening at a small tensile strain (<0.5%) due to the de-crimping effect of undulated yarns under tension. Moreover, the straightening of yarns tend to influence the tensile behaviour in the other direction. Therefore, the biaxial tensile testing rig, as shown in Figure 2.15(a), is typically used to characterise the tensile stiffness of woven fabrics. The fabric specimen is prepared to be similar in shape to a cruciform, where the square central region is the area of interest. Due to the low structural integrity of dry woven fabrics, the transverse yarns in the arms of the specimen can be easily removed without significantly influencing the direction of the longitudinal yarns parallel to the loading direction. This ensures the longitudinal yarns are uncrimped as the load is applied. Tests can be performed according to a range of ratios between strains in the warp and weft directions to generate a "tension surface" for describing the tensile behaviour of fabrics, as shown in Figure 2.15(b). For NCFs, the yarns in each ply are almost straight as they are not interlaced, but the tensile behaviour appears to be non-linear due to the influence of stretching the stitches during the test.

While the in-plane tensile behaviour of fabrics is nonlinear and dependent on the biaxial strain ratio, the axial stiffness in the principal yarn directions is often assumed to be linear and independent from each other in process simulations. This assumption has been adopted in simulations for both woven fabrics [59, 106-108] and NCFs [21, 30, 109] without significantly compromising the accuracy of the predictions. Forming simulations based on the explicit finite element solution require the time increment during the analysis to be small enough to ensure numerical stability. For isotropic linear elastic materials without damping, the maximum size of the stable time increment Δt in Abaqus/Explicit can be estimated by the characteristic length of the element L_e , material density ρ_e and modulus E_e [110]:

$$\Delta t = L_e \sqrt{\frac{\rho_e}{E_e}} \tag{2.1}$$

Similar effects apply to the value of the fabric modulus in the forming simulation. Consequently, large values for the Young's modulus in the yarn directions (i.e. >100 GPa) can lead to unaffordable run times for FE-based forming simulations. Hence, an appropriate reduction in Young's modulus (i.e. < 10 GPa) is recommended to reduce the run time, whilst ensuring the artificial modulus is sufficient to ensure that the axial strain does not surpass 1% [80].
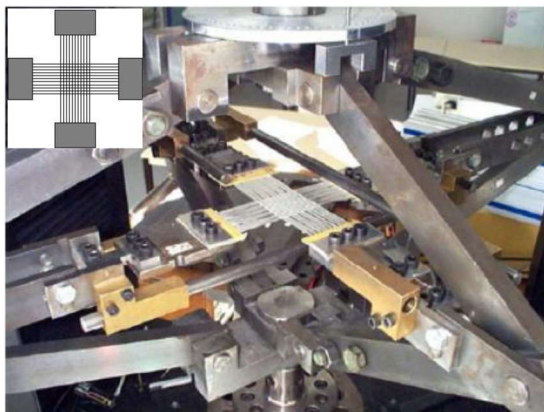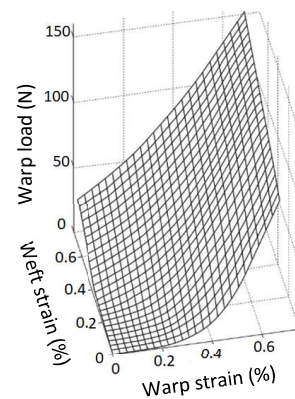
(a)   (b)

Figure 2.15: Biaxial tension characterisation: (a) biaxial tensile testing rig [111] and (b) typical tension surface of a woven fabric [55].

2.4.2   In-plane shear

The in-plane shear behaviour of biaxial fabrics can be characterised by either picture frame shear tests or bias extension tests [104, 112].

In the picture frame shear test, a cross-shaped fabric specimen is clamped by a square frame hinged at the four corners, with the primary yarns aligned with the edge of the frame as shown in Figure 2.16(a). One vertex is connected to the cross-head and the opposite one is attached to the ground. A displacement is then applied through the cross-head to drive the hinged 4-bar linkage to apply in-plane shear deformation to the specimen. The cross-head force is recorded by a load cell and its displacement is measured by a displacement sensor. The shear deformation of the fabric specimen can be calculated according to the changes in the shape of the rig through trigonometric relations, using either the cross-head displacement or by optically measuring the yarn orientation at the centre of the specimen [104]. Several tests should be performed without specimens loaded in the frame to obtain the cross-head force to balance the weight and inertia of the rig during the test [104]. This additional force should be deducted from the recorded cross-head force to extract the shear force derived from shearing the fabric. The shear force should be normalised to enable the comparison of fabric shear behaviour using different specimen dimensions [60, 104, 113].

In the bias extension test, a rectangular fabric specimen is clamped by the grips connected to the cross-heads of a testing machine, with the yarns initially oriented at ±45° to the direction of the tensile load applied, as shown in Figure 2.16(b). The whole fixture is loaded into a universal testing machine, with a vertical displacement applied to the clamp edge to produce shear deformation in the central region of the specimen (i.e. Zone A in Figure 2.16(b)). The tensile load is recorded by a load cell during the test. Ideally, Zone C should remain un-deformed and the shear deformation in Zone A should be twice the shear angle in Zone B [114]. The total length of the specimen must be at least twice the width to ensure the deformation in region A is equivalent to pure shear [112]. However, slippage between yarns at their crossovers easily occurs during shear deformation, particularly for woven fabrics, which can affect the pure shear condition in Zone A. It was therefore suggested by Harrison et al. [80] that the intra-ply yarn slippage near the boundary of Zone C and Zone B can be mitigated by bonding a triangular aluminium foil to Zone C to enhance the 'encastre' boundary condition. The shear angle in Zone A can be obtained by analysing timed images recorded during the test, and the shear force can be determined by normalising the cross-head force using an iterative procedure to ensure consistency for specimens with different dimensions [115].
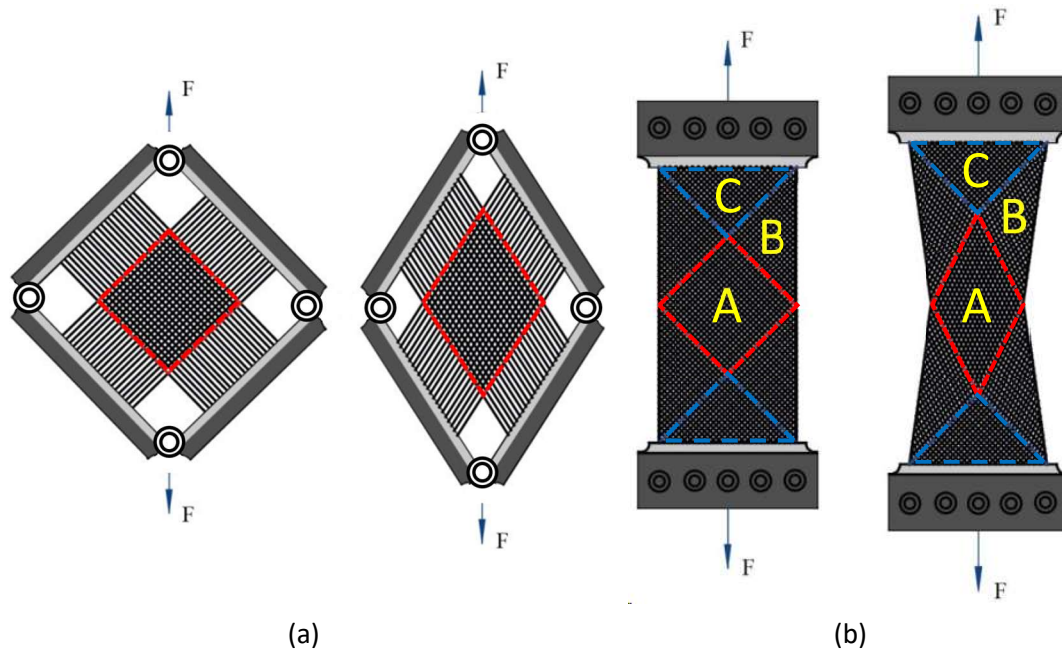
Figure 2.16: Schematics of the testing mechanism in (a) picture frame shear test and (b) bias-extension test. [38]

In general, both of these two tests are simple to perform, but the validity of each test is commonly debated in the literature because the shear kinematics involved in each test are different [104, 112]. The pin-jointed square frame used in the picture frame test ensures homogenous shear deformation over almost the entire specimen, and the shear rate can be easily controlled during the test. However, unintentionally, the picture frame introduces tension in the yarns, which can influence the cross-head force during the test [60], leading to poor repeatability . Therefore, careful attention needs to be paid to aligning the specimen in the rig and appropriate clamping conditions need to be applied at the boundary. Whereas in bias extension test, the shear deformation in different regions of the specimen are different (i.e. Zone A, B and C in Figure 2.16(b)), inter-yarn slippage can therefore occur around the boundary of each region, leading to inaccuracies [116]. Moreover, when characterising fabrics with low shear resistance, it is difficult to avoid initial pre-shearing of the fabric due to installing the specimen in the testing machine. This can adversely affect the measured shear load and shear angle [117]. The wrinkling behaviour of fabrics during the bias extension provides an effective way to characterise the onset point of "shear locking", but this can also result in errors (up to 20%) in the perceived shear angle due to the wrinkled specimen surface [117]. To mitigate the growth of wrinkles during the bias extension test, a pair of anti-wrinkle plates are recommended by Harrison et al. [102] to provide some out-of-

plane clamping to the specimen, enabling more reliable and repeatable data compared to the conventional bias extension test.

The selection of a suitable characterisation method is dependent on the type of fabrics. In the bias extension test, the sliding between the two unidirectional layers within a biaxial NCF can disrupt the kinematics of the test [118, 119]. For pillar stitched NCFs, stitch failure can occur locally when the cross-head extension is parallel to the stitch direction of the specimen during bias extension testing [72]. This stitch failure can propagate as the shear deformation develops, leading to significant sliding between yarns and hence non-uniform shear deformation. As a result, the expected pure shear condition in the central region of the specimen (i.e. Zone A in Figure 2.16(b)) is no longer valid.

2.4.3   Out-of-plane bending

It is important to characterise the bending behaviour of fabrics to provide reliable input parameters for the bending stiffness, so that the shape and size of wrinkles can be explicitly predicted during process simulations [97]. Three-point bending can be used to characterise the bending behaviour of thick fabric reinforcements or prepregs with large bending stiffness [120, 121]. However, this method is less relevant to 2D fabrics with low bending stiffness as the bending deformation is easily affected by gravity.

The conventional cantilever testing method developed by Peirce [122] has been widely used for characterising the bending stiffness of cloths and fabrics, with two dedicated test standards available [123, 124]. Figure 2.17(a) shows a typical apparatus for the conventional cantilever test, in which the specimen is placed on the platform with a steel rule on top. The specimen deforms under its own weight as the steel rule is pushed forwards, until the specimen tip reaches the specified deflection angle of the plate. The bending stiffness can then be calculated based on the specimen overhang and the deflection angle. This approach is simple to perform but it only provides a constant bending stiffness describing the fabric bending behaviour. Therefore, modifications have been made to the conventional cantilever test to characterise the non-linear behaviour of fabric bending.

Clapp et al. [125] added an optical module to record the shape of the deformed specimen in more detail, using numerical differentiation to calculate the bending moment and curvature at discrete points along the specimen. This provides a non-linear relation to describe the fabric bending behaviour as a function of curvature. Bilbao et al. [82] modified the cantilever rig to progressively increase the overhang of the specimen, with a series of deformed

specimen shapes captured by a camera. During the test, each section along the specimen length was initially loaded with the maximum bending load at the embedded point and then unloaded as the overhang increased. The bending behaviour during unloading can be characterised by tracking the moment and curvature of a specific section of the specimen during the test. This enables the inelastic behaviour of the fabric to be characterised. To improve the accuracy of the bending profile, Liang et al. [83, 126] used a 'skeletonisation' method to extract the midline of the specimen through the images taken by the camera. This bending profile was fitted using a quartic B-spline to provide a smooth variation of curvatures along the specimen. Specimens should be positioned vertically to avoid tip twist during the test, with the bending load applied horizontally using an additional mass [127, 128] or linear actuator [84], as shown in Figure 2.17(b) and Figure 2.17(c) respectively. The precision of the calculated moment and curvature is highly dependent on the accuracy of the measured profile of the deformed specimen, but using optical methods may produce parallax error. Therefore more accurate photogrammetry methods are required to obtain more accurate 3D representation of the specimen rather than a 2D profile from image analysis.

(a)   (b)   (c)
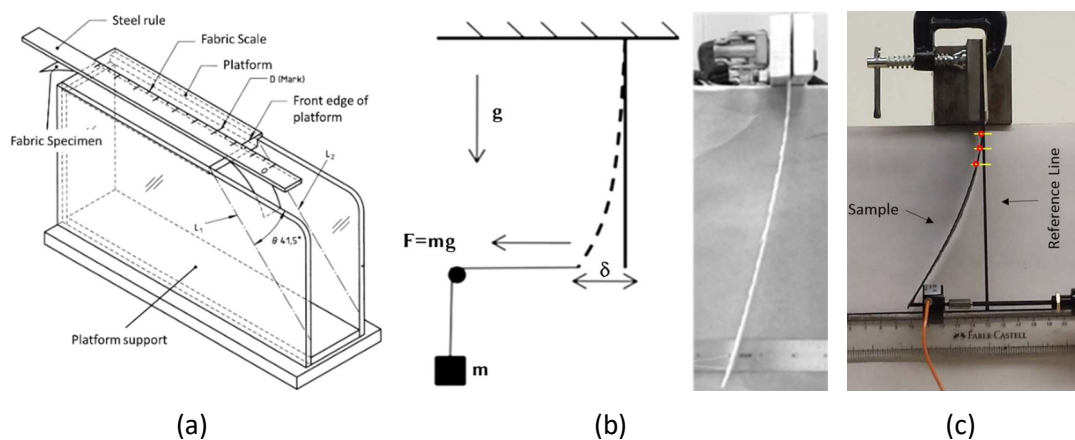
Figure 2.17: Setups of different forms of cantilever tests. (a) Conventional cantilever test loaded by gravity [123] and vertical cantilever tests loaded by (b) a mass [128] and (c) a linear actuator [84].

The Kawabata bending tester is designed to produce a pure bending configuration for fabric specimens, enabling the bending moment-curvature relationship to be directly measured [82, 86, 129]. As shown in Figure 2.18(a), a specimen is held between a fixed clamp and a moving clamp. The moving clamp rotates following a circular path to induce a constant curvature along the specimen length, with the bending moment directly measured by the device. This method enables the loading rate and loading path to be controlled during the test, therefore

it can be used to characterise the rate-dependent or hysteretic behaviour of fabrics during bending. As shown in Figure 2.18(b), Sachs et al. [130] proposed a similar fixture to use in a rheometer to control the temperature and bending rate. Compared with the Kawabata bending tester, this simplified fixture (See Figure 2.18(b)) can easily be incorporated into a thermal chamber to characterise the effect of forming temperature on the bending behaviour of prepregs.
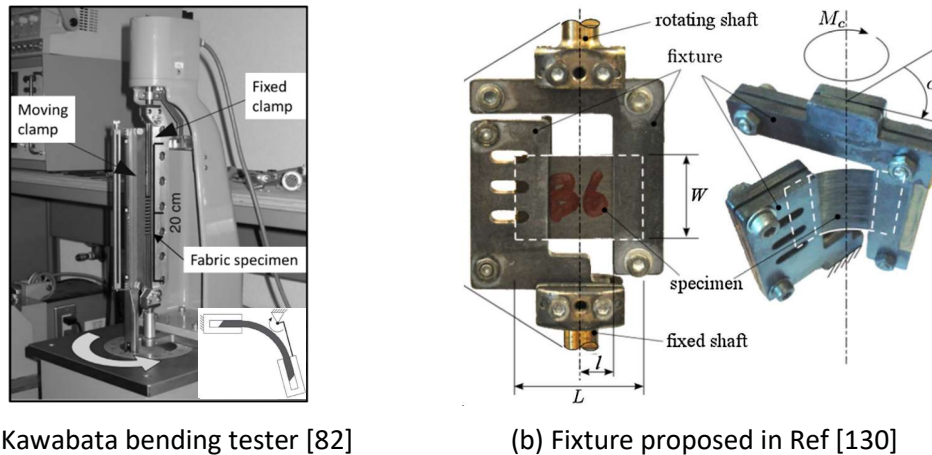
(a) Kawabata bending tester [82]   (b) Fixture proposed in Ref [130]

Figure 2.18: Bending test setups using the principal of Kawabata bending tester. [82, 130]

In summary, the selection of bending tests is dependent on the type of fabric reinforcement and the required input parameters for process simulation. The focus of this thesis is exclusively 2D dry fabrics, where their bending stiffness is typically much smaller than values reported for prepregs or thick interlock fabrics. The cantilever test has therefore been revised to characterise their bending stiffness. A nonlinear elastic bending behaviour under monotonic loading is considered in this thesis, since forming simulations do not generally require the hysteretic bending behaviour [57].

2.4.4   Friction behaviour

The "sled test" and "ply pull out test" are common approaches for measuring the interfacial friction experienced during forming processes [21, 131, 132]. The schematics of these two test are shown in Figure 2.19.
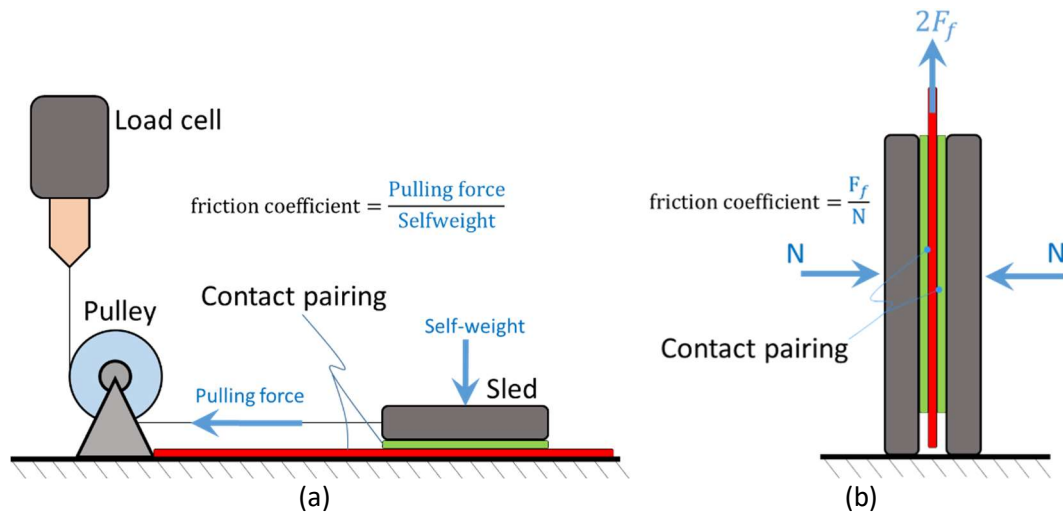
Figure 2.19: Schematics of typical friction test setups. (a) Sled test and (b) ply pull out test.

For the sled test, material specimens are attached to the surfaces of the sled and the table to represent the surface pairings in the forming process, as shown in Figure 2.19(a). The sled is loaded with its own weight to apply a normal pressure at the contact surface. The tangential force required to move the sled at a constant velocity across the table is measured. The friction behaviour is characterised by the ratio between the pulling force and the normal force. In order to reduce edge effects, the specimen attached to the sled is usually designed to cover the front edge of the sliding block [132]. Rotation of the sled needs to be prevented during the test, in order to ensure a uniform pressure distribution at the friction surface. This can be achieved by adjusting either the position of the normal force or the vertical offset of the horizontal pulling force to eliminate any possible moment.

For the ply pull out test, a central fabric ply is sandwiched between two other plies, held together by a controlled normal pressure, as shown in Figure 2.19(b). The fabric specimen is pulled out and the pulling force and normal pressure are recorded during the test. The friction behaviour can be characterised according to the relation between the pulling force and the normal pressure. During the "pull out test", new uncompressed material is pulled into the contact area and subsequently subjected to normal compressive force, which can lead to additional shear in the specimen [132]. This can be minimised by guiding the middle specimen in the contact area using rigid metal foils, or by inserting additional metal shims [132]. When testing biaxial fabrics with different fibre orientations on both sides, the central specimen in Figure 2.19(b) can be replaced by a rigid plate with fabric specimens attached to both sides. Thus, the relative fibre orientation for both contact areas is the same with respect to the pulling direction.

The "sled test" is simpler to perform compared to the "ply pull out test", as it does not require specific fixtures to be developed to hold the specimens in place. The contact area remains constant during the "sled test", ensuring a uniform and constant normal pressure over the contact area. However, since a dead weight is typically used to apply the normal force, the magnitude of the normal pressure is not necessarily representative of the forming pressure; particularly for the DDF process (1×10^5 Pa). In comparison, the normal pressure during the "ply pull out test" can be controlled as required, but the contact area decreases as the central specimen is pulled out, which leads to a non-uniform normal pressure at the contact surface [133]. Gorczyca-Cole et al. [134] extended the length of the central specimen over the opposite edge of the pull-out direction, in order to ensure the contact area and normal pressure were constant during the test, but this may lead to edge effects as the fabric enters the contact region.

2.5   Process simulation and design

2.5.1   Simulation approaches

2.5.1.1   Kinematic approach

Kinematic forming simulations are primarily based on geometrical mapping, in which the fabric is modelled as a pin-jointed net of rigid bars that can only undergo shear deformation at the crossover points. As shown in Figure 2.20(a), two geodesic paths (i.e. lines marked in bold) are generated as a starting point and then the other yarns are subsequently mapped onto the surface of the tool by solving geometric equations [135]. The obtained net shape of the preform (see Figure 2.20(b)) can be used as a ply cutting template. When forming fabrics with asymmetric shear behaviour (i.e. NCFs), an iterative scheme is recommended to improve the accuracy of the prediction, by searching for the mapping pattern that results in the minimum shear energy [135].

(a)   (b)
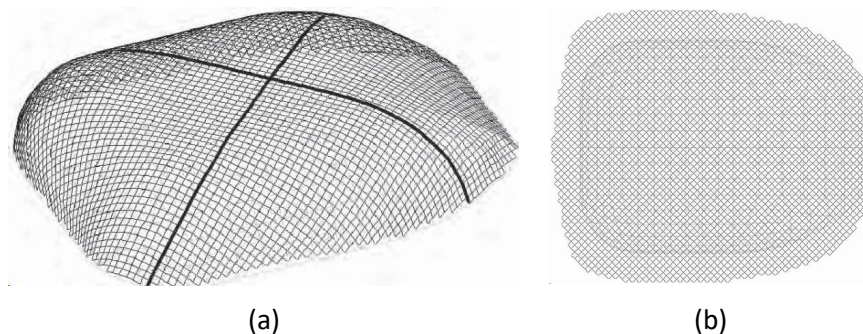
Figure 2.20: An example of kinematic draping simulation. (a) Yarn pattern based on initial geodesic paths (marked in bold). (b) Predicted net-shape for ±45° ply. [135]

Kinematic forming simulations can provide a fast prediction for fabric shear deformation, but they overlook all of the material properties and boundary conditions associated with the forming process. In kinematic analyses, the formability of fabrics with respect to a certain tool geometry are examined by comparing the local shear angle against the shear locking angle measured from experiments. However, the explicit shape of defects and the forming load required to deform the fabric are overlooked [61]. Moreover, the inter-ply frictional behaviour is not considered, which can further comprise the precision of the predicted shear angle, particularly for multi-layered fabric plies. Therefore, a simulation technique considering the constitutive relations of materials and all boundary conditions is required to deliver more realistic forming analyses.

2.5.1.2   Finite element approach

Finite Element (FE) simulations enable the physics of the forming problem to be modelled and therefore consider the influence of process parameters, including contacts and friction between the components. Consequently, they can be used for more detailed analyses to indicate the likelihood of defects, such as fabric wrinkling, bridging and ply splitting. The fabric forming process is a quasi-static process, which can be simulated by either implicit or explicit finite element methods [49, 136]. The implicit method is generally suited to static and quasi-static processes, but the computational cost can be high, as a system of non-linear equations needs to be solved multiple times. With an implicit algorithm the new state cannot be calculated directly from the old state, so a coupled system of equations must be solved. The time increment is not limited by stability issues and therefore much larger time increments can be used compared to explicit analyses. However for simulating a forming process, large nonlinearities, large sliding and frequent changes of contact conditions can easily lead to convergence difficulties, causing more iterations or a reduction in the stable time increment. Convergence problems may also occur due to the formation of forming induced wrinkles where the force and contact equilibrium is difficult to achieve due to fabric buckling. The implicit technique is therefore not ideal for fabric forming simulations. In comparison, explicit analyses determine the current deformation state based on a forward Euler integration scheme, enabling the deformation state at the end of a time increment to be determined by integrating the acceleration at the starting point of the time increment. This algorithm does not require iterative analyses to reach force equilibrium within each time increment, it basically uses an extrapolation. Contact changes or wrinkling instabilities

therefore do not lead to convergence issues. An explicit solver is therefore considered to be more suitable for fabric forming simulations.

Numerical approaches for forming simulation include the continuous approach, discrete or mesoscopic model and the semi-discrete element formulation. Whilst the yarns are explicitly constructed using finite elements in discrete or mesoscopic models, the mechanical response of fabrics is calibrated based on the material properties characterised at the macro-scale [137].

(1) Continuous approach

Fabric reinforcements are homogenised and are considered to be continuous mediums with this approach. Their mechanical properties are modelled via the constitutive relations characterised by experimental data. This approach has been widely used in forming simulations, as it can be easily implemented into classic finite element codes without modifying element formulations. However, special treatments are required in the material model to track the changes in fibre directions, since the fabric material experiences large shear deformation between warp and weft yarns during forming,. This can be achieved by employing either hypoelastic or hyperelastic laws to describe the forming behaviour of fabrics.

- Hypoelastic continuous model

When the fabric material behaviour is described under the framework of a hypoelastic law, non-orthogonal constitutive relations are typically used to track the re-orientation of yarns. Yu et al. [138] developed a non-orthogonal model for woven fabrics by analysing the deformation kinematics and force equilibrium of a fabric unit cell. This model has been extended to model NCFs [109], incorporating a constant bending rigidity by assigning different values for the tensile and compressive moduli at the integration points through the thickness of the shell element [77]. However, the membrane and bending rigidities are not independently controlled with this approach, which may lead to unrealistic results when the element cross-section is subjected to combined loads. Harrison et al. [139] combined this model with a rate and temperature dependent unit cell energy model [140] to predict the viscous shear behaviour of woven fabrics. This hybrid FE model was used by Lin et al. [64] to optimise the distribution of the blank holder force to minimize wrinkling defects.

Based on the stress and strain transformations between orthogonal and non-orthogonal coordinate systems, Xue et al. [141] proposed a non-orthogonal constitutive model to describe the material behaviour of woven fabrics under large deformation. It was shown that

overlooking the non-orthogonality in woven fabrics can significantly over-predict (> 1000%) the shear force in picture frame tests, demonstrating the importance of using non-orthogonal constitutive models for fabric forming simulations. Peng et al. [142] derived a constitutive matrix expressed in the orthogonal coordinate system for woven fabrics, by transferring the constitutive matrix defined in the non-orthogonal coordinate system coincident with the primary yarns. Both the orthogonal and non-orthogonal constitutive models were used by Peng et al. [143] to simulate a hemispherical forming, with the predicted shear angle, material draw-in and punch load compared against experimental data. Results indicate that using an orthogonal constitutive model for forming simulation can significantly over-estimate the rigidity of the fabric, whereas the prediction by the non-orthogonal constitutive model was in good agreement with the experimental data.

However, directly defining the constitutive relation of fabrics in the Green-Naghdi frame is questioned in Badel et al [144] as this may lead to spurious stresses during large shearing of an element. Therefore, the stresses are calculated through the constitutive relation defined in the fibre parallel frames and then transformed back to the Green-Naghdi frame to update the stress to ensure an objective derivative [144]. This approach was validated by simulating the forming process using a hemispherical tool [106] and a double dome tool [145] for woven fabrics. Based on the same principal, Chen et al. [30] developed a non-orthogonal constitutive relation to predict the asymmetric shear behaviour of a NCF with a pillar stitch pattern. This model was used by Chen et al. [30] to identify potential defects in a NCF preform with a complex shape produced by double diaphragm forming process. Boisse et al. [97] reported that the wavelength and amplitude of wrinkles are dependent on the magnitude of the bending stiffness used in the fabric forming simulation. However, the bending stiffness is overlooked when membrane elements are used to represent the fabric plies. Consequently, membrane-element-based forming simulations are unable to deliver realistic predictions for the shape of wrinkling defects, even when using a fine mesh discretisation.

Recent works have extended the non-orthogonal hypoelastic model to simulate the bending behaviour of fabrics by modifying the FE discretisation for fabric plies. Dörr et al. [146] assembled membrane elements and shell elements in the through-thickness direction to model the fabric ply, which enables the in-plane stiffness and bending stiffness to be independently controlled in the simulation framework. Consequently the bending behaviour can be updated with the fabric shear deformation, as the bending contribution of each fibre is defined in the fibre parallel frame that rotates as the fabric shears. Schirmaier et al. [27] have extended this model to simulate the forming of stitched unidirectional non-crimp

fabrics. The hypoelastic fabric model developed by Thompson et al. [147] used a single layer of membrane elements sandwiched between two layers of shell elements to model the fabric ply, where the two surface shells account for the fabric bending behaviour. However, these models do not take full advantage of the continuous approach because additional elements are introduced to represent the bending stiffness of the fabrics, which can considerably increase the computation costs.

- Hyperelastic continuous model

Hyperelastic constitutive models for fabrics are typically derived from the strain energy functions associated to different deformation modes. Aimène et al. [148] implemented an anisotropic hyperelastic model into membrane elements to model the forming behaviour of woven fabrics, by defining the total strain energy terms as a sum of energies from the yarn tensile and fabric shearing contributions. This model assumed that the coupling effect between tension and shear is negligible; with the model parameters determined using two tensile tests in the warp and weft directions and one pure shear test. A similar method was used by Peng et al. [149] to model a benchmark double dome forming. These models were proposed for 2D fabrics, but the bending stiffness was still overlooked.

Charmetant et al. [121] developed a hyperelastic model for simulating a 3D woven interlock fabric. The strain energy density function was assembled by six strain energy functions related to six deformation modes (i.e. transverse compression, in-plane shear, tension in the warp and weft directions, transverse shear in the warp and weft directions, as shown in Figure 2.21). The material parameters were determined by four mechanical tests, i.e. in-plane tensile, transverse compression, in-plane shear and transverse shear tests, corresponding to the deformation modes assumed in the numerical model. The bending behaviour is inherently considered by the transverse shear and compression modes in the numerical model, but the predicted bending deformation differs from experimental observations for the three point bending tests, as shown in Figure 2.22(a) and Figure 2.22 (b). To improve the performance, beams elements were added to continuum elements to correct the predicted bending deformation, which inevitably increased the degrees of freedom (DOFs) of the model.
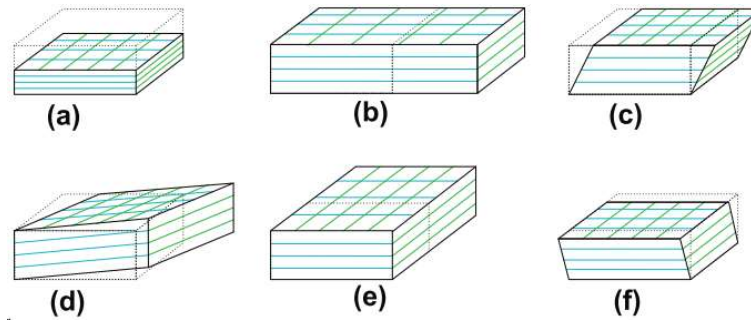
Figure 2.21: Typical deformation modes in a hyperelastic model for interlock reinforcements. (a) transverse compression, (d) in-plane shear, (b and e) tension, (c and f) longitudinal shear. [121]
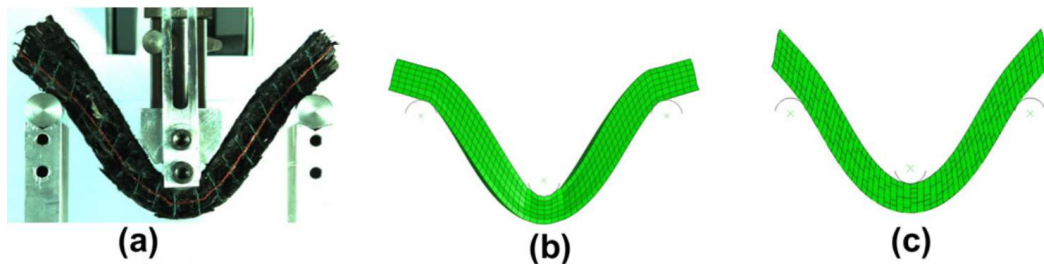
Figure 2.22: Comparison between experiment and simulation for three-point bending tests: (a) Experiment, (b) simulation by the hyperelastic model in [121] and (c) simulation by combining the hyperelastic model in [121] and additional beams. [121]

Guzman-Maldonado et al. [150] developed a viscous-hyperelastic constitutive model with fabric thermal properties to model the forming process of thermoplastic prepregs, by including the strain energy that results during bending deformation. The fabric bending behaviour was characterised by a cantilever test and the bending deformation in the numerical model was described by a curvature tensor.

The formability of thick interlock fabrics or prepregs is derived from multiple deformation modes (see Figure 2.21), therefore hyperelastic models are more relevant for simulating the forming process for these materials. In comparison, the hypoelastic model, using a non-orthogonal constitutive relation, is more commonly used for modelling thin 2D fabric sheets, where out-of-plane wrinkles are the typical form of defects.

(2) Discrete or mesoscopic model

Both discrete and mesoscopic models are based on the meso-structure of the fabric unit cell. In discrete models, the yarns are explicitly built using 1D elements (i.e. truss or beam elements) and superimposed on 2D elements (i.e. membrane or shell elements) to replicate the fabric unit cell. Updating the yarn orientation following any shear deformation is

generally not required, since these are automatically tracked by the rotation of the 1D elements representing the corresponding yarns. However, the number of DOFs in discrete models is generally larger than the continuous approach and the element edge has to be aligned with the fibre directions.

Sharma and Sutcliff [151] built a square fabric unit cell by connecting four truss elements via pin joints, with an additional truss element placed in the diagonal direction to take the shear stiffness into account, as shown in Figure 2.23(a). Skordos et al. [152] modified this model by employing two truss elements along both diagonal directions of the square unit cell to model the non-linear shear behaviour of woven fabrics, as shown in Figure 2.23(b). The compressive strain in the diagonal truss elements was used to indicate the wrinkling defects. Fabric unit cells were modelled using a network of spring elements (see Figure 2.23(c)) including rotational springs at the cell corners to account for the flexural rigidity of fabrics [153]. The rotational spring defines the relation between the bending moment and the rotational degrees of freedom at the cell corners, therefore enabling the strain energy derived from fabric bending to be considered. However, a network of 1D elements without surface elements is unable to appropriately model the ply-tool and ply-ply interactions during forming.
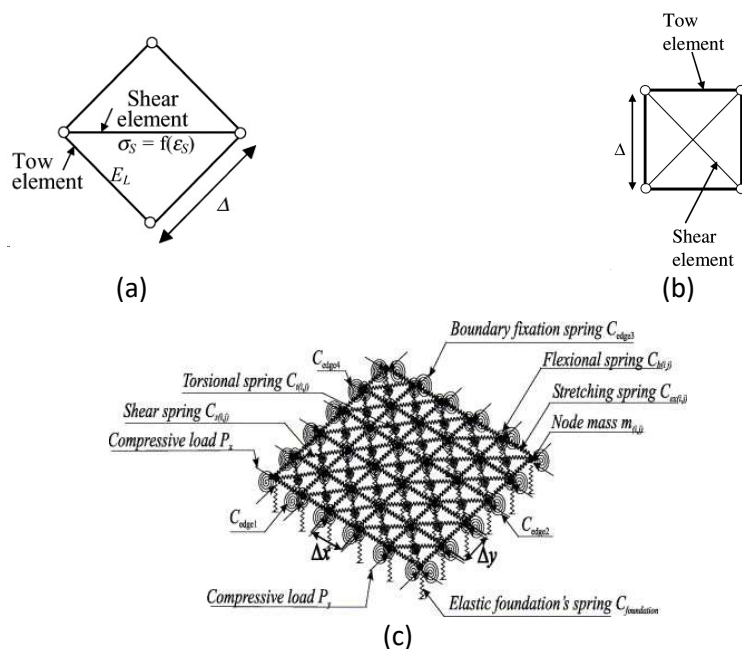
Figure 2.23: Schematics of typical discrete fabric unit cells established using 1D elements. (a) A square unit cell with one diagonal truss [151], (b) a square unit cell with two diagonal truss [152] and (c) fabric unite composed of a network of spring elements [153].

Recently, Harrison [108] developed a pantographic model by superimposing beam and membrane elements to build the fabric unit cell, as shown in Figure 2.24. The in-plane shear resistance is implemented in the membrane element, while the bending and torsional rigidities were incorporated by beam elements, enabling the in-plane and out-of-plane stiffness to be independently controlled. A comprehensive characterisation methodology was proposed in [80] to provide the input data for forming simulation. The out-of-plane bending stiffness was calibrated from a cantilever test, which allows wrinkling behaviour to be included in the simulation of the bias-extension test. Similarly, Dangora et al. [128] proposed a fabric unit cell composed of beam and shell elements, with the bending rigidity implemented by assigning different tensile and compressive moduli to the through-thickness integration points in the beam elements. These models allow bending stiffness to be implemented in the simulation framework, but the reported computational costs is still high due to the large number of (DOFs) introduced by structural elements and connectors. Thus, simulations using discrete models are usually limited to small domains. In addition, a constant bending stiffness is typically used in these models for simplicity, but non-linear bending behaviour has been observed in experimental studies [57] due to the friction between fibres and local fibre buckling. Different bending stiffnesses were also reported for biaxial NCFs made up of two stitched unidirectional plies when tested at different specimen orientations [81].
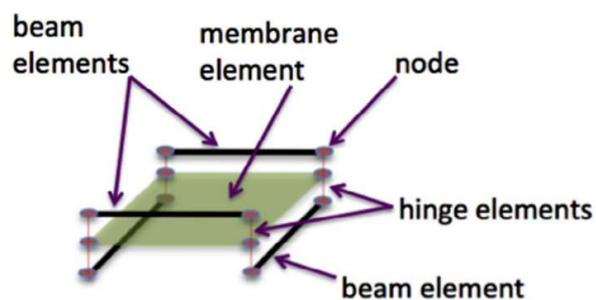
Figure 2.24: Schematic of the mutually constrained pantographic beam & membrane mesh. [108]

A mesoscopic model is a more detailed version of a discrete model, in which yarns are explicitly defined using 2D or 3D elements and the contact interactions between yarns and stitches are also included. Badel et al. [154] proposed a mesoscopic unit cell model for woven fabrics by explicitly defining the weft and warp yarns using 3D solid elements (see Figure 2.25(a)), and the inter-yarn interaction was modelled using a Coulomb friction model. A

hypoelastic constitutive model [144] was employed to describe the mechanical behaviour of the individual yarns. This model is able to replicate changes in the cross-section of yarns due to biaxial tensile and in-plane shear, but it is too expensive to be used to simulate the forming process of large structures. Simplifications were therefore made by Gatouillat et al. [155, 156] to reduce the DOFs of the fabric unit cell by modelling the yarn cross-section with a single shell element, as shown in Figure 2.25(b). The capability of this model for predicting macro-scale wrinkling defects and "unweaving" phenomena of yarns was demonstrated by simulating a hemisphere. A similar model was developed by Tavana et al. [157] to model the slippage between yarns during forming, but the yarns were considered as a transversely isotropic linear elastic material.

Simplification

47214 DOF
(a)

416 DOF
(b)
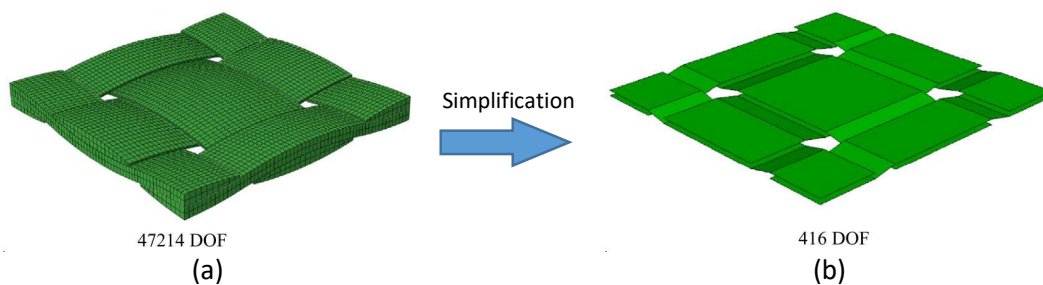
Figure 2.25: (a) Mesoscopic model of a woven fabric unit cell built by solid elements. (b) Simplified unit cell model using shell elements. [155]

Creech and Pickett [71] have proposed a mesoscopic model for the forming simulation of biaxial NCFs with a tricot stitch pattern. In this model, yarns were modelled by two layers of solid elements with bar elements interconnected to approximate the stitching effect, as shown in Figure 2.26. The yarn-stitch interaction was modelled using a contact algorithm and additional connection elements. The model is capable of capturing the asymmetric shear behaviour of NCFs and yarn sliding during the bias-extension test.

Stitching bars
Layer 1 soilds
Layer 2 soilds
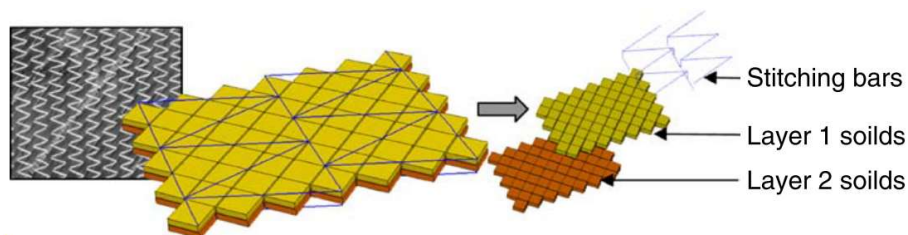
Figure 2.26: Mesoscopic model of a non-crimp fabric. [71]

The update of yarn directions is naturally considered in the mesoscopic approach, therefore constitutive laws for tracking yarns reorientation are not required. Moreover, some forms of mesoscale defects such as yarn-spacing, yarn-sliding and yarn-unweaving can be predicted by mesoscopic models. However, complex interactions between yarns and stitches, as well as the large number of DOFs, may compromise the computational efficiency of the model, and therefore limits the applicability of this approach.

(4) Semi-discrete element formulation

The semi-discrete element is formulated based on the behaviour of a mesoscale fabric unit cell, and the strain energy of the element is determined as the sum of the energy terms resulting from individual deformation modes, i.e. biaxial tension, in-plane shear and out-of-plane bending. This approach was first proposed by Boisse et al. [158], considering only the axial behaviour of the yarns, but was later extended to take into consideration the in-plane shear behaviour [159, 160]. Hamila et al. [161] developed a three-node triangular element to incorporate axial tension, in-plane shear and out-of-plane bending into the formulation of the semi-discrete element. As shown in Figure 2.27(a), the directions of the warp and weft yarns are independent from the edges of the element. The bending curvature of a yarn is calculated based on the nodal displacements in the corresponding direction of the yarn (see Figure 2.27(b)), which enables a curvature-dependent bending behaviour to be implemented into the forming simulation [89]. This semi-discrete finite element approach has subsequently been used to model the preforming of non-crimp fabric reinforcements [162], by employing bar elements to represent the stitches.

| | |
| (a) | (b) |
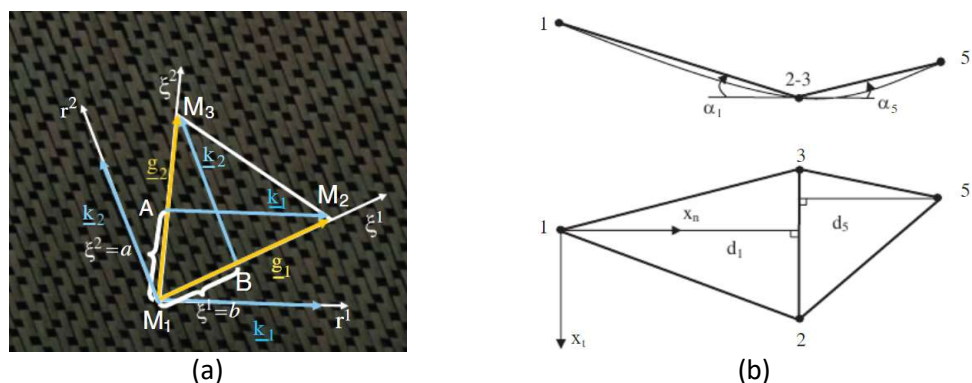
Figure 2.27: (a) Three-node triangular element of woven cells and (b) bending configuration of two adjacent elements. [161]

In summary, the advantages and disadvantages of the different modelling approaches are compared in Table 2.3. The continuous approach takes advantage of the classical finite element methodology; therefore no additional elements are required in the numerical model for yarns at mesoscale. However, this approach requires specialist constitutive models to be developed, but is unable to explicitly model the deformation features and defects at the mesoscale. This is the main advantage of discrete or mesoscopic models, enabling interactions between yarns and stitches to be modelled to predict forming related defects. However, a great number of elements are required for constructing yarns or stitches at the mesoscale, leading to high computational costs for process simulation. Thus, this approach is typically limited to small or laboratory-scale specimens. Moreover, time consuming material characterisation tests and homogenisation procedures are required to determine the material parameters for numerical modelling. Semi-discrete elements are formulated based on continuous finite elements, therefore this approach shares the same advantages but it needs specialist element formulations that are not readily available in commercial FE codes.

Table 2.3: Advantages and disadvantages of typical simulation approaches, i.e. continuous approach, discrete or mesoscopic model, semi-discrete element.

Modelling approach	Advantages	Disadvantages
Continuous approach	• Small number of DOFs. • Applicable to classical FE model.	• Requirement for specialised constitutive model. • Cannot model deformation characteristics or defects at mesoscale
Discrete or mesoscopic model	• Close to the natural architecture of fabrics. • Can model the interaction between yarns and stitches. • Can model occurrence of mesoscale defects.	• Large number of DOFs. • Limited to small structures. • Needs specialised homogenisation procedure to determine material parameters in numerical model.
Semi-discrete element	• Small number of DOFs. • Applicable to classical FE model.	• Needs specialised element formulation. • Not readily available in commercial FE codes.

2.5.2   Wrinkle prediction and characterisation

Out-of-plane fabric wrinkles introduced during the preforming stage can lead to fibre misalignment and resin-rich zones in the cured composite component [95, 96]. Damage can initiate from these sites, which can subsequently propagate to far-field regions under external load [96, 163]. Parametric studies [164, 165] indicate that laminate failure stresses decrease with increasing wrinkle angle in the loading direction, with a predicted >40% knock-down in compressive failure stress reported when the out-of-plane wrinkle angle increases from 4° to 28° [16].

It is therefore vital to be able to predict the occurrence of critical macro-scale defects during forming processes. It is common for FE forming simulations to use a membrane approach to model the fabric plies [109, 143], to minimise the number of degrees of freedom and reduce the computation time. Membrane elements can be used to take into account the in-plane shear behaviour between the primary yarns and has been successfully used to predict yarn orientation [145] and material draw-in during forming. Macroscale wrinkles can be identified from the shear angle distribution by locating areas that have exceeded the "locking angle" [30]. This is a computationally efficient method but it is only a qualitative approach for detecting defects, as it is unable to characterise the true size and shape of wrinkles [83, 97]. A semi-discrete shell approach considering only the in-plane fabric behaviour (i.e. tensile and shear) has been successfully used to predict the occurrence of wrinkles, but the predicted shapes were unrealistic [159, 166].

A number of studies [83, 97, 108, 146] have indicated the importance of incorporating the effects of fabric bending resistance for predicting more realistic wrinkle patterns. Fabric bending stiffness is typically measured to be much lower than the axial stiffness in the fibre directions due to fibre sliding [83]. In commercial finite element software, the bending stiffness is typically derived from the axial moduli for standard shell elements. However, this can overestimate the bending stiffness of fabrics, leading to unrealistic predictions for forming induced wrinkles. Hybrid membrane and beam/shell meshes [108, 146, 167], bespoke semi-discrete shell elements [97] and laminate layup approaches [81] have been proposed to decouple the fabric bending behaviour from the axial moduli.

By incorporating bending stiffness into the semi-discrete shell element, Boisse et al. [97] simulated the wrinkling behaviour during punch forming processes and reported that the number and shape of wrinkles are related to the magnitude of the bending stiffness. Simulations were performed by Liang et al. [83] for similar punch geometries using a bending

stiffness characterised from a modified cantilever test. Results showed that smaller values of bending stiffness can lead to more wrinkles of smaller amplitude than wrinkle patterns produced by simulations using larger bending stiffness values. Experimental studies have reported that the bending stiffness of fabrics generally decreases as the bending curvature increases, therefore this nonlinearity can influence the wrinkling behaviour during forming, which needs further investigation. A recent study by Abdul-Ghafour et al. [89] compared the internal forces of fabrics predicted by nonlinear elastic and inelastic models and reported that both models can effectively capture the shape of wrinkles, but the elastic model over-predicts the required forming force by 30%-50%. The commercial software PAM-FORM is also capable of defining a non-linear bending stiffness for modelling the forming behaviour of fabrics, but the selected nonlinear relation is limited to a 3rd order polynomial function, which is not sufficiently representative for the moment-curvature relations observed here [168].

Accurately comparing wrinkle patterns between simulations and experimental data for complex geometries can be problematic and is generally qualitative. Whilst the shape and location of out-of-plane wrinkles can be approximated by incorporating the effects of the fabric bending stiffness [59, 97, 146], detailed evaluation relies on observations from the deformed FE mesh. The distance deviation between the deformed fabric ply and the baseline tool surface provides a quantitative measure for the amplitude of wrinkles [29, 169, 170], but this is unable to assess the local radius of individual wrinkles, since the surface curvature is overlooked [171]. To quantitatively measure wrinkling behaviour, Dörr et al. [172] calculated the nodal curvature for the deformed fabric by taking a weighted average of the angular differences between the normals of elements sharing a common node, as shown in Figure 2.28. However, the curvature obtained was dependent on the local mesh discretisation and was unable to accurately measure the radius of the local ply waviness, since the curvature was calculated in an average manner. Recent works by Shen et al. [170] and Viisainen et al. [98] used a combination of multiple metrics (i.e. maximum wrinkle amplitude, wrinkle ratio) to evaluate the overall severity of wrinkling in fabrics. In summary, the wrinkle amplitude and surface curvature can be employed together to evaluate the severity of wrinkling defects. A high wrinkle amplitude indicates poor fabric-tool conformity, whilst zero amplitude indicates that the preform is fully conformed to the tool surface. Similarly, a high curvature value represents severe fabric folds, even though the wrinkle amplitude can be small, whereas a low curvature value indicates wrinkles with insignificant waviness.
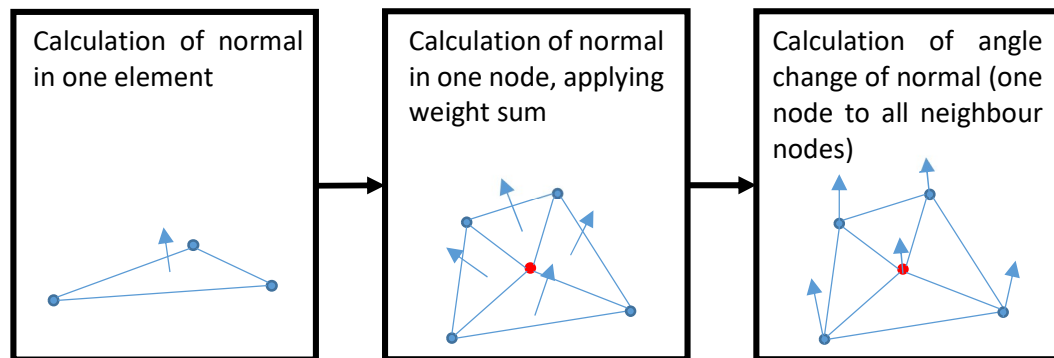
Figure 2.28: The method for curvature determination used in [173].

2.5.3   Multi-scale forming simulation

Due to the multi-scale nature of fabric reinforcements (see Figure 2.29), numerical models have to be considered at different scales, i.e. micro-scale (the scale capturing individual fibres to a yarn, 10^{-6}m), the mesoscale (the scale from the yarn to the fabric unit cell, 10^{-3}m) and the macro-scale (the scale from the fabric unit cell to the entire ply, 10^{-0}m).
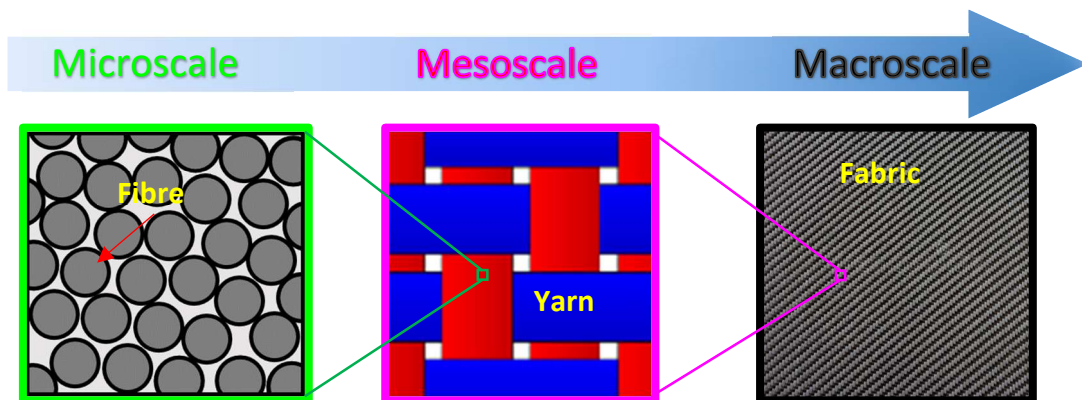
Figure 2.29: Illustration of three different scales for woven fabric composites.

As shown in Figure 2.29, fibres of individual yarns are explicitly defined in the microscopic model, it is therefore generally impractical to conduct process simulations using models at this scale due to the extremely large number of DOFs. For full-scale mesoscopic models, all yarns in the fabric plies and their contacts are explicitly defined, providing a complete representation of the fabric architecture. Full-scale mesoscopic models are capable of replicating deformation characteristics and forming related defects in great detail, but naturally demand a significant computational resource that prohibits their practical use for

process simulation. By applying appropriate constitutive laws to macro-scale models, the primary deformation modes of fabric forming (i.e. in-plane tension, in-plane shear and out-of-plane bending) can be well replicated, but defects occurring at the mesoscale cannot be effectively modelled. Multi-scale simulations provide a viable way to balance computational efficiency and simulation accuracy.

Based on the concept of a sequential global-to-local modelling strategy originally developed for structural analysis, Iwata et al. [167, 174] proposed a "macro-meso zoom" (MMZ) simulation approach for forming woven fabrics, as shown in Figure 2.30. In this approach, fabric forming was first simulated using a membrane-shell hybrid mesh at the macro-scale to provide displacement boundary conditions for the local mesoscopic simulation of a small region. Compared to the macroscopic modelling, the MMZ simulation predicted mesoscopic deformations such as tow buckling and slippage, but the run time was just 17% of the full-scale mesoscopic modelling. However, the local regions of interest for the detailed mesoscopic modelling were randomly selected, therefore new criteria are required to accurately determine these critical regions containing defects.
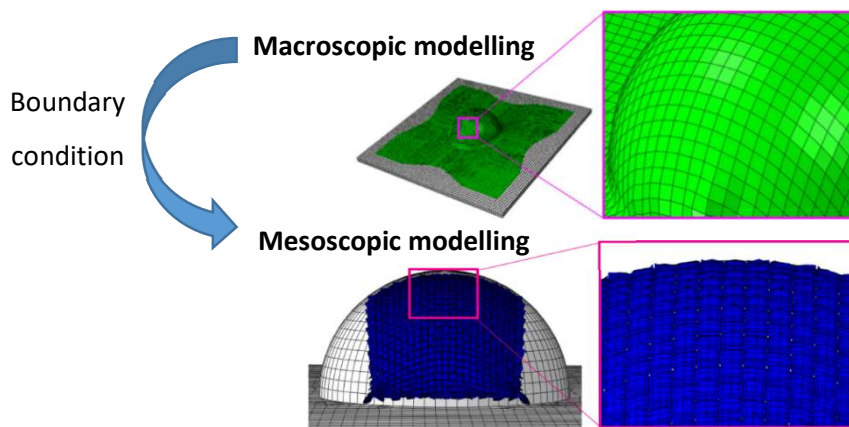
Figure 2.30: Macro-meso zoom (MMZ) simulation approach proposed in [167].

Wang et al. [175] proposed a macro-to-meso simulation approach for 3D woven fabrics by interpolating the nodal displacements obtained from macroscale modelling onto mesoscopic unit cells virtually embedded in the macroscale mesh, as shown in Figure 2.31.

**Macroscale model
&
Embedded mesoscopic model**

**Displacement interpolation at
element level**

Deformation at yarn level
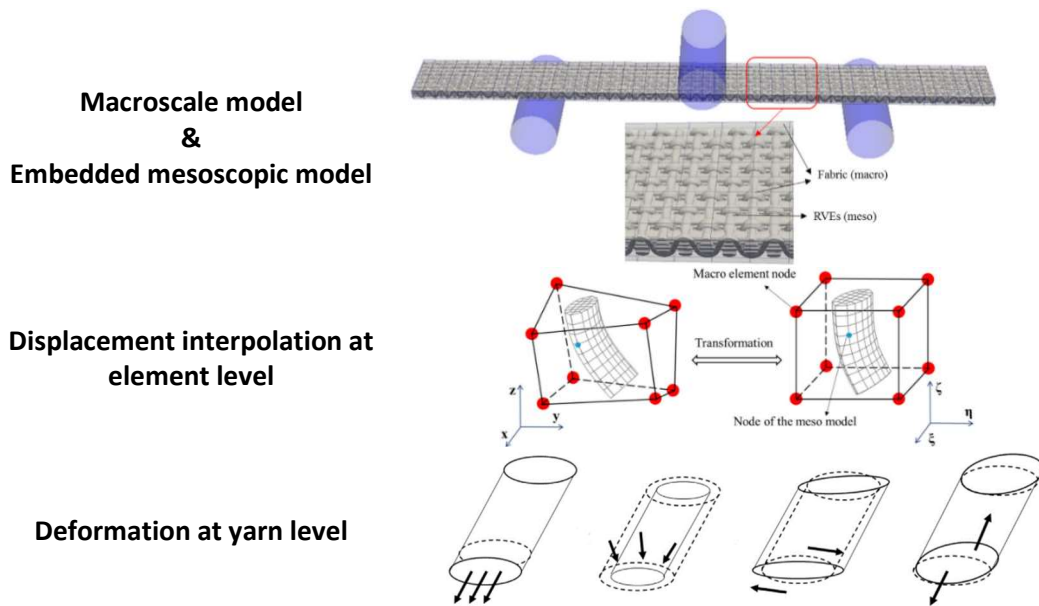
Figure 2.31: Modelling scales for a mesoscopic model embedded in a macroscopic model. [175]

This enables a fast prediction for the stress and strain of the yarns in the embedded mesoscopic model. However, yarn elongation at the mesoscale can be over-predicted because yarn slippage is not explicitly considered in the macroscopic modelling, which influences the displacement field for the embedded mesoscopic unit cells. To overcome this drawback, local mesoscale FE simulations are performed based on a relaxed displacement field obtained from the embedded mesoscopic modelling. However, the determination of relaxing nodes and DOFs are highly dependent on the deformation modes in relation to the forming configuration.

The selection of a modelling scale is generally dependent on the dominant forms of defects resulting from the forming process. Macroscale defects, i.e. wrinkling and bridging defects, are the most commonly observed forms of defects during double diaphragm forming (DDF). The formation of these defects can be numerically predicted by implementing macroscale constitutive material models in finite element (FE) simulations. Potential defect sites can be identified using efficient membrane element models, using field variables such as the fibre shear angle and the magnitude of in-plane strains along the principal fibre directions to indicate regions of fibre buckling [21, 101]. Whilst this method is computationally efficient, it is only qualitative and is unable to characterise the true size and shape of the wrinkles. More realistic defect patterns can be identified by using shell elements to incorporate the bending behaviour of the fabric [100, 147]. A high resolution mesh (relative to the wrinkle amplitude) is typically required to ensure accuracy, with a small time increment needed to

maintain the stability of the explicit dynamic integration algorithm [110, 176]. In addition, material non-linearity and complex contact interactions demand further computational efforts, which further increase the computation time. It is therefore impractical to identify critical defects at sufficient resolution when these methods are applied to industrial applications with a large length scale (e.g. >10 m), particularly for laminate designs containing a considerable number of plies (e.g. >20). However, large scale components such as aerospace wing spars and ribs [44] generally exhibit a moderate variation in surface curvature along their length. Defects in this case are usually concentrated around small local regions with doubly-curved features, with the rest of the component being free of forming related defects [100]. There is a demand for multi-resolution simulation tools to quickly locate small critical defects in large-scale structures. Sub-modelling [177-179] provides a viable solution to acquire high-fidelity results in local regions of interest within larger global models. This modelling technique has been successfully used for structural analysis [180, 181] and has been built into commercial FE software to provide a robust solution [110].

2.5.4   Process refinement

2.5.4.1   Matched tool forming

In matched tool forming, the quality of preforms can be improved by modifying some process parameters listed in Table 2.4.

Table 2.4: Critical process parameters during matched tool forming and possible approaches for defect mitigation corresponding to each process parameter.

Process parameter	Possible methods for defect mitigation
Clamping / Blank holder force	• Optimising the position of blank holders or clampers to modify fabric in-plane shear deformation and hence material draw-in • Increasing the magnitude of clamping or blank holder force
Selective inter-ply stitching	• Adding inter-ply stitches to modify the in-plane shear deformation of fabrics
Inter-ply friction	• Reducing the inter-ply friction resistance to reduce fibre compression
Punching sequence	• Optimising the forming sequence of segmented punches to control the location of wrinkles and the regions of high shear

An appropriate level of blank holder force (BHF) can generate some tensile force along the fibre directions, therefore preventing wrinkling defects from occurring. By adjusting the position of individual blank holders, Lin et al. [64] found that wrinkles can be minimised by optimising the distribution of BHF. Arnold et al. [29] reported that increasing BHF would generally reduce the wrinkle amplitude but the effectiveness is dependent on the architecture of the fabrics. Similarly, optimising the distribution of clamping force can alleviate the maximum shear angle in the preform, which can potentially mitigate possible wrinkling defects [65]. It was reported that local stitch-bonds can affect the shear deformation of fabrics by transferring shear force into un-sheared regions [182]. Chen et al. [66] proposed a numerical optimisation scheme for optimising the location of inter-ply stitches between multiple plies during a hemisphere forming. Results showed that an optimised local stitching pattern can reduce the maximum shear angle in the preform by globally modifying the shear deformation. When forming multi-ply woven fabric plies stacked in different ply orientations, individual plies tend to undergo different shear deformation, causing the tendency of inter-ply sliding. Fibre compression therefore occurs when this deformation trend is restricted by inter-ply friction resistance, causing unwanted fabric buckling or wrinkles. Guzman-Maldonado et al. [59] reported that reducing inter-ply friction resistance can alleviate the severity of compression induced wrinkles during forming multi-ply woven fabrics using a hemispherical tool. In addition, the quality of preforms can be improved by employing a multi-punch sequential forming technique, in which the location of wrinkles and high shear regions can be controlled by adapting the forming sequence [183].

2.5.4.2   Double diaphragm forming

Various approaches have been proposed to mitigate wrinkling and bridging defects in diaphragm forming, by modifying process parameters and the deformation mode as summarised in Table 2.5. Additional metal rods and plates were introduced to the conventional diaphragm arrangement to increase the out-of-plane constraint applied to the fabric plies to reduce wrinkles during forming, but impressions can occur on the surface of the final component due to excessive compression [44]. Stretching the diaphragms during forming can induce tensile stresses in the fabric plies along the primary yarns, preventing out-of-plane buckling during forming. Additional in-plane tensile deformation can be artificially introduced into the diaphragms by positioning risers (rigid blocks) around the male tool under the fabric-diaphragm assembly prior to forming [50]. This method is similar in effect to applying in-plane constraints during matched tool forming, using blank holders for example [35, 65]. The position of additional risers was optimised by Chen et al. [101] for a

hemisphere tool, where wrinkling defects were eliminated by changing the shear angle distribution in the preform. However, risers are unable to remove bridging defects and need to be further validated for multi-ply forming using more complex tool geometries. Darts can be introduced to alleviate the bridging force over concave areas of the tool, therefore facilitating material draw-in to provide better fabric-tool conformity [21], but darts introduced fibre breakage leading to a reduction in the mechanical properties of the final component. Excessive bridging around the perimeter of the tool can be effectively modified by tailoring the shape of the initial blank [21], or elevating the forming temperature to soften the in-plane stiffness of the diaphragms. Reducing inter-ply friction has been considered as an effective way to mitigate wrinkling defects in the DDF process. This can be achieved by optimising the forming temperature for UD or woven prepregs [45, 99, 184], as the impregnated thermoset resin typically exhibits a lower viscosity within a certain temperature window [93]. However, this method is not always applicable to multi-ply preforms, particularly quad axial layups with low formability, therefore the layup sequence needs to be designed to enable sufficient drape to minimise forming related wrinkles [94, 185]. Reducing the sliding velocity from 10 mm/s to 1 mm/s during friction testing can lead to a 56% reduction in the frictional coefficient for UD prepregs [186], therefore a low forming rate is recommended for the DDF process to achieve better surface conformity when using materials with viscoelastic behaviour[46].

Table 2.5: Critical process parameters during double diaphragm forming and possible approaches for defect mitigation corresponding to each process parameter.

Process parameter	Defect mitigation methods
Out-of-plane constraint	• Adding additional stiff materials to the fabric or diaphragms to reinforce the out-of-plane constraint • Adding an external out-of-plane support (e.g. support pillar or compression roller) to locally improve fabric-tool conformity by changing the seed point (first point of contact) of the fabric ply with the tool.
Local diaphragm stretching	• Positioning risers to modify the diaphragm-stretching-induced tensile force in fabrics • Positioning darts in fabrics to modify bridging force in fabrics • Trimming the fabric shape to locally modify the tensile force in fabric and diaphragms
Inter-ply friction	• Pre-heating prepregs to increase the viscosity of resin prior to forming • Altering the layup sequence and orientation to achieve compatible inter-ply deformation • Lowering the forming rate to reduce inter-ply friction force

2.6   Chapter conclusions

Volume production of composite structures incorporating biaxial fabrics requires a preforming step to convert flat 2D plies into complex 3D shapes prior to liquid moulding. Press-based matched tool forming and vacuum-based diaphragm forming are two mainstream processes commonly used for producing preforms. Matched tool forming is suitable for producing large volumes, but the scale of components is currently limited by the size of the hydraulic press. Double diaphragm forming (DDF) is of interest in this thesis, since the process is highly scalable due to the relatively low forming forces and it generally requires lower capital investment, particularly for large-scale components (+ 10 m), as proven by GKN Aerospace in the production of A400M wing spars [53].

Whilst in-plane shear is the dominant deformation mode during fabric forming, out-of-plane bending deformation occurs to enable biaxial fabrics to conform to curved features of the tool without damaging the fibres. Due to the absence of rigid blank holders, out-of-plane wrinkles and bridging defects are two of the most common defect modes experienced during DDF. This literature review has reported that fabric wrinkling is essentially a buckling

behaviour dominated by the bending properties of the ply, therefore it is important to incorporate the true bending stiffness of the fabric into the simulation framework, to enable realistic predictions of the formation and development of macroscale wrinkles during DDF.

The bending stiffness of a fabric ply is different to that of other ordinary continuums due to intra-ply fibre slippage that occurs during forming, resulting in a nonlinear relationship with the bending curvature. Biaxial non-crimp fabrics can exhibit asymmetric fibre architectures in the through-thickness direction, which may lead to different bending resistances depending on the fibre direction with respect to the direction of the bending moment. Specialised material characterisation methods and modelling approaches are therefore required to capture this unique material behaviour at the macroscale.

Finite element models based on continuum mechanics have been demonstrated to be suitable for simulating the forming behaviour of fabrics at the macroscale. Compared to the discrete and mesoscopic models, the continuous approach requires less degrees of freedom in the FE model and hence less computational time costs, especially when considering complex contact behaviours and large components with complex layups. However, the modelling scale must be selected according to the scale of the smallest feature within the component geometry, which in this case is the scale of the smallest critical defect that occurs during DDF. Studies in the literature have commonly demonstrated that the location and shape of wrinkles with amplitudes of up to several millimetres can be predicted for components with length scales of the same order of magnitude (i.e. millimetres rather than metres). This literature review has therefore established the need for an efficient modelling strategy to enable fast prediction of fabric wrinkles for components with length scales exceeding 10 m, without significantly compromising precision.

Inter-ply friction plays an important role in the formation of forming related defects. Reducing the frictional resistance at the contact interface was shown to be an effective way to mitigate defects, but more effective and practical approaches for inter-ply lubrication are still required. While the forming mechanisms for single fabric layers or multi-layered fabrics with the same ply orientations are well reported, this literature review has highlighted that the forming mechanism for multi-layered fabrics with different ply orientations are more complicated and require further investigation.

The following chapters will build upon the knowledge gained from the literature to develop new experimental methods to characterise the draping behaviour of biaxial fabrics and to develop a robust forming process simulation tool. A revised cantilever test will be used to

characterise the non-linearity of the fabric bending behaviour to provide input data for the process simulation, enabling the prediction of macroscale wrinkles and bridging defects during forming. The surface curvature of the ply will be used to evaluate the severity of wrinkling defects quantitatively, which will also enable wrinkling defects to be isolated from fabric bridging defects. A multi-resolution modelling strategy will be proposed to predict the shape and position of defects explicitly in local regions of large preforms using reasonable computation times. The simulation tool will be used to seek practical solutions to mitigate the formation of defects during the forming of multi-layered fabric plies at different orientations.

Chapter 3   Material characterisation and modelling

3.1   Introduction

This chapter presents a novel macroscale finite element (FE) model to simulate the forming behaviour of biaxial fabrics, incorporating the effects of bending stiffness to account for fabric wrinkling. The dependency of the bending stiffness on the fibre orientation is considered by extending an existing non-orthogonal constitutive framework for biaxial fabric materials [30].

The validity of the modified constitutive model for bi-axial fabrics is verified using data from two carbon fibre reinforcements, i.e. a biaxial NCF and a balanced twill-weave fabric. The bending behaviour of the fabrics is characterised by two types of cantilever test. Firstly, constant values of bending stiffness are measured according to the standard method [123]. Secondly, a revised cantilever method is developed to define a non-linear relationship between the bending stiffness and the degree of specimen curvature, using structured white light scanning (SWLS). Picture frame shear testing is conducted to determine the shear resistance of the woven fabric, and data from the literature is used for the NCF. The characterised material parameters are implemented into the constitutive model to investigate the material behaviour during picture frame, bias-extension and cantilever bending tests. Results are compared with experimental data to validate the proposed material model.
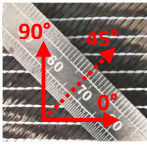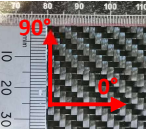
3.2   Material characterisation

3.2.1   In-plane shear behaviour

Two carbon fibre fabric reinforcements were used in this study; a NCF from Hexcel (FCIM359) and a balanced 2×2 twill-weave fabric from Carr Reinforcements Ltd (38616). The NCF fabric consists of two unidirectional plies, with yarn orientations at ±45°, assembled by pillar stitches in the 0° direction. The woven fabric is assembled by two primary yarns in 0° and 90° directions. Material parameters for both fabrics are listed in Table 3.1. Picture frame shear testing was conducted to determine the shear resistance of the woven fabric, using the methodology outlined by Harrison et al [112]. The transverse fibre bundles in the arms of the cruciform specimen were removed to eliminate the shear force contribution from these corresponding areas. The normalised shear force versus shear angle curve was fitted using a

7th order polynomial function, as presented in Table 3.1. The shear resistance for the NCF is from the literature [30].

Table 3.1: Material parameters for the non-crimp fabric and the woven fabric.

Materials	Parameters		Normalised shear curve
Non-crimp fabric (NCF, FCIM359)	Ply thickness	0.4 mm	$F_{norm}^{NCF} = F_{norm}^{yarn\ rotation} + F_{norm}^{stitch}$ [30]
	Areal mass	440 gsm	$F_{norm}^{yarn\ rotation} =$ $(29.56\gamma_{12}^5 - 65.56\gamma_{12}^4 + 137.06\gamma_{12}^3 + 94.73\gamma_{12}^2 + 112.19\gamma_{12})$ N/m
	Fibre orientation	±45°	
	Stitch orientation	0°	$F_{norm}^{stitch} =$ $\begin{cases} (2000\gamma_{12} - 120)\ \text{N/m}, & 0.06 \leq \gamma_{12} < 0.5 \\ (-3520\gamma_{12} + 2640)\ \text{N/m}, & 0.5 \leq \gamma_{12} < 0.75 \\ 0\ \text{N/m}, & \text{else} \end{cases}$
	Fibre tow size (K)	24	
Woven fabric (38616)	Ply thickness	0.3 mm	
	Areal mass	210 gsm	$F_{norm}^{wov} = (37.35\gamma_{12} - 322.61\gamma_{12}^2 + 1458.51\gamma_{12}^3 - 3539.56\gamma_{12}^4 + 4727.84\gamma_{12}^5 - 3275.20\gamma_{12}^6 + 930.53\gamma_{12}^7)$ N/m
	Fibre orientation	0°/90°	
	Fibre tow size (K)	3	

3.2.2   Out-of-plane bending behaviour

The bending behaviour of these two fabrics was determined using two different methods to provide input data for forming simulations. Firstly, the standard cantilever method was used to produce a constant value for the bending stiffness, according to BS EN ISO 9073-7; 1998 [123]. Secondly, a revised cantilever method [82, 126] was used to define a non-linear relationship between the bending stiffness and the degree of specimen curvature.

According to BS EN ISO 9073-7 [123], a cantilevered fabric strip subjected to gravity, exhibits a constant bending stiffness per unit specimen width (N·m), B, for a given cantilever overhang (m), L, and weight per unit area (N·m^{-2}), w:

$$B = \frac{1}{\frac{\tan(\phi)}{\cos(0.5\phi)}} \times \frac{wL^3}{8}$$

(3.1)

The angular deflection, ϕ, is the angle measured from the horizontal to the secant line, drawn between the fixed end and the free end of the cantilevered fabric strip, as shown in Figure 3.1. Typically, either $\phi = 41.5°$ or $\phi = 7.1°$ is recommended for the measurement [123].
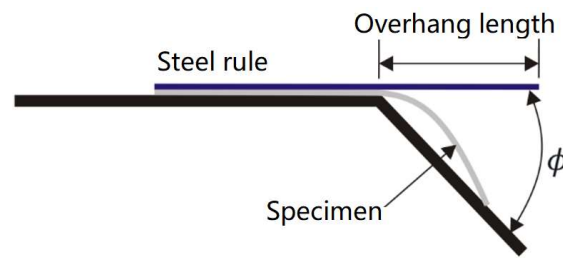
Figure 3.1: Schematic of the standard cantilever test in [123]

Fabric specimens were cut by a rotary knife into 250mm × 30mm strips, containing 20 fibre bundles across the width of each NCF specimen and 15 fibre bundles for each the woven fabric specimen. A steel rule was used to set the overhang length of each fabric specimen on the rig, as shown in Figure 3.1. A rubber layer was added to the surface of the rule to increase the coefficient of friction, preventing relative movement between the rule and the fabric specimen. Each specimen was pushed forward over the clamping edge until the tip of the fabric specimen touched the slope at the desired angle ϕ. Six woven fabric specimens were tested in both the warp and weft directions, with the results presented in Figure 3.2(a). For the NCF material, six specimens were tested in two different configurations as the bending stiffness may depend on the fibre architecture in the through-thickness direction (see Figure 3.2(b)). The 0° fibres were positioned on both the uppermost surface and the lowermost surface about the mid-plane of the specimen.

(a)   (b)

Figure 3.2: Bending stiffness per unit width of fabric specimens. (a) Constant bending rigidities measured for the woven fabric in warp (blue) and weft (red) directions at angular deflections of 7.1° and 41.5°. (b) Constant bending rigidities measured for the NCF in positive (blue) and negative (red) bending configurations at angular deflections of 7.1° and 41.5°.

Since the woven fabric is balanced in both directions, the average bending stiffness from six specimens was identical for warp and weft directions. The average bending stiffness obtained from a small deflection angle (7.1°) is 0.00036 N m, compared to 0.00022 N m calculated from a large deflection angle (41.5°), indicating a nonlinear bending behaviour for the woven fabric.

Results for the NCF using both bending configurations are compared in Figure 3.2(b), indicating that the macroscale bending response is dependent on the 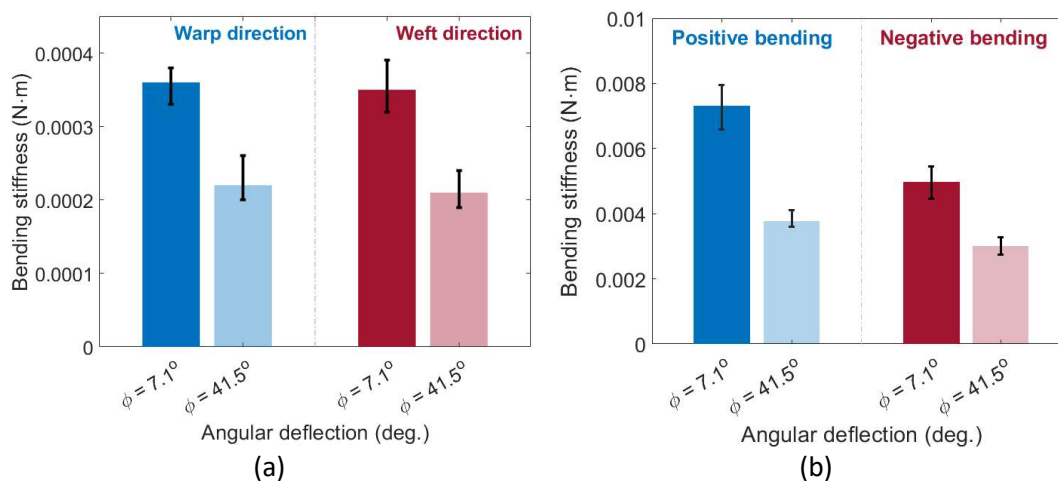bending direction. For an angular deflection value of 7.1°, the stiffness in the positive bending direction is 0.0073 N·m compared to 0.0057 N·m for the negative direction. Similar to the woven fabric, the bending stiffness calculated from the large deflection angle (41.5°) is lower than the value resulting from the small deflection angle (7.1°), which also confirms that the bending stiffness for this NCF fabric is non-linear.

In order to characterise the non-linear bending behaviour of this material, a revised cantilever bending testing method was used [82], however bending moments and curvatures were not determined as a function of loading. A curve was drawn using a single loading configuration, establishing the curvature and the bending moment as functions of curvilinear coordinates along the specimen. A Structured White Light Scanner (HP-Pro S3) was employed to provide an accurate representation of the curvature of the specimen, avoiding parallax error commonly experienced with other photogrammetry methods. The SWLS is a 3D scanning device based on coherence scanning interferometry (CSI). A series of white light patterns are projected onto the deformed fabric specimen and the distortion of these patterns caused by the surface curvature is captured by a camera. The change in fringe pattern can be used to reconstruct the surface shape of the specimen.

The overhang length was fixed to be 130 mm for the woven fabric and 210 mm for the NCF specimens to ensure a wide range of curvature along the specimen. 3D point clouds of the deformed specimens were acquired, with a precision of up to 0.05% over the scan area. Due to potential twist of the specimen, measurements were taken over the centre of the specimen corresponding to 5% of the specimen width (the yellow strip in Figure 3.3(a)). A polynomial was used to fit the deflection curve, but it is possible for negative curvatures to occur at certain points due to fitting errors. The order of the fitting function was therefore adjusted to ensure a positive and monotonic curvature variation for a wide range of the deflection curve. Consequently, problem areas were restricted to either the free tip or the fixed end of the cantilevered specimen. For the fabrics studied, the deflection curve was obtained by fitting a 6th order polynomial function to the projected points from six specimens.
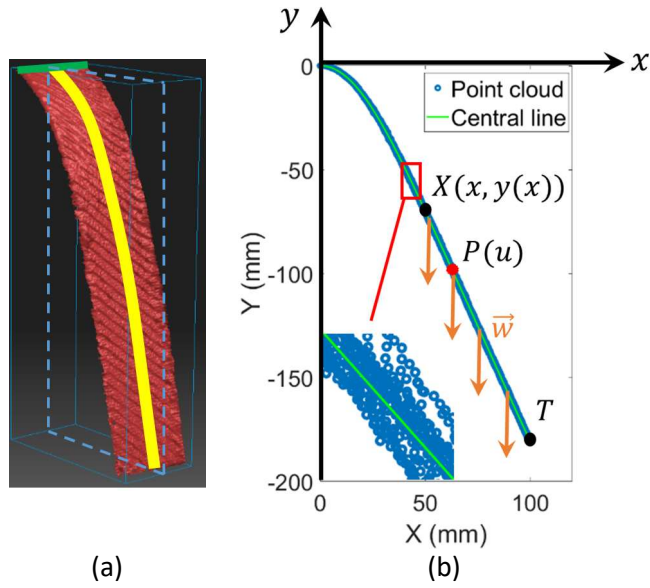
Figure 3.3: Bending stiffness characterisation using structured light scanning: (a) point cloud from scanning and (b) central profile fitting.

The bending moment per unit width of specimen M, and the curvature κ at an arbitrary point $X(x, y(x))$ on the deflection curve (See Figure 3.3(b)) were calculated as

$$M = \int_{S}^{L} \overrightarrow{XP} \times \overrightarrow{w}\,du \tag{3.2}$$

$$\kappa = \frac{y''}{(1 + y'^2)^{3/2}} \tag{3.3}$$

where s is the curvilinear distance measured from the clamping to Point X; L is the length of overhang; $\overrightarrow{w}$ is the vector of the weight per unit length of the fabric specimen; u is the curvilinear distance measured from Point X to Point P, moving along the segment between Point X and the tip of the overhang T. y' and y'' in Eq.(3.3) are the first and second derivatives of the fitted deflection curve with respect to x, see Figure 3.3(b).

The relationship between M and κ was fitted using Voce's model [187], where the root mean square error (RMSE) was calculated to be less than 5% of the experimental data:

$$M(\kappa) = R_0 \cdot \kappa + R_\infty[1 - \exp(-\kappa/\kappa_{\text{lim}})] \tag{3.4}$$

Here, R_0 and R_∞ are fitting constants and κ_{lim} is the exponential saturation parameter.

The nonlinear bending behaviours obtained from the revised cantilever bending are plotted in Figure 3.4 and Figure 3.5 for the woven fabric and the NCF respectively, where the bending stiffness decreases with an increase in curvature for each material.

Figure 3.4: (a) Bending moment per unit width of specimen vs. curvature and (b) bending stiffness per unit width vs. curvature for the woven fabric ($B_{Nonlinear}$ denotes the non-linear bending stiffness per unit width measured by the revised cantilever test; $B_{41.5°}$ denotes the constant bending stiffness per unit width measured by the standard cantilever test at an angular deflection of 41.5° according to BS EN ISO 9073-7 [123]).

The dashed straight lines in Figure 3.4(b) and Figure 3.5(b) denote constant bending stiffness values. $B_{41.5}$ denoted the constant bending stiffness measured at a fixed deflection angle of 41.5° using the standard cantilever test [123]. $B_{41.5}^{wov}$ was measured to be 0.00022 Nm, but different bending stiffnesses were measured for the NCF in the positive and negative bending configurations, i.e. $B_{41.5}^{NCF,pos}$ = 0.0038 Nm and $B_{41.5}^{NCF,neg}$ = 0.0032 Nm respectively, due to the fabric asymmetry. The value B_{init} represents the stiffness at zero curvature and the asymptote value B_{inf} represents the stiffness at large curvatures, which were both derived

from the revised non-linear cantilever test data [188]. The functions of the nonlinear bending behaviours are presented in Table 3.1 for both materials. For both materials, the slopes of the nonlinear curves at zero curvature ($B_{init}^{NCF,pos}$ = 0.008 N·m, $B_{init}^{NCF,neg}$ = 0.0056 N·m and B_{init}^{wov} = 0.00039) are close to the bending rigidities measured by the standard testing method at ϕ=7.1° (0.0073 N·m compared to 0.0057 N·m for positive and negative bending of the NCF, and 0.00036 N m for the woven fabric). This indicates that the bending behaviour is approximately linear elastic under small curvatures.
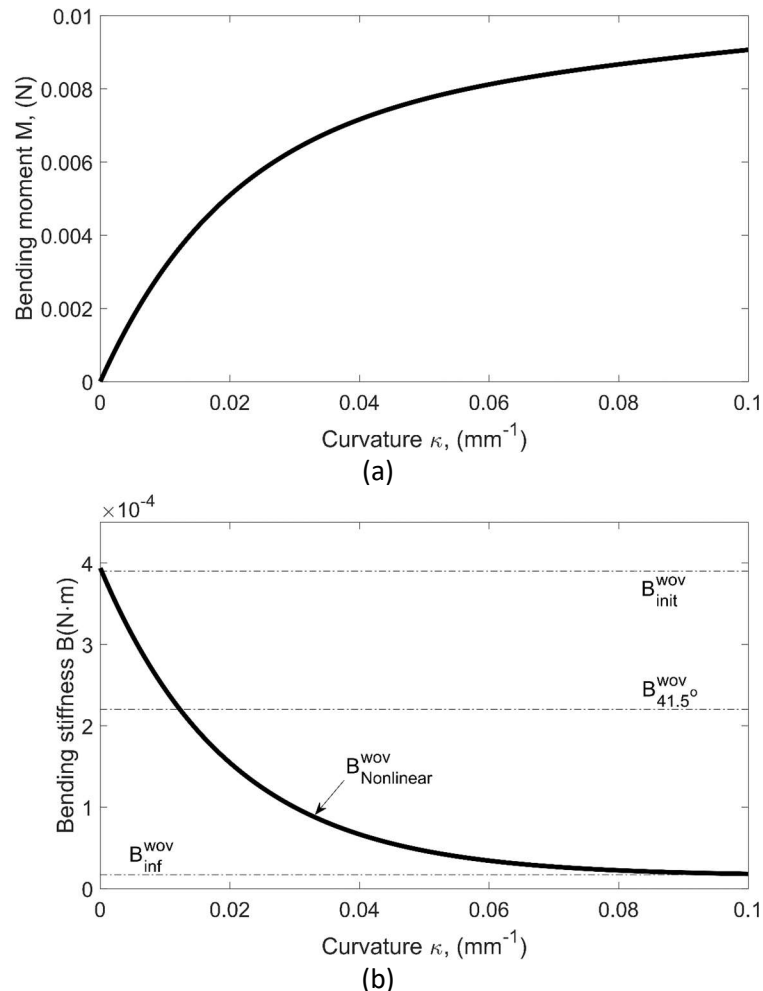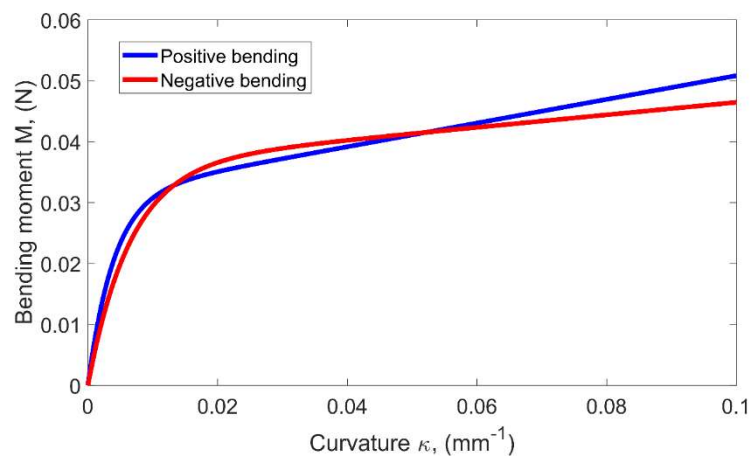

(a)
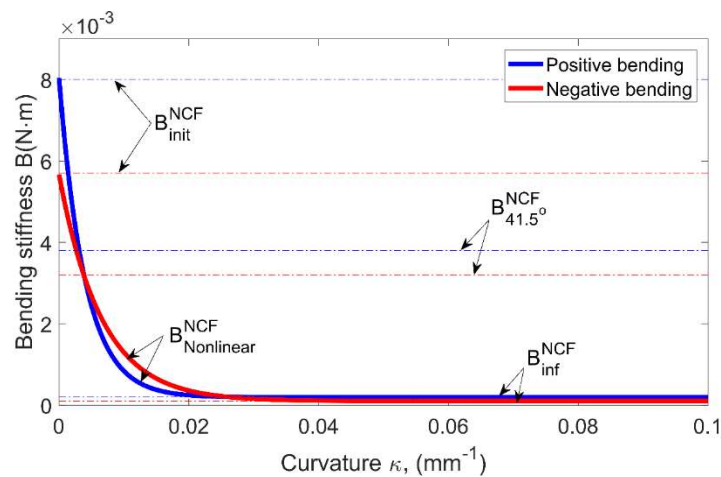
(b)

Figure 3.5: (a) Bending moment per unit width of specimen vs. curvature and (b) bending stiffness per unit width vs. curvature relations for the NCF ($B_{Nonlinear}$ denotes the non-linear bending stiffness per unit width measured by the revised cantilever test; $B_{41.5°}$ denotes the constant bending stiffness per unit width measured by the standard cantilever test at an angular deflection of 41.5° according to BS EN ISO 9073-7 [123]).

Overall, the bending stiffness for the NCF is significantly higher than the woven material over the range of curvature values presented (note difference in magnitude of y-axes between Figure 3.4(b) and Figure 3.5(b)). The nonlinearity of the bending behaviour for woven fabrics is mainly due to the slippage between inextensible fibres within the ply [57]. By scanning the surface of the bent NCF specimen (see Figure 3.6) using the SWLS, local buckling of the unidirectional layer can be observed on the compressive side of the specimen for each fibre orientation, which compromises the bending resistance of the fabric under large curvature. This tow buckling also causes the bending stiffness for the NCF specimens to decrease more rapidly with respect to curvature compared to the woven material (note the more rapid decrease in the bending stiffness of the NCF in Figure 3.5(b) compared with the decrease for the woven fabric in Figure 3.4(b)). As shown in Figure 3.5(a), the obtained $M(\kappa)$ curves for the two bending directions are similar but exhibit different gradients at the start and end of the curves (see Figure 3.5(b)). This indicates the dependency of the bending stiffness on the mesoscale architecture, which may be more pronounced for different NCF stitch patterns.

Table 3.2: Bending properties of the woven fabric and NCF measured by the standard cantilever test and the revised cantilever test, assuming linear and nonlinear bending relations respectively. $B_{41.5°}$ denotes the constant bending stiffness per unit width measured by the cantilever test at an angular deflection of 41.5°, according to BS EN ISO 9073-7 [123]. B_{init} is the bending stiffness per unit width at zero curvature and B_{inf} is the value taken from the asymptote of the non-linear bending curve as it approaches infinity. M denotes the bending moment per unit width of the specimen.

Materials	Bending property	
	Linear bending model (LBM)	Non-linear bending model (NLBM)
Woven fabric (38616)	B_{init}^{wov} = 0.00039 Nm $B_{41.5°}^{wov}$ = 0.00022 Nm B_{inf}^{wov} = 0.00002 Nm	$M_{nonlinear}^{wov} = 0.01549 \cdot \kappa + 0.00757\left(1 - e^{(-\kappa/0.02)}\right)$ N
Non-crimp fabric (NCF, FCIM359)	$B_{init}^{NCF,pos}$ = 0.0080 Nm; $B_{init}^{NCF,neg}$ = 0.0057 Nm $B_{41.5°}^{NCF,pos}$ = 0.0038 Nm; $B_{41.5°}^{NCF,neg}$ = 0.0032 Nm $B_{inf}^{NCF,pos}$ = 0.0002 Nm; $B_{inf}^{NCF,neg}$ = 0.0001 Nm	$M_{nonlinear}^{NCF,pos} = 0.19457 \cdot \kappa + 0.03139\left(1 - e^{(-\kappa/0.0040)}\right)$ N $M_{nonlinear}^{NCF,pos} = 0.10279 \cdot \kappa + 0.03619\left(1 - e^{(-\kappa/0.0065)}\right)$ N

(a)   (b)
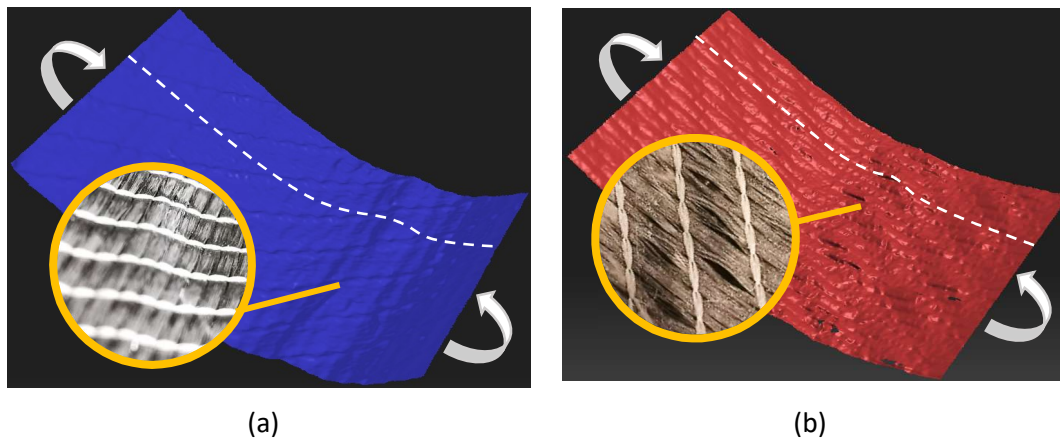
Figure 3.6: Surface scans of the compressive side of cantilevered bend NCF specimens under (a) positive and (b) negative bending. Inset photos show details of fibre buckling.

3.3   Material modelling

3.3.1   Decoupling membrane and bending stiffness

The bending stiffness of fabrics is not directly related to the tensile modulus of fibre material due to fibre slippage and tow buckling. This renders classic beam or shell elements invalid for modelling the bending behaviour of these fabric materials. According to Döbrich et al. [81], the membrane and bending behaviours of fabric material can be decoupled, therefore in the current work the Abaqus Composites Layup Toolset was employed to assemble these individually defined contributions using a laminate shell element. As shown in Figure 3.7, decoupling the membrane and bending stiffness was achieved by tailoring the layer thickness and the number of integration points within the layup. Three artificial layers were defined for each shell element (S4R, using the default hourglass control in Abaqus/Explicit), where the two outer surface layers were used to define the bending behaviour, while the central layer was used to control the membrane behaviour. The total thickness of the element, h, was the same as the fabric thickness, and the thickness of the two surface layers were assumed to be identical.
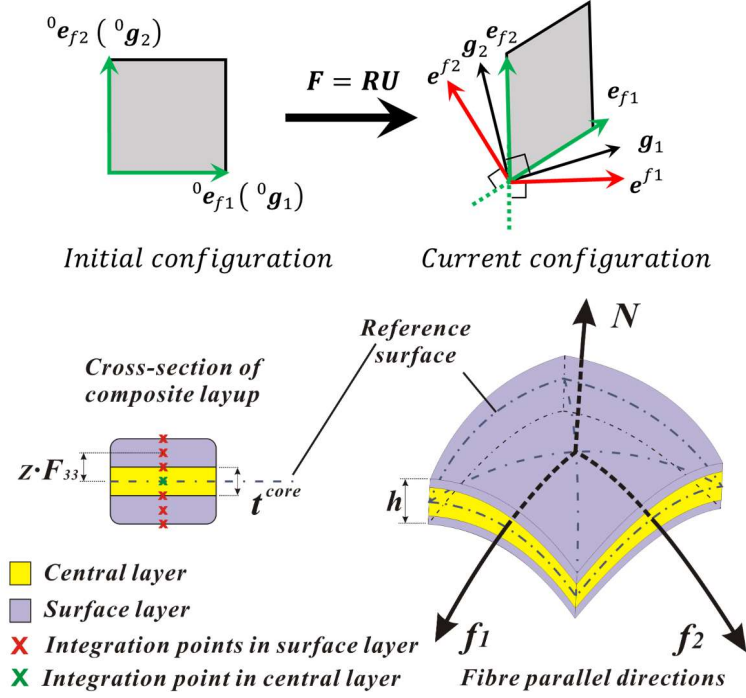
Figure 3.7: Schematic diagram of the shear deformation of biaxial fabric unit cell and the laminate layup model for membrane or bending stiffness decoupling.

The bending moment along each fibre direction in the deformed configuration, M_{fi}, acting at the shell cross-section, was calculated by integrating the moment resulting from the fibre stress $\sigma_{fi}(z)$ at the integration points over the thickness of the shell element.

$$M_{fi} = \int_{-h/2}^{+h/2} \left\{ \sigma_{fi}(z) \cdot \bar{F}_{33}^2 \cdot z \right\} dz. \tag{3.5}$$

Due to the incompressibility of the shell element, the thickness change $\bar{F}_{33}$ was determined by the in-plane components of the deformation gradient $\bar{F}_{ij}(i, j = 1,2)$, i.e.

$$\bar{F}_{33} = \frac{1}{\bar{F}_{11}\bar{F}_{22} - \bar{F}_{12}\bar{F}_{21}}. \tag{3.6}$$

Equation (3.5) implies that the stresses on the shell reference surface (i.e. the mid-plane of the shell element, where $z = 0$) has no contribution to the out-of-plane bending moment (or stiffness) of the shell element. Thus, a single integration point was assigned to the central layer to eliminate its bending contribution to the laminate layup. As a result, the bending stiffness only depends on the properties of the two surface layers.

Since the thickness of each fabric ply is much smaller than the in-plane dimensions of the specimen blank, the ply can be assumed to be a thin-walled shell in order to derive the macro bending resistance per unit length in the fibre directions. An identical Young's modulus (i.e.

E_{fi}^{surf}) was assigned to the top and bottom surface layers, whereby the bending stiffness in the ith fibre direction (i.e. B_{fi}, i=1, 2) was obtained as

$$B_{fi} = \frac{1}{12} E_{fi}^{surf} \left[h^3 - \left(t^{ctral} \right)^3 \right]$$ (3.7)

where, t^{ctral} denotes the thickness of the central layer.

According to Eq. (3.7), the expected bending stiffness B_{fi} can be achieved by adjusting either E_{fi}^{surf} or t^{ctral} or both. However, modifying E_{fi}^{surf} is considered to be the most practical way to control the bending stiffness B_{fi} due to a linear relationship between them.

Since the stress-strain relationship at the integration points was assumed to be elastic, a three-point Simpson's integration approach is sufficient for calculating the bending moment on the shell cross-section. Only one integration point was therefore assigned to each surface layer to reduce the computational cost. Thus, three integration points in total were used through the thickness direction of each fabric ply, eliminating the inertial moment of each layer with respect to its centroid axis. Therefore, the bending stiffness parallel to the fibres, B'_{fi}, can be written as

$$B'_{fi} = \frac{1}{16} E_{fi}^{surf} \left(h - t^{ctral} \right) \left(h + t^{ctral} \right)^2$$ (3.8)

The nominal Young's modulus of each fabric ply along the ith yarn (i.e. E_{fi}^{lam}) was determined according to the Rule of Mixtures

$$E_{fi}^{lam} = E_{fi}^{surf} \left(\frac{h - t^{ctral}}{h} \right) + E_{ctral} \left(\frac{t^{ctral}}{h} \right)$$ (3.9)

In practice, the laminate modulus, E_{fi}^{lam}, and the bending stiffness, B_{fi} or B'_{fi}, are input parameters, based on which the moduli values of each layer within the layup were determined. These were updated during the analysis to approximate the measured tensile and bending stiffness for each fibre direction.

3.3.2   Non-orthogonal constitutive framework

As shown in Figure 3.7, an established non-orthogonal constitutive model [30] was modified to define the bending contribution of each primary yarn based on the current fibre orientation frame, which is dependent on the rotation of the yarns during in-plane shear. The bending property of each yarn was added to the constitutive model by updating the moduli values of three layers within the composite shell element for each fibre direction. This approach enables the change in fibre orientation to be tracked during forming, updating

the bending stiffness term as the fabric shears in-plane. The material model was implemented through a user material subroutine (VUMAT) based on Abaqus/Explicit.

An established non-orthogonal constitutive model [30, 106, 145] was employed to track the in-plane fibre direction during forming, enabling the bending contribution of each yarn to be taken into consideration in order to update the fabric bending behaviour according to the in-plane shear deformation. In Abaqus/Explicit, the strain increment is supplied in the Green-Naghdi (GN) frame at each integration point. As shown in Figure 3.7, the base vectors of the GN frame in the initial configuration, $^0\boldsymbol{g}_\alpha$ (α = 1, 2, 3), can be updated using the rotation tensor $\boldsymbol{R}$ obtained from the polar decomposition of the deformation gradient $\boldsymbol{F}$

$$R = FU^{-1} \tag{3.10}$$

$$\boldsymbol{g}_\alpha = \boldsymbol{R} \cdot {}^0\boldsymbol{g}_\alpha \tag{3.11}$$

where $\boldsymbol{U}$ is the right stretch tensor. Let $^0\boldsymbol{e}_{fi}$ denote the initial fibre directions, where the current fibre directions, $\boldsymbol{e}_{fi}$, are traced using deformation gradient, $\boldsymbol{F}$,

$$\boldsymbol{e}_{fi} = \frac{\boldsymbol{F} \cdot {}^0\boldsymbol{e}_{fi}}{\left\|\boldsymbol{F} \cdot {}^0\boldsymbol{e}_{fi}\right\|} \tag{3.12}$$

The corresponding contravariant vectors of $\boldsymbol{e}_{fi}$ are

$$\boldsymbol{e}^{fi} = \frac{\boldsymbol{e}_{fi} - \left(\boldsymbol{e}_{fi} \cdot \boldsymbol{e}_{fj}\right) \cdot \boldsymbol{e}_{fj}}{\left\|\boldsymbol{e}_{fi} - \left(\boldsymbol{e}_{fi} \cdot \boldsymbol{e}_{fj}\right) \cdot \boldsymbol{e}_{fj}\right\|}, i \neq j \tag{3.13}$$

The normal vectors of the fabric surface are determined as

$$\boldsymbol{e}_{f3} = \boldsymbol{e}^{f3} = \frac{\boldsymbol{e}_{f1} \times \boldsymbol{e}^{f2}}{\left\|\boldsymbol{e}_{f1} \times \boldsymbol{e}^{f2}\right\|} = \frac{\boldsymbol{e}^{f1} \times \boldsymbol{e}_{f2}}{\left\|\boldsymbol{e}^{f1} \times \boldsymbol{e}_{f2}\right\|} \tag{3.14}$$

Consequently, the current fibre coordinate frames corresponding to $\boldsymbol{e}_{f1}$ and $\boldsymbol{e}_{f2}$ are established based on two sets of base vectors, i.e. $[\boldsymbol{e}_{f1}, \boldsymbol{e}^{f2}, \boldsymbol{e}^{f3}]$ and $[\boldsymbol{e}^{f1}, \boldsymbol{e}_{f2}, \boldsymbol{e}^{f3}]$ respectively. The transformation matrices between the GN frame and the fibre frames are

$$\boldsymbol{Q}_{f1} = \boldsymbol{Q}_{f1 \to GN} = \begin{bmatrix} \boldsymbol{g}_1 \cdot \boldsymbol{e}_{f1} & \boldsymbol{g}_1 \cdot \boldsymbol{e}^{f2} & \boldsymbol{g}_1 \cdot \boldsymbol{e}^{f3} \\ \boldsymbol{g}_2 \cdot \boldsymbol{e}_{f1} & \boldsymbol{g}_2 \cdot \boldsymbol{e}^{f2} & \boldsymbol{g}_2 \cdot \boldsymbol{e}^{f3} \\ \boldsymbol{g}_3 \cdot \boldsymbol{e}_{f1} & \boldsymbol{g}_3 \cdot \boldsymbol{e}^{f2} & \boldsymbol{g}_3 \cdot \boldsymbol{e}^{f3} \end{bmatrix} \tag{3.15}$$

$$\boldsymbol{Q}_{f2} = \boldsymbol{Q}_{f2 \to GN} = \begin{bmatrix} \boldsymbol{g}_1 \cdot \boldsymbol{e}^{f1} & \boldsymbol{g}_1 \cdot \boldsymbol{e}_{f2} & \boldsymbol{g}_1 \cdot \boldsymbol{e}^{f3} \\ \boldsymbol{g}_2 \cdot \boldsymbol{e}^{f1} & \boldsymbol{g}_2 \cdot \boldsymbol{e}_{f2} & \boldsymbol{g}_2 \cdot \boldsymbol{e}^{f3} \\ \boldsymbol{g}_3 \cdot \boldsymbol{e}^{f1} & \boldsymbol{g}_3 \cdot \boldsymbol{e}_{f2} & \boldsymbol{g}_3 \cdot \boldsymbol{e}^{f3} \end{bmatrix} \tag{3.16}$$

The strain increment in the GN frame, $\mathrm{d}\boldsymbol{\varepsilon}_{GN}$ can be transformed to the fibre frames

$$\mathrm{d}\boldsymbol{\varepsilon}_{fi} = \boldsymbol{Q}_{fi}^T \cdot \mathrm{d}\boldsymbol{\varepsilon}_{GN} \cdot \boldsymbol{Q}_{fi} \tag{3.17}$$

Thus, stress increments in the fibre frames can be computed using the corresponding strain increments

$$\mathrm{d}\boldsymbol{\sigma}_{fi} = \boldsymbol{C}_{fi} : \mathrm{d}\boldsymbol{\varepsilon}_{fi} \tag{3.18}$$

where $\boldsymbol{C}_{fi}$ is the constitutive tensor in the ith fibre direction. The explicit forms of Eq. (3.18) can be determined for the two fibres by assuming the elastic moduli in the fibre directions and the shear modulus are the only non-zero values:

$$\begin{bmatrix} \mathrm{d}\sigma_{11} \\ \mathrm{d}\sigma_{22} \\ \mathrm{d}\sigma_{12} \end{bmatrix}_{f1} = \begin{bmatrix} E_{f1}^* & 0 & 0 \\ 0 & 0 & 0 \\ 0 & 0 & G_{12}(\gamma) \end{bmatrix} \begin{bmatrix} \mathrm{d}\varepsilon_{11} \\ \mathrm{d}\varepsilon_{22} \\ \mathrm{d}\varepsilon_{12} \end{bmatrix}_{f1} \tag{3.19}$$

$$\begin{bmatrix} \mathrm{d}\sigma_{11} \\ \mathrm{d}\sigma_{22} \\ \mathrm{d}\sigma_{12} \end{bmatrix}_{f2} = \begin{bmatrix} 0 & 0 & 0 \\ 0 & E_{f2}^* & 0 \\ 0 & 0 & G_{12}(\gamma) \end{bmatrix} \begin{bmatrix} \mathrm{d}\varepsilon_{11} \\ \mathrm{d}\varepsilon_{22} \\ \mathrm{d}\varepsilon_{12} \end{bmatrix}_{f2} \tag{3.20}$$

where, γ is the shear angle ($\gamma = 2\varepsilon_{12}$), and the superscript '*' denotes the through-thickness location of the integration point in the laminate shell element. If the integration point is in the central layer then $E_{fi}^* = E_{fi}^{core}$, otherwise $E_{fi}^* = E_{fi}^{surf}$. It is assumed that the contribution from each yarn to the fabric shear force is equal [106], therefore $G_{12}(\gamma)$ can be determined from the normalised shear force (F_{norm}) in Table 3.1:

$$G_{12}(\gamma) = \frac{F_{norm}(\gamma)}{h} \tag{3.21}$$

The stress tensor in each fibre frame at the end of the time increment, $\boldsymbol{\sigma}_{fi}^{new}$, is computed by adding the stress increment tensor to the stress tensor at the beginning of this time increment $\boldsymbol{\sigma}_{fi}^{old}$

$$\boldsymbol{\sigma}_{fi}^{new} = \boldsymbol{\sigma}_{fi}^{old} + \mathrm{d}\boldsymbol{\sigma}_{fi} \tag{3.22}$$

Finally, the stress tensor in the fibre frames are transformed back to the GN frame and superimposed for updating the stress tensor at the integration point:

$$\boldsymbol{\sigma}_{GN}^{new} = \boldsymbol{Q}_{f1} \cdot \boldsymbol{\sigma}_{f1}^{new} \cdot \boldsymbol{Q}_{f1}^T + \boldsymbol{Q}_{f2} \cdot \boldsymbol{\sigma}_{f2}^{new} \cdot \boldsymbol{Q}_{f2}^T \tag{3.23}$$

Unlike the hybrid beam-membrane/shell meshes reported in the literature [108, 128], where bending stiffness is considered via additional elements with rotational degrees of freedom (DOFs), the current method requires less DOFs and is mesh-independent for non-orthogonal fibres [66].

3.3.3   Curvature updating

According to the Koiter-Sanders shell theory [189], in-plane strain at an integration point through the thickness of the S4R element can be determined by superposition of the

membrane strain on the reference surface, $\bar{\varepsilon}$ and the bending strain related to the element curvature, κ. Thus, the fibre strain, ε_{fi}, (i=1, 2), in the fibre coordinate system can be determined by the fibre strain on the shell reference surface (i.e. $\bar{\varepsilon}_{fi}$) and the curvature of reference surface (i.e. κ_{fi}):

$$\varepsilon_{fi} = \bar{\varepsilon}_{fi} + \bar{F}_{33} z_0 \kappa_{fi} \qquad (3.24)$$

where, z_0 is the initial distance from the integration point to the mid-plane of the shell element and $\bar{F}_{33}$ is the thickness change defined in Eq. (3.6).

The procedure for updating the bending moment and curvature is shown in Figure 3.8. During each time increment, the non-orthogonal constitutive framework is employed to determine the strain along each fibre direction. Eq. (3.24) is then used to calculate the current curvature of each yarn, which relates to the bending stiffness. Thus, their relationship should be measured as material inputs to update the bending stiffness. This procedure was implemented in a VUMAT based on Abaqus/Explicit. However, the calculation of the bending moment and curvature in the fibre parallel systems for each element requires data from adjacent integration points in the thickness direction, which is not directly available in the VUMAT. A user defined subroutine VEXTERNALDB was therefore employed to access a global data array for passing and updating element information between time increments. The subroutine VUMAT is typically called multiple times in each time increment, whilst the VEXTERNALDB subroutine is called once at the start and once again at the end of each time increment. The global data array containing fibre curvatures is initially passed into the VUMAT when the VEXTERNALDB is called at the start of the time increment. Based on these curvature values, the bending stiffness and the corresponding Young's modulus can be determined for each layer within the laminate shell element. Subsequently, the VUMAT is called multiple times to update stresses and strains at each integration point, which are also written into the global data array. Once all integration points have been processed in the VUMAT, the VEXTERNALDB is called again at the end of the time increment to update fibre curvatures ready for the next time increment, based on the strains previously stored in the global data array. Using this strategy, the bending stiffness in the current time increment was determined based on the curvature in the previous time increment. This does not adversely affect the accuracy of the model, since the time increment in the explicit analysis is typically small compared to the step time (time length of loading history).
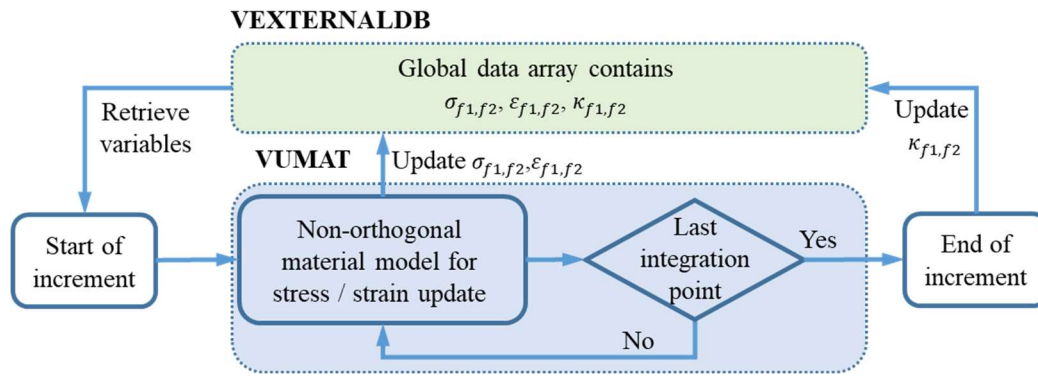
Figure 3.8: Flowchart for the implementation of the non-linear bending stiffness into Abaqus VUMAT: bending moment and curvature update.

3.4   Model validation

3.4.1   Picture frame test simulation

Picture frame tests were simulated to confirm that decoupling the membrane stiffness and the bending stiffness does not have an adverse effect on the in-plane shear response. Shear compliance curves for the woven fabric and NCF [30] were taken as the simulation input (see Table 3.1). In order to reduce the computational time, the axial Young's modulus along the fibre direction was chosen to be 3 GPa throughout this work and the fibre strain was limited to <1%, as recommended by Harrison et al [80]. All fabric plies were modelled using Abaqus shell elements (S4R) with an edge size of 3 mm × 3 mm, as established by a mesh density study in [30].

As shown in Figure 3.9(a), the cross-head force increases rapidly at the beginning of the picture frame test, due to intra-tow friction (see inset image), but the magnitude of these forces is relatively low (0.15 N). Overall, the curve for the cross-head force predicted by the current model for the woven fabric closely mimics the curve obtained from the experiment, with the root mean square error (RMSE) for the peak value being less than 0.3%. For the FCIM359 NCF [30], the predicted cross-head force closely matches the experiment data in Figure 3.9(b), with the RMSE less than 3%. These comparisons indicate that the predicted in-plane shear behaviour is not adversely affected by incorporating the bending stiffness term into the model for both woven fabrics and NCF.

(a)   (b)
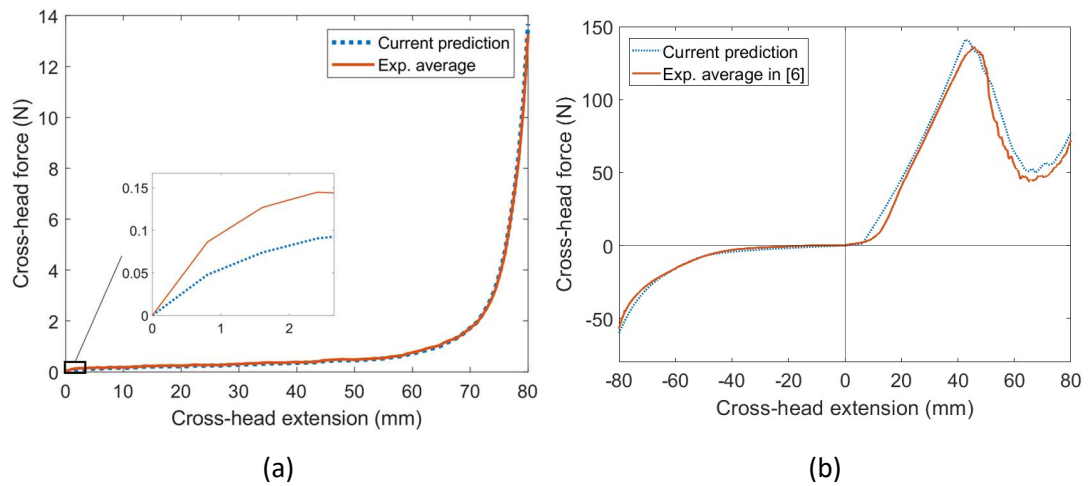
Figure 3.9: Comparison of experimental and predicted in-plane shear compliance curves for (a) the woven fabric (38616) and (b) the NCF (FCIM359).

3.4.2   Cantilever test simulation

Bending simulations were performed for both the woven fabric and NCF specimens subjected to gravity, using the linear bending model (LBM) and the nonlinear bending model (NLBM) described in Section 3.2.2. These simulations are compared against experimental data for the woven fabric in Figure 3.10 and for the NCF in Figure 3.11.

Figure 3.10: Comparison of bending deflections of the woven fabric (38616) for experimental SWLS data (including error bars) and FEA predictions. FEA predictions assume linear (FEA, B41.5) and non-linear (FEA, BNL) bending stiffnesses.

The edge profile simulated by the nonlinear bending model falls within the error bars of the experimental data, with the difference in the tip deflection being less than 0.3 mm. The

profile simulated using the constant bending stiffness approach at an angular deflection of 41.5° (denoted as FEA, $B_{41.5}$ in Figure 3.10) over-predicts the experimental mean curve, with the simulated tip deflection being 4 mm higher than the experimental point.

NCF coupons were simulated in both positive and negative bending configurations. The edge profile of the simulated NCF coupons falls within the corresponding error bars from the experimental study. The difference in the tip deflection between the experimental coupons and the profile predicted by the non-linear bending model is less than 0.5 mm for positive bending and less than 1.5mm for negative bending. A small difference in angular deflections (less than 4°) is observed between the positive and negative bending directions. For comparison, simulations were also performed using a constant bending stiffness value measured by the standard cantilever test at an angular deflection of 41.5° (denoted as FEA, $B_{41.5}$ in Figure 3.11). The deflected shape sits significantly above the experimental data, indicating that the standard cantilever test [123] may not be suitable for the NCF.

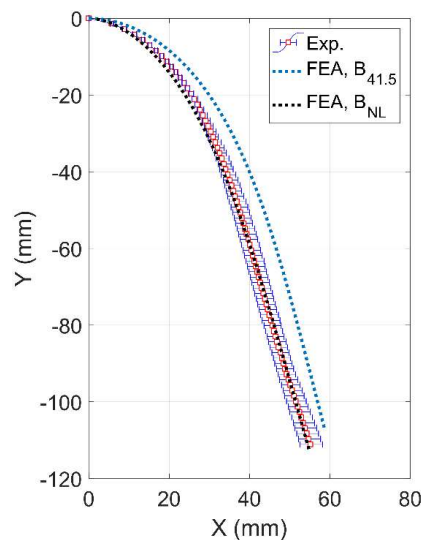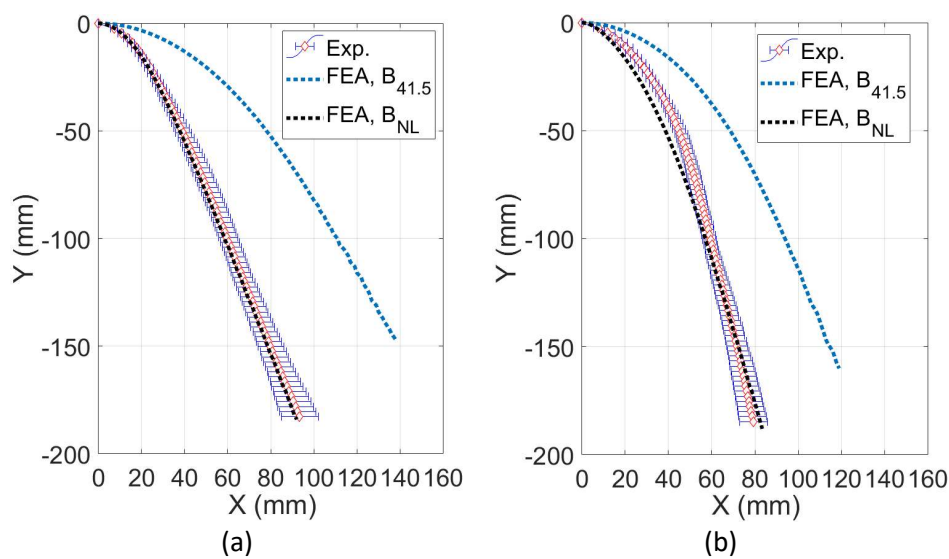*Figure 3.11: Comparison of bending deflections of NCF (FCIM359) for experimental SWLS data (including error bars) and FEA predictions for (a) positive and (b) negative bending configurations. FEA predictions assume linear (FEA, $B_{41.5}$) and non-linear (FEA, B_{NL}) bending stiffnesses.*

3.4.3   Bias extension test simulation

Bias extension testing was used to generate controlled macroscale out-of-plane wrinkles in fabric specimens. The in-plane shear curves and the non-linear $M(\kappa)$ bending curve from Section 3.2 used as material model inputs to simulate the bias-extension test for both the woven fabric and NCF. For the woven fabric, the effective specimen area was 300 mm by 150

mm, with the shorter edge clamped at one end and a 60 mm displacement applied at the other. For the NCF, the effective specimen area was 200 mm by 100 mm, with a 40 mm displacement applied to the shorter edge during the test. The fabric was modelled using quadrilateral laminate shell elements (2 mm × 2 mm) with reduced integration (S4R). The true areal density of fabrics (0.44 kg/m^2 for the NCF and 0.21 kg/m^2 for the woven fabric) was assigned to the FE model.

The surface waviness of wrinkled specimens was obtained by photogrammetry approaches to validate the FE model, using both Digital Image Correlation (DIC) and SWLS for the NCF specimens and SWLS for the woven fabric specimens. A powder-based Flaw developer (Ambersil Flaw Developer 3) was uniformly applied on fabric specimens prior to SWLS to remove reflections from carbon fibres, enabling SWLS to capture the deformed shape of the specimen. When performing DIC, a graphite spray (Kontakt Graphit 33 Spray) was applied to the NCF specimens and the flaw developer was subsequently used to produce a spackle pattern on the pre-treated specimens. Due to the low integrity of fibre tows and low stiffness of the woven fabric, this two-step spraying treatment to enable DIC measurements may significantly affect the shear behaviour of the woven fabric. Thus, only SWLS was used to acquire the shape of the shear-induced wrinkles at different crosshead displacements for the woven material.

All tests were carried out on a universal testing machine at a crosshead speed of 20 mm/min. A GOM DIC setup with two cameras was mounted in front of the testing machine to monitor the deformation of the speckled NCF specimen, enabling full-field out-of-plane displacements and local shear angles to be calculated. Shear angle variations at individual points were obtained by correlating the relative angle from facet points (subset size: 15 × 15 pixels) located along the fibre tows. As suggested in [80], the initiation point of wrinkling in the bias-extension test was captured when the wrinkle amplitude at the central cross-section of the specimen first exceeded 1 mm. Based on the point cloud generated by SWLS, an open-source software, CloudCompare [190], was used to determine wrinkle amplitudes at different cross-head displacements by comparing the point cloud of the deformed specimen against the reference cloud at zero extension.

Out-of-plane displacements from the FE simulations are compared with experimental results for different loading stages. For the woven fabric, wrinkling starts when the shear deformation reaches an angle of 50° (extension = 45 mm), as shown in Figure 3.12. A primary wrinkle occurs along the central line of the specimen. The wrinkle amplitude increases to peak values (i.e. 4.2 mm for positive amplitude and 3.6 mm for negative amplitude) at an

extension of 52 mm. Figure 3.13 compares the amplitude of the largest wrinkle in the centre of the specimen (see Section A-A in Figure 3.12) taken from the simulation and experiment at two extensions, i.e. 45 mm and 52 mm. There is good agreement between the experimental and simulation data sets (RMSE ≤ 4.5 %) at an extension of 45 mm. At an extension of 52 mm, the predicted wrinkle profile agrees well with the experimental data across the width of the specimen (i.e. between -20 mm and 20 mm in Figure 3.13(b)), with a RMSE of less than 5.0%.
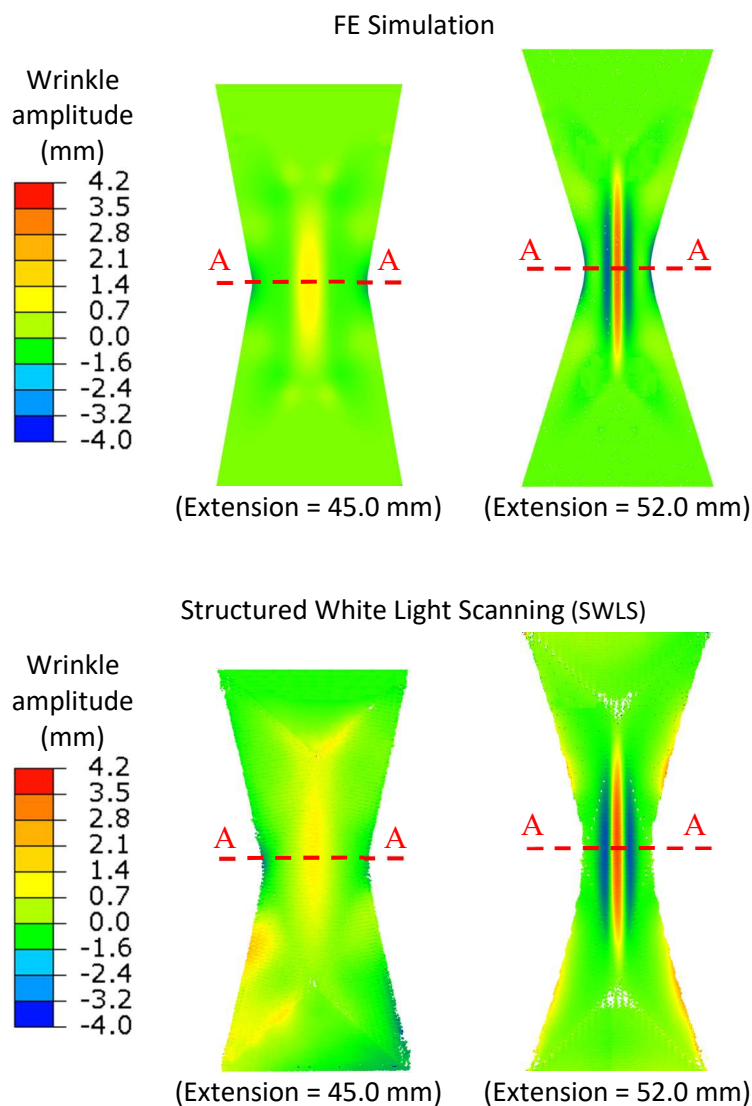

Figure 3.12: Out-of-plane wrinkling from bias-extension simulation (top row) against SWLS (bottom row) measurements.

For the NCF specimen, fabric wrinkling starts when the shear deformation reaches an angle of 8° (extension = 7.5mm) due to yarn compaction and the absence of constraints along the free edges of the specimen. However, this shear angle may not be a suitable threshold for the onset of wrinkling during forming, since tension in the fibres and through-thickness compression from the blank holder may prevent wrinkles from occurring. The wrinkle amplitude rapidly increases to a peak value (~3.6 mm) at an extension of 14.1 mm. The maximum out-of-plane displacement varies within the range of 3.0–3.5 mm until stitches start to fail at an extension of 23.0 mm. The wrinkle patterns monitored by DIC and SWLS are approximately symmetric about the central axis in the loading direction, with the greatest waviness occurring in the centre of the specimen (see Section A-A in Figure 3.14), which agrees with the FE simulations. The amplitude of the largest wrinkle taken from the simulation is compared against DIC and SWLS measurements for 12 specimen repeats in Figure 3.15. There is a good agreement between the experimental and simulation data sets (RMSE < 2.5%).

The DIC setup was unable to track the speckle pattern on the specimen once stitches started to fail and intra-ply fibre slippage occurred. In comparison, SWLS was more effective for characterising out-of-plane wrinkles throughout the test. According to the SWLS data in Figure 3.14, the waviness amplitude and the wrinkled area both decrease during the test for the NCF specimens due to the release of constraints, implying that the local removal of intra-ply stitches could be a potential way to eliminate forming-induced wrinkles for biaxial NCFs
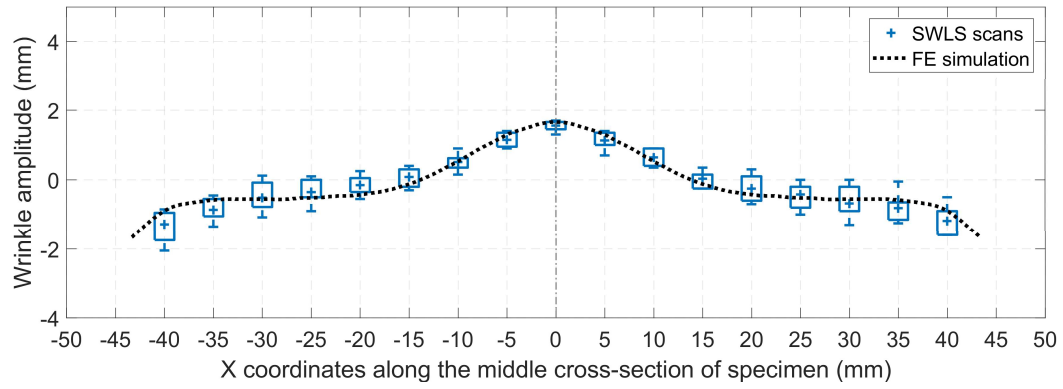
(a) Applied displacement = 45 mm
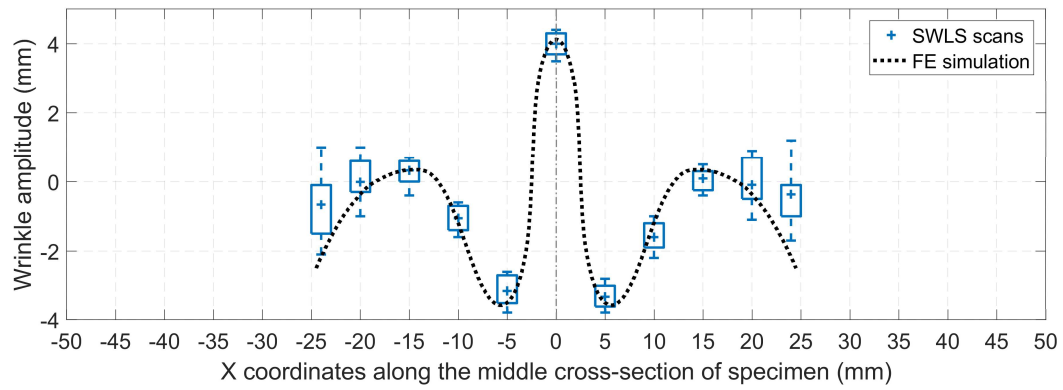
(b) Applied displacement = 52 mm

Figure 3.13: Deformed cross-sectional shape (Section A-A in Figure 3.12) at the centre of a bias extension specimen (Woven fabric). The dotted line represents the prediction from the FE simulation and the box plots represent data points measured by SWLS.
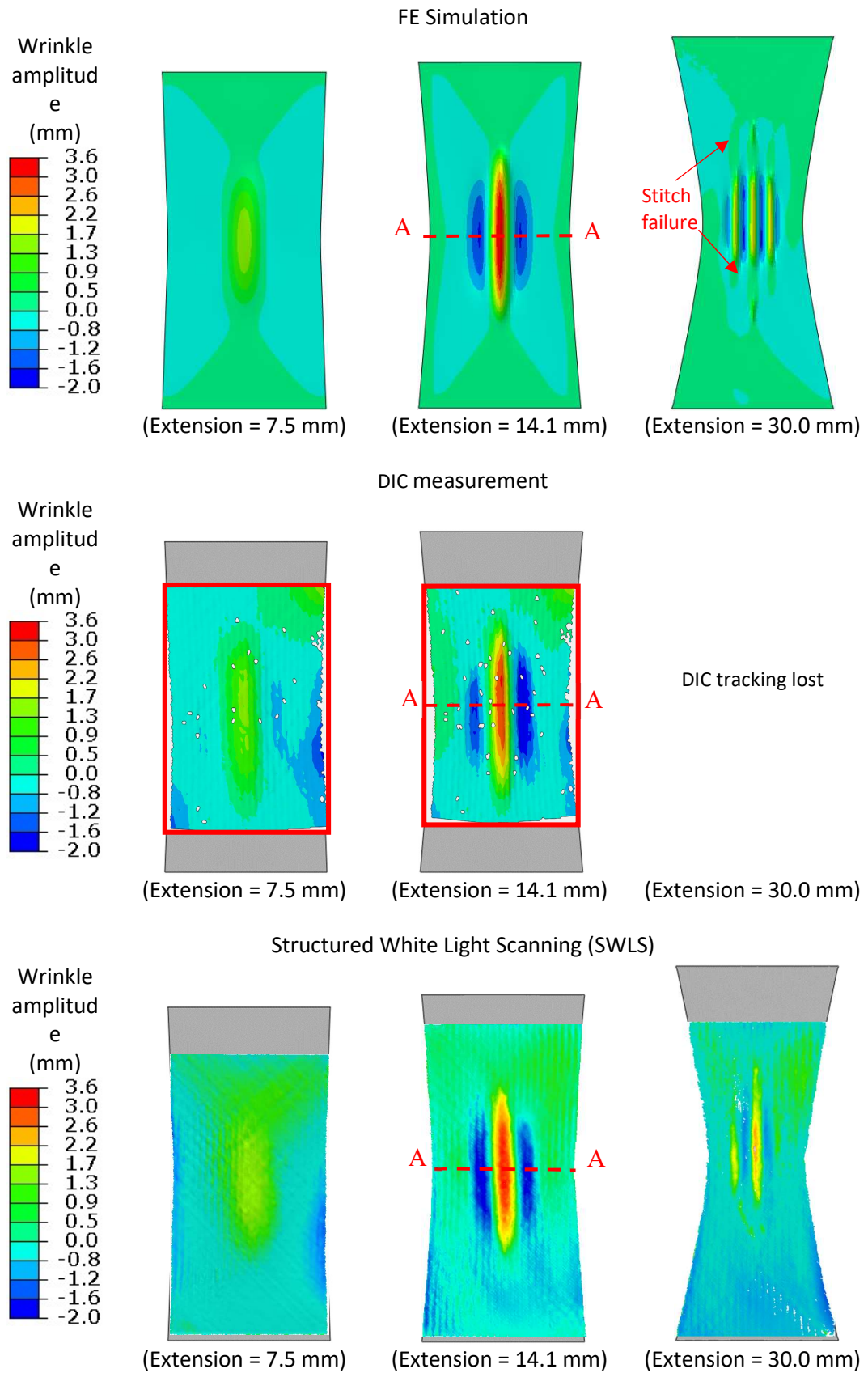
Figure 3.14: Out-of-plane wrinkling from bias-extension simulation (top row) against DIC (middle row) and SWLS (bottom row) measurements.
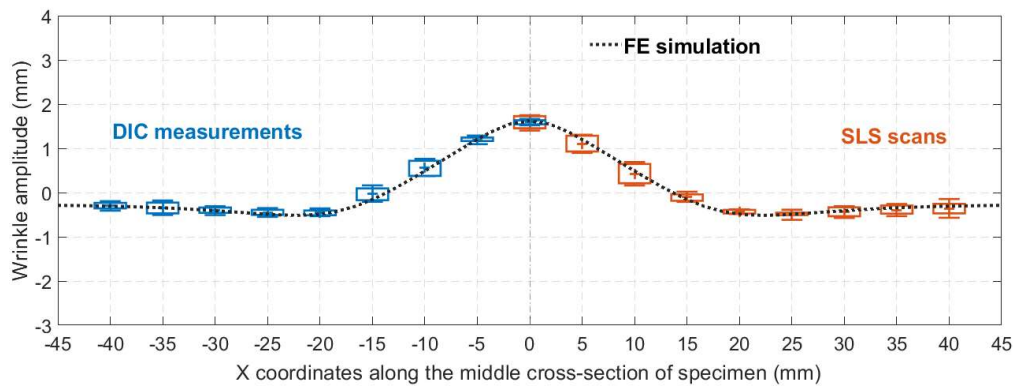
(a) Applied displacement = 7.5 mm
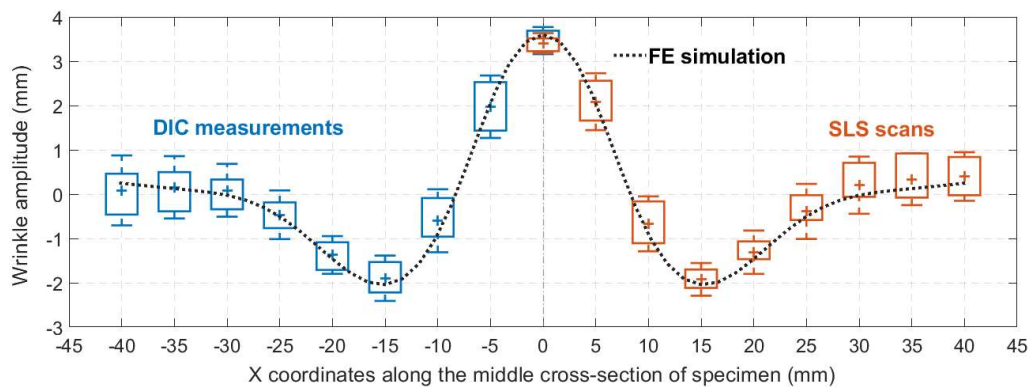
(b) Applied displacement = 14.1 mm

Figure 3.15: Deformed cross-sectional shape (Section A-A in Figure 3.14) at the centre of a bias extension specimen (NCF). The dotted line represents the prediction from the FE simulation and the box plots represent data points measured by DIC and SWLS.

3.4.4   Validity of bias-extension test

Compared with the picture frame test, bias extension test is advantageous in characterising the shear resistance for woven fabrics since it is simple to perform. However, it is difficult to ensure uniform shear within the central diamond region of the NCF specimen (the region indicated by the black dashed line in Figure 3.16) when fabric wrinkling occurs or stitches fail. This can clearly affect the measured shear angle distribution, causing inaccurate shear compliance curves [117]. As shown in Figure 3.16(a), the shear angle distribution in the central diamond region of a bias extension specimen becomes non-uniform as a result of wrinkling, even though the shear deformation is small. The pure shear condition in the bias-extension test is disrupted by local stitch failure at an extension of 30 mm. In comparison, as shown in Figure 3.16(b), the picture frame shear test at the same shear angle is able to ensure uniform shearing due to the absence of wrinkling in the central zone. The pure shear condition is maintained across the entire specimen area within the 4-bar linkage system,

although stitches have failed. Therefore, the picture frame shear test is considered to be a more relevant test for characterising the in-plane shear behaviour of biaxial NCF fabrics.

(a)

(b)
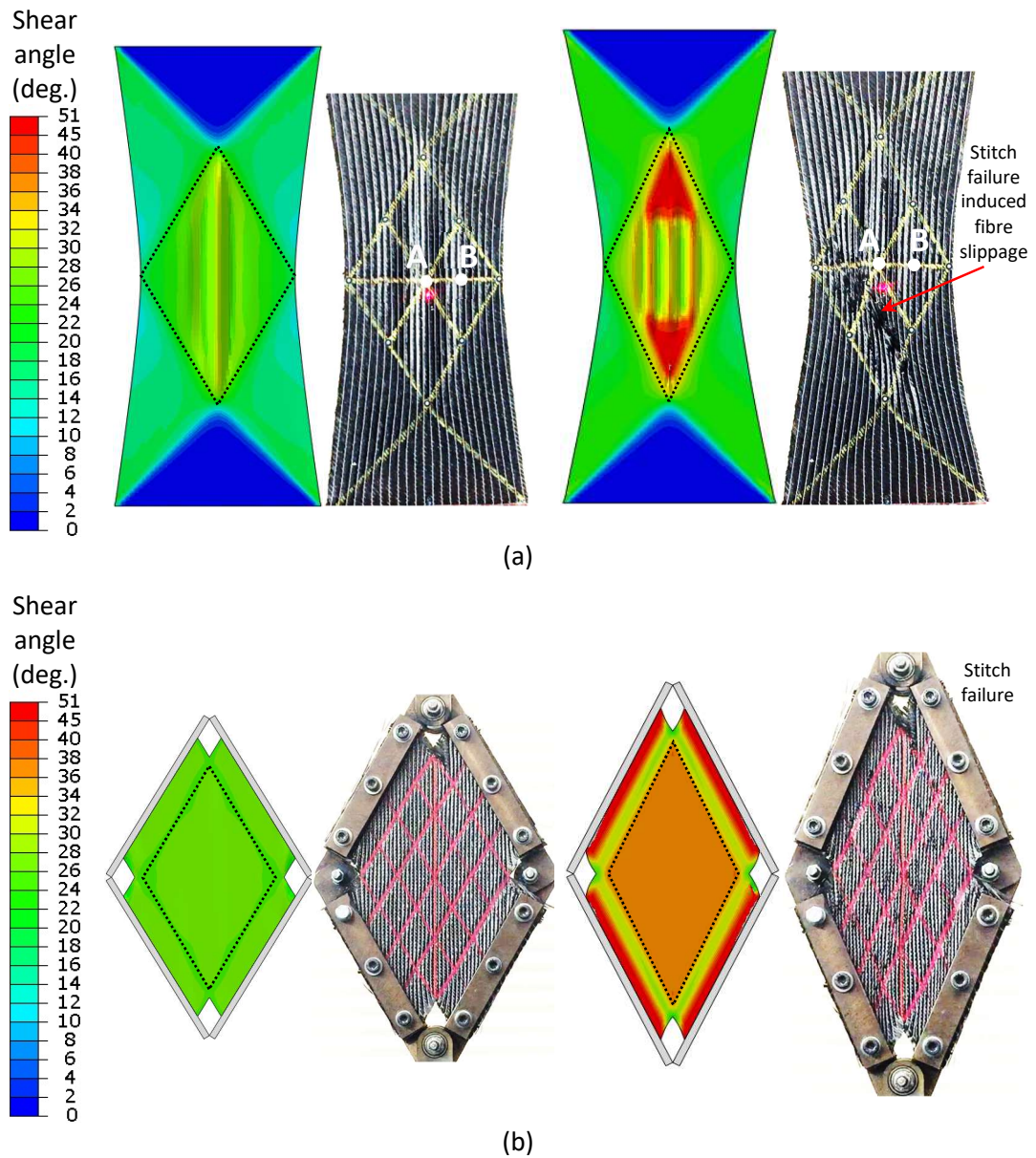
Figure 3.16: Comparison of predicted and measured shear deformation in (a) bias extension test and (b) picture frame shear test. The right hand pair of images in each case indicate the shear deformation following stitch rupture. The central diamond regions bounded by the black dotted lines indicate areas of interest for in-plane shear characterisation.

The severity of the non-uniform shear condition in bias extension testing has been explored further by considering the shear angle distribution at two discrete points within the central diamond shaped "pure shear" zone, marked A and B (see Figure 3.16). Average shear angles

derived from DIC measurements taken from the surface of six specimen repeats are plotted in Figure 3.17 for points A and B. For comparison, shear angles from the FEA simulations are also included. All curves appear to be similar prior to wrinkling, but all are lower than the theoretical curve [80] which assumes a perfect pin-jointed net. This discrepancy has previously been attributed to intra-ply fibre slippage and size effects caused by the specimen width [118].

The shear angles at Points A and B increase linearly with the crosshead displacement, but then deviate from each other after wrinkling occurs at an extension of 7.5 mm. This confirms that the shear angle distribution becomes non-uniform when wrinkling starts, and therefore the pure shear assumption in the central diamond region is no longer valid. The difference in shear angle at Points A and B increases gradually, reaching a maximum difference of 8° before the DIC speckle pattern breaks down (extension of 20 mm). The bifurcation point at an extension of 7.5 mm denotes the onset of wrinkling in this bias extension test, raising concerns over the quality of the in-plane shear data. Although the measured shear angle variation at Point A is close to the theoretical curve, it does not match the shear load derived from the crosshead force based on the assumption of an ideal pin-jointed net. This is due to the redistribution of shear load within the central diamond region.

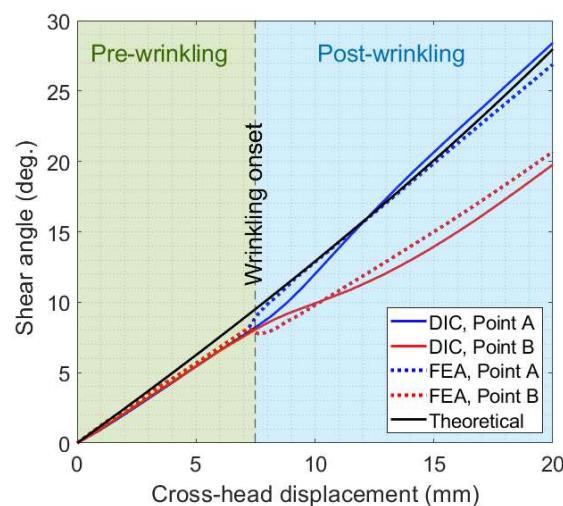*Figure 3.17: Shear angle vs. crosshead displacement curves derived from DIC, FEA and theoretical shear kinematics for Points A and B on the specimen in Figure 3.16.*

3.5   Chapter Summary

A macro-scale FE model has been developed to simulate the forming behaviour of biaxial fabrics. Fibre-orientation dependent non-linear bending has been integrated into a non-

orthogonal fabric model. The mechanical behaviour of the fabric is defined using a material subroutine in Abaqus/Explicit, avoiding the need for a bespoke element formulation. Comparisons with experimental data have shown the suitability of the proposed method to replicate the macroscale deformation of bi-axial fabrics.

Bending behaviours of a pillar-stitched NCF and a balanced twill weave woven fabric have been characterised by a revised cantilever test. A polynomial function is used to fit the deflection shape acquired by a Structured White Light Scanner to obtain the non-linear bending moment as a function of curvature at all points along the specimen.

The model is validated by studying out-of-plane wrinkle formation during bias extension testing for both the woven fabric and the NCF. A combination of digital image correlation (DIC) and SWLS are used to measure the wrinkle amplitude from experimental bias extension coupons. The predicted shape and magnitude of wrinkles matches well with the experimental data, with the root mean square error of the wrinkle amplitude being less than 5%.

Since the woven fabric exhibits low shear resistance, wrinkling starts at a large shear angle (~50°). In comparison, wrinkling of the NCF specimen is initiated at much smaller shear deformation (~8°) and the amplitude of these wrinkles remains constant until stitches started to fail (~29°). Subsequently, the wrinkle amplitude reduces as stitches progressively fail, indicating that the in-plane shear compliance affects the onset and propagation of wrinkles. Reducing the fabric shear resistance by locally removing stitches may therefore be a potential way to reduce or delay the onset of wrinkling.

From both DIC measurements and the FEA simulation, it is concluded that the picture frame test is a more robust method for producing in-plane shear curves for NCF fabrics compared to the bias extension test. The bias extension test may not be able to produce uniform shearing in the central area of the NCF specimen, due to the presence of out-of-plane wrinkles and stitch failure causing fibre slippage.

Chapter 4   Simulation and evaluation of forming induced wrinkling

4.1   Introduction

The fabric constitutive model developed in Chapter 3 is used in this chapter to investigate the forming-induced wrinkling behaviour for bi-axial fabrics. The two fabrics characterised in Chapter 3 are used here to conduct forming experiments and simulations, using both the linear (LBM) and nonlinear bending modelling (NLBM) approaches. A new methodology is developed to quantitatively evaluate the severity of fabric wrinkles based on the results from the FE simulation. The nodal distance between the surface of the preform and the mould tool is used to locate areas with out-of-plane defects, using the principal curvature to distinguish between fabric buckles and areas of poor conformity.
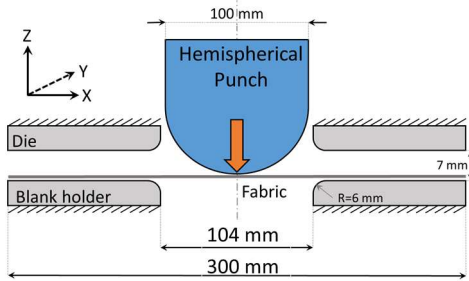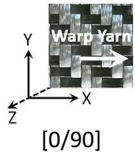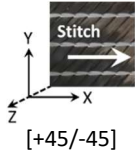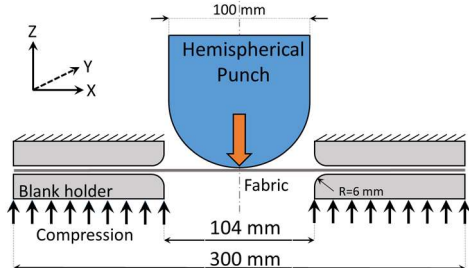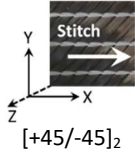
4.2   Experiments

4.2.1   Press tool forming test

Press tool forming trials were conducted for both fabrics using a hemisphere rig. Two forming configurations were considered, as shown in Table 4.1. For Case A, a controlled 7 mm gap was introduced between the blank holder and die to enable the fabric blank to wrinkle out-of-plane in a controlled manner during the stroke of the punch. For Case B, a clamping force of 1000 N was applied to the closed blank holder (no gap) to control the material draw-in during forming, preventing the fabric blank from excessively wrinkling. A single fabric ply was used each time for Case A, using both fabric types. Two NCF plies of the same fibre orientation were used for Case B. The warp yarn direction of the woven fabric (0°/90°) and the stitch direction of the NCF were initially aligned with the edge of the blank holder prior to forming, as shown in Table 4.1. A constant punch velocity of 100 mm/min was used at ambient temperature. The stroke length was 50mm, measured from the initial point of contact with the upper surface of the fabric blank. A small amount (6%wt) of reactive binder (Momentive Epikote 620) was evenly distributed on the upper surface of each ply prior to forming. The powder binder was activated by cartridge heaters embedded in the blank holders and the punch once the final stroke had been reached. The temperature was subsequently ramped up to 165 °C and held for 10 minutes to cure the binder in order to keep the shape of the produced preform.

Table 4.1: Forming configuration, material, ply orientation and clamping method used for forming trials.

Forming configuration		Material	Ply orientation	Clamping method
Case A		Woven fabric 38616	[0/90]	Controlled gap (7 mm)
		NCF FCIM 359	[+45/-45]	Controlled gap (7 mm)
Case B		NCF FCIM 359	[+45/-45]$_2$	Clamping force (1000 N)

4.2.2   Wrinkle measurement

The shapes of the deformed hemisphere specimens were captured using the SWLS. Ambersil Flaw Detector was uniformly sprayed onto the deformed fabric specimens once removed from the forming tool, to eliminate excessive reflection from the carbon fibres. The prepared specimens were positioned on a turntable connected to the scanner to take a series of scans at different angles, to capture full 3D representations of each preform. Open-source software, CloudCompare [190], was used to determine the wrinkle amplitude of the preforms produced by forming Case B, by comparing the point cloud of the deformed specimen against the punch geometry and the bottom blank holder. The probability density was calculated based on the nodal deviation distance between the blank and the tool surface over the entire fabric area, as shown in Figure 4.1 and Figure 4.2 respectively. The repeatability associated with the SWLS measurements for forming Case A was found to be high, with a root mean square error (RMSE) of less than 3% for the woven fabric and less than 8% for the NCF.

Figure 4.1: Probability density of wrinkle amplitude measured from three experimental repeats for the woven fabric for forming Case A. Inset image shows an example of the experimental 3D scan data, where the scale indicates wrinkle amplitude in millimetres.

(b)

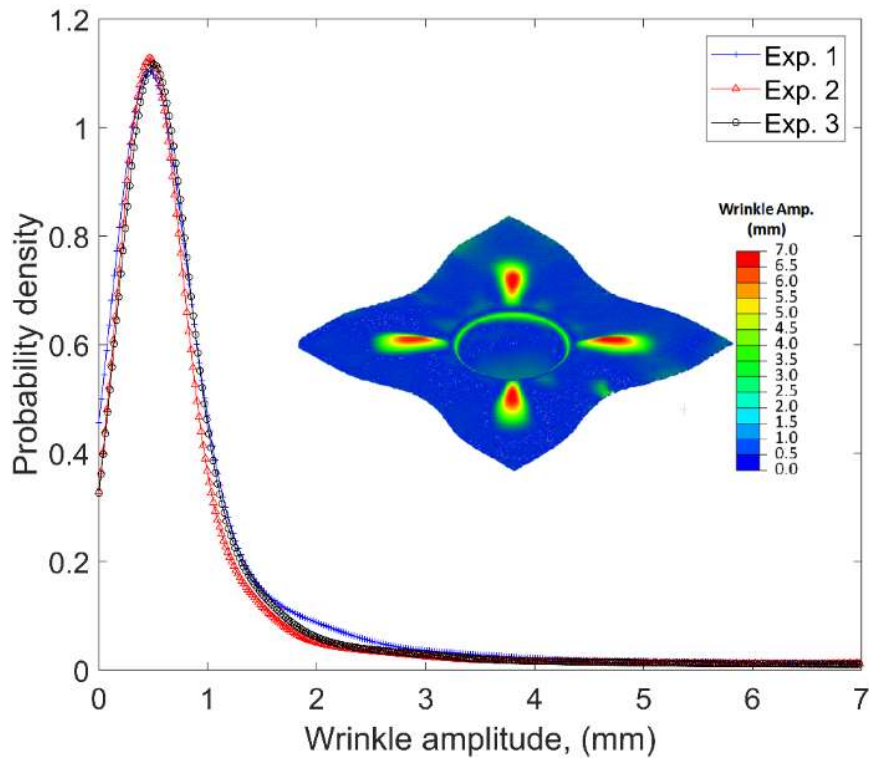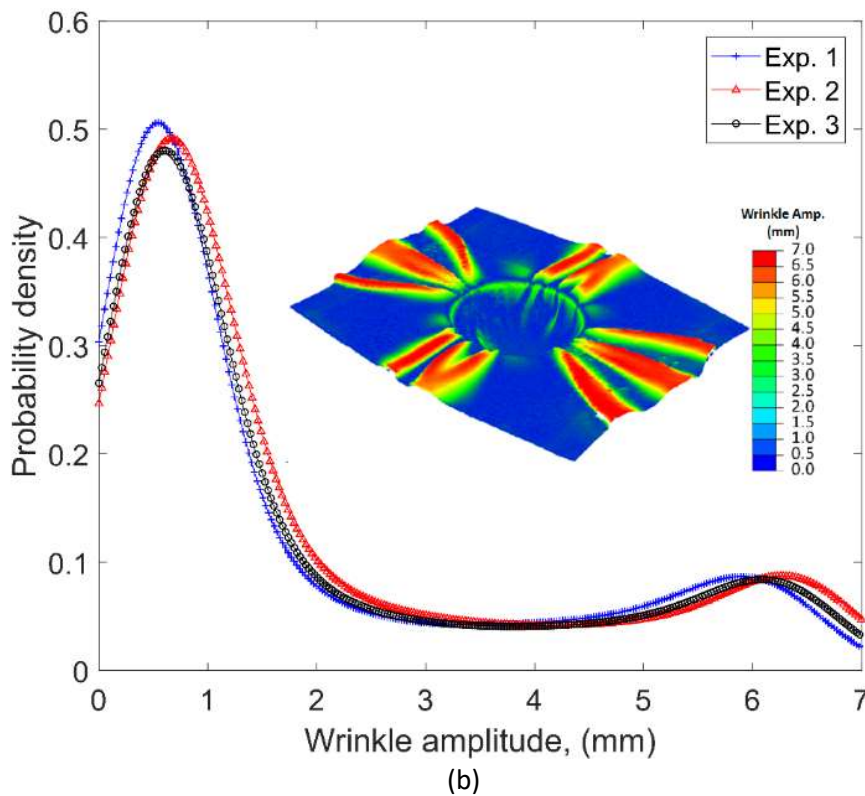*Figure 4.2: Probability density of wrinkle amplitude measured from three experimental repeats for the NCF for forming Case A. Inset image shows an example of the experimental 3D scan data, where the scale indicates wrinkle amplitude in millimetres.*

4.3   Simulation approach

4.3.1   Model setup

The constitutive model developed in Chapter 3 was used to simulate the forming behaviour of fabrics for the forming cases listed in Table 4.1. For Case A, the laminate shell element approach (using S4R elements) was compared to a membrane element approach [30] (using quadrilateral membrane elements M3D4R) to demonstrate the significance of incorporating the bending stiffness term into the simulation for predicting realistic fabric wrinkle patterns. The element edge length was 2 mm for both fabrics. The polynomials representing the in-plane shear compliance for each material are presented in Table 3.1. All parts of the tooling, including the hemispherical punch and the blank holders, were modelled as rigid bodies. Interactions at all interfaces were modelled using a penalty contact algorithm, assuming an isotropic Coulomb-based friction model. The tool-fabric and fabric-fabric friction coefficients were measured to be 0.23 and 0.36 respectively [30]. A vertical displacement of 50 mm was applied to the punch. The axial fibre modulus was assigned to be 3.0 GPa in each case to limit the axial strain in the fibre direction to less than 1%. [80]. Both linear and non-linear bending relations were implemented using the laminated shell element approach, to evaluate the sensitivity of the predicted wrinkle patterns to the bending stiffness input.

For forming simulations using an explicit algorithm, the total time of the loading history (known as the step time in Abaqus) can be scaled to be smaller than the actual time duration observed in experiments [176]. This can be used to reduce the CPU time without significantly compromising accuracy [80]. Alternatively, Mass Scaling can be used to speed up the forming simulation by increasing the size of the time increment during the explicit analysis [21, 108, 176]. These two techniques can be used either independently or together in Abaqus/Explicit to accelerate simulations for quasi-static processes [176].

For Case A, the total step time was assigned to be 3 seconds (compared to 30 seconds for the experiment), but no mass scaling was used. The run time for the shell element approach was approximately 16 hours for the NLBM and 12 hours for the LBM. In comparison, the run time for the membrane element-based approach was 2.5 hours for the same step size. (The computer specification was the same for both cases: Intel Xeon CPU E5-1620 v3 @ 3.50GHz).

For Case B, only the NLBM was used to simulate the bending behaviour of the fabrics, and the element edge size was assigned to be 1 mm to capture small wrinkles. The blank holder was subjected to a clamping force of 1000N, which was applied as a uniform pressure over the surface area. The step time was assigned to be the same as the time duration of the

forming experiment (i.e. 30 s), but mass scaling was applied to accelerate the analysis by effectively increasing the time increment to ~3E-6 s. The total run time for Case B (26 hours) was longer than Case A using the same computer specification. All other model parameters remained the same. For both cases, the kinetic energy calculated from the simulation was <5% of the total strain energy, which indicates that the forming process was successfully modelled as a quasi-static procedure.

4.3.2   Wrinkle evaluation

All forms of macroscale defects, including wrinkling, bridging and fabric folding, exhibit a deviation in the distance measured from the tool surface to the formed fabric part. Therefore, this nodal deviation can be used to locate the position of surface defects and measure the amplitude. As shown in Figure 4.3, the nodal distance d_P measured from Node P on the deformed mesh of the fabric ply to Point P' on the tool surface is:

$$d_P \; = \; \left\| \overrightarrow{PP'} \right\| = \left\| \overrightarrow{OP} - \overrightarrow{OP'} \right\| \tag{4.1}$$

where Point O is the origin of the coordinate system and Node P' on the tool surface is the closest point to Node P on the fabric mesh.
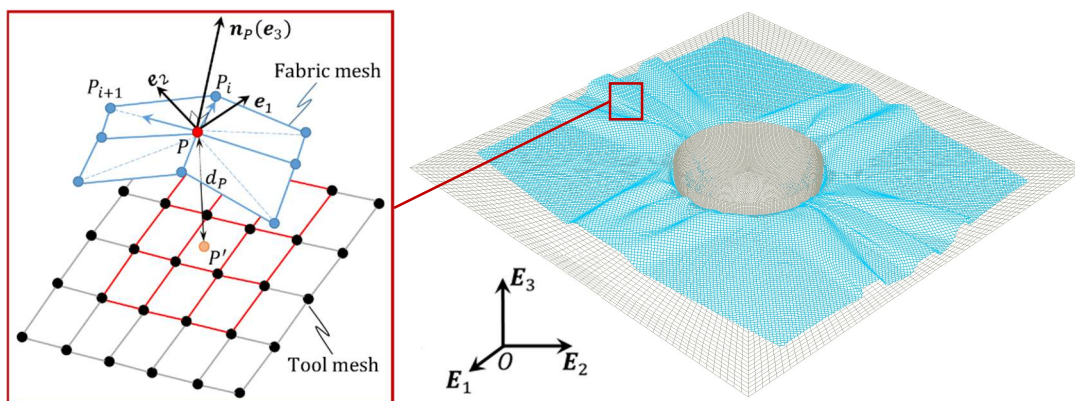
Figure 4.3: Schematic diagram to illustrate how the minimum nodal distance and nodal curvature is calculated between the fabric mesh and tool mesh.

In practice, a local sub-region of the tool mesh was determined to reduce the computation time (region enclosed by red lines in Figure 4.3). Nodes on the tool mesh in the vicinity of Node P were determined using a bounding sphere, using built-in Python functions within Abaqus. The radius of the bounding sphere was adjusted to ensure that the sub-region comprised at least nine elements. The location of P' was subsequently determined by

searching for the closest point on the tool surface to Node P within the sub-region, where Point P' does not necessarily coincide with the nodes on the tool mesh.

As shown in Figure 4.4, out-of-plane defects were detected if the nodal distance d_P exceeded a critical value d_P^{crit}, the distance from the mid-plane of each fabric ply to the tool surface. For example, d_P^{crit} is equal to half of the ply thickness if a single-ply preform is used. Elements on the fabric mesh that contain nodal distances greater than this threshold are considered to exhibit at least one form of out-of-plane defect, i.e. bridging or wrinkling. The surface curvature was subsequently calculated for these elements to isolate fabric wrinkles (Zone A in Figure 4.4) from fabric bridging (i.e. poor conformity, denoted by Zone B in Figure 4.4). Zone C in Figure 4.4 indicates curved regions that correctly match features on the surface of the tool where no defects were detected. The maximum absolute value of the principal curvatures was employed to determine the wrinkle radius:

$$\kappa_P^{\max} = \text{Max}\left(\left|\kappa_{1,P}\right|, \left|\kappa_{2,P}\right|\right) \tag{4.2}$$

where, $\kappa_{1,P}$ and $\kappa_{2,P}$ are the first and second principal curvatures for node P, respectively.
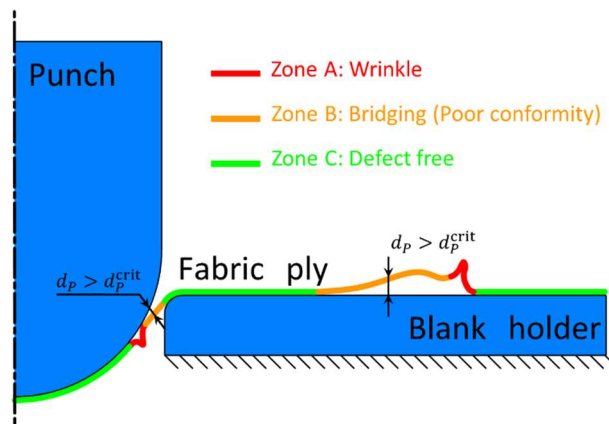
Figure 4.4: Schematic diagram to illustrate how the minimum nodal distance and nodal curvature is calculated between the

Since a smooth surface geometry can be locally approximated using a quadratic polynomial surface, an iterative quadric fitting technique was used to determine the nodal curvatures over the fabric ply [191]. This method has previously been validated [192] for accurately computing curvatures for unstructured meshes with complex geometric features. The procedure was implemented using Abaqus/Python scripting, as described below.

According to the method presented in Ref. [191], the mesh assembled by a series of finite elements can be locally approximated using a quadric polynomial surface at each node of interest. As shown in Figure 4.3, the nodal normal $\boldsymbol{n}_P$ defines a local tangent plane of a quadric surface fitted by the nodes within the neighbourhood of the node P. By assuming that the quadric surface passes through the node P, a quadric polynomial of the following form is employed to perform data fitting

$$z = ax^2 + bxy + cy^2 + dx + ey \tag{4.3}$$

where $(x, y, z)^T$ are the coordinates at the local coordinate system, with the origin at the node P. The nodal curvature at P can be determined according to the following steps:

1. Find elements sharing the node P, and split each quadrilateral element into triangles as shown in Figure 4.3.

2. Estimates the nodal normal at P by taking a weighted average over the normal vectors of triangle facets sharing the node P. The nodal normal, $\boldsymbol{n}_P$ is calculated as follows:

$$\boldsymbol{n}_P = \sum_{i=1}^{N} \frac{\overrightarrow{PP_i} \times \overrightarrow{PP_{i+1}}}{\left\|\overrightarrow{PP_i}\right\|^2 \cdot \left\|\overrightarrow{PP_{i+1}}\right\|^2} \tag{4.4}$$

where N is the number of triangle facets around the node P. P_i and P_{i+1} are nodes of the ith triangle facet arranged in a counter-clockwise order. The plane defined by the normal $\boldsymbol{n}_P$ is therefore the tangent plane of the quadric surface at the node P.

3. A local coordinate system $\{\boldsymbol{e}_1, \boldsymbol{e}_2, \boldsymbol{e}_3\}$ is established on the tangent plane of the node P to perform quadric fitting, where $\boldsymbol{e}_3$ is aligned with the nodal normal $\boldsymbol{n}_P$. The basis vector $\boldsymbol{e}_1$ can be determined by projecting the first basis vector of the global coordinate system $\{\boldsymbol{E}_1, \boldsymbol{E}_2, \boldsymbol{E}_3\}$ onto the tangent plane

$$\boldsymbol{e}_1 = \frac{\boldsymbol{E}_1 - (\boldsymbol{E}_1 \cdot \boldsymbol{e}_3)\boldsymbol{e}_3}{\|\boldsymbol{E}_1 - (\boldsymbol{E}_1 \cdot \boldsymbol{e}_3)\boldsymbol{e}_3\|} \tag{4.5}$$

$\boldsymbol{e}_2$ can be determined by taking the cross product of $\boldsymbol{e}_3$ and $\boldsymbol{e}_1$

$$\boldsymbol{e}_2 = \frac{\boldsymbol{e}_3 \times \boldsymbol{e}_1}{\|\boldsymbol{e}_3 \times \boldsymbol{e}_1\|} \tag{4.6}$$

In practice, if $\boldsymbol{n}_P$ is parallel to $\boldsymbol{E}_1$ then the projection of $\boldsymbol{E}_2$ on the tangent plane can be used to form the local frame.

4. Select the nodes of the elements sharing the node P for quadric fitting, as shown in Figure 4.3. The coordinates of the selected nodes expressed in the global coordinate system need

to be mapped to the local coordinate system. Let X_G be the coordinates of a node expressed in the global coordinate system, then the coordinates of that node in the local coordinate system are expressed as

$$x = R(X_G - X_P)$$
(4.7)

where X_P denotes the coordinates of the node P expressed in the global coordinate system. R is the transformation matrix , which takes the following form

$$R = \begin{bmatrix} e_1 \cdot E_1 & e_1 \cdot E_2 & e_1 \cdot E_3 \\ e_2 \cdot E_1 & e_2 \cdot E_2 & e_2 \cdot E_3 \\ e_3 \cdot E_1 & e_3 \cdot E_2 & e_3 \cdot E_3 \end{bmatrix}$$
(4.8)

5. The coefficients in Eq. (4.3) are obtained by solving the linear least squares fitting problem

$$\begin{bmatrix} x_1^2 & x_1 y_1 & y_1^2 & x_1 & y_1 \\ \vdots & \vdots & \vdots & \vdots & \vdots \\ x_N^2 & x_N y_N & y_N^2 & x_N & y_N \end{bmatrix} \begin{bmatrix} a \\ b \\ c \\ d \\ e \end{bmatrix} = \begin{bmatrix} z_1 \\ \vdots \\ z_N \end{bmatrix}$$
(4.9)

6. Estimate the new nodal normal at P using

$$n_P^{\text{new}} = \frac{[-d, -e, 1]^T}{\sqrt{d^2 + e^2 + 1}}$$
(4.10)

Consequently, the nodal coordinates can be mapped to a new local coordinate system by assigning the normal e_3 in Step 2 to be $R^T n_P^{\text{new}}$. The procedure from Step 2 to Step 6 is repeated until the incremental change in the nodal normal falls below a defined tolerance.

7. Estimate the surface curvatures as follow

$$K_P = \frac{4ac - b^2}{(1 + d^2 + e^2)^2}$$

$$H_P = \frac{a + c + ae^2 + cd^2 - bde}{(1 + d^2 + e^2)^{3/2}}$$
(4.11)

$$\kappa_{1,2} = H_P \pm \sqrt{H_P^2 - K_P}$$

where $K_P = \kappa_1 \kappa_2$, which is the Gauss curvature. $H_P = \frac{1}{2}(\kappa_1 + \kappa_2)$ is the mean curvature at the node P. $\kappa_{1,2}$ is the first and second principal curvatures.

The distance between the fabric and the tool surface, d_P^{crit} was initially used to identify regions containing out-of-plane defects, but local changes in the distribution of κ_P^{max} were used to isolate regions containing out-of-plane wrinkles. Areas of bridging on the hemisphere tool are straight-forward to identify, as they are typically found around the equator of the

dome (see R = 6mm in Table 4.1), but this method becomes more relevant as the complexity of the formed shape increases.

4.4   Wrinkling behaviour prediction and defect isolation

4.4.1   Woven fabric

Simulation results for the woven fabric are compared against the experimental data in Figure 4.5 for a range of scenarios using the laminated shell element model for forming Case A. An output from the membrane element model is also included for comparison, which overlooks the influence of fabric bending.

The wrinkle pattern for the experimental specimen in Figure 4.5(a) is broadly symmetric about the x and y axes, since the shear behaviour of this woven fabric is symmetrical in the positive and negative shear directions. Wrinkles lie along the diagonal directions of the ply where the fabric undergoes large shear deformation (see the magnified view of the sheared fabric yarns in Figure 4.5(a)). There are no apparent wrinkles in the dome area where the fabric contacts the hemispherical punch. The wrinkle amplitude presented in Figure 4.5(b) was simulated using the membrane element model. Due to the lack of constraint from the blank holder (i.e. 7mm gap), each membrane element was unable to carry the bending load. Consequently, elements distorted locally until reaching a balanced status, leading to irregular wrinkle patterns in the fabric ply. Previous forming simulation studies have indicated that areas of high in-plane shear correlate well to areas of wrinkling [30, 64-66, 72]. However in the current study, the membrane element approach is unable to deliver a stable analysis for the fabric forming process because the blank is not suitably constrained between the blank holders, causing unrealistic out-of-plane deformation. The bending behaviour therefore seems to dominate the wrinkling behaviour.

Figure 4.5(c) shows the simulated results for the laminated shell element approach using the NLBM. One primary wrinkle is predicted in each quadrant, which is in good agreement with the experimental scan data. Figure 4.5(d) to Figure 4.5(f) show the predicted wrinkle patterns using the laminated shell element approach with a linear bending model (LBM), assuming a range of constant bending rigidities taken from the experimental data in Table 3.2, i.e. $B_{\text{init}}^{\text{wov}}$, $B_{41.5°}^{\text{wov}}$ and $B_{\text{inf}}^{\text{wov}}$. Generally, the number of predicted wrinkles decreases as the bending stiffness increases. Whilst the experimental stiffness values are easier to measure and the

LBM is simpler to implement, none of these simulations produce realistic wrinkle patterns compared to the experimental data.

Figure 4.5: Experimental wrinkle amplitude for the bi-axial woven fabric from forming Case A, measured by SWLS. Corresponding simulated wrinkle amplitudes using (b) membrane elements without bending stiffness, (c) non-linear bending model (NLBM), (d) linear bending model (LBM) using B_{init}, (e) LBM using the bending stiffness derived a constant angular deflection of 41.5° and (f) LBM using the asymptote stiffness value B_{inf}.

To provide further clarity, the cross-sectional shapes of the simulated wrinkles from Sections A-A' and B-B' (see Figure 4.5(a)) have been compared against the experimental data in Figure 4.6. For Section A-A' (see Figure 4.6(a)) both the LBM and NLBM are in reasonable agreement with the experimental curve. The RMSE for the LBM using the $B_{41.5°}^{\text{wov}}$ bending stiffness value is 8.3 %, compared with 6.4% for the NLBM. For Section B-B' (see Figure 4.6 (b)), additional wrinkles are predicted by the LBM ($B_{41.5°}^{\text{wov}}$) compared to the experimental data, since the bending stiffness is assumed to be constant. The curve (LBM $B_{41.5°}^{\text{wov}}$) represents the solution if the bending stiffness is determined using the standard cantilever test. In comparison, the wrinkle amplitude predicted by the NLBM is consistent with the experimental curve, with a RMSE of 1.1%. This demonstrates the importance of incorporating the non-linear bending response of the fabric into the forming simulation for this lightweight woven material, which generally exhibits a low bending stiffness.
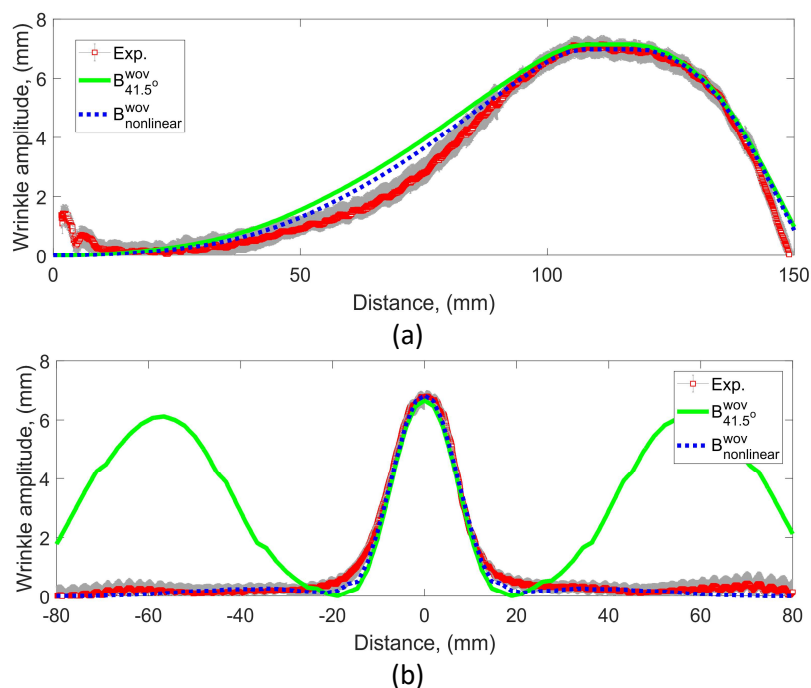
Figure 4.6: Wrinkle amplitudes for the woven material from forming Case A, predicted by the laminated shell element approach, using both linear and non-linear bending models along (a) path A-A' and (b) path B-B' (See Figure 4.5 for path definitions). Experimental data included for comparison.

The root mean square of the bending moments along the warp and weft yarns, M_f^{RMS}, is plotted in Figure 4.7(a), with the maximum value found in areas where the fabric ply passes through the edge of the hole of the blank holder. In Figure 4.7 (b), the probability of M_f^{RMS} shows that the bending moment obtained using the LBM is much higher than that predicted

by the NLBM. This indicates that the linear model, which is dependent on the constant stiffness value derived by the standard cantilever test, is likely to overestimate the internal bending moment of the fabric.
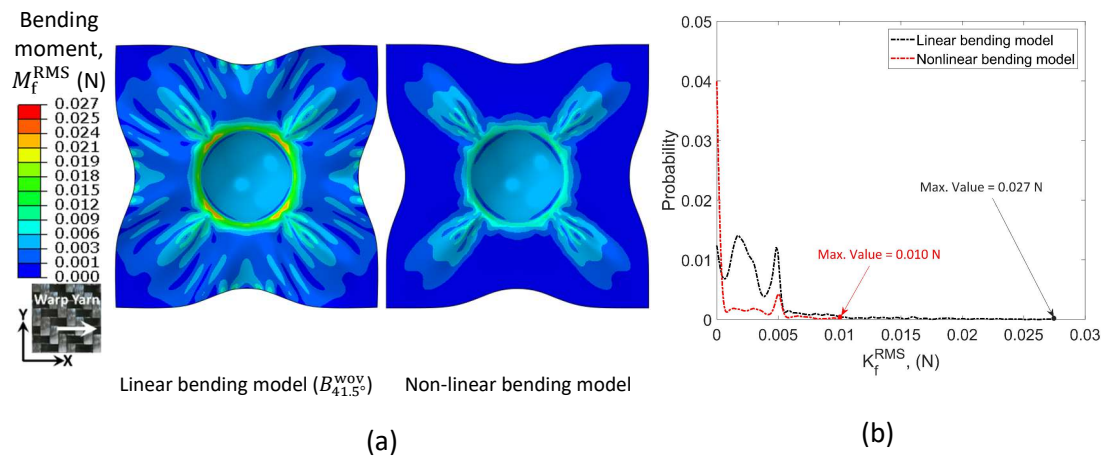
Figure 4.7: (a) The root mean square of the bending moments along the fibre directions, M_f^{RMS} and (b) the corresponding probability density function for the woven fabric from Case A, predicted by the linear and non-linear bending models.

4.4.2   Non-crimp fabric

Simulation results for the NCF are compared against experimental data in Figure 4.8. Results from the membrane element approach are not presented here because similar irregular wrinkle patterns in the fabric ply were observed as for the woven material above, therefore only results from the laminate shell approach have been included. The same material models (LBM and NLBM) have been considered as for the woven material, to investigate the suitability of the LBM for higher bending stiffness materials.

Three primary wrinkles can be observed in both the positive and negative sheared areas of the NCF ply from the experimental data in Figure 4.8(a). The negative shear induced wrinkles (top and bottom of the hemisphere in the y-direction) are wider and longer than wrinkles resulting from the positive shear region (left and right of the hemisphere in the x-direction), which indicates the influence of the asymmetric shear resistance on the wrinkling behaviour.

The wrinkling pattern predicted by the NLBM (see Figure 4.8(b)) agrees well with the experimental data, indicating the suitability of the NLBM for simulating the wrinkling behaviour of the NCF. Figure 4.8(c) to Figure 4.8(e) present the wrinkle patterns predicted using constant bending stiffnesses in the LBM, i.e. B_{init}^{NCF}, $B_{41.5°}^{NCF}$ and B_{inf}^{NC} respectively. As

the bending stiffness input parameter increases, the number of individual wrinkles decreases and the general size of each wrinkle increases, as previously observed for the woven material.
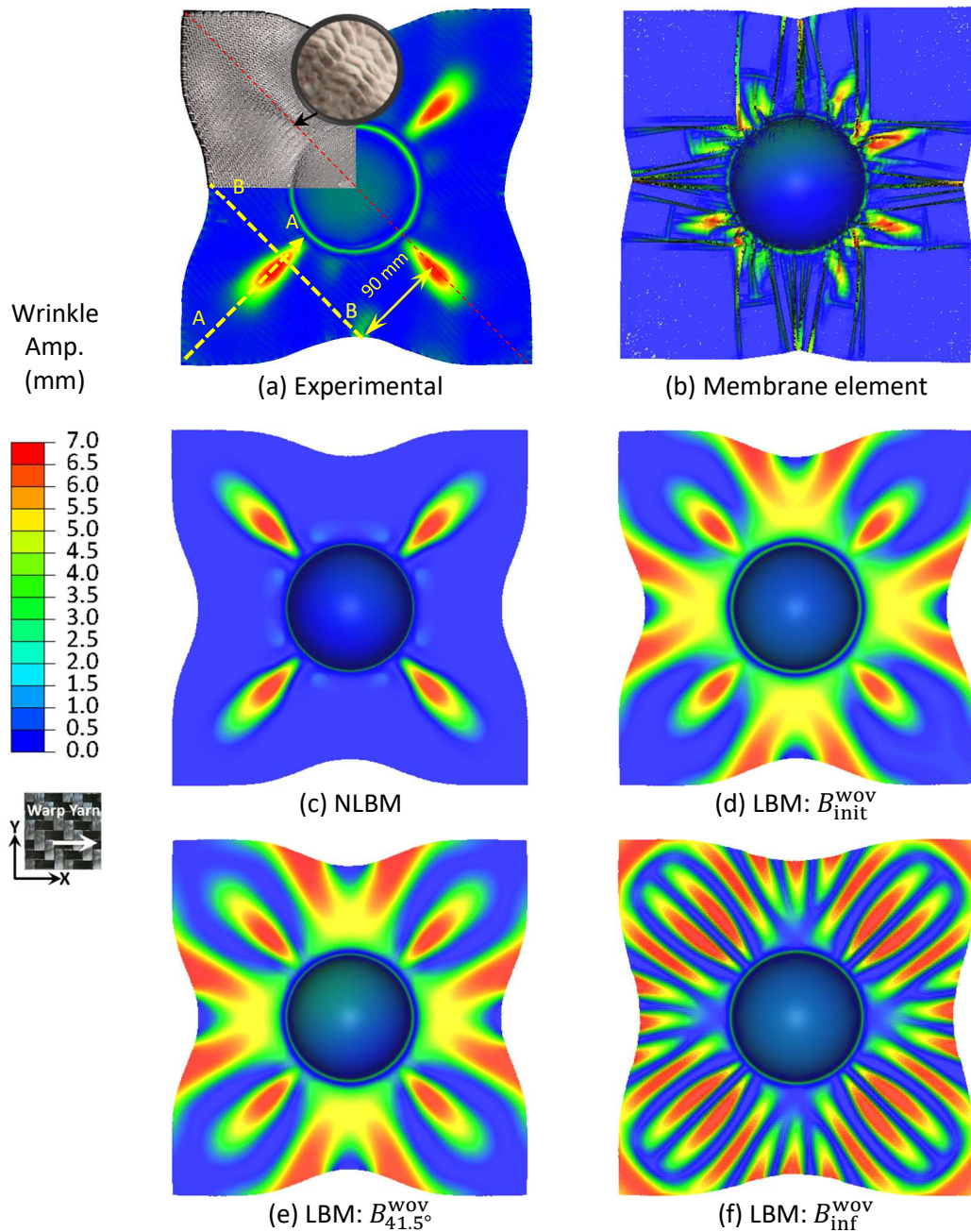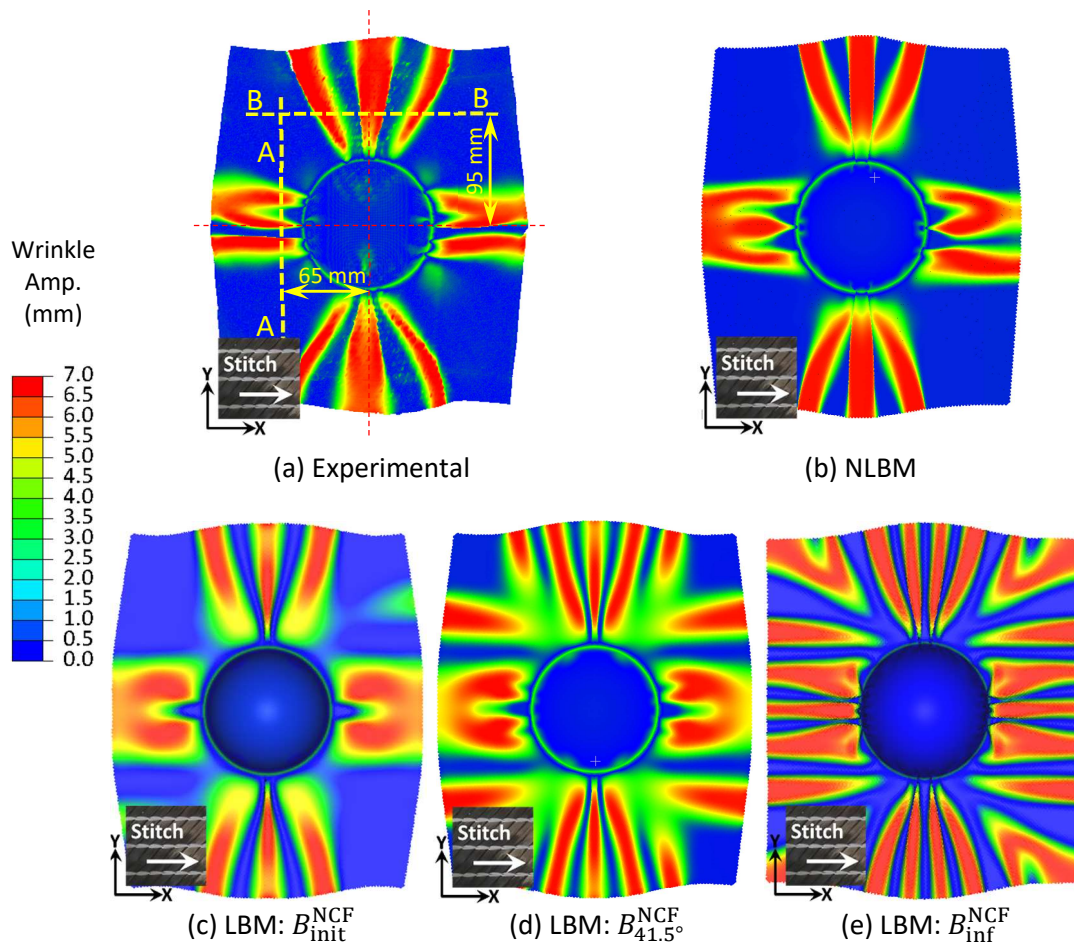

Figure 4.8: (a) Experimental wrinkle amplitude for the NCF from Case A measured by SWLS. Corresponding simulated wrinkle amplitudes using (b) Non-linear bending model (NLBM), (c) linear bending model (LBM) using B_{init}, (d) LBM using the bending stiffness derived from a constant angular deflection of 41.5° according to BS EN ISO 9073-7 [123] and (e) LBM using the asymptote stiffness value B_{inf}.

The predicted formed shape using the initial bending stiffness $B_{\text{init}}^{\text{NCF}}$ with the LBM exhibits a similar wrinkle pattern to the NLBM prediction, but this model is unable to capture some of the features along the wrinkle edges where significant fabric bending occurs. This is because these regions experience higher levels of curvature and therefore tow buckling is likely to occur, which is not captured by the LBM. However, the NLBM requires more computational effort compared to the LBM (16 hours compared to 12 hours), so further refinement of the LBM may be worthwhile for approximating the wrinkle pattern for fabrics with high initial bending stiffness. According to a previous study [188], B_{init} can be approximated successfully using the standard cantilever test [123] using a low angular deflection.

Wrinkle amplitudes taken through Sections A-A' and B-B' (see Figure 4.8(a) for positions) were compared against experimental data from 3 repeat hemispheres, as shown in Figure 4.9. The grey areas correspond to the range of wrinkle amplitudes determined from the three experimental repeats. In the positive shear region (Section A-A'), the wrinkle amplitude predicted by the NLBM captures the shape of the experimental measurements, but the wrinkle area is narrower than the experimental data. The wrinkle amplitude predicted by the NLBM is generally within the error band of the experimental data in the negative shear region (Section B-B'). These sectioned views demonstrate that the NLBM is more reliable for predicting the wrinkle patterns than either of the two LBMs shown ($B_{41.5°}^{\mathrm{NCF}}$ or $B_{\mathrm{inf}}^{\mathrm{NCF}}$).
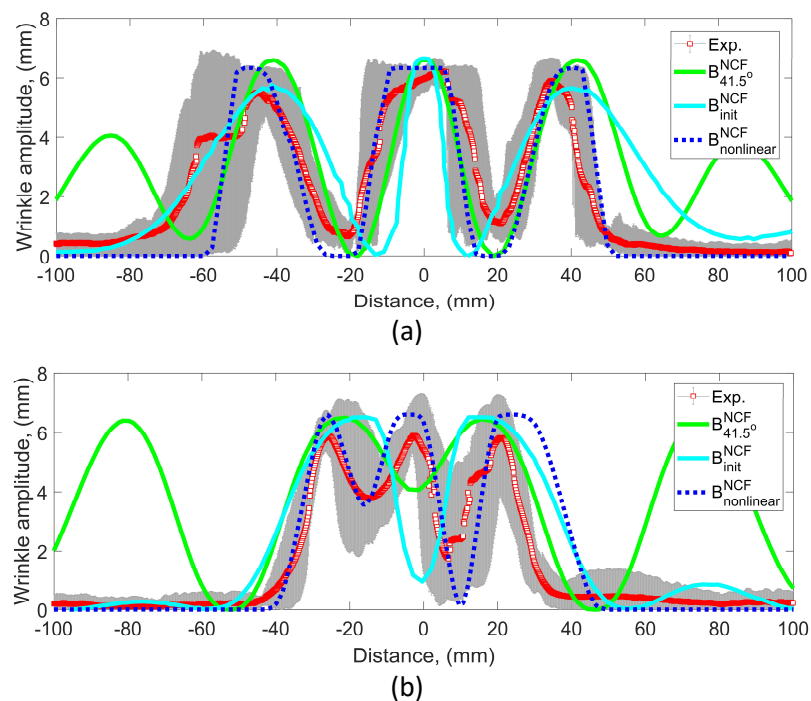
Figure 4.9: Wrinkle amplitudes for the NCF along paths (a) A-A' and (b) B-B' (see Figure 4.8(a) for path definitions) from Case A. Experimental data measured by SWLS, predictions produced by the linear (LBM) and non-linear bending models (NLBM).

Figure 4.10 shows how the simulated wrinkle patterns develop as the punch displacement increases from 30 mm to 50 mm, according to the shear angle θ_{shr} and the nodal distance d_P . At a punch displacement of 30 mm, areas of the fabric experiencing high in-plane shear (both positive and negative) undergo out-of-plane deformation (see Figure 4.10(a)). This indicates a positive correlation between areas of high in-plane shear and out-of-plane deformation for the NCF, potentially leading to out-of-plane wrinkles. The wrinkled fabrics in areas of positive shear undergo further buckling at a punch displacement of 40 mm, since

the bending stiffness decreases with increasing curvature, resulting in more wrinkles to accommodate the material draw-in (see Figure 4.10(b)). Results at different displacements therefore indicate that wrinkle initiation is caused by excessive shear deformation, but wrinkle propagation is dominated by the fabric bending stiffness as it changes with increasing curvature and in-plane shear.

(a) Shear angle, θ_{shr}

(b) Wrinkle amplitude, d_p
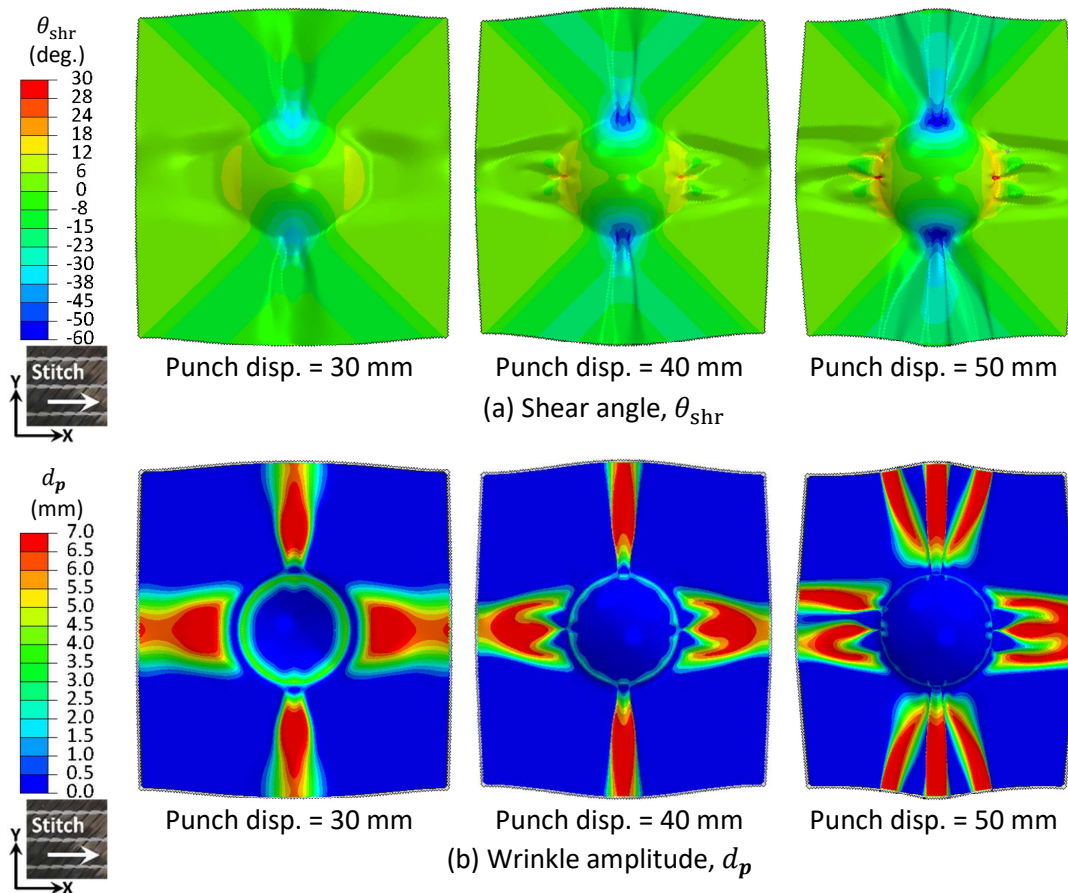
Figure 4.10: (a) Shear angle θ_{shr} and (b) wrinkle patterns according to the nodal deviation d_p at different punch displacements for the NCF material from Case A.

Figure 4.11(a) shows the distribution of the bending moment M_f^{RMS} for both the linear and non-linear bending models (where $B_{41.5°}^{NCF}$ is used as the input for the LBM, since it is the commonly derived bending stiffness from the standard cantilevered bending test). The NLBM predicts significantly lower levels of bending moment for the NCF material compared to the LBM, as previously observed for the woven fabric. A summary of the bending moment is presented in Figure 4.11(b), which shows that the probability of M_f^{RMS} (i.e. the root mean square of moments along two primary fibre directions) predicted by the NLBM is lower than the curve for the LBM. Using a constant bending stiffness for the LBM produced higher

bending moments, since the bending stiffness does not vary with the bending deformation to account for fibre buckling, leading to large unrealistic areas of wrinkling over the ply surface.

Linear bending model
$(B_{41.5°}^{NCF})$

Non-linear bending model

(a)

(b)
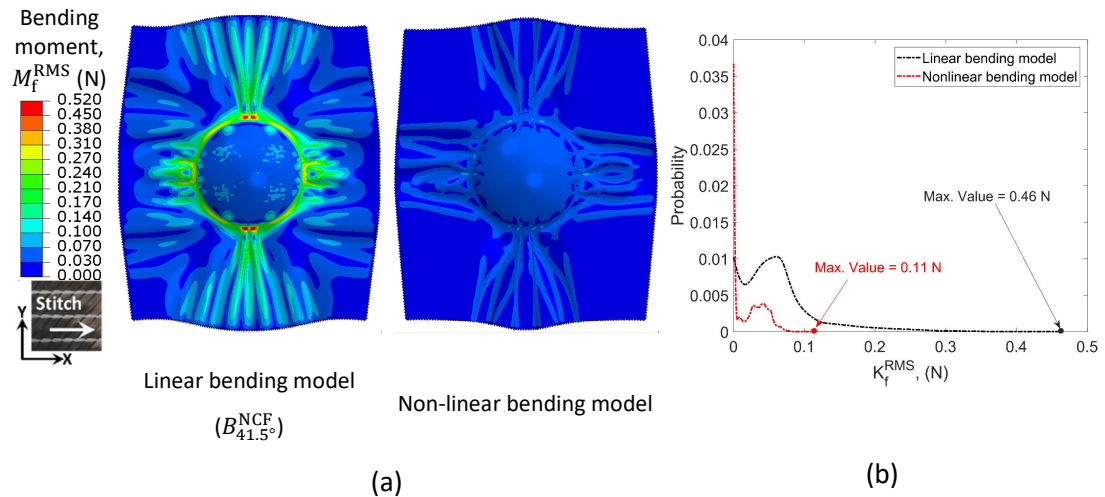
Figure 4.11: Bending moment along the warp yarn of the NCF from Case A, predicted by the linear and non-linear bending models.

4.4.3   Isolation of defect type

The wrinkle evaluation method presented in Section 4.3.2 was used to identify forming induced defects for the forming Case B in Table 4.1, using only simulation results produced by the NLBM.

The distribution of defects according to the nodal deviation d_P and curvature κ_P^{max} for the woven fabric are plotted in Figure 4.12, using the nodal coordinates from the deformed fabric mesh. Only the curved region of the hemisphere preform is of interest for this study, since the blank holder prevents any out-of-plane defects in the flat region. There is clearance between the punch and the hole in the blank holder, since the hemisphere rig uses a punch and die arrangement, rather than matched male and female tools. The deformed fabric mesh therefore correctly exhibits a distance deviation from the tool surface of approximately 1mm around the equator of the hemisphere as expected (see Figure 4.12(a)). However, there is no apparent change in the distribution of surface curvature κ_P^{max} in this region (see Figure 4.12(b)), indicating that no wrinkles are present. This agrees with the SWLS images of the formed samples presented in Figure 4.12(c).
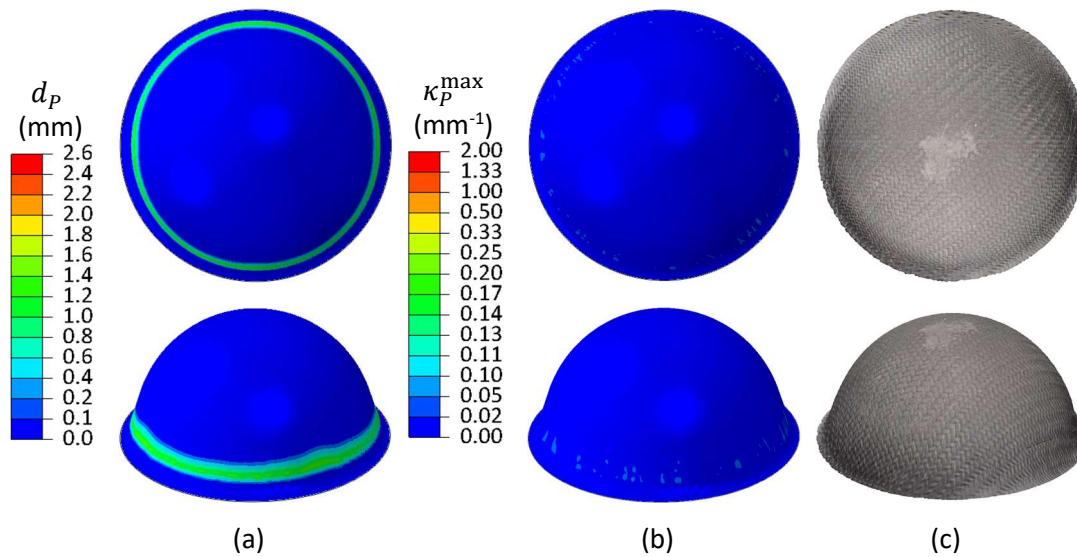
Figure 4.12: (a) predicted nodal deviation d_p and (b) surface curvature κ_p^{max} for the woven fabric for forming Case B. (c) shows 3D scanned images from the SWLS.

Figure 4.13(a) presents the deformed shape of the experimental NCF specimen scanned from both the concave and convex sides, since only one fibre orientation is visible from each side. Numerous wrinkles are observed in the positive shear regions highlighted in red in Figure 4.13(a), which correlate well with the simulated wrinkle pattern in Figure 4.13(b). The longitudinal orientation of the wrinkles in the scanned images follow the same direction as the stitches on the hemisphere. The stitches in these regions are subjected to tensile strain, influencing the out-of-plane wrinkle pattern.

Figure 4.13(c) shows plots of the nodal deviation d_P for the mid-plane of the topmost ply on the convex side to the forming tool reference surface. Similar to the prediction for the woven fabric, an area of bridging is found around the base of the hemisphere. The predicted maximum amplitude is 2.6 mm in this region, but the average amplitude is similar to the woven material case at approximately 1.0 mm. By plotting the surface curvature, κ_P^{max} in Figure 4.13(d), wrinkling defects are isolated from the regions of fabric bridging. The distribution of κ_P^{max} also generally follows the longitudinal direction of the macroscale wrinkles, with the critical areas highlighted in red (0.5 mm^{-1} < κ_P^{max} < 1.5 mm^{-1}) found in the positive shear region. These correspond to a wrinkle radius of 0.7 – 2.0 mm.
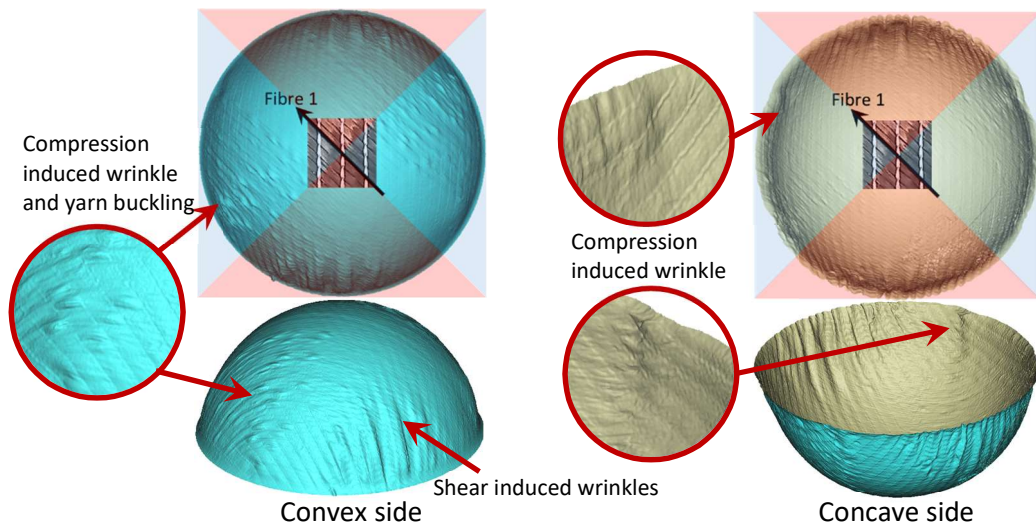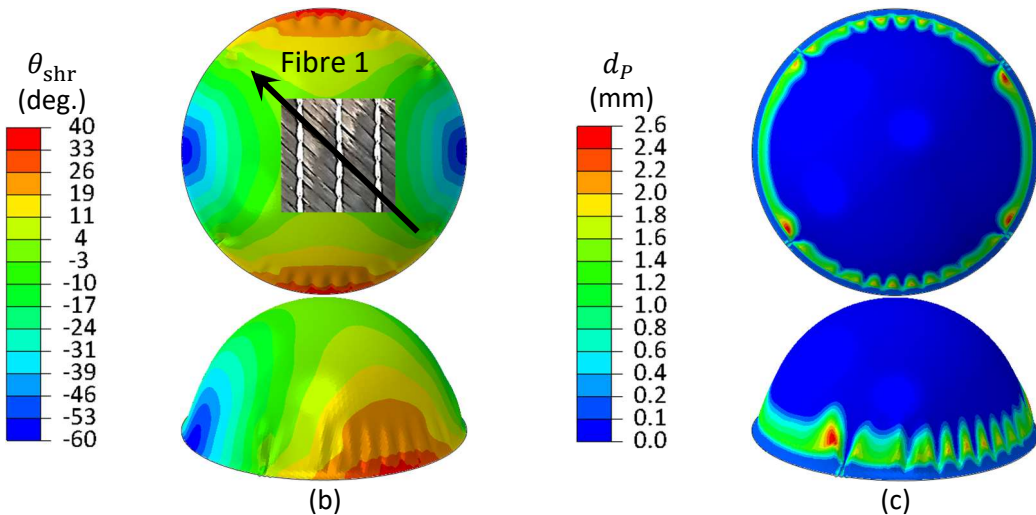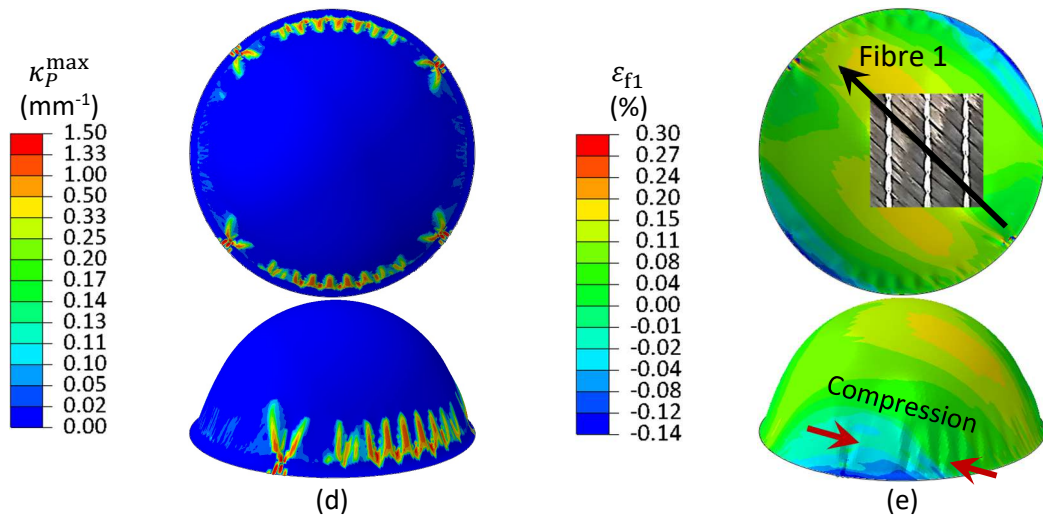
Figure 4.13: (a) Wrinkle shape captured by SWLS for both the concave and convex surfaces of the hemisphere. (b) Shear angle θ_{shr}, (c) predicted nodal deviation d_p , (d) surface curvature κ_p^{max} and (e) fibre strain along one fibre direction ε_{f1} for the NCF forming case B.

Figure 4.13(e) presents the axial fibre strain, ε_{f1}, along one of the primary yarn directions. Wrinkles observed along the boundary of the positive and negative shear regions are induced by compressive strains along the primary yarns, as indicated by the negative values for ε_{f1}. These compression induced wrinkles are also observed in the same locations in the experimental scan data (Figure 4.13(a)), with yarn buckling typically observed on each side of the NCF ply. The macroscale FE simulation captures the main wrinkling characteristics, but it cannot precisely replicate detailed features that occur due to the mesoscale architecture, such as the influence of the stitch direction and the discrete yarn orientations on each side of the NCF ply.

4.5   Chapter summary

Experiments and numerical simulations were performed to investigate the forming induced wrinkling behaviour for two bi-axial fabrics, a balanced twill weave and a pillar-stitched NCF. Controlled wrinkle patterns were generated by introducing a gap between the blank holder and the die during experimental hemisphere forming tests. Symmetrical wrinkle patterns were observed when forming the balanced woven fabric, whereas wrinkles exhibited different shapes in regions of positive and negative shear for the NCF, due to the asymmetric shear resistance caused by the through-thickness pillar stitching. This indicates the dependency of the wrinkling behaviour on the mesoscale architecture of the fabric.

Due to the absence of bending resistance, simulations using membrane elements were unable to produce realistic deformed shapes when the fabric ply was poorly constrained out of plane with the open blank holder. This indicates the importance of accounting for the fabric bending stiffness when explicitly modelling the wrinkling behaviour of fabrics during complex forming scenarios.

A linear bending model (LBM) was employed for fabric forming simulations using a laminate shell element approach, with results indicating that a constant bending stiffness measured from the standard cantilever test may overestimate the internal bending moment along the fibre directions, leading to large unrealistic areas of wrinkling over the ply surface. In contrast, employing a non-linear bending model (NLBM) with a locally variable bending stiffness produced more realistic predictions for the formed shape containing large macroscale wrinkles, regardless of the fabric stiffness or mesoscale fibre architecture. Analyses on the local surface deviation and the internal bending moment indicate that the evolution of fabric bending with increasing punch displacement dominates the propagation of wrinkles during

the forming simulation, with areas subjected to high in-plane shear more likely to experience out-of-plane wrinkles.

A strategy was developed to quantitatively visualise the severity of macroscale defects by post-processing the simulation results. The nodal distance between the fabric and tool was shown to be a logical way to locate surface defects. The maximum principal curvature was identified as a suitable measure to determine the radius of preform wrinkles enabling them to be isolated from areas of fabric bridging. Results show that the distribution of the maximum value of the principal curvatures coincides with the longitudinal direction of wrinkles.

Chapter 5   Multi-resolution forming simulation

5.1   Introduction

A high resolution finite element mesh (relative to the wrinkle amplitude) is generally required to ensure forming defects can be predicted accurately, but it is typically impractical to use high-fidelity simulations for industrial-scale applications (e.g. >10 m), particularly for laminate designs containing a considerable number of plies. Therefore, a multi-resolution simulation strategy is required to reduce run time without comprising accuracy.

In this chapter, a two-stage global-to-local modelling strategy is presented in Section 5.2, based on a sub-modelling approach to predict the formation of macroscale defects in bi-axial non-crimp fabric (NCF) preforms, produced by double diaphragm forming (DDF). A tool with local features of double curvature is introduced in Section 5.3 to conduct forming experiments to validate the proposed modelling strategy. A full-scale global simulation is initially performed using a coarse membrane element mesh to locate areas containing potential defects, using the methodology established in Section 5.4. The results from the global simulation are presented in Section 5.5.1, highlighting areas requiring refinement based on the established defect criteria. In Section 5.5.2, local simulations are subsequently performed using a high fidelity shell-element mesh to predict the shape of forming induced defects explicitly in these areas, using boundary conditions derived from the global simulation. The methodology is evaluated by comparing the simulation results against experimental data in Section 5.5.3, with the run time saving presented for this two-stage approach.

5.2   Global-to-local sub-modelling approach

5.2.1   General strategy

A global-to-local sub-modelling strategy has been developed to enable small-scale defects (<10 mm) to be rapidly identified for large components containing local defect-sensitive features (e.g. doubly-curved joggles). In Step I, a DDF simulation is performed for the full-scale geometry using a membrane element model (MEM) to determine the location of defects using the proposed defect criteria in Section 5.2.2. In Step II, problem areas are simulated using high-fidelity local shell element models (SEMs) to identify critical defects (wrinkle amplitude of ~1mm), by extracting the boundary conditions from the global model in Step I. Displacements from the global MEM were directly interpolated to determine the

boundaries of the local sub-models. The consistency in energy dissipation between the local models and the corresponding regions in the global model was not considered.

In this work, simulations have been performed on a demonstrator component with local areas of double curvature to validate the proposed approach, using the surface curvature to distinguish between two types of surface defects, i.e. wrinkling and bridging. The dimensions of the tool are shown in Section 5.3 and the details of the FE model for DDF simulations are presented in Section 5.4.

5.2.2   Defect criteria

Whilst the deformation of biaxial fabrics during forming is relatively well understood [54, 57, 136], the severity of defects in preforms formed by DDF can be different to those from matched tool forming. Fabric plies are constrained less during DDF due to the lack of a rigid blank holder. The vacuum-based clamping force applied to the thin polyamide-based diaphragms (typically < 100 µm thick) is unable to prevent fabric buckling and material thickening as the plies shear, which can lead to severe out-of-plane fibre wrinkling [21]. The effect of inter-ply friction is also more significant for DDF, having a greater influence over the quality of the formed component [47]. For some concave geometries, the vacuum-only forming pressure is unable to overcome the frictional forces between diaphragm-ply or ply-ply interfaces over large planar regions. This limits the shear strain in each ply, preventing material draw-in into concave regions, which is commonly referred to as fabric bridging [101].

Although empirical decisions can be made to determine suitable regions of interest to apply sub-modelling, there is a need for robust criteria to enable designers to intelligently determine where critical manufacturing defects may occur. Previous forming simulation work has provided a foundation for establishing these defect criteria [21, 30, 159, 166]. Shear-induced wrinkling has typically been observed in regions of double curvature where yarns have become compacted and the ply thickness locally increased [21, 44, 100]. FE simulations considering only in-plane fabric behaviour (i.e. tensile and shear) have successfully been used to predict the occurrence of these wrinkles, but the predicted shapes have been unrealistic [159, 166].

It is assumed that the thin diaphragm material (80 µm) provides little out-of-plane constraint to the fabric, therefore the wrinkling angle observed during bias extension tests (i.e. 8° in the positive shear direction determined in Chapter 3) has been adopted as the critical value for the onset of shear-induced wrinkling. A value of 50° has been used to identify the onset of wrinkling under negative shear, according to the work of Chen et al [101].

Fabric over-shear is not the only cause of defects during DDF, therefore a second criteria is required to identify regions of poor fabric-tool conformity. Since the formation of bridging in DDF is largely dependent on the in-plane tensile force and tool/diaphragm friction [21], simulations using the MEM can be used to approximate the location of fabric bridging. These defects can be identified if the nodal distance between the deformed fabric mesh and the tool mesh exceeds the distance between the mid-plane of each fabric ply to the tool surface. Consequently, both shear angle and nodal distance are employed concurrently in the current work to locate forming related defects, based on the results from the global MEM. The total area with potential macroscale defects is determined by superimposing areas corresponding to fabric over shear and poor fabric-tool conformity.

Diaphragm pinching can be caused by anticlastic bending, which is a result of the contraction of the diaphragm material in the transverse direction due to the Poisson's ratio. This can lead to a compressive force in the diaphragms along the pinching direction, especially for thick diaphragms [21]. A diaphragm thickness of just 80 μm was used in the current work, therefore the bending stiffness of the diaphragm film was much lower than that of the fabric. Whilst a small number of wrinkles in the diaphragm were observed due to this pinching effect, they had negligible effect on the underlying NCF and were not the cause of wrinkles in the fabric plies.

5.2.3   Step I: Global modelling

Since the thickness of the diaphragm (80 μm) is much lower than the thickness of the NCF ply (0.4 mm), the representative bending resistance of the diaphragm is orders of magnitude lower than that of the fabric. Therefore, both the fabric and diaphragm were modelled using membrane elements in the global simulation to provide boundary conditions for the local models, extracted in Step II.

Based on the defect criteria presented in Section 5.2.2, the area with potential defects is determined by superimposing the region of fabric over-shear and the region of poor conformity, as denoted by the yellow and green shaded areas in Figure 5.1(a) respectively. The boundary lines of the corresponding sub model were chosen to enclose the defective area and to be parallel to the axes of the global coordinate system, as denoted by the red dashed lines in Figure 5.1(a).
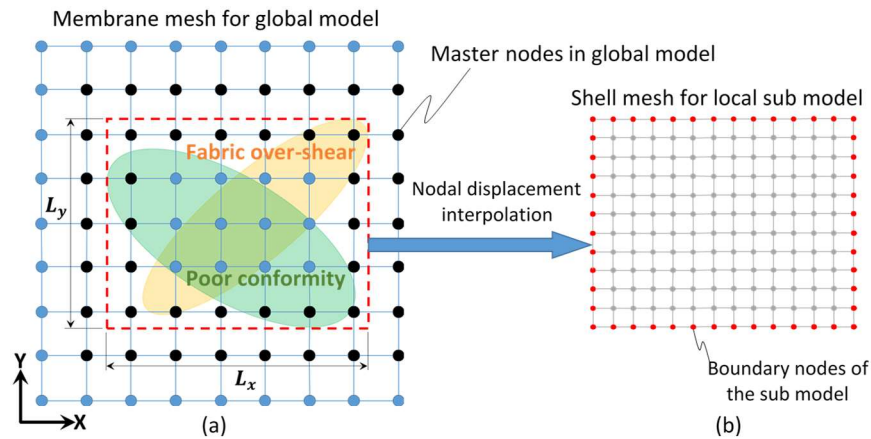
Figure 5.1: Schematic of the general strategy for Global-to-local sub modelling. (a) Global membrane mesh (b) Local shell mesh. (Local simulations for critical areas were performed for the entire forming history, i.e. from 2D flat fabric to 3D shape.)

The black dots in Figure 5.1(a) denote the master nodes in the global model which are used to derive the displacement boundary conditions for the corresponding local sub model (see Figure 5.1(b)). These master nodes are determined by searching for elements in the global model that encompass the boundary of the corresponding sub model (i.e. nodes adjacent to the red dashed lines in Figure 5.1(a)). The displacements of the master nodes in the global model are then interpolated to provide the displacement boundary conditions for the nodes of the sub-model (i.e. red dots in Figure 5.1(b)).

5.2.4   Step II: Local modelling

The areas containing potential defects, as determined in Step I, were manually extracted from the global model in the current work and re-discretised using finer shell elements to build local models. It is possible to automate the process for defining these areas of interest by implementing the proposed selection criteria in Section 5.2.3 via Abaqus/Python scripting. The displacement boundary conditions from the global simulation in Step I were mapped onto the corresponding nodes around the boundary of each local model for the fabric plies and the diaphragms, using the in-built nodal interpolation algorithm in Abaqus v2018. The pressure-time history in the local simulation was identical to the global simulation. The fabric plies were modelled using the SEM approach to account for the non-linear bending behaviour of the NCF. The local modelling was performed after the global modelling in Step I. The element edge length for the sub-models was assigned to be 1.0 mm, to ensure wrinkles with an amplitude ∼ 1 mm were captured.

The deformed mesh from the sub-model was used to calculate the distance between the fabric and the tool surface to identify regions containing out-of-plane defects. Local changes in the distribution of surface curvature were subsequently calculated to separate regions containing out-of-plane wrinkles and bridging, as discussed previously in Section 4.3.2.

5.3   Forming experiments and diaphragm characterisation

5.3.1   Double diaphragm forming

A double diaphragm forming (DDF) machine developed at the University of Nottingham was used for experimental forming trials [21]. A tool with varying cross-section was used to demonstrate the capability of the global-to-local modelling approach. As shown in Figure 5.2, the total tool length was 620 mm to produce a U-shaped preform of length 480 mm. Two 10 mm ramps (height change in the Z-direction) were introduced along the longitudinal direction of the tool, both asymmetrical about the width, creating local regions of double curvature (joggles) on the preformed shape.
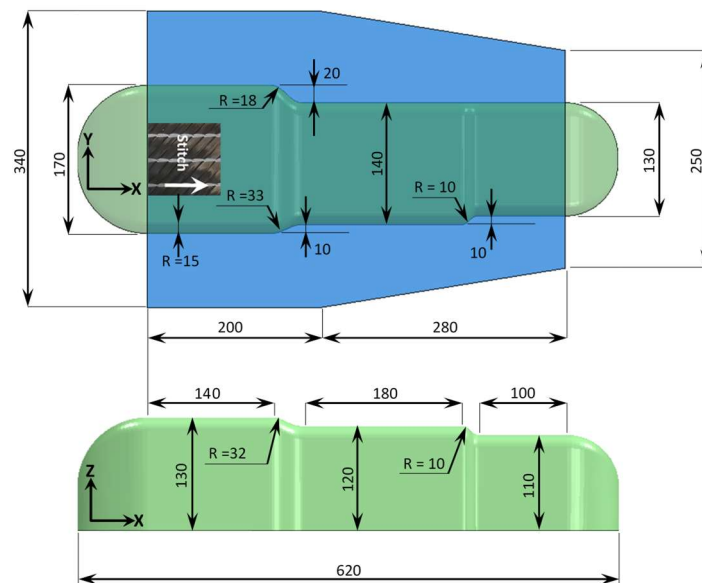
Figure 5.2: Geometry used for DDF simulations. Blue area indicates starting shape and position of fabric blank (All dimensions in mm).

The preform consisted of two ±45° NCF plies, i.e. $(\pm45)_2$, with the stitch direction aligned along the longitudinal direction of the tool (X direction). The size of the fabric blank was selected so that the overall depth of the preform was less than the depth of the tool (z-direction), preventing fabric bridging around the base of the tool where it meets the bed of the DDF machine. The effective area of the diaphragms was 1.8 m × 1.5 m.

5.3.2   Measurement

The SWLS was used to capture the final formed shape of the preforms. The preforms were scanned in-situ on the DDF machine whilst maintaining the vacuum. Ambersil Flaw Detector was uniformly sprayed onto the outer diaphragm to avoid excessive reflection during scanning. Reference points were marked onto the diaphragm using a red marker pen before scanning to assist with the alignment and stitching of individual scans taken at different angles, in order to create a full 3D representation of the preform. Due to the applied in-bag vacuum, it was assumed that there was no clearance between the diaphragms and the fabric plies. Open-source software, CloudCompare [190], was used to visualise the distribution of defects by performing post-scan measurements on the point cloud.

5.3.3   Diaphragm characterisation

A high elongation vacuum bag film, StretchLon HT-350 (supplied by Tygavac Ltd UK), was selected for the diaphragm material. The thickness of each diaphragm layer was measured to be 0.08 mm. A series of mechanical tests (i.e. uniaxial tensile, equibiaxial tensile and planar shear tests) were performed on a universal testing machine at a strain rate of $0.03s^{-1}$ to characterise the in-plane behaviour of the diaphragm material, following the methodology presented by Chen et al. [21]. All tests were carried out at ambient temperature. The dimensions of the uniaxial tensile specimens were 250 mm × 5 mm × 0.08 mm. The dimensions of specimens for equibiaxial tensile and planar shear tests were 75 mm × 75 mm × 0.08 mm. Three specimen repeats were tested for each deformation mode to produce a mean stress-strain curve, as shown in Figure 5.3. The mean experimental data were fitted using exponential functions, as listed in Table 5.1.

In DDF simulations, the mechanical behaviour of the diaphragm material was modelled by Marlow model [193] for hyperelastic materials, in which the experimental uniaxial tensile data (see Figure 5.3(a)) was used to derive the stress-strain curves for the other two deformation modes (i.e. equibiaxial tension and planar shear) of the hyperelastic diaphragm. There is a good agreement between the experimental data and the derived curves for each deformation mode, as shown in Figure 5.3(b) and (c), with Root Mean Square Error values of 7.5%, 4.1% calculated for the equibiaxial tension and planar shear curves respectively over the strain ranges presented. This validates the use of the Marlow model [193] for describing the deformation behaviour of the diaphragm material.
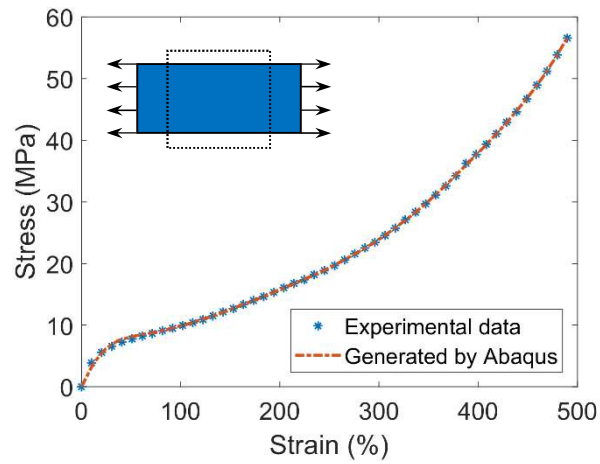
(a) Uniaxial tension
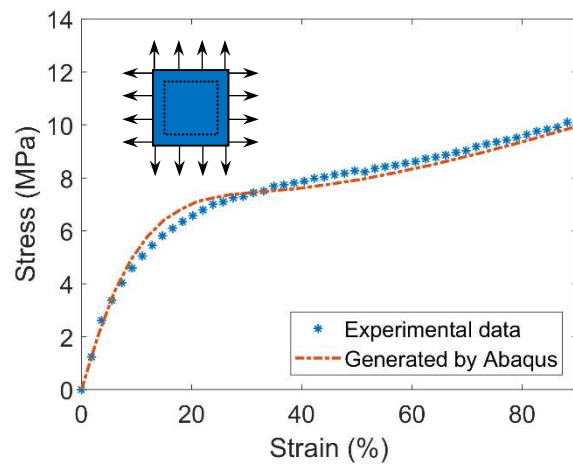
(b) Equibiaxial tension
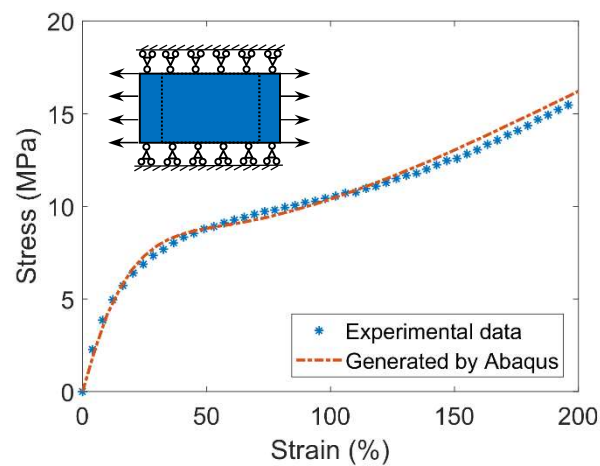
(c) Planar shear

Figure 5.3: Characterisation of the diaphragm material using Marlow's hyperelastic model. (a) The experimental uniaxial tensile data in Table 5.1 was used as the input for the Abaqus in-built Marlow model to generate the curves for (b) biaxial tension and (c) planar shear.

Table 5.1: Analytical expressions derived from the in-plane experimental data (see Figure 5.3) for the diaphragm material. σ and ε denote nominal stress and nominal strain respectively.

Deformation mode	Expression
Uniaxial tension	$\sigma = 6.364 \times (e^{0.004451\varepsilon} - e^{-0.07545\varepsilon})$MPa, $0 \leq \varepsilon \leq 500\%$
Equibiaxial tension	$\sigma = 6.482 \times (e^{0.004871\varepsilon} - e^{-0.12040\varepsilon})$MPa, $0 \leq \varepsilon \leq 100\%$
Planar shear	$\sigma = 7.238 \times (e^{0.003774\varepsilon} - e^{-0.08312\varepsilon})$MPa, $0 \leq \varepsilon \leq 200\%$

5.4   DDF simulation model

5.4.1   Material modelling

Two material models developed in Chapter 3 are used for simulating the forming behaviour of bi-axial NCFs, utilising membrane and shell elements respectively to represent the fabric plies. The membrane element model (MEM) incorporates the in-plane behaviour of the fabrics into a simulation framework and the bending stiffness of fabric is overlooked, while the shell element model (SEM) extends the MEM model by including out-of-plane bending behaviour through the Composites Layup Toolset in Abaqus, as presented in Section 3.3.

Both the MEM and SEM are implemented via a user defined fabric material subroutine (VFABRIC) in Abaqus/Explicit. Each element (M3R4D) in the MEM has 12 degrees of freedom (DOFs) and 1 integration point, compared with 24 DOFs and 3 integration points for the SEM elements (S4R) (one integration point in each layer). The parameters used for modelling the FCIM359 biaxial NCF material are presented in Table 3.1 and Table 3.2, including in-plane shear and out-of-plane bending properties.

The mechanical behaviour of the diaphragm material was modelled using the Marlow model for hyperelastic materials in Abaqus/Explicit [193]. The material data from the three independent material tests (i.e. uniaxial tension, equibiaxial tension and planar shear) is presented in Section 5.3.3.

5.4.2   Process modelling

The FE mesh representing the fabric plies was positioned between the mesh for the two diaphragms, as shown in Figure 5.4(a). The perimeter of the diaphragm mesh was constrained in the x-y plane to replicate the constraints from the forming rig. All parts of the tooling were modelled as rigid bodies.
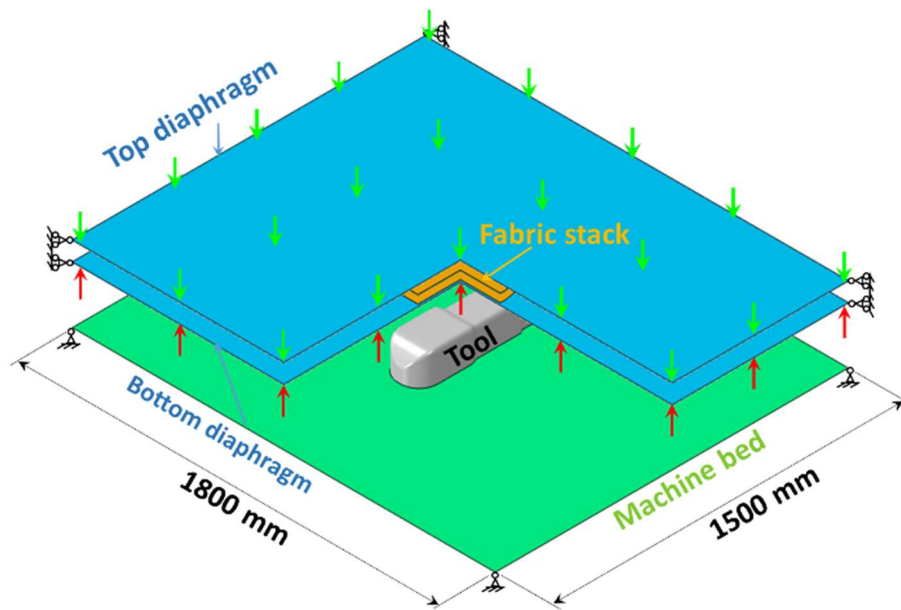
(a)
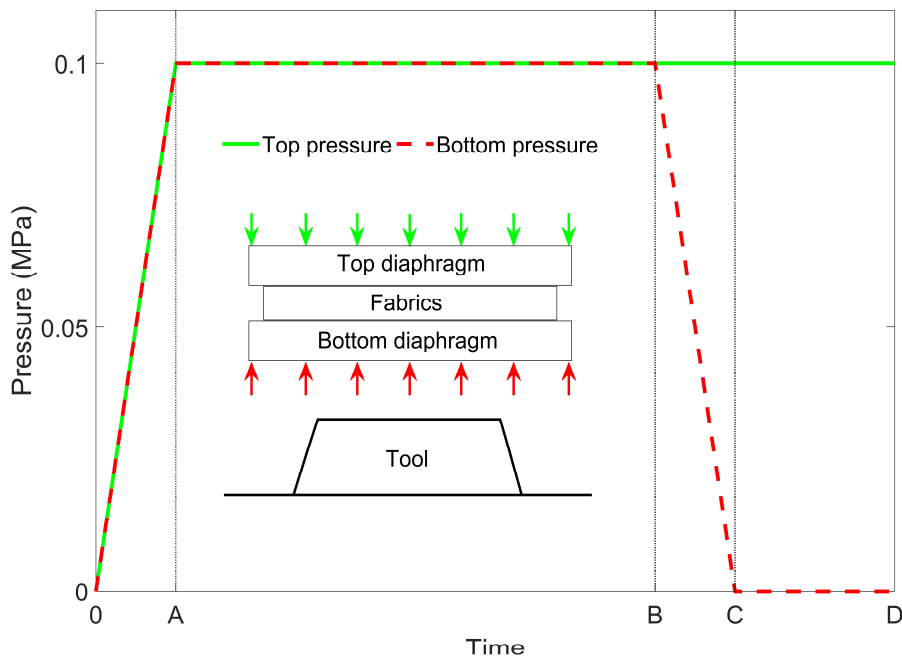
(b)

Figure 5.4: (a) FE model of the double diaphragm forming process. A quadrant from the two diaphragms and the fabric stack has been removed for clarity. Green and red arrows indicate the direction of the normal pressure applied to the top and bottom diaphragms respectively. (b) Graph indicating the pressure variation for the top and bottom diaphragms as a function of time.

Interactions between all parts were modelled using the in-built Abaqus penalty contact algorithm with Coulomb friction. The friction coefficients for tool-diaphragm, fabric-

diaphragm and fabric-fabric interactions were measured to be 0.51, 0.40 and 0.35 respectively, using the testing method used by Chen et al. [21].

The in-bag vacuum between the two diaphragms was modelled using two pressures, which were equal in magnitude (1×10^5 Pa) but opposite in direction between times A and B in Figure 5.4 (b). By applying displacement boundary conditions to the frame, the sandwich arrangement was draped over the tool until the edge of the lower diaphragm made contact with the machine bed. The pressure between the bottom diaphragm and the machine bed was then reduced to zero to generate a pressure gradient (from time B to C in Figure 5.4 (b)), drawing the diaphragm assembly into contact with the tool surface. Due to the low thickness of the diaphragms and the high pressure applied, significant surface penetration can occur during the analysis, leading to unrealistic deformations and excessive element distortion. Thus, a scaling factor of 20 was assigned to the penalty contact algorithm to increase the contact stiffness to avoid unwanted penetration between contact pairs. However, this requires a reduction in the time increment to ensure stability, and therefore increases the run time. All analyses were performed using 16 CPUs (Intel Xeon Gold 6138 20C 2.0GHz CPU).

In the global DDF simulation, displacement output was requested for master nodes during each of the 100 displacement increments, as the DDF frame was closed and the vacuum pressure was applied (i.e. between times A-B and B-C in Figure 5.4Figure 5.1(b)), in order to achieve a smooth interpolation of the boundary conditions for the sub-model. The shear angle data used to determine the defect locations was only output for the final displacement increment at the end of the analysis, in order to minimise the size of the report file produced by the global simulation.

5.5   Simulation results and model performance

5.5.1   Global simulation

5.5.1.1   Mesh sensitivity study

A mesh sensitivity study was performed for the full-scale MEM approach to determine an appropriate element size for the global simulation. Elements with edge lengths of 3 mm, 5 mm, 10 mm, 15 mm, 20 mm were investigated. Figure 5.5 presents a box-and-whisker plot of the shear angle distribution achieved for each element size. The median, 25th percentile and 75th percentile are all within 10% for each data set, indicating that these element edge lengths produce a representative range of shear angles for the current preform geometry.

The maximum values for the predicted shear angles in positive and negative shear increased by 17.1% and 21.5% respectively, as the element edge length decreased from 20 mm to 10 mm.
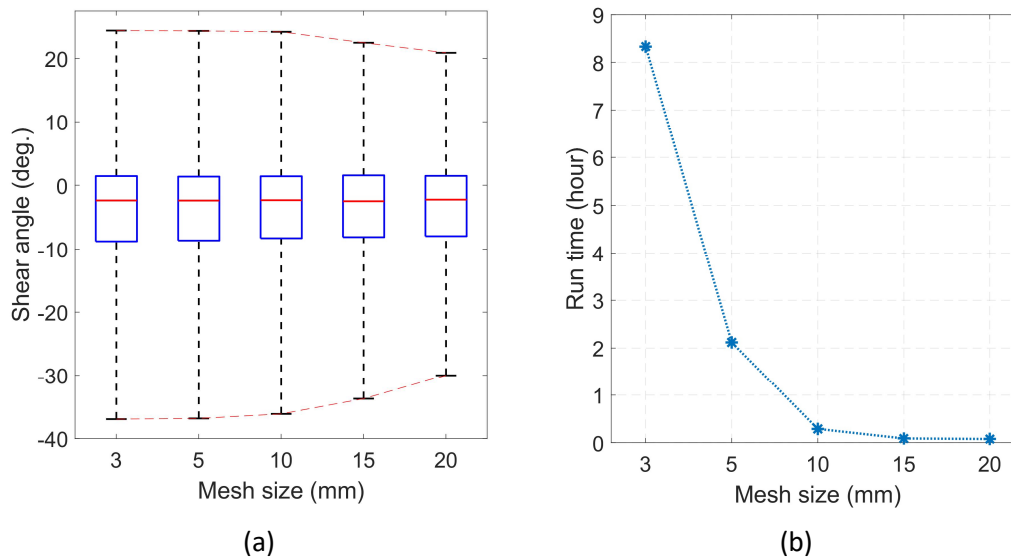
Figure 5.5: (a) Box-and-whisker plot to summarise shear angles from a range of FE simulations using different mesh sizes. The central red line represents the median shear angle, the horizontal edges of the box represent the 25th and 75th percentiles and the dotted black lines represent the maximum and minimum values in each case. (b) CPU-times for a range of FE simulations using different mesh sizes (All analyses were performed using an Intel Xeon Gold 6138 20C 2.0GHz, with 16 CPUs).

The maximum and minimum shear angle values for elements with a 3 mm edge length are 24.5° and -37.0° respectively. Convergence for the maximum and minimum shear angles starts at an element edge length of 10 mm, with an error of 1.9% and 2.3% compared to the 3 mm edge length. CPU times indicate that the simulations using 3 mm elements take approximately 29 times longer than those with 10mm elements, as shown in Figure 5.5 (b). Results indicate that an element edge length of ≤ 10 mm is suitable to ensure an acceptable precision for shear angle prediction. However, mesh conformity between the deformed fabric ply and the mould surface should also be considered to accommodate local features of the mould. In this case, a global mesh size of 5 mm was found to provide adequate mesh conformity between the deformed fabric ply and the mould surface, which required a minimum fillet radius of 10 mm for the global MEM simulation. In practice, a finer mesh could be assigned locally for required mesh conformity to further reduce computation times.

5.5.1.2   Determination of defects areas

By employing the defect criteria presented in Section 5.2.2, potential defects can be visualised in Figure 5.6 for each ply within the layup, according to shear angle and the deviation distance between the ply and tool surface.
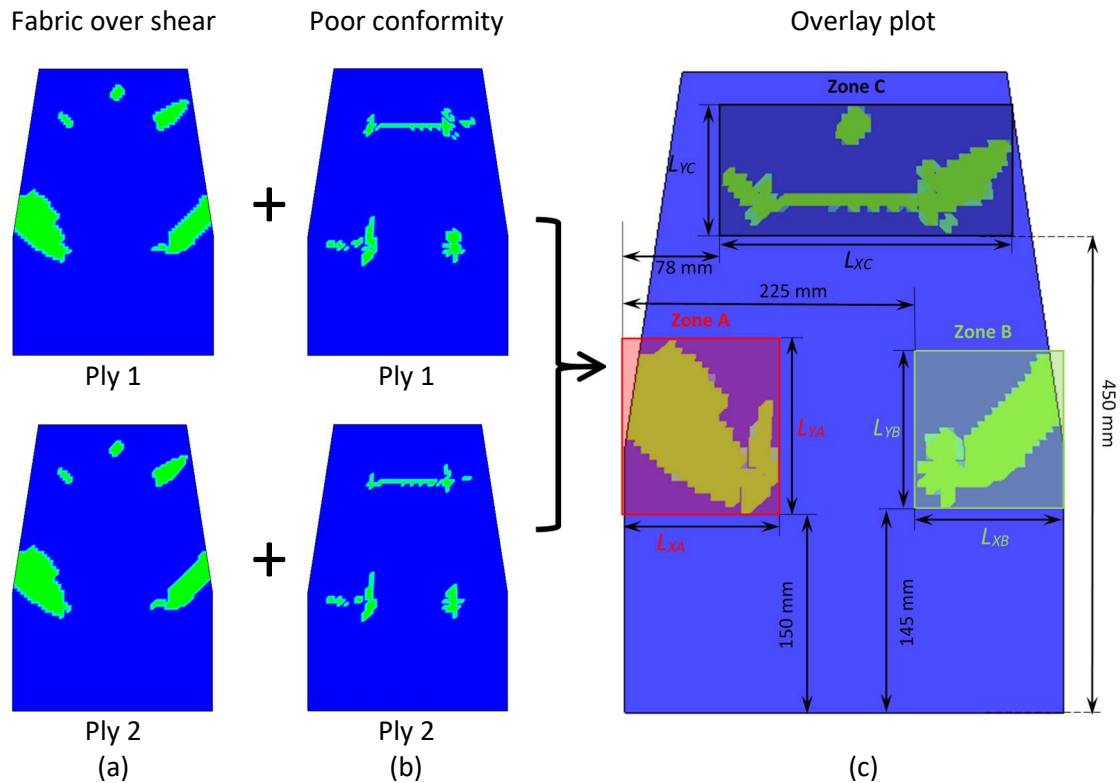
Figure 5.6: Defect areas for two biaxial fabric plies determined according to (a) fabric over-shear and (b) poor fabric-tool conformity. (c) Defect plot using superposition of the two defect modes (The dimensions of defect region are listed in Table 5.2). Ply 1 is the upper ply and Ply 2 is the lower ply (closer to male tool). (Results are plotted on the undeformed finite elements).

As shown in Figure 5.6 (a), similar shear angle distributions are observed for both plies with the same initial fibre orientation. Since a high degree of in-plane fabric shearing is required for the ply to conform to the concave regions near the joggles along the spar, out-of-plane wrinkles are likely to occur when the shear angle exceeds the critical value. Figure 5.6 (b) shows the nodal deviation distance between the expected mid-plane position of the fabric ply and the tool surface. Again, poor conformity is concentrated around the joggles, indicating the likelihood of further wrinkling and bridging defects. Three distinct groups of defects (Zones A, B and C in Figure 5.6(c)) can be determined by superimposing these individual defect plots, enabling local simulations to be performed using the refined SEM mesh.

5.5.2   Local simulation

5.5.2.1   Parametric study on sub-model dimensions

Table 5.2 lists the dimensions of the bounding boxes surrounding the localised defects determined according to the method presented in Section 5.2.3, which represent the geometries of the local models. The locations for these local models are presented in Figure 5.6(c). Since the displacement boundary conditions for the local SEMs are extracted from the coarser global MEM, the interpolation of the boundary nodes can potentially affect the accuracy of the size, shape and exact location of the predicted defects, particularly if the defects are close to the boundary nodes of the local model. A parametric study was performed to determine if a moderate increase in the dimensions of these local models may be required to minimise these boundary effects.

The influence of the dimensions for Zone A (see Figure 5.6(c)) were studied to determine if they influence the defect pattern within the local sub model. A series of local SEM simulations were performed for Zone A using different model dimensions, i.e. 1.0, 1.05, 1.15, 1.20 times both L_x and L_y, as shown in Figure 5.6(c). The element edge length in the local simulations was assigned to be 1 mm to capture wrinkles of amplitude $\sim$ 1mm.

Table 5.2: Dimensions of defect regions in Figure 5.6(c).

Defect regions	L_X	L_Y
Zone A	121 mm	130 mm
Zone B	115 mm	115 mm
Zone C	217 mm	94 mm

Figure 5.7 shows plots of the defect patterns predicted by local simulations for Zone A of different dimensions. Two wrinkles (denoted as Wrinkle 1 and 2 in Figure 5.7(a)) occur around the corner of the joggle and fabric bridging appears on the side of the preform. As shown in Figure 5.8(a), the length of Wrinkle 1 (on the left-side view in Figure 5.7) is constant at approximately 68.0 mm for all model dimensions, while the length of Wrinkle 2 converges to 84.0 mm when the original dimensions of Zone A are increased by 15 %. Figure 5.8(b) shows that the area of bridging predicted by the local simulation also converges to 625.0 mm^2 as the increase in model dimensions approaches 15%. Therefore, 15% increase was chosen to be the optimal extension for the dimensions of all local models. As shown in Figure

5.8(c), a 15% increase in the dimensions of the zone leads to a 67% increase in the CPU time of the local simulation. However, the converged values for wrinkle length and bridging area are only 10% different from the results predicted by the smallest model for Zone A, and the defect patterns appear to be consistent for all dimensions. However, a 15% increase in dimensions was used for all local sub models evaluated in this study.
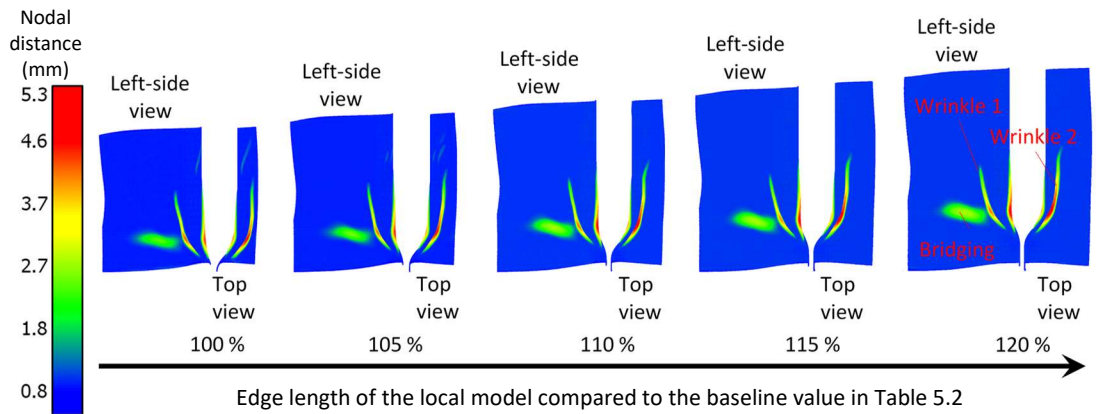
Figure 5.7: Effect of increasing edge length on the wrinkle pattern of local model in Zone A (Baseline values taken from Table 5.2) on defect patterns.
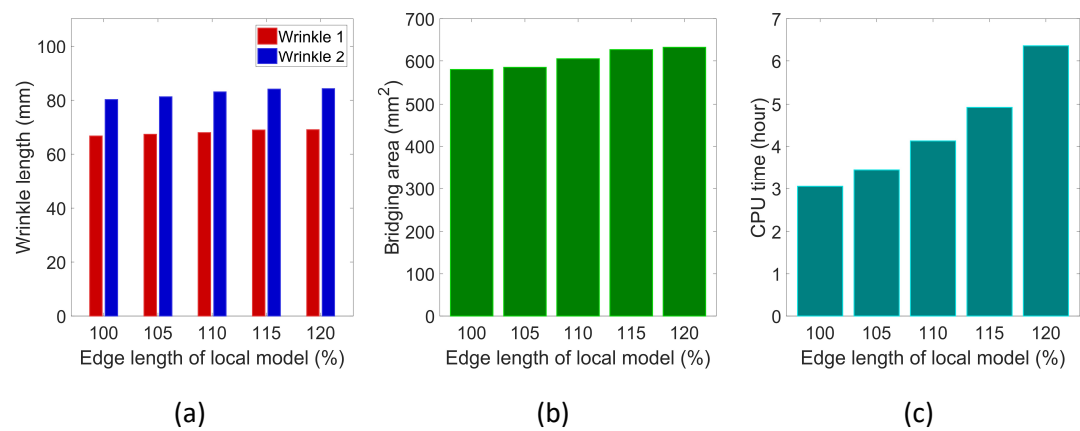
Figure 5.8: Effect of increasing edge length of local model in Zone A (Baseline values taken from Table 5.2). (a) wrinkle lengths (see Figure 5.7 for wrinkle patterns), (b) bridging areas, (c) CPU times (All analyses were performed using an Intel Xeon Gold 6138 20C 2.0GHz, with 16 CPUs)

5.5.2.2   Defect identification

Figure 5.9(a) shows the surface of the experimental preform measured by SWLS. Macroscale defects are plotted in Figure 5.9(b) by comparing the point cloud from the SWLS of the preform against the mesh of the tool surface. Figure 5.9(c)-(e) shows plots of the defects predicted by local simulations for Zone A, B and C.
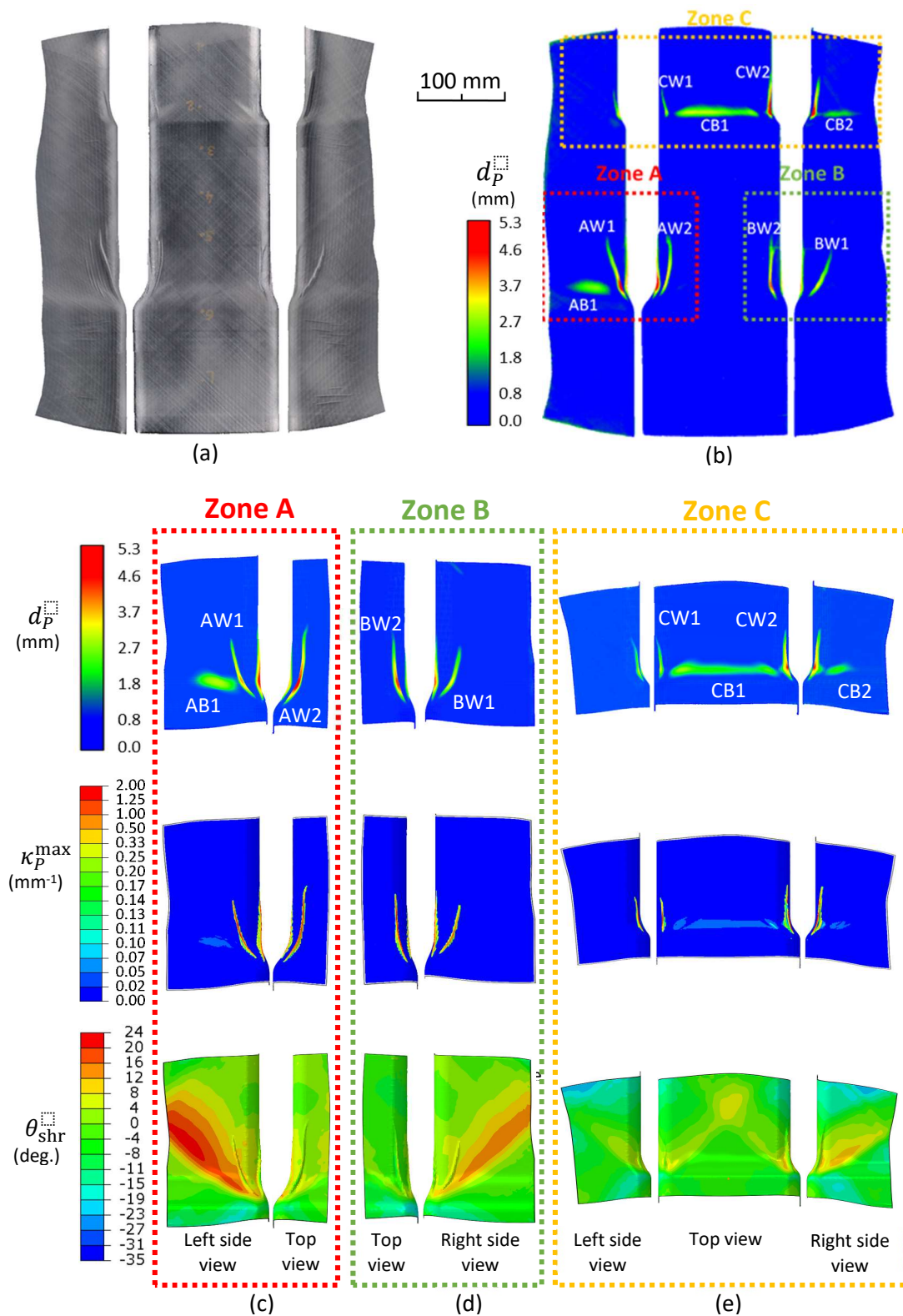
Figure 5.9: (a) Experimental images using SWLS (b) Nodal Distance determined d_P from experimental scan data; (c) – (e) Predictions of Nodal Distance d_P, Max Principal Curvature κ_P^{max} and Shear Angle θ_{shr} from local simulations.

The nodal distance between the mesh of the uppermost fabric ply (Ply 1) and the tool surface was used to visualise the defect patterns (images in the top row in Figure 5.9(a)-(c)). In

addition to the nodal distance, the absolute value of the maximum principal curvature was calculated to further highlight wrinkling defects (images in the middle row of Figure 5.9(c)-(e)), where the wrinkle directions are indicated by the distribution of the principal curvature. The principal curvature enables wrinkles to be isolated from bridging defects based on the output from the FE simulation, thereby quantitatively evaluating the severity of wrinkling defects. The maximum value of the principal curvature is 2 mm^{-1}, corresponding to a wrinkle radius of 0.5 mm, which indicates a tight ply fold in the regions labelled AW1, AW2, BW1, BW2, CW1 and CW2. All other areas of nodal deviation in Figure 5.9(c)-(e) are considered to be areas of fabric bridging and are labelled as AB1, CB1 and CB2.

Overall, the defect patterns predicted by local simulations agree well with the defect pattern from the experimental data, validating the capability of the proposed global-to-local modelling strategy for capturing the quantity, shape and location of defects. A quantitative comparison between the results from the experiment (blue bars) and the local simulations (red bars) is presented in Figure 5.10 for the wrinkle length and bridging area. In general, the simulation results are in good agreement with the experimental data, exhibiting the same trend. The predicted wrinkle lengths and bridging areas are typically within 10% of the experimental values.
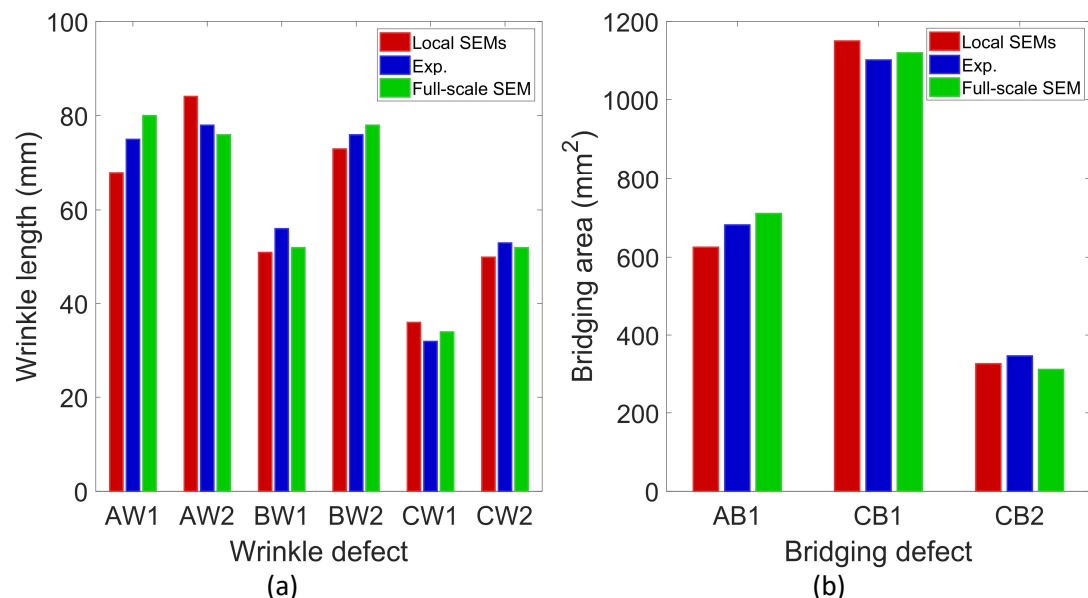
Figure 5.10: Comparison for (a) wrinkle length and (b) bridging area between experimental data and predictions from simulations. The red bars denote results from local shell element models (SEMs), the blue bars denote experimental data, and the green bars denote results from the full-scale shell element model (SEM). The labels on the x-axis of each graph correspond to the defect locations indicated in Figure 5.9(b)

The shear angle distributions are plotted in the bottom row of Figure 5.9(c)-(e) for the three local regions. Wrinkles AW2 and BW2 on the top surface generally follow the longitudinal direction of the tool, but the shear deformation in these areas is relatively low (< 8°). This indicates that these wrinkles are more likely to be caused by fabric bridging, where the tensile load in the direction of the wrinkle causes compressive strain perpendicular to the bridging path. In Zones A and B, a large positive shear deformation (up to 24.5°) is required for the fabric plies to draw into the concave geometry of the tool on the sides of the joggle (bottom row in Figure 5.9(c) and (d)). This results in wrinkles on both sides of the preform (AW1 and BW1), where the direction of these wrinkles follow the shear angle distribution. In Zone C (Figure 5.9(e)), no additional wrinkles are observed on the sides of the preform, but fabric bridging occurs (CB1 and CB2) due to the change in cross-sectional shape around the joggle.

5.5.3   Performance analysis

To further validate the local modelling approach, a full-scale DDF simulation of the current geometry was performed using the SEM model. The length scale of the current geometry was short enough to make this full-scale SEM study feasible, but it is acknowledged that this step would not be practical for large commercial applications due to the CPU time and memory requirement. This supports the need for the current global-to-local modelling scheme.

Both diaphragms and NCF plies were modelled using shell elements for this simulation, using an element edge length of 1 mm for both meshes. As shown in Figure 5.11(a) and (c), the pattern of defects and shear angle distribution compare well with the results predicted by the local simulations presented in Figure 5.9(c)-(e), indicating some consistency between the simulations by the full-scale shell model and the local shell models. The absolute value of maximum principal curvatures is plotted in Figure 5.11(b) to highlight the wrinkling defects, which can be distinguished from the poor fabric-tool conformity shown in Figure 5.11(a). As shown in Figure 5.10, the wrinkle lengths predicted by the full-scale SEM (green bars) follow the same trend as the experimental data and the local SEM.
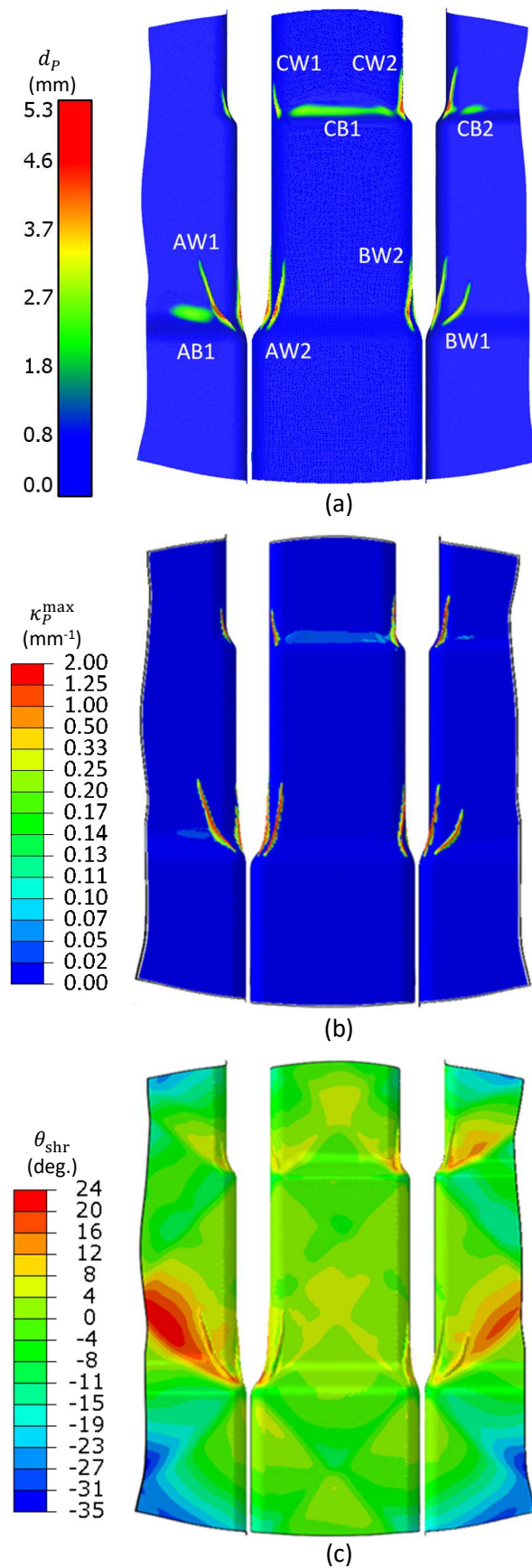
Figure 5.11: (a) Nodal distance between fabric and mould surface, (b) maximum absolute value of principal curvature, and (c) shear angle distribution predicted by the reference simulation for a full-scale model using shell elements.

The average relative error between the full-scale SEM and the experimental data is 4.5% and 5.2% for the wrinkle length and the bridging area respectively, supporting the use of the composite shell element approach to capture the bending behaviour of the fabric plies. The average relative error between the full-scale SEM and the local SEM is 7.2% and 6.4% for the wrinkle length and the bridging area respectively, which could be improved by refining the mesh density of the global MEM and scale of the local models as discussed previously. Furthermore, the occurrence of wrinkles within the sub-modelling regions can result in additional material draw-in, which in turn can affect the deformation field of the global model. Whilst this may lead to some discrepancies between the results predicted by the full-scale SEM and the local SEMs, the influence was shown to be limited for this case. The deformations in these local sub-model regions were therefore assumed to have insignificant influence on the global deformation at the sub-model boundaries for this geometry.

The CPU times for the full-scale SEM and the global-to-local simulations are compared in Table 5.3. The reference simulation using the full scale SEM with 1mm element edge length took over 120 hours to complete, compared to a total CPU time of 15.7 hours (i.e. the sum of CPU times for the global MEM and all three local SEM simulations) by the proposed global-to-local modelling strategy. The global simulation using the full scale MEM with 5 mm element edge length took approximately 2.0 hours to complete and the maximum CPU time for the local sub modelling was about 5.0 hours for Zone C. As demonstrated, this approach enables the location, size and shape of macroscale defects to be predicted with confidence at an affordable computational cost.

Table 5.3: CPU times for the full-scale shell model and the global-to-local simulation. All analyses were performed using an Intel Xeon Gold 6138 20C 2.0GHz, with 16 CPUs.

Type of simulation		Element edge length	CPU time
Full-scale shell model		1 mm	124 h
Full-scale membrane model		5 mm	2 h 5 min
Local simulation shell model	Zone A	1 mm	4h 55min
	Zone B	1 mm	3h 30min
	Zone C	1 mm	5h 10min

5.6   Chapter summary

A two-stage global-to-local sub model has been developed to reduce the computation time required to predict the size and location of critical defects during the preforming stage of composite components. A membrane element approach based on the fabric constitutive model has been implemented within Abaqus/Explicit to rapidly identify the location of defects, such as fabric wrinkling and bridging, based on empirical defect criteria. The output from this global approach was then used to identify local sub-models to investigate these areas in more detail, extracting appropriate boundary conditions from the global behaviour of the fabric plies. A laminated shell approach was used to incorporate the bending response of the biaxial fabric into the forming simulation framework, to explicitly model out-of-plane fabric wrinkles.

The methodology has been validated by forming a fabric blank over a generic geometry comprising local changes in cross-sectional shape, in order to invoke forming induced defects in a controlled manner. The defective areas predicted by the simulation agree well with the locations observed from the forming experiments, including the shape and length of surface visible defects such as fabric wrinkling and bridging. Comparisons with experimental data indicated that this approach is capable of correctly replicating the macroscale wrinkling and bridging defects that occur during double diaphragm forming (DDF), with the length of wrinkles and area of fabric bridging predicted within 10%. The CPU time was reduced from 120 hours for the full-scale high fidelity model, to just 15.7 hours (~13.1%) for the two-stage global-to-local approach. These reductions will become more significant as the overall length scale of the component are increased for components produced by DDF.

Chapter 6   Double diaphragm forming of multi NCF plies

6.1   Introduction

This chapter investigates the effect of inter-ply sliding between multiple biaxial Non-Crimp Fabric (NCF) plies, as they are processed into preforms by Double Diaphragm Forming (DDF). A generic geometry was selected to contain features that exhibit moderate variation in curvature along the length of the component, which enabled the inter-ply movement between the NCF plies to be the dominant defect formation mechanism. Forming simulations and experiments were conducted to understand the influence of ply layup sequence and interfacial frictional behaviour on the formation of out-of-plane wrinkles, in order to investigate the feasibility of using inter-ply lubrication to produce defect-free multi-ply NCF preforms.

6.2   Interfacial friction characterisation

Interfacial frictional behaviour plays an important role in the formation of defects during multi-ply fabric forming [90, 92], as areas of compression in the direction of the yarns can occur between contacting plies with dissimilar orientations. Reducing the inter-ply friction is therefore important to ensure that the plies can slip more freely to avoid the formation of defects [59, 194].

A liquid resin was applied during this study to lubricate the contact interfaces between all plies and the diaphragm films, to reduce the frictional resistance during DDF. A sled test (ASTM D1894, ISO8295) was employed to characterise the friction behaviour for different material contact pairings. The coefficient of friction (CoF) between the fabric-fabric, fabric-diaphragm, diaphragm-diaphragm and diaphragm-tool contacts were characterised by measuring the relative movement between the sled and the supporting plate. Friction tests were conducted for dry surface pairings and lubricated surface parings. The lubricated tests used a liquid epoxy resin (i.e. Prime^{TM} 20LV, supplied by Gurit, UK). As shown in Figure 6.1, material specimens in each contact pair were attached to the surface of the sled and the supporting plate using double-sided adhesive tape to represent the contact interaction in the forming process. The weight of the sled was used to calculate the applied normal force to the contact surface. The tangential force required to move the sled at a constant velocity across the supporting plate was recorded by a 1kN load cell connected to the crosshead of a

universal testing machine (Instron 5581). All tests were carried out at ambient temperature (21°C).

The CoF was calculated from the ratio of the tangential (pulling) force and the normal force. For the lubricated surface pairings, a small amount of liquid resin (18.75g) was carefully applied on the surface of the base specimen (300 mm × 125 mm) using a syringe and then evenly distributed using a resin application roller to ensure the average areal weight of the liquid resin was 500g/m^2. Similarly, the liquid resin was evenly applied to the fabric (125 mm × 50 mm) attached to the sled, with the same areal weight as the base specimen.
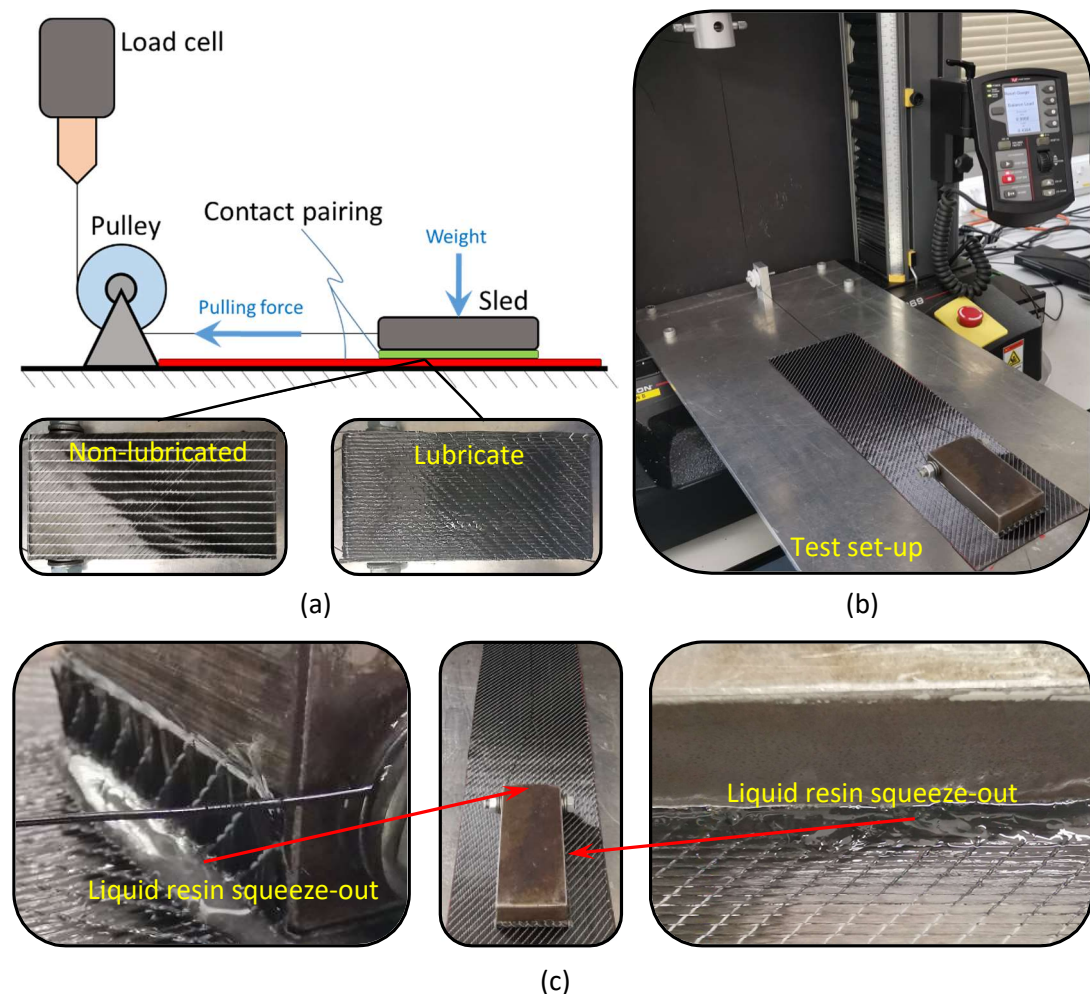
Figure 6.1: (a) Schematic of the friction test and the surface condition of the specimens attached to the sled (b) Experimental set-up (c) Photographs showing liquid resin squeezing out beneath the sled during the test.

Six different fibre angle pairings were considered at the interface for the fabric-fabric contacts, (i.e. 0°/0°, 0°/45°, 0°/90°, +45°/-45°, +45°/90°, 90°/90° shown in Figure 6.2). For the

fabric-diaphragm contact, the diaphragm film was attached to the supporting plate and the fibre orientation of the fabric specimen on the sled was set to be 0°, 45° and 90° with respect to the sliding direction. Five test repeats were performed for each fibre orientation pairing and the average friction force versus sliding displacement curves are presented in Appendix A. The dynamic CoF for each test repeat was derived by taking an average of the dynamic CoFs between 100 mm and 200 mm in Figure 6.3-Figure 6.4. The mean values and the corresponding standard deviations for the CoF are presented in Figure 6.2.
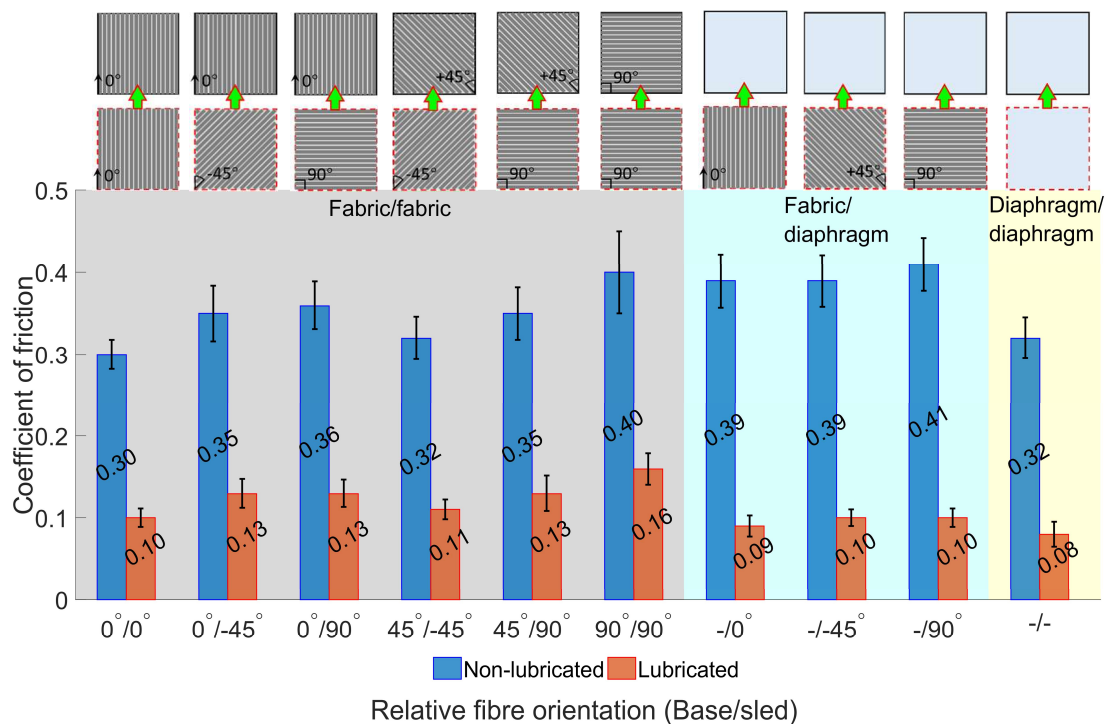
Figure 6.2: Dynamic coefficient of friction for different material pairings, i.e. fabric-fabric (grey region), fabric-diaphragm (blue region) and diaphragm-diaphragm (yellow region), measured with and without liquid resin lubrication. Error bars denote the standard deviation from 5 experimental repeats.

It is understood that there are shortcomings for testing the lubricated fabric friction in this way, as resin is initially squeezed out at the interface, which affects the thickness of the lubricating layer and therefore the CoF, as demonstrated in Figure 6.1(c). However, this method provides a qualitative assessment to support the simulation results. Relative to the dry fabric contact, the application of the liquid resin nominally reduces the CoF by 75% for the fabric-diaphragm contact pairing, and approximately 63% for the fabric-fabric contact pairing. It was noted during the friction test that the liquid resin was squeezed out by the

weight of the sled (see Figure 6.1(c)), which is reflected in the force versus displacement curves in Appendix A (see Figure 6.3-Figure 6.4). The thickness of the lubricating layer (interfacial separation distance) is non-constant, which causes the pulling force to increase with increasing sliding distance. The effect of increasing the applied normal pressure and the resin viscosity on the inter-ply friction were not considered in this work.
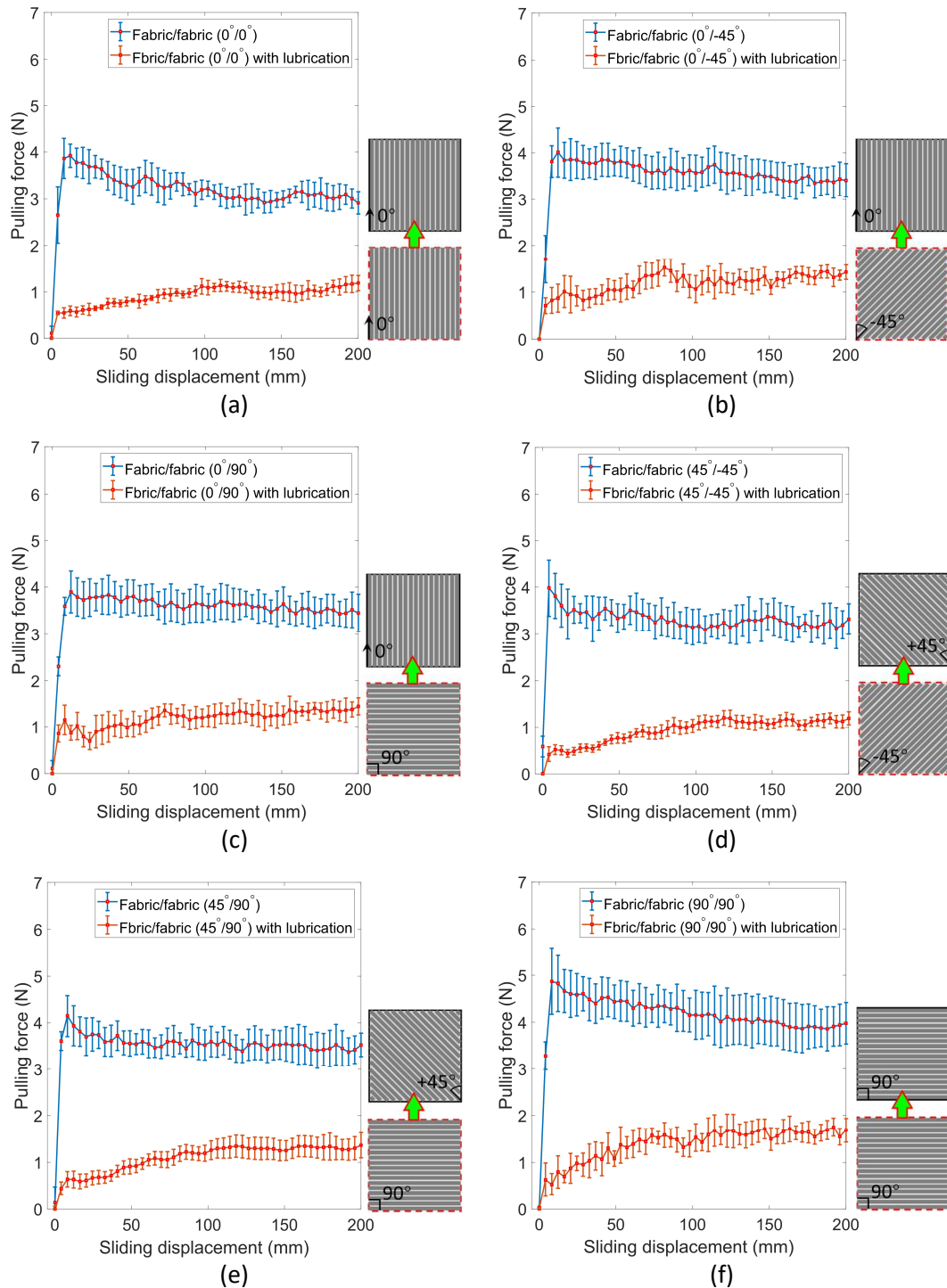
Figure 6.3: Pulling force vs. sliding displacement curves for fabric-fabric interfaces corresponding to different ply-ply relative orientations, measured with and without the liquid resin lubrication. Error bars denote the standard deviation from 5 experimental repeats.
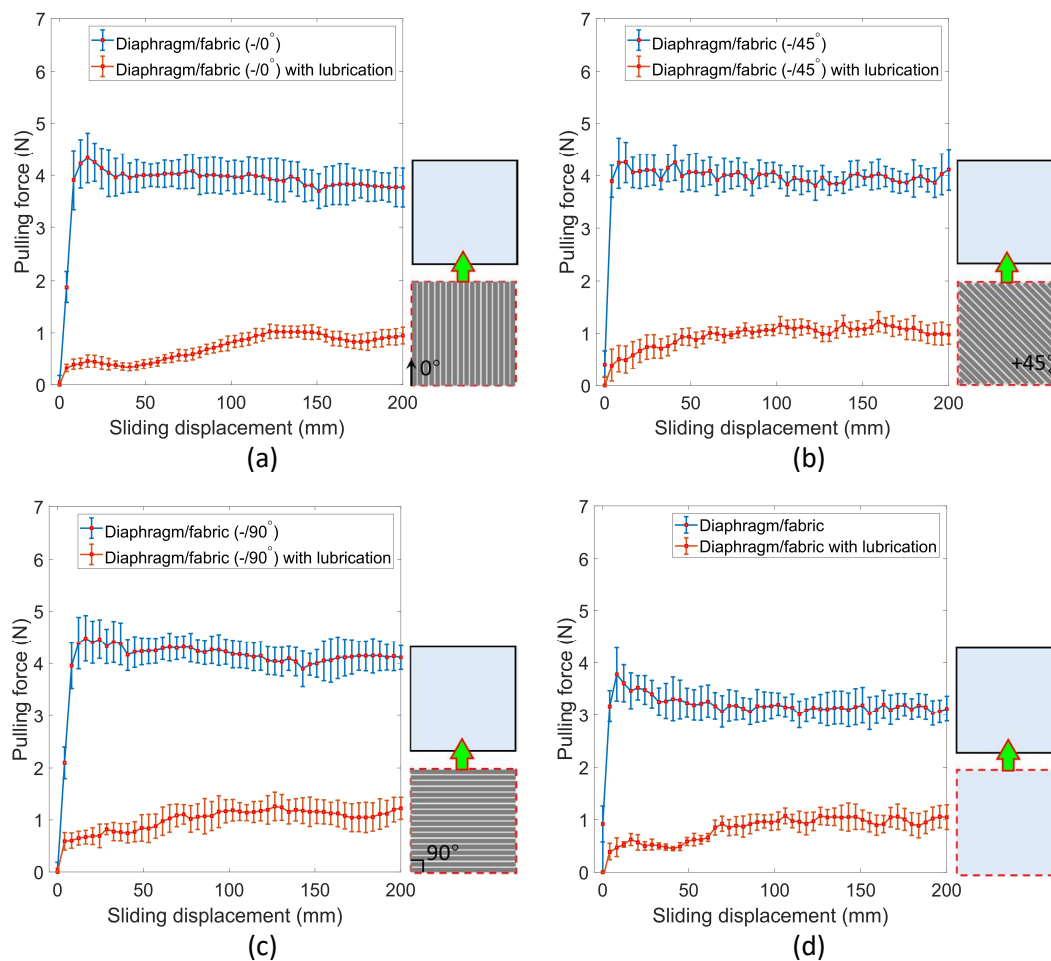
Figure 6.4: Pulling force vs. sliding displacement curves for (a)-(c) fabric-diaphragm and (d) diaphragm-diaphragm interfaces corresponding to different ply-ply relative orientations, measured with and without the liquid resin lubrication. Error bars denote the standard deviation from 5 experimental repeats.

6.3   Process design and forming experiments

6.3.1   Tool geometry

Fabric plies were encapsulated by two layers of elastomer diaphragms and subsequently drawn over a male tool by a vacuum between the lower diaphragm and the machine bed. The tool was similar in shape to the ramped spar geometry used by Johnson et al. [185]. As shown in Figure 6.5, recess features were assigned to both top and side faces of the spar, promoting some shear deformation to induce macro-scale defects. The tool was 640 mm in length and the in-plane dimension of the fabric plies was 400 mm × 250 mm. Since the ramp ratios of both the top and side surfaces of the tool were relatively small in magnitude (i.e. 1:18 for the top surface and 1:36 for the side surfaces), a small shear deformation (≤ 10°)

around the recessed region enabled the fabric plies to conform to the tool. Thus, the relative inter-ply movement dominated the formation of defects.
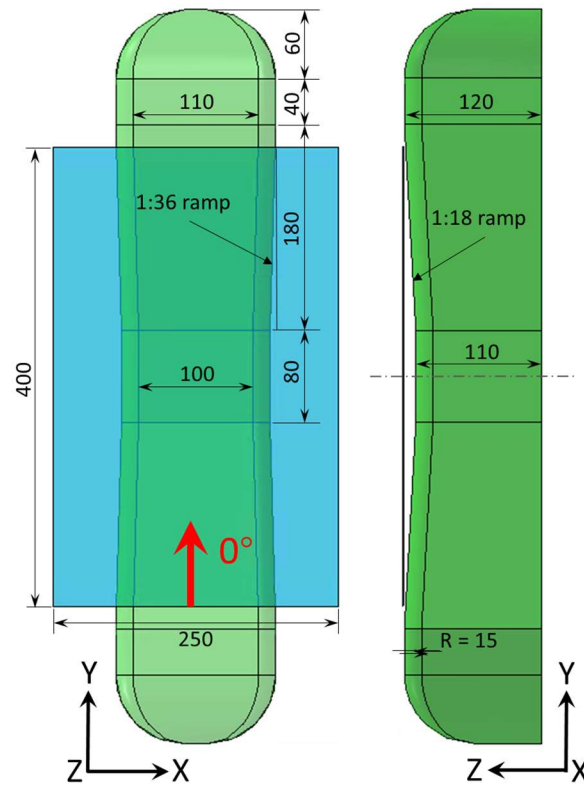
Figure 6.5: The dimensions of the tool geometry and fabric plies.
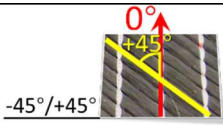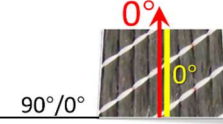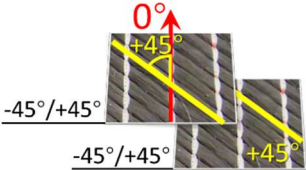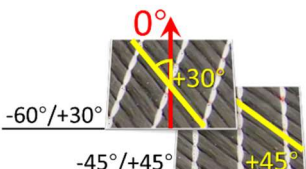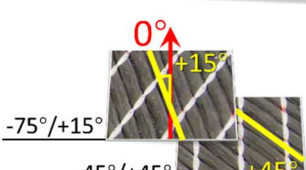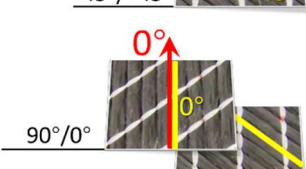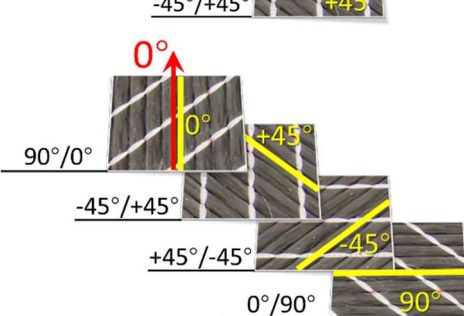
6.3.2   NCF layup sequence

Forming experiments were performed using different multi-ply layups to investigate the formation of defects during DDF, along with mono-ply configurations formed for comparison. All layup configurations are listed in Table 6.1, where M1 and M2 are mono-ply cases and L1 – L5 are multi-ply cases. The red arrow in the schematic in Table 6.1 is in line with the longitudinal direction of the tool and the yellow line in each configuration denotes the direction of the fibre tows on the top side of the ply. (The fibre direction on the other side of the ply is perpendicular to this yellow line).

As listed in Table 6.1, a single NCF ply was tested in each mono-ply case (M1 and M2), where the fibre orientations were assigned to be -45°/+45° and 90°/0° respectively. Layups L1-L4 in Table 6.1 consisted of two NCF plies, where the fibre orientation of the bottom ply (Ply 1) was fixed at -45°/+45° and the uppermost ply (Ply 2) was prepared with different fibre orientations. At the contact interface between the adjacent plies, the relative difference in

fibre orientation varied from 90° to 45° in increments of 15°. The layup L5 in Table 6.1 comprised four NCF plies laid up in a balanced symmetric sequence, i.e. [0°/90°, +45°/-45°]$_s$.

Table 6.1: Layup configurations for DDF trials. 0° direction (red arrow) is in line with the longitudinal direction of the tool in Figure 6.5. The layup sequence is expressed from the lowermost side (closest to tool) to the uppermost side. For each biaxial NCF ply, the yellow line denotes the direction of the fibre tows on the upper side of the NCF ply, while the tows on the other side are perpendicular to the yellow line.

Layup	Layup schematic	Fibre orientation
M1		[-45°/+45°]
M2		[90°/0°]
L1		[-45°/+45°, -45°/+45°]
L2		[-45°/+45°, -60°/+30°]
L3		[-45°/+45°, -75°/+15°]
L4		[-45°/+45°, 90°/0°]
L5		[0°/90°, +45°/-45°]s (i.e. [0°/90°, +45°/-45°, -45°/+45°, 90°/0°])

DDF experiments were initially performed for all configurations (M1, M2 and L1 – L5) using dry fabric plies. Experiments were then repeated for L4 and L5 using liquid resin applied to the surfaces of each fabric ply to investigate the effect of lubrication on the forming behaviour.

6.3.3   Defect visualisation

SWLS was used to capture the shapes of the produced preforms and the consolidated components. The preforms were scanned in-situ on the DDF machine whilst maintaining the vacuum consolidation pressure. Ambersil Flaw Detector was uniformly sprayed onto the surface of the outer diaphragm to avoid excessive reflection during scanning. Reference points were marked onto the diaphragm using a red marker pen before scanning to assist with the alignment and stitching of individual scans taken at different angles, in order to create a full 3D representation of the preform. Due to the applied in-bag vacuum, it was assumed that there was no clearance between the top diaphragm and the uppermost fabric ply. The same scanning method was applied to the consolidated components and the tool surface. Open-source software, CloudCompare [190], was used to visualise the distribution of defects by performing post-scan measurements on the point cloud.

6.4   Process modelling

The DDF model established in Section 5.4 is employed herein to simulate the forming behaviour of multiple NCF plies, using the fabric constitutive model developed in Chapter 3. All parts of the tooling were modelled as rigid bodies. Interactions between them were modelled using the in-built Abaqus penalty contact algorithm with Coulomb friction. For fabric-fabric and fabric-diaphragm pairing, average values for the CoF at different fibre orientations were assigned in the FE model, as presented in Figure 6.2. All CoF values used in the forming simulations are listed in Table 6.2, where $C_{\text{fab}-\text{f}}^{\text{fric}}$, $C_{\text{fab}-\text{d}}^{\text{fric}}$, $C_{\text{dia}-\text{dia}}^{\text{fric}}$ and $C_{\text{dia}-\text{tool}}^{\text{fri}}$ denote the coefficients for the fabric-fabric, fabric-diaphragm, diaphragm-diaphragm and diaphragm-tool interfaces respectively.

Table 6.2: Coefficient of friction values used in forming simulations for contact interfaces with and without lubrication. C_{fab-f}^{fric} , C_{fab-d}^{Fric} are determined as the average value of friction coefficients at different fibre orientations for the corresponding surface pairing, according to the data shown in Figure 6.2.

Interface pairing	Friction coefficient	
	Non-Lubricated	Lubricated
Fabric-fabric, $C_{fab-fab}^{fric}$	0.35	0.13
Fabric-diaphragm, $C_{fab-dia}^{Fric}$	0.40	0.10
Diaphragm-tool, $C_{dia-tool}^{Fric}$	0.25	-
Diaphragm-diaphragm, $C_{dia-dia}^{Fric}$	0.32	0.08

The tool used in this study for the demonstrator component only has a moderate variation in surface curvature, therefore poor fabric-tool conformity related to fabric bridging was considered to be negligible. Out-of-plane fabric wrinkles were the only form of defect observed in this case and the nodal distance between the mesh of the uppermost fabric ply and the tool surface was used to quantify this. The total length of all wrinkles was calculated based on the simulation results to quantitatively assess wrinkling severity for each scenario.

6.5   Results and discussion of multi-ply NCF forming

6.5.1   Wrinkling mechanism in multi-ply forming

The results from the mono-ply cases (i.e. M1 and M2 in Table 6.1) are shown in Figure 6.6, where no visible wrinkles are observed on the preform. This confirms that the current tool geometry has a negligible effect on the formation of wrinkles, therefore the inter-ply movement is highlighted to be the dominant factor during multi-ply NCF forming.

(a)

(b)
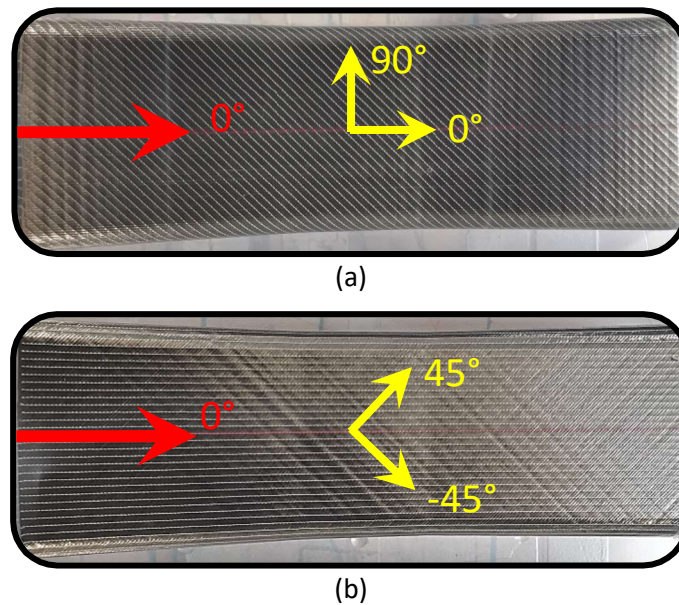
Figure 6.6: Mono-ply NCF preforms produced by DDF. (a) [90°/0°] and (b) [-45°/+45°]. The red arrow denotes the longitudinal direction of the tool and the yellow arrow denotes the fibre direction prior to forming.

DDF simulations were performed for a series of layups comprising two NCF plies to investigate the influence of ply orientation on the severity of wrinkling defects. As shown in Figure 6.7(a), the stitch directions for the two NCF plies were initially aligned along the longitudinal direction of the tool (Y axis direction in Figure 6.7(a)). The stitch direction of the uppermost ply was rotated clockwise in the X-Y plane, at an angular increment of 5°, producing a range of relative fibre angles at the contact interface between the two plies of 90° through to 0°. The nodal distance between the deformed mesh of the uppermost fabric ply and the tool surface was calculated to visualise the surface defects.
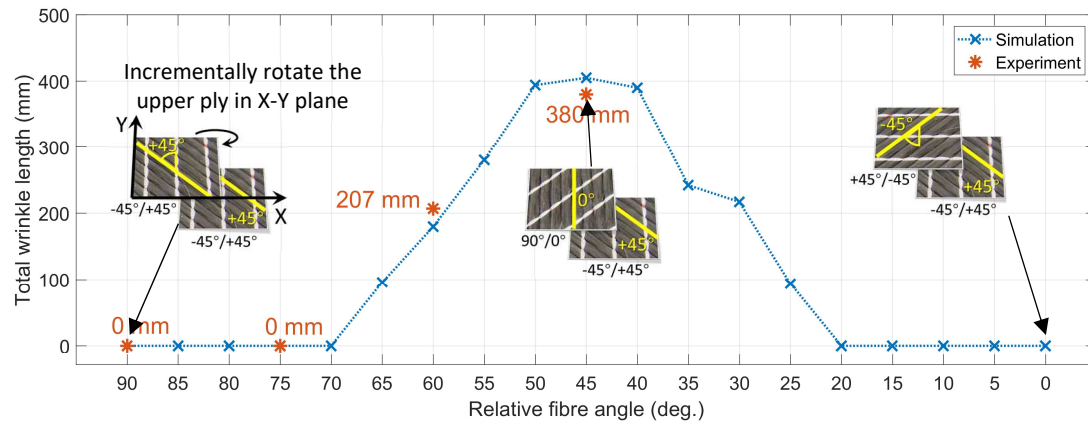
(a)
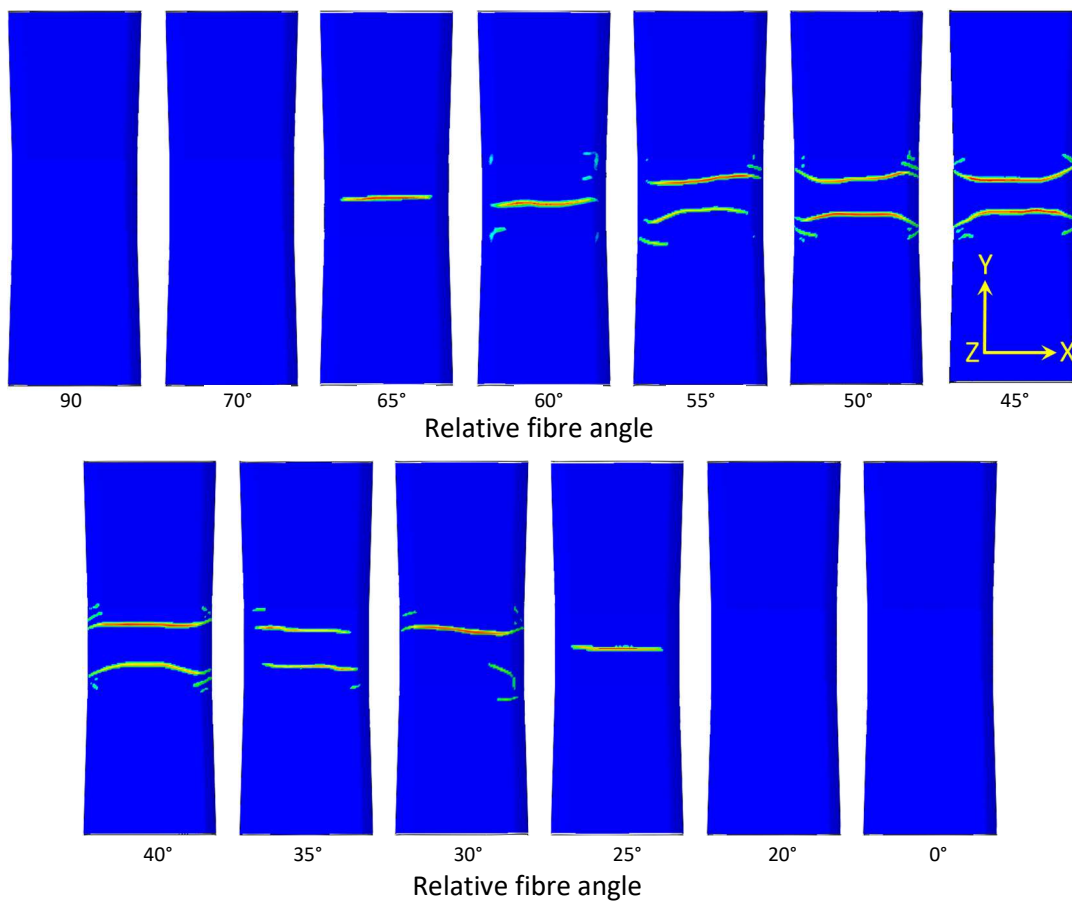
(b)

Figure 6.7: (a) Length of wrinkles predicted from different layup orientations, compared with experimentally measured wrinkle lengths for the layups L1 - L4. (b) The wrinkle patterns predicted for different layup orientations

The total wrinkle lengths (sum of the length of all wrinkles with an amplitude greater than 1 mm) for all layups are plotted in Figure 6.7(a), along with the corresponding wrinkle patterns in Figure 6.7(b). Wrinkling occurs in all preforms with relative fibre angles at the interface

ranging from 20° to 70°. The total wrinkle length peaks at a value of 401 mm when the relative fibre angle reaches 45°. The distribution is symmetrical about this point and the total wrinkle length is reduced as the relative fibre angle tends to 0° or 90°. The relative fibre orientation at the contact interface is demonstrated to have a significant influence on both the severity of wrinkles and the pattern, since the friction coefficients used for all ply-ply combinations was identical. A relative fibre angle of 45° at the ply interface is most likely to induce wrinkles in the preform, especially when the geometry of the formed shape causes relative displacement between the plies. Similar findings have been reported in the literature [94, 185] during the forming of multi-layered UD prepregs.

The wrinkling patterns for layups L1 – L4 (see Table 6.1 for layup sequences) produced by the forming simulation are compared with the experimental results in Figure 6.8 to validate the FE model. There is good agreement between the simulations and experiments for layups L1 and L2, where no wrinkles are found in the preform. For layup L4, two wrinkles with similar length (~138 mm on average) occur in the middle recessed region of the preform, which is close to the wrinkle pattern and length (~142 mm on average) predicted by the FE model. A primary wrinkle length of 113 mm is generated in the middle of the L3 experimental layup, compared with 109 mm in the FE simulation, but the orientation of the main wrinkle differs from that from the experimental result. In addition, some minor wrinkles also occurred around the fillet edges of the tool, which are captured by the FE model.

Figure 6.9(a) shows the shear angle distributions overlaid onto the undeformed blank for the four layups, (L1 – L4 in Table 6.1). Since the tool exhibits gentle ramp ratios on all surfaces (see Figure 6.5), the bridging effects related to the recess area of the tool are insignificant. As a result, the positive shear deformation required for the fabric plies to conform to the tool surface in the ramp area is relatively small in magnitude (<10°) for all layup configurations. However, Figure 6.9(a) demonstrates that the layups comprising two plies of different fibre orientations (L2, L3 and L4) undergo different shear deformations during forming, leading to incompatible inter-ply movements. This is restricted by the frictional resistance at the ply-ply contact interfaces, causing local compression along the fibre directions, as shown in Figure 6.9(b). Consequently, this local compressive strain causes the fibres to buckle and therefore wrinkle in the corresponding areas. The magnitude of the compressive strain increases as the relative fibre angle at the interface decreases from 90° to 45° for the four layups presented, highlighting the dependency of fabric wrinkling on the layup sequence. The likelihood of inter-ply sliding is dominated by the layup sequence for the current geometry, with the interfacial frictional force activated only when relative inter-

ply sliding occurs. The effect of the interfacial CoF on the severity of wrinkling is studied in more detail in Section 6.5.2.
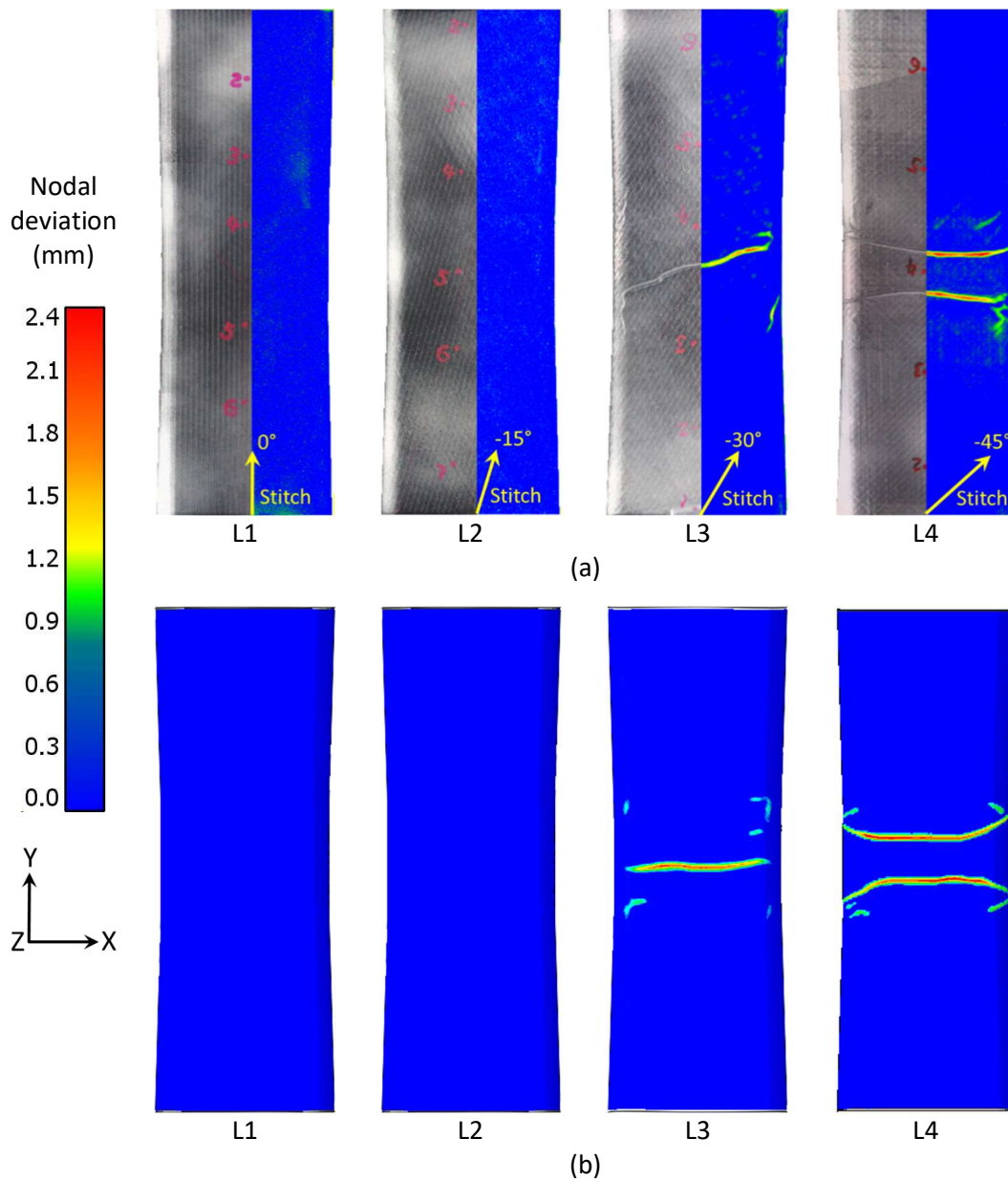
Figure 6.8: Experimental and simulation results for the forming cases L1-L4 in Table 6.1: (a) Experimental scans (b) Numerical simulations.
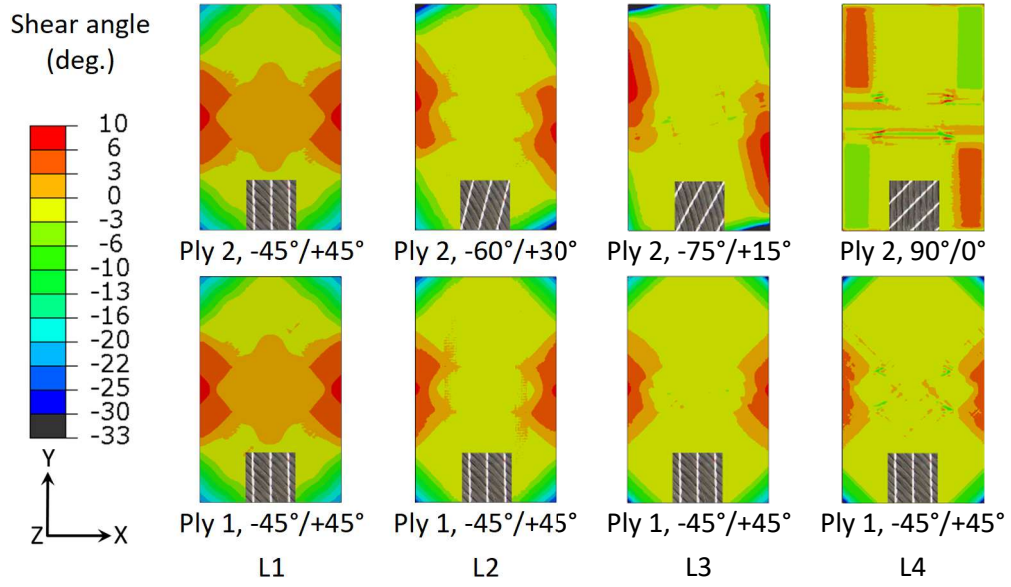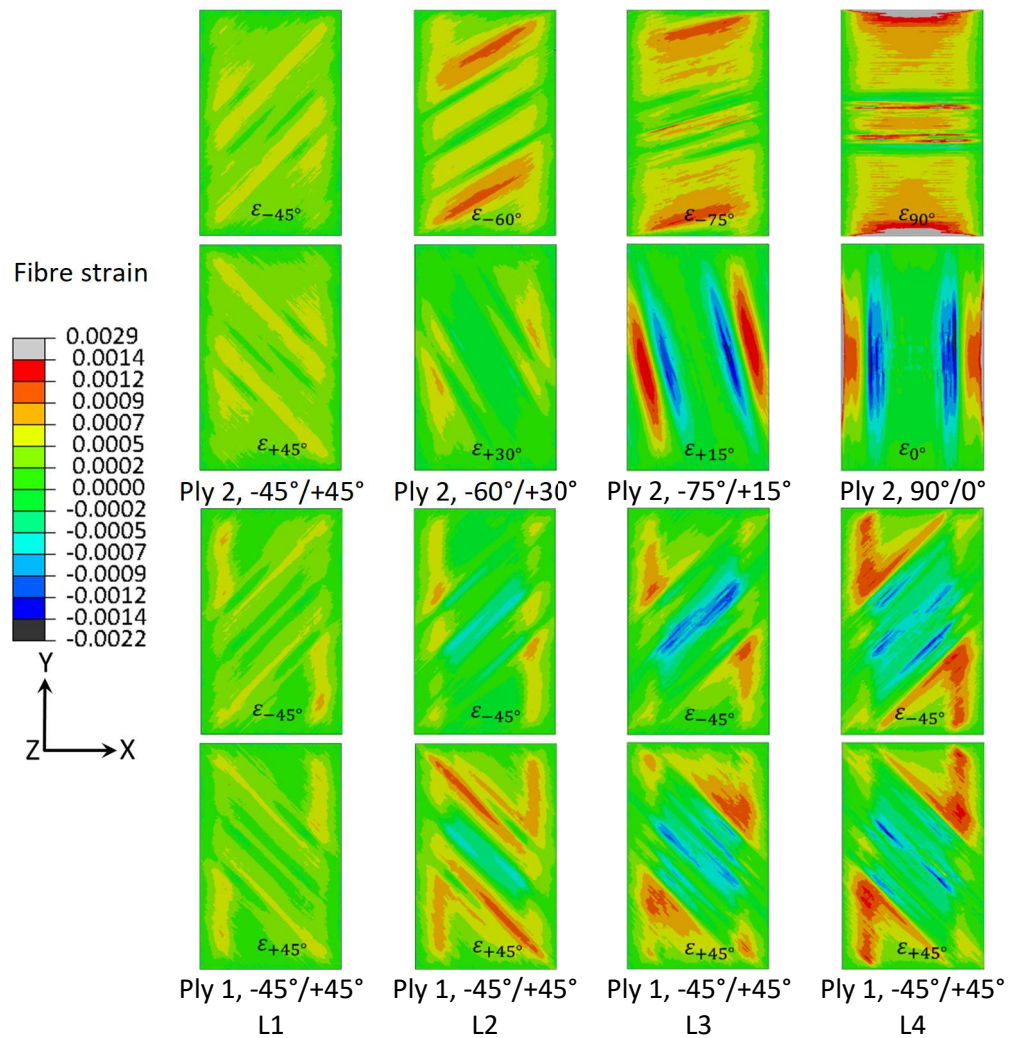
Figure 6.9: Numerical predictions for the forming cases L1-L4 in Table 6.1. (a) Shear angle and (b) Fibre strain.

Based on the changes in nodal coordinates of the deformed mesh, the relative displacement along the longitudinal direction of the tool (Y-axis in Figure 6.10) was calculated at three cross-sections in the central recess region of the specimen (i.e. Sections A-A', O-O' and B-B' in Figure 6.10) for layups L3 and L4, as shown in Figure 6.10.

L3: [-45°/+45°, -75°/+15°]

(a)

L4: [-45°/+45°, 90°/0°]

(b)
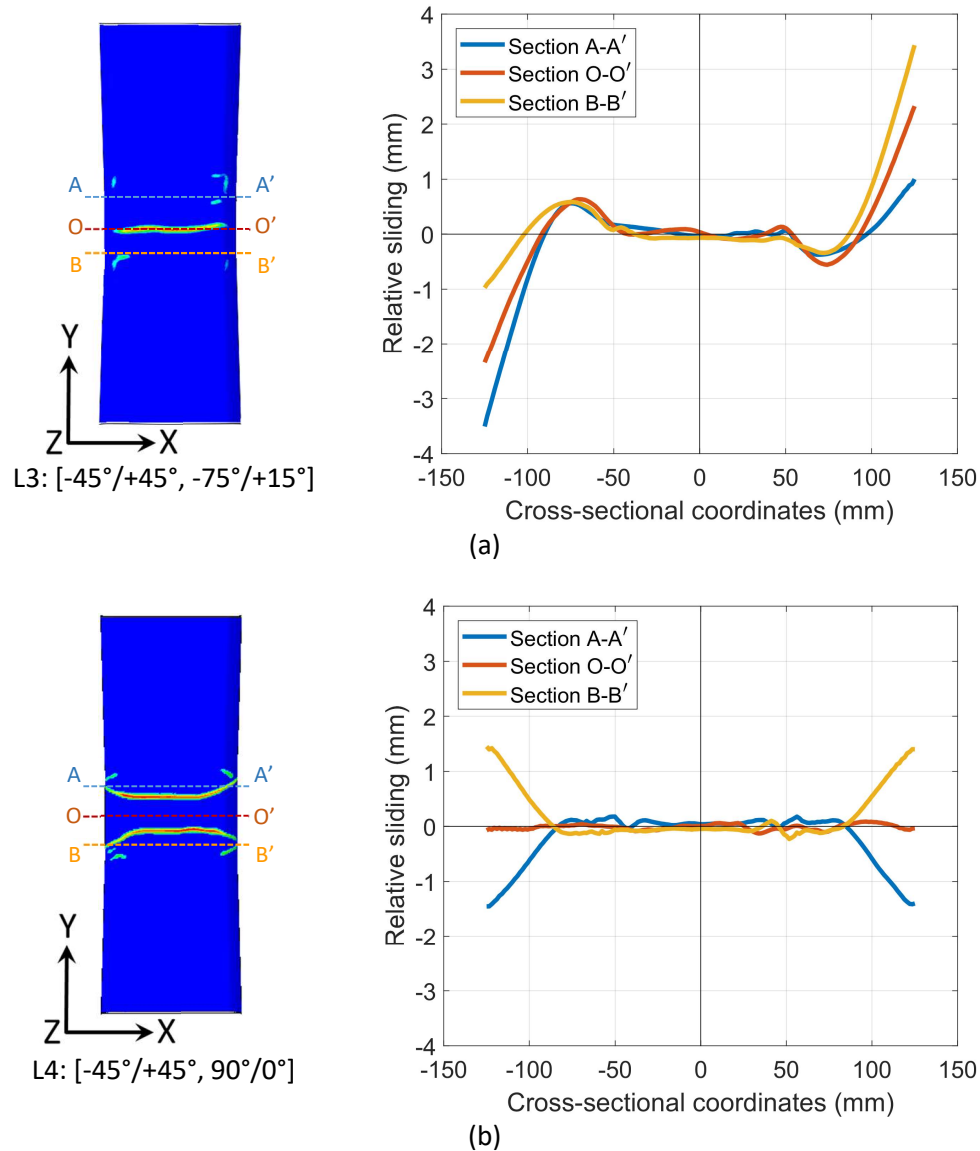
Figure 6.10: Relative sliding displacement of the upper ply with respect to the lower ply for the layups (a) L3 and (b) L4 in the longitudinal direction of the tool (Y-axis). Section O-O' is taken from the middle of the specimen and sections A-A' and B-B' are taken at 30 mm spacings from the middle section O-O'.

Section O-O' is at the geometric centre of the specimen, and the vertical distance from Section O-O' to A-A' and B-B' is 30 mm in each case. The relative sliding at the three cross-sections for layup L4 ([-45°/+45°, 90°/0°]) are presented in Figure 6.10(b). All three sections exhibit symmetrical sliding about the longitudinal direction of the tool, resulting in a

symmetrical wrinkle pattern. For layup L3 ([-45°/+45°, -75°/+15°]), the relative sliding displacements at all three cross-sections are asymmetric about the length of the specimen (see Figure 6.10(a)), indicating a counter-clockwise rotation of the upper ply with respect to the lower ply. This relative rotation is restricted by the resistance from the inter-ply friction, leading to an oblique wrinkle across the middle of the specimen. Furthermore, the frictional force caused by this asymmetric inter-ply motion is dependent on the fibre orientation and the stitch pattern at the contact interface, both of which influence the size and shape of the asperities at the contact surface and therefore the CoF. The orientation dependence of the CoF has not been studied in detail in the current work, therefore a constant value has been assumed, which may contribute to the error in the prediction of the wrinkle orientation for layup L3 in Figure 6.8. An isotropic Coulomb friction model has been employed, but an anisotropic model maybe required to account for this orientation dependence.

6.5.2   Influence of interfacial friction

A parametric study was performed using DDF simulations with different combinations of fabric-fabric and fabric-diaphragm coefficients of friction to evaluate the influence of friction on the formation of fabric wrinkles. Layups L3 and L4 (Table 6.1) were selected for this study, where the fabric-fabric friction coefficient was varied from 0.05 to 0.35 in increments of 0.025 and the fabric-diaphragm friction coefficient was varied from 0.05 to 0.4 in increments of 0.05.

Contour plots for the maximum wrinkle length, using different friction coefficient combinations, are shown in Figure 6.11(a) and Figure 6.12(a) for layups L3 and L4 respectively. These maps were created by interpolating the discrete data points at the grid intersections, which denote different combinations of the friction coefficients. The corresponding wrinkle patterns are plotted for L3 and L4 at the data points near the boundary between the wrinkle-free and the wrinkled region in the maps, as shown in Figure 6.11(b) and Figure 6.12(b) respectively.

(a)

(b)
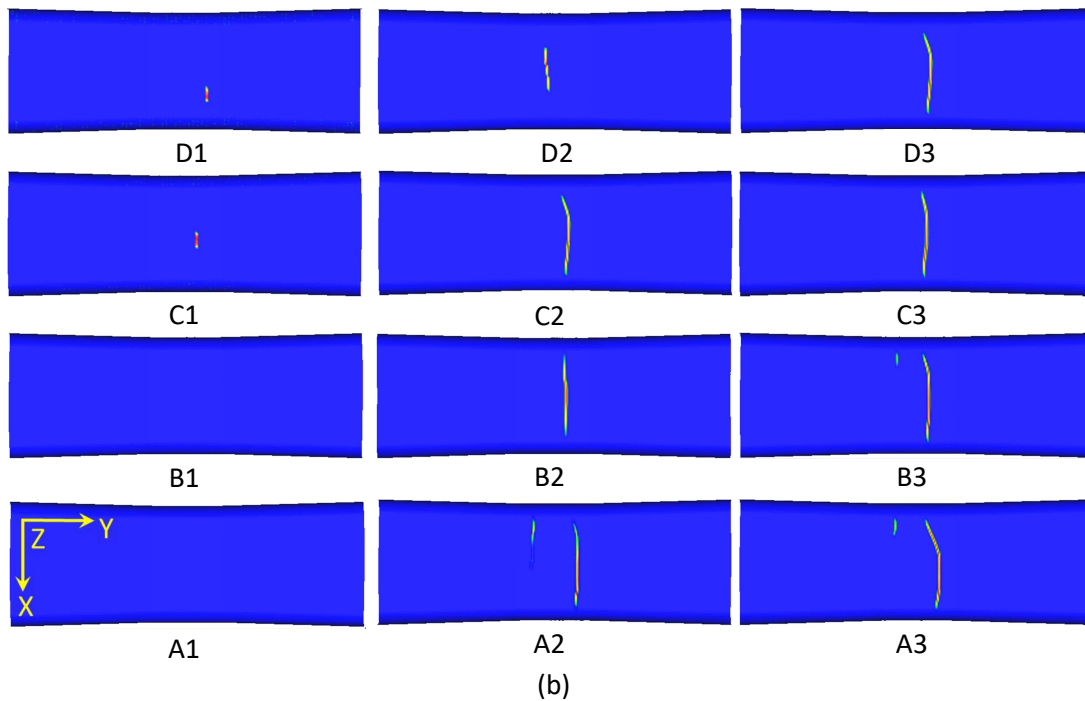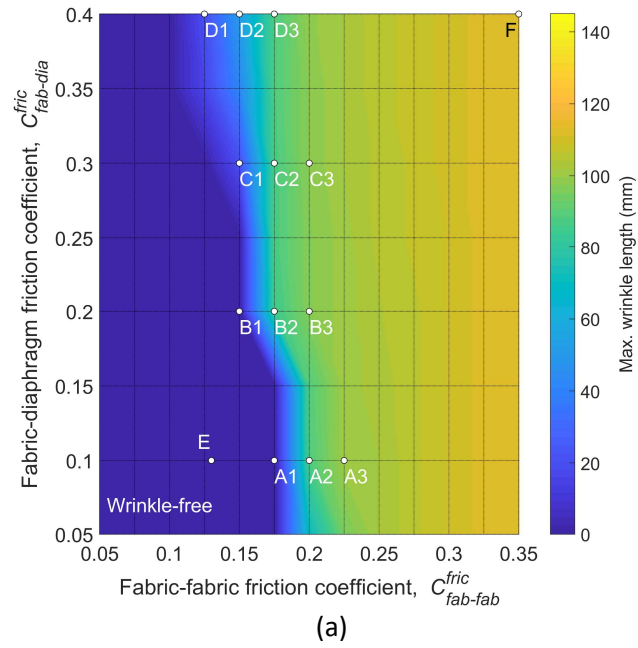
Figure 6.11: (a) Contour map of the maximum wrinkle length predicted by the FE model using different friction coefficients for the ply layup L3 [-45°/+45°,-75°/+15°] (b) Typical wrinkle patterns corresponding to the data points on the contour plot.

(a)

(b)
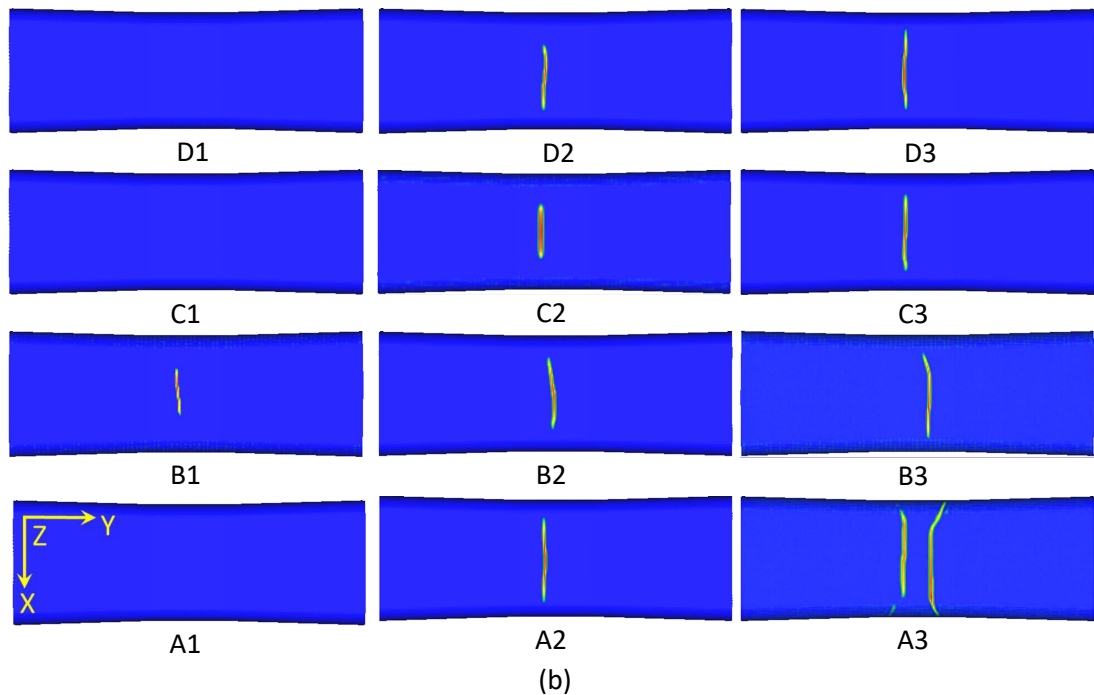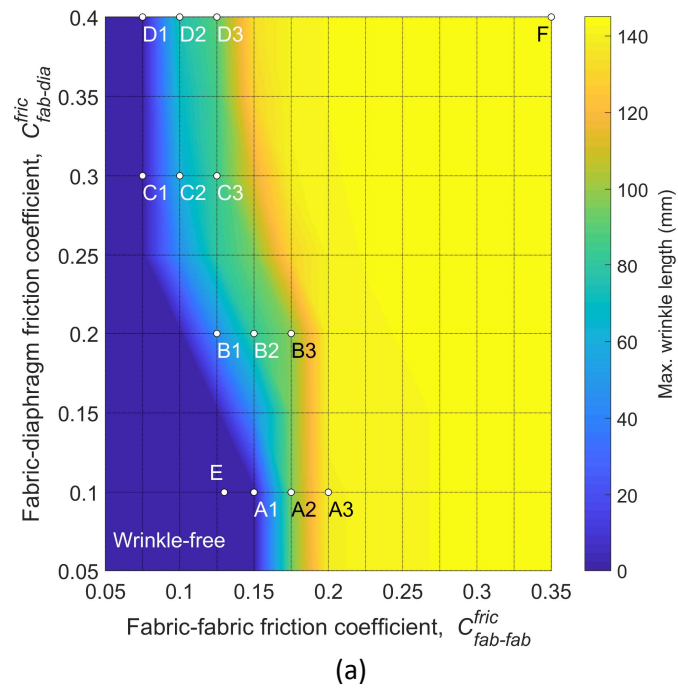
Figure 6.12: (a) Contour map of the maximum wrinkle length predicted by the FE model using different friction coefficients for the layup L4 [-45°/+45°, 90°/0°] and (b) Typical wrinkle patterns corresponding to the data points (i.e. black dots) in (a)on the contour plot.

On average, the severity of wrinkles, represented by the maximum wrinkle length (Figure 6.11(b) and Figure 6.12(b)), increases with the increase in both $C_{\text{fab}-\text{fab}}^{\text{fric}}$ and $C_{\text{fab}-\text{dia}}^{\text{fric}}$ friction coefficients. The preform is free of wrinkles for the entire range of $C_{\text{fab}-\text{dia}}^{\text{fric}}$ (i.e. $0.05 \leq C_{\text{fab}-\text{fab}}^{\text{fric}} \leq 0.4$) when $C_{\text{fab}-\text{fab}}^{\text{fric}}$ is small. For layup L3, $C_{\text{fab}-\text{fab}}^{\text{fr}}$ must be less than or equal to

0.125, and for L4 $C_{\text{fab}-\text{fab}}^{\text{fric}}$ must be less than or equal to 0.075. As $C_{\text{fab}-\text{fab}}^{\text{fric}}$ increases, wrinkles are inevitable for all values of $C_{\text{fab}-\text{dia}}^{\text{fric}}$ when $C_{\text{fab}-\text{fab}}^{\text{fric}}$ exceeds 0.20 for L3 and 0.175 for L4. This indicates that the occurrence of wrinkles is more sensitive to the fabric-fabric friction resistance than the fabric-diaphragm friction resistance in this case. As shown in Figure 6.11(a) and Figure 6.12(a), the area of the wrinkle-free region (dark blue) for L4 [-45°/+45°, 90°/0°] is smaller than the one for L3 [-45°/+45°, -75°/+15°], which suggests that the layup with a relative fibre angle of 45° at the ply interface is more likely to induce wrinkles. The influence of $C_{\text{fab}-\text{f}}^{\text{fric}}$ is likely to become more dominant as the number of plies and therefore ply interfaces increases within the layup.

A qualitative assessment of fibre lubrication was conducted experimentally to understand the influence of the reduced inter-ply coefficient of friction on the wrinkle pattern. Friction coefficients $C_{\text{fab}-\text{fab}}^{\text{fric}}$ and $C_{\text{fab}-\text{dia}}^{\text{fric}}$ were measured following liquid resin lubrication, as listed in Table 6.2. The corresponding combinations ($C_{\text{fab}-\text{fab}}^{\text{fric}}$, $C_{\text{fab}-\text{dia}}^{\text{fric}}$) are represented by Point E in Figure 6.11(a) and Figure 6.12(a), which falls in the wrinkle-free regions for both L3 and L4. Comparing the dry (non-lubricated) friction case for each layup (Point F) with the resin lubricated friction case (Point E), demonstrates that local resin lubrication could be a potential solution for mitigating wrinkles caused by interfacial interaction during multi-ply fabric forming.

6.5.3   Wrinkle mitigation validation

Layups L4 and L5 were experimentally formed (see Table 6.1) to validate the concept of applying the liquid resin as an inter-ply lubricant for wrinkle mitigation. L4 consists of two biaxial NCF plies, i.e. [-45°/+45°, 90°/0°], while the layup in case L5 is more generic, comprising four biaxial NCF plies laid up in a balanced symmetric sequence [0°/90°, +45°/-45°, -45°/+45°, 90°/0°].

Figure 6.13(a) shows a 3D scan of the uppermost surface of the consolidated part produced using layup L4 (i.e. [-45°/+45°, 90°/0°]), compared with the corresponding simulation result. The deviation distance is calculated by comparing the surface of the component against the tool surface, with the average thickness of the component deducted from the deviation distance to visualise any potential wrinkling defects. Results show that out-of-plane wrinkling has been successfully eliminated compared to the experimental scan for the same layup without liquid resin lubrication (see L4 in Figure 6.8(a)). A DDF simulation was performed using the friction coefficients measured with lubrication (see Table 6.1). As shown in Figure 6.13(b), the distribution of the predicted shear angles in each ply is similar to those predicted

for the same layup in Figure 6.9(a) without lubrication. However in contrast, the compressive strains in the fibre directions are alleviated by the lubrication effect, compared to the results for L4 without lubrication in Figure 6.9(b), due to the reduction in the interfacial friction.

(a)

(b)
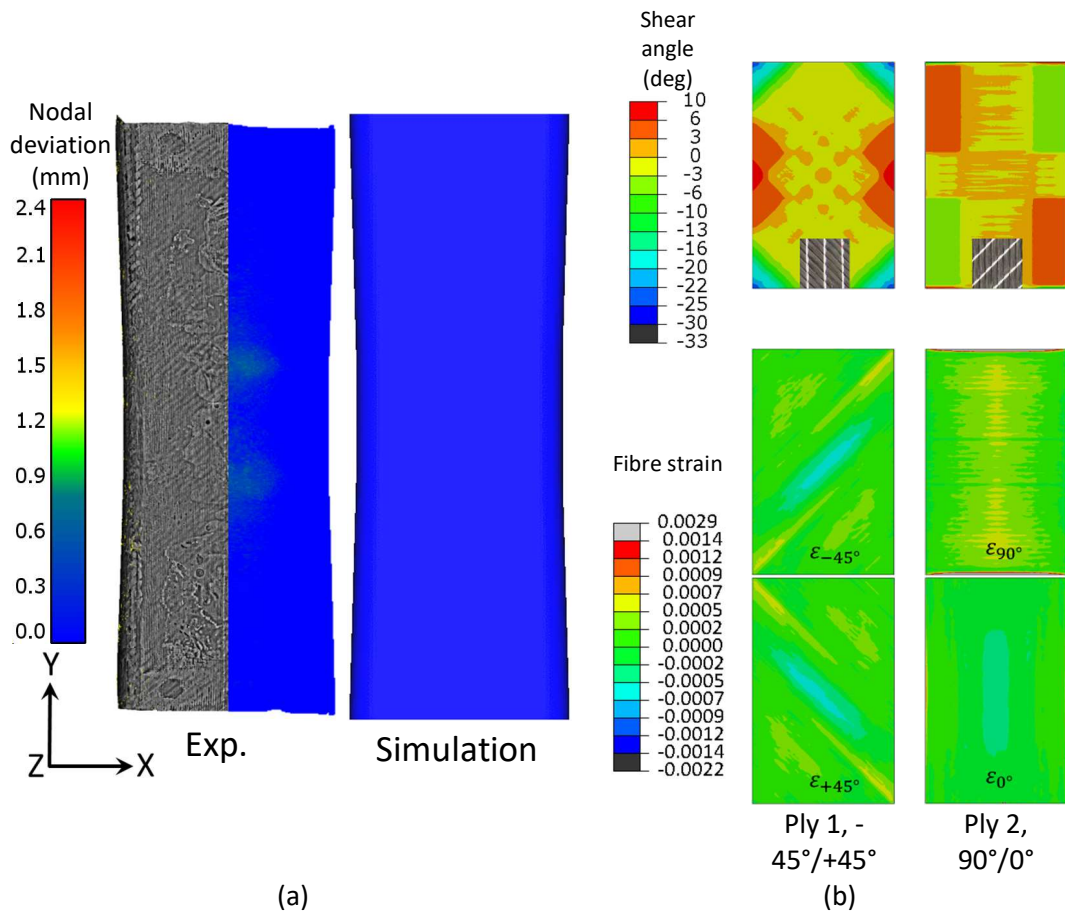
Figure 6.13: (a) Surface scan of the consolidated layup L4 [-45°/+45°, 90°/0°]. (b) Shear angle and fibre strains of individual plies within the layup predicted using the reduced inter-ply friction coefficients listed in Table 6.1

For the balanced symmetric layup L5 (i.e. [0°/90°, +45°/-45°, -45°/+45°, 90°/0°]), two curved wrinkles are observed near the central ramp area of the tool, which are similar in shape to those from the FE prediction, as shown in Figure 6.14(a). In the experiment, the two primary wrinkles are initiated at the edge fillet as the ply stack bends. As shown in Figure 6.14(b), Ply 1 and Ply 2 undergo very different shear deformations, which generates dissimilar slippage between fibres at the contact interface. This is also observed at the interface between Ply 3 and Ply 4.

(a)

Ply 1, 0°/90°   Ply 2, +45°/-45°   Ply 3, -45°/+45°   Ply 4, 90°/0°

(b)
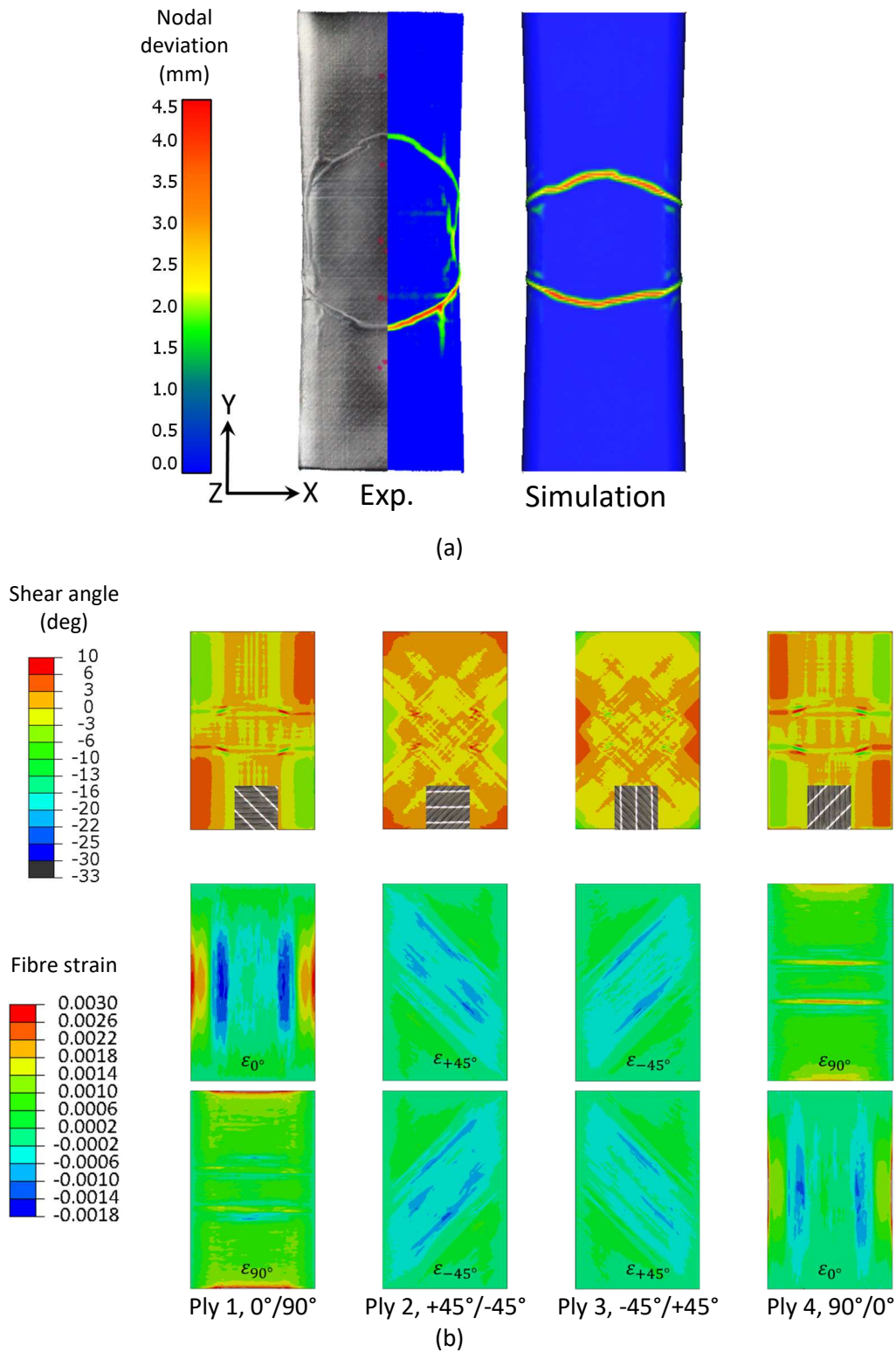
Figure 6.14: (a) Comparison of wrinkle patterns obtained from experiment and simulation for the layup L5 (i.e. [0°/90°, +45°/-45°]s) without lubrication. (b) Shear angle and fibre strains predicted by the FE model using friction coefficients of dry material interfaces listed in Table 6.1.

The predicted shear angles of the inner plies (Ply 2 and Ply 3) are similarly distributed but are opposite in sign. This indicates that the yarns in the contact pairing between Ply 2 and Ply 3 rotate in the same direction at each point in the contact region, as shown in the schematic in Figure 6.15. Thus, the relative movement of the yarns at the contact interface between Ply 2 and Ply 3 is negligible. Consequently, the compressive strains along the fibre directions in Figure 6.14(b) are caused by relative yarn rotation at the interfaces between Ply 1 and Ply 2 and between Ply 3 and Ply 4, where the relative fibre angle at both interfaces is 45°.

The prediction from the FE simulation for L5 produces a wrinkle pattern similar in shape, but the peak distance between the wrinkles is smaller in the longitudinal direction of the tool (Figure 6.14(a)). When the thickness of the fabric layup is considerably larger than that of the diaphragms, the fabric-fabric interaction becomes one of the dominant factors in defect formation during multi-ply forming. This reinforces the need for an anisotropic friction model to capture the complex inter-ply behaviour. The friction coefficient is dependent on the normal force applied during compaction, which will therefore be influenced by local variations in the through-thickness compaction pressure produced by the in-bag vacuum. This compaction may also influence the bending and shear stiffness of the fabric plies by increasing the inter-fibre friction [52, 56]. The material behaviour may need to be characterised in-situ within the diaphragms to take into account the effect of the vacuum pressure [52].
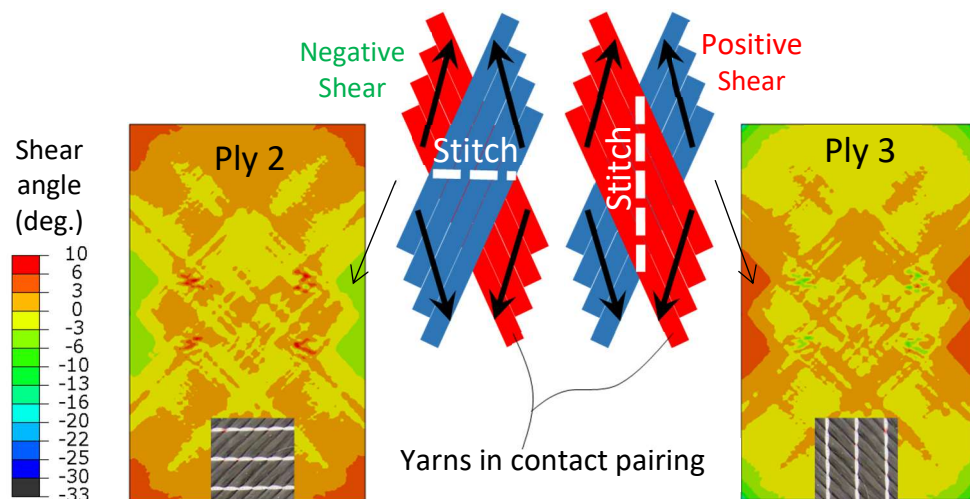
Figure 6.15: Schematic of yarn rotation for a local contact region at the interface between Ply 2 and Ply 3 in Figure 6.14(b).

Liquid resin was also used as a lubricant for layup L5 (see Table 6.1) and no wrinkles were observed on the corresponding consolidated component, as shown in Figure 6.16(a).

(a)

(b)
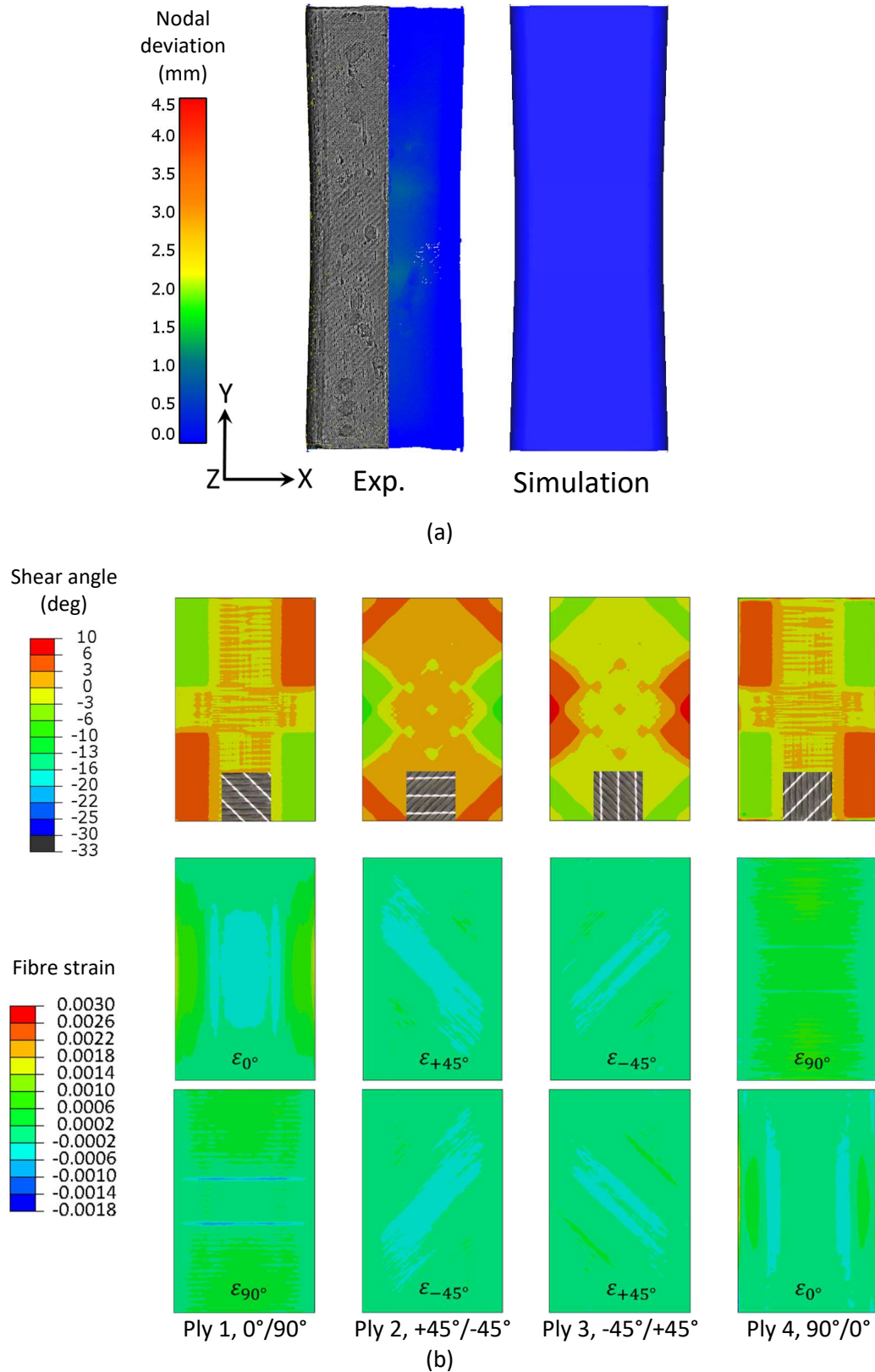
Figure 6.16: (a) Surface scan and nodal deviation distance of the consolidated layup L5 [0°/90°, +45°/-45°]s. (b) Shear angle and fibre strains of individual plies within the layup predicted using the reduced inter-ply friction coefficients listed in Table 6.1.

According to the simulation results, the fibre compressive strain (Figure 6.16(b)) has been significantly reduced by approximately 70% compared to the case without lubrication (see Figure 6.14(b)). This highlights the importance of reducing interfacial friction to mitigate wrinkles during multi-ply NCF forming.

6.6   Chapter summary

The forming of multiple NCF plies via DDF has been investigated, using a combination of experiments and numerical simulations. The influence of relative ply orientation and interfacial friction was investigated for a spar geometry to understand the mechanism of wrinkle formation. Simulation results show that dissimilar shear deformation between adjacent plies can cause relative sliding at the contact interface, leading to compressive stresses in fibres and consequently out-of-plane wrinkling.

A relative fibre angle of 45° at the ply interface was found to be undesirable in terms of the overall formed quality of multi-ply NCF preforms. A parametric study was performed to establish if the quality of the formed shape could be improved for layups containing relative fibre angles of 45° for adjacent plies, by controlling the coefficient of friction at the inter-ply interface. Results indicate that the severity of wrinkles is strongly affected by the the fabric-fabric friction resistance between the NCF plies, whereas the fabric-diaphragm friction appears to be less significant.

Experimental friction tests showed that fabric lubrication using liquid resin can result in a reduction in frictional force by over 64% for the NCF and diaphragm materials used. Using a liquid resin as a lubricant was identified to be an effective approach to eliminating macroscale wrinkles induced by excessive inter-ply siding.

Chapter 7   Conclusion

This thesis is primarily concerned with developing simulation tools for the prediction and evaluation of macroscopic defects found in biaxial fabrics, following the preforming stage during composites manufacturing. Double diaphragm forming (DDF) is the focus, as it enables the production of large components with lower capital investment and labour costs compared with press-based forming or hand-layup based autoclaving respectively.

The bending behaviour of biaxial fabrics was characterised and a macro-scale constitutive model was developed to facilitate the prediction and identification of forming related defects at the macro scale, in the form of wrinkles and bridging. A multi-resolution simulation approach was developed to enable efficient prediction for the macro-scale defects that occur in local regions of large-scale components. The defect formation mechanisms during multi-ply fabric forming have been investigated by simulation and experiments, with a practical solution proposed and validated for controlling macro-scale wrinkling. The conclusions are divided into four key areas according to the content of each chapter.

7.1   Fabric characterisation

Lateral fibre compaction, induced by excessive in-plane shear, is one of the primary causes for the formation of macroscale wrinkles during forming. This mechanism is particularly significant for DDF as the diaphragm assembly provides insufficient out-of-plane constraint to the fabric plies during forming, compared to using rigid blank holders in matched-tool forming. Whilst in-plane shear angle can be used to indicate the likelihood of defects qualitatively, incorporating the bending stiffness into the constitutive framework is vital for explicitly predicting the shape and number of wrinkles.

The picture frame test (PFT) was used to characterise the in-plane shear compliance for two biaxial fabrics (a twill weave woven fabric and a NCF with pillar stitches). Bias-extension testing (BET) was then employed to characterise the onset point of shear induced wrinkling for the two fabrics. The shear deformations induced during PFT and BET were compared for the NCF to demonstrate the limitation of the BET, as the presence of wrinkles in the central shear zone can misrepresent the measured shear force versus shear angle relationship.

Due to the constraints from the pillar stitches, the in-plane shear resistance of the NCF is significantly higher than that of the woven fabric. Consequently, shear induced wrinkling occurred at a small shear angle (~8°) for the NCF during the bias extension test, whereas the wrinkling in the woven fabric was initiated from a larger shear angle (~50°). The bias-

extension test was shown to be an effective way to determine the critical angle for shear-induced wrinkling, but it may not be suitable to produce uniform shearing in the central area of the NCF specimen, due to the presence of out-of-plane wrinkles and stitch failure causing fibre slippage. In comparison, the picture frame test was shown to be a more robust method for producing in-plane shear curves for the NCF.

The bending resistance of the two fabrics was characterised by different cantilever testing methods, with the results analysed to understand the limitation of the standard cantilever test.

i.   The balanced woven fabric exhibits identical bending stiffness along its warp and weft directions, whereas the bending stiffness of the NCF is dependent on the bending direction due to its asymmetric through-thickness fibre architecture. The standard cantilever test (BS EN ISO 9073-7: 1988) results in different bending stiffnesses measured at different bending deformations (i.e. angular deflections at 7.1° and 41.5°). The value measured at a large angular deflection (41.5°) can be up to 48% lower than the value measured at a smaller angular deflection (7.1°) for the fabrics studied. This indicated that the bending stiffnesses for these two fabrics were non-linear and dependent on the bending deformation.

ii.   A revised cantilever test was developed to characterise the non-linear relation between the bending moment and curvature for the biaxial fabrics, based on the deflection shape of the specimens captured using a Structured White Light Scanner. For the fabrics studied, the bending stiffness decreases as the specimen curvature increases. Compared to the initial bending stiffness at zero curvature, the ultimate bending stiffness at infinite curvature reduced by ~95% for the woven fabric and by ~98% for the NCF. Whilst fibre slippage was reported to be a cause for the reduction in fabric bending stiffness, fibre buckling was found to be another important mechanism leading to a significant reduction in the bending stiffness of the NCF specimen under large bending deformation.

7.2   Model development and validation

Fabric bending stiffness is typically dependent on the bending deformation, which can influence not only the onset, but also the growth of wrinkling defects in forming simulations. Furthermore, the change in fibre reorientation due to in-plane shear can also influence the bending resistance of biaxial fabrics during forming. A macroscale constitutive model has been developed by integrating the fibre-orientation dependent non-linear bending

behaviour into a non-orthogonal constitutive model, in order to simulate the forming behaviour of biaxial fabrics. Interpretation of the simulation results was also required to provide a metric for defect identification and evaluation. A strategy was therefore developed to quantify the severity of macroscale defects by post-processing the simulation results. Comparisons between simulation results and experimental data indicate:

  i.   The model can independently control the in-plane and out-of-plane stiffnesses of the fabric, enabling both the in-plane shear response and out of plane wrinkling behaviour to be precisely replicated during fabric forming.

 ii.   The non-linear bending model produced more realistic predictions for the fabric response during bending, with the error in the tip deflection being within 1% of the experimental data for the fabrics studied. In comparison, the bending deflection was under predicted by 18% for the NCF specimen and 4% for the woven fabric when using a constant bending stiffness measured from the standard cantilever test (BS EN ISO 9073-7: 1998).

iii.   Forming simulations using the constant bending stiffness tended to overestimate the internal bending moment along the fibre directions, leading to unrealistic wrinkle predictions. This highlighted the importance of using a non-linear bending stiffness versus curvature relationship for delivering realistic wrinkle predictions.

 iv.   The nodal distance between the deformed fabric mesh and the tool surface was shown to be an effective metric to locate macro-scale defects based on the simulation results, with the wrinkling defects isolated from areas of fabric bridging by the maximum principal curvature. In addition, the distribution of the maximum value of the principal curvatures was successfully used to identify the longitudinal direction of wrinkles.

7.3   Multi-resolution simulation

The developed fabric constitutive model was used to predict macroscale defects (i.e. wrinkles and bridging) that occur during DDF. Whilst a high-fidelity FE model is required to ensure features can be realistically replicated, it is typically impractical to use high-resolution finite element meshes to identify critical defects of small size relative to the preform scale, due to the computational cost. When producing preforms for large scale components with small double-curved features, defects are typically concentrated around these small local regions where large shear deformation or large amounts of material draw-in are required for plies to conform to the tool.

A multi-resolution simulation approach has been developed to reduce the run time required to predict the shape and size of surface visible defects during DDF, based on a two-stage global-to-local sub modelling strategy. The global model using a coarse membrane mesh (element edge length = 5mm) to rapidly locate areas containing potential macro-scale defects by employing an empirical defect criteria based on shear angle and out-of-plane nodal deviation. Local sub modelling using more refined shell elements successfully enabled wrinkles of amplitude ~ 1mm to be detected, by implementing the fabric bending properties into the simulation framework. The RMSE between the predicted wrinkle length and fabric bridging area was within 10% of the experimental data. The proposed multi-resolution modelling approach reduced the CPU time by ~87% compared to the full-scale high fidelity shell-element model. In the current work, around 34% of the ply area was considered to contain potential defects, with the maximum wrinkle length predicted to be within 17% of the length of the tool. The reduction in runtime will become more significant when the dimensions of local features on the tool surface become more localised compared to the overall length scale of components.

7.4   Defects formation and mitigation for multi-ply forming

Individual fabric plies are typically stacked according to specific layup sequences to meet stiffness and strength requirements, but this increases the risk of wrinkling as the forming deformation of each ply affects the deformation of adjacent plies. Multi-ply NCF forming behaviour in double diaphragm forming was investigated via experiments and simulations to enable a feasible solution for controlling the formation of macro-scale wrinkling. Simulation and experiment results show:

i.   When forming multi-ply fabric with different ply orientations, dissimilar shear deformation between plies was identified to be the primary cause for relative ply sliding at the interface, which can lead to compressive stresses in the fibres and consequently out-of-plane wrinkling. The severity of wrinkles was strongly affected by the the fabric-fabric friction resistance between the NCF plies, whereas the fabric-diaphragm friction appeared to be less significant.

ii.   A relative fibre angle of 45° at the ply interface was found to be undesirable in terms of the overall formability of multi-ply NCF preforms. Simulation results indicated that the quality of the formed shape can be improved by reducing the coefficient of friction at the contact interfaces.

iii.   Lubrication using liquid resin can reduce the inter-ply frictional force by over 64% for the NCF and diaphragm materials studied. This liquid resin lubrication was identified as an effective way to mitigate wrinkles during multi-ply NCF forming, in particular for quad-axial layups comprising 0°, 90° and ±45° fibre angles. This indicated that reducing inter-ply friction resistance was an effective approach to eliminating macroscale wrinkles induced by excessive inter-ply sliding.

Appendix A: List of publications

The following papers have been produced from this research.

Journal papers:

(1) Yu, F., S. Chen, J.V. Viisainen, M.P.F. Sutcliffe, L.T. Harper, and N.A. Warrior, *A macroscale finite element approach for simulating the bending behaviour of biaxial fabrics.* Composites Science and Technology, 2020. **191** DOI: 10.1016/j.compscitech.2020.108078.

(2) Yu, F., S. Chen, L.T. Harper, and N.A. Warrior, *Simulating the effect of fabric bending stiffness on the wrinkling behaviour of biaxial fabrics during preforming.* Composites Part A: Applied Science and Manufacturing, 2021: p. 106308 DOI: 10.1016/j.compositesa.2021.106308.

(3) Yu, F., S. Chen, L.T. Harper, and N.A. Warrior, *Double diaphragm forming simulation using a global-to-local modelling strategy for detailed defect detection in large structures.* Composites Part A: Applied Science and Manufacturing, 2021. **147**: p. 106457 DOI: 10.1016/j.compositesa.2021.106457.

(4) Yu, F., S. Chen, L.T. Harper, and N.A. Warrior, *Investigation into the effects of inter-ply sliding during double diaphragm forming for multi-layered biaxial non-crimp fabrics.* Composites Part A: Applied Science and Manufacturing, 2021. **150**: p. 106611 DOI: 10.1016/j.compositesa.2021.106611.

(5) S. Chen, A. Joesbury, Yu F., L.T. Harper, N.A. Warrior, *Optimisation of intra-ply stitch removal for improved formability of biaxial non-crimp fabrics.* Composites Part B: Engineering, 2022. **229**: p. 109464 DOI: 10.1016/j.compositesb.2021.109464.

References

[1]   Kaufmann, M., D. Zenkert, and P. Wennhage, *Integrated cost/weight optimization of aircraft structures.* Structural and Multidisciplinary Optimization, 2009. **41**(2): p. 325-334DOI: 10.1007/s00158-009-0413-1.

[2]   Timmis, A.J., A. Hodzic, L. Koh, M. Bonner, C. Soutis, A.W. Schäfer, and L. Dray, *Environmental impact assessment of aviation emission reduction through the implementation of composite materials.* The International Journal of Life Cycle Assessment, 2014. **20**(2): p. 233-243DOI: 10.1007/s11367-014-0824-0.

[3]   Rana, S. and R. Fangueiro, *1 - Advanced composites in aerospace engineering*, in *Advanced Composite Materials for Aerospace Engineering*, S. Rana and R. Fangueiro, Editors. 2016, Woodhead Publishing. p. 1-15.

[4]   Maria, M., *Advanced composite materials of the future in aerospace industry.* Incas Bulletin, 2013. **5**(3): p. 139-150DOI: 10.13111/2066-8201.2013.5.3.14.

[5]   Gardiner, G. *Injection-forming for high-performance, unitized thermoplastic structures.* 2019 Aug 24, 2021]; Available from: https://www.compositesworld.com/articles/injection-forming-for-high-performance-unitized-thermoplastic-structures.

[6]   Feraboli, P. and H. Kawakami, *Damage of Carbon/Epoxy Composite Plates Subjected to Mechanical Impact and Simulated Lightning.* Journal of Aircraft, 2010. **47**(3): p. 999-1012DOI: 10.2514/1.46486.

[7]   Wu, Z., X. Wang, K. Iwashita, T. Sasaki, and Y. Hamaguchi, *Tensile fatigue behaviour of FRP and hybrid FRP sheets.* Composites Part B: Engineering, 2010. **41**(5): p. 396-402DOI: 10.1016/j.compositesb.2010.02.001.

[8]   Jacob, A., *Carbon fibre and cars – 2013 in review.* Reinforced Plastics, 2014. **58**(1): p. 18-19DOI: 10.1016/s0034-3617(14)70036-0.

[9]   Roquette, D., F. Meyer, and L. Herbeck, *High Volume Manufacturing of Carbon Fiber Reinforced Plastics for Body in White*, in *Conference Materialien des Karosseriebaus 2017*. 2017: Bad Nauheim.

[10]   *Carbon Core - die neue BMW 7er Karosserie. Karosseriebautage Hamburg 2016*. in *14th ATZ Conference*. 2016. Wiesbaden: Springer Vieweg.

[11]   Aliyeva, N., H.S. Sas, and B. Saner Okan, *Recent developments on the overmolding process for the fabrication of thermoset and thermoplastic composites by the integration of nano/micron-scale reinforcements.* Composites Part A: Applied Science and Manufacturing, 2021. **149**: p. 106525DOI: 10.1016/j.compositesa.2021.106525.

[12]   Rosenthal, S., F. Maaß, M. Kamaliev, M. Hahn, S. Gies, and A.E. Tekkaya, *Lightweight in Automotive Components by Forming Technology.* Automotive Innovation, 2020. **3**(3): p. 195-209DOI: 10.1007/s42154-020-00103-3.

[13]   Tri-Mack. *Tri-Mack's latest hybrid molding processes combine thermoplastic composites with injection molding to capture the key advantages of both*. 2021 24 Aug, 2021]; Available from: http://www.trimack.com/hybrid-molding.

[14]   Zhang, J., V.S. Chevali, H. Wang, and C.-H. Wang, *Current status of carbon fibre and carbon fibre composites recycling.* Composites Part B: Engineering, 2020. **193**: p. 108053DOI: 10.1016/j.compositesb.2020.108053.

[15]   Katsiropoulos, C.V., A. Loukopoulos, and S.G. Pantelakis, *Comparative Environmental and Cost Analysis of Alternative Production Scenarios Associated with a Helicopter's Canopy.* Aerospace, 2019. **6**(1): p. 3DOI: 10.3390/aerospace6010003.

[16]   Xie, N., R.A. Smith, S. Mukhopadhyay, and S.R. Hallett, *A numerical study on the influence of composite wrinkle defect geometry on compressive strength.* Materials & Design, 2018. **140**: p. 7-20DOI: 10.1016/j.matdes.2017.11.034.

[17]   Shih, C.-H. and L.J. Lee, *Tackification of Textile Fiber Preforms in Resin Transfer Molding.* Journal of Composite Materials, 2001. **35**(21): p. 1954-1981DOI: 10.1177/002199801772661452.

[18]   Yoo, H.M., J.W. Lee, J.S. Kim, and M.K. Um, *Influence of Non-Reactive Epoxy Binder on the Permeability and Friction Coefficient of Twill-Woven Carbon Fabric in the Liquid Composite Molding Process.* Applied Sciences, 2020. **10**(20): p. 7039DOI: 10.3390/app10207039.

[19]   Gardiner, G. *HP-RTM on the rise*. 2015   26 Aug, 2021]; Available from: https://www.compositesworld.com/articles/hp-rtm-on-the-rise.

[20]   Hsiao, H.M. and I.M. Daniel, *Effect of fiber waviness on stiffness and strength reduction of unidirectional composites under compressive loading.* Composites Science and Technology, 1996. **56**(5): p. 581-593.

[21]   Chen, S., O.P.L. McGregor, A. Endruweit, M.T. Elsmore, D.S.A. De Focatiis, L.T. Harper, and N.A. Warrior, *Double diaphragm forming simulation for complex composite structures.* Composites Part A: Applied Science and Manufacturing, 2017. **95**: p. 346-358DOI: 10.1016/j.compositesa.2017.01.017.

[22]   Long, A.C., *Introduction*, in *Design and Manufacture of Textile Composites*, A.C. Long, Editor. 2005, Woodhead Publishing. p. xiii-xvi.

[23]   Lomov, S., *Introduction*, in *Non-Crimp Fabric Composites*, S.V. Lomov, Editor. 2011, Woodhead Publishing. p. xvi-xix.

[24]   Akkerman, R. and S.P. Haanappel, *6 - Thermoplastic composites manufacturing by thermoforming*, in *Advances in Composites Manufacturing and Process Design*, P. Boisse, Editor. 2015, Woodhead Publishing. p. 111-129.

[25]   Farboodmanesh, S., J. Chen, Z. Tao, J. Mead, and H. Zhang, *Base fabrics and their interaction in coated fabrics.* 2019: p. 47-95DOI: 10.1016/b978-0-08-102428-7.00003-1.

[26]   Schnabel, A. and T. Gries, *1 - Production of non-crimp fabrics for composites*, in *Non-Crimp Fabric Composites*, S.V. Lomov, Editor. 2011, Woodhead Publishing. p. 3-41.

[27]   Schirmaier, F.J., D. Dörr, F. Henning, and L. Kärger, *A macroscopic approach to simulate the forming behaviour of stitched unidirectional non-crimp fabrics (UD-NCF).* Composites Part A: Applied Science and Manufacturing, 2017. **102**: p. 322-335DOI: 10.1016/j.compositesa.2017.08.009.

[28]   Truong, T.C., M. Vettori, S. Lomov, and I. Verpoest, *Carbon composites based on multi-axial multi-ply stitched preforms. Part 4. Mechanical properties of composites and damage observation.* Composites Part A: Applied Science and Manufacturing, 2005. **36**(9): p. 1207-1221DOI: 10.1016/j.compositesa.2005.02.004.

[29]   Arnold, S.E., M.P.F. Sutcliffe, and W.L.A. Oram, *Experimental measurement of wrinkle formation during draping of non-crimp fabric.* Composites Part A: Applied Science and Manufacturing, 2016. **82**: p. 159-169DOI: 10.1016/j.compositesa.2015.12.011.

[30]   Chen, S., O.P.L. McGregor, L.T. Harper, A. Endruweit, and N.A. Warrior, *Defect formation during preforming of a bi-axial non-crimp fabric with a pillar stitch pattern.* Composites Part A: Applied Science and Manufacturing, 2016. **91**: p. 156-167DOI: 10.1016/j.compositesa.2016.09.016.

[31]   Lee, J.S., S.J. Hong, W.-R. Yu, and T.J. Kang, *The effect of blank holder force on the stamp forming behavior of non-crimp fabric with a chain stitch.* Composites Science and Technology, 2007. **67**(3-4): p. 357-366DOI: 10.1016/j.compscitech.2006.09.009.

[32]   Habboush, A., N. Sanbhal, H. Shao, J. Jiang, and N. Chen, *Characterization and Analysis of In-Plane Shear Behavior of Glass Warp-Knitted Non-Crimp Fabrics Based on Picture Frame Method.* Materials (Basel), 2018. **11**(9)DOI: 10.3390/ma11091550.

[33]   Elkington, M., C. Ward, A. Kirby, M. Libby, and N. Gandhi. *Collaborative human-robotic layup*. in *Composites Advanced Manufacturing Exposition 2017*. 2017.

[34]   Hwang, S.-F. and K.-J. Hwang, *Stamp forming of locally heated thermoplastic composites.* Composites Part A: Applied Science and Manufacturing, 2002. **33**(5): p. 669-676DOI: https://doi.org/10.1016/S1359-835X(02)00004-0.

[35]   Harrison, P., R. Gomes, and N. Curado-Correia, *Press forming a 0/90 cross-ply advanced thermoplastic composite using the double-dome benchmark geometry.* Composites Part A: Applied Science and Manufacturing, 2013. **54**: p. 56-69DOI: 10.1016/j.compositesa.2013.06.014.

[36]   Perry, J. *How an i3 is born*. 2014   28 Aug, 2021]; Available from: https://www.automotivemanufacturingsolutions.com/how-an-i3-is-born/33285.article.

[37]   Baran, E. and R. Brooks. *High-Speed, High-Volume, High-Definition Composite Forming*.   2015   31   Aug,   2021];   Available   from: https://www.forgingmagazine.com/picture-this/media-gallery/21923789/highspeed-highvolume-highdefinition-composite-forming.

[38]   Chen, S., *Fabric forming simulation and process optimisation for composites*. 2016, University of Nottingham: Nottingham, UK.

[39]   Langlois, G., *Diaphragm Forming: Innovation and Application to Ocean Engineering*, in *Department of Ocean Engineering*. 1994, Massachusetts Institute of Technology: Cambridge, Massachusetts.

[40]   Krebs, J., K. Friedrich, and D. Bhattacharyya, *A direct comparison of matched-die versus diaphragm forming.* Composites Part A: Applied Science and Manufacturing, 1998. **29**(1): p. 183-188DOI: https://doi.org/10.1016/S1359-835X(97)82706-6.

[41]   Bersee, H.E.N. and A. Beukers, *Diaphragm forming of continuous fibre reinforced thermoplastics: influence of temperature, pressure and forming velocity on the forming of Upilex-R® diaphragms.* Composites Part A: Applied Science and Manufacturing, 2002. **33**(7): p. 949-958DOI: https://doi.org/10.1016/S1359-835X(02)00037-4.

[42]   Friedrich, K., M. Hou, and J. Krebs, *Chapter 4 Thermoforming of continuous fibre/thermoplastic composite sheets*, in *Composite Materials Series*, D. Bhattacharyya, Editor. 1997, Elsevier. p. 91-162.

[43]   Pantelakis, S.G. and E.A. Baxevani, *Optimization of the diaphragm forming process with regard to product quality and cost.* Composites Part A: Applied Science and Manufacturing, 2002. **33**(4): p. 459-470DOI: https://doi.org/10.1016/S1359-835X(01)00147-6.

[44]   Truslow, S.B., *Permanent Press, No Wrinkles: Reinforced Double Diaphragm Forming of Advanced Thermoset Composites*, in *Mechanical Engineering*. 2000, Massachusetts Institute of Technology: Cambridge, Massachusetts.

[45]   Sun, J., Y. Gu, M. Li, X. Ma, and Z. Zhang, *Effect of forming temperature on the quality of hot diaphragm formed C-shaped thermosetting composite laminates.* Journal of Reinforced Plastics and Composites, 2012. **31**(16): p. 1074-1087DOI: 10.1177/0731684412453778.

[46]   Bian, X.X., Y.Z. Gu, J. Sun, M. Li, W.P. Liu, and Z.G. Zhang, *Effects of Processing Parameters on the Forming Quality of C-Shaped Thermosetting Composite Laminates in Hot Diaphragm Forming Process.* Applied Composite Materials, 2013. **20**(5): p. 927-945DOI: 10.1007/s10443-012-9310-7.

[47]   Hallander, P., M. Akermo, C. Mattei, M. Petersson, and T. Nyman, *An experimental study of mechanisms behind wrinkle development during forming of composite laminates.* Composites Part A: Applied Science and Manufacturing, 2013. **50**: p. 54-64DOI: 10.1016/j.compositesa.2013.03.013.

[48]   Dumont, F. and C. Weimer, *19 - Non-crimp fabric: preforming analysis for helicopter applications*, in *Non-Crimp Fabric Composites*, S.V. Lomov, Editor. 2011, Woodhead Publishing. p. 449-460.

[49]   Margossian, A., S. Bel, J.M. Balvers, D. Leutz, R. Freitas, and R. Hinterhoelzl, *Finite element forming simulation of locally stitched non-crimp fabrics.* Composites Part A: Applied Science and Manufacturing, 2014. **61**: p. 152-162DOI: 10.1016/j.compositesa.2014.02.020.

[50]   McGregor, O., S. Chen, L. Harper, A. Endruweit, and N. Warrior. *Defect reduction in the double diaphragm forming process*. in *21st International Conference on Composite Materials*. 2017. Xi'an.

[51]   Yu, X., L. Ye, Y.-W. Mai, B. Cartwright, D. McGuckin, and R. Paton, *Finite element simulations of the doublediaphragm forming process.* Revue Européenne des Éléments Finis, 2012. **14**(6-7): p. 633-651DOI: 10.3166/reef.14.633-651.

[52]   Alshahrani, H. and M. Hojjati, *Influence of double-diaphragm vacuum compaction on deformation during forming of composite prepregs.* Journal of Science: Advanced Materials and Devices, 2016. **1**(4): p. 507-511DOI: 10.1016/j.jsamd.2016.09.003.

[53]   Griffiths, B. *Composite wing spars carry the enormous turboprop engines*. 2010 31 Aug, 2021]; Available from: https://www.compositesworld.com/articles/composite-wing-spars-carry-the-western-worlds-biggest-turboprop-engines.

[54]   Lomov, S.V., *6 - Deformability of textile performs in the manufacture of non-crimp fabric composites*, in *Non-Crimp Fabric Composites*, S.V. Lomov, Editor. 2011, Woodhead Publishing. p. 117-144e.

[55]   Long, A.C., P. Boisse, and F. Robitaille, *2 - Mechanical analysis of textiles*, in *Design and Manufacture of Textile Composites*, A.C. Long, Editor. 2005, Woodhead Publishing. p. 62-109.

[56]   Liang, B., J. Colmars, and P. Boisse, *A shell formulation for fibrous reinforcement forming simulations.* Composites Part A: Applied Science and Manufacturing, 2017. **100**: p. 81-96DOI: 10.1016/j.compositesa.2017.04.024.

[57]   Boisse, P., J. Colmars, N. Hamila, N. Naouar, and Q. Steer, *Bending and wrinkling of composite fiber preforms and prepregs. A review and new developments in the draping simulations.* Composites Part B: Engineering, 2018. **141**: p. 234-249DOI: 10.1016/j.compositesb.2017.12.061.

[58]   Farnand, K., N. Zobeiry, A. Poursartip, and G. Fernlund, *Micro-level mechanisms of fiber waviness and wrinkling during hot drape forming of unidirectional prepreg composites.* Composites Part A: Applied Science and Manufacturing, 2017. **103**: p. 168-177DOI: 10.1016/j.compositesa.2017.10.008.

[59]   Guzman-Maldonado, E., P. Wang, N. Hamila, and P. Boisse, *Experimental and numerical analysis of wrinkling during forming of multi-layered textile composites.* Composite Structures, 2019. **208**: p. 213-223DOI: 10.1016/j.compstruct.2018.10.018.

[60]   Launay, J., G. Hivet, A.V. Duong, and P. Boisse, *Experimental analysis of the influence of tensions on in plane shear behaviour of woven composite reinforcements.* Composites Science and Technology, 2008. **68**(2): p. 506-515DOI: 10.1016/j.compscitech.2007.06.021.

[61]   Prodromou, A.G. and J. Chen, *On the relationship between shear angle and wrinkling of textile composite preforms.* Composites Part A: Applied Science and Manufacturing, 1997. **28**(5): p. 491-503.

[62]   Zhu, B., T. Yu, and X. Tao, *An experimental study of in-plane large shear deformation of woven fabric composite.* Composites Science and Technology, 2007. **67**(2): p. 252-261DOI: 10.1016/j.compscitech.2006.08.011.

[63]   Long, A.C., C.D. Rudd, M. Blagdon, and P. Smith, *Characterizing the processing and performance of aligned reinforcements during preform manufacture.* Composites

Part A: Applied Science and Manufacturing, 1996. **27**(4): p. 247-253DOI: https://doi.org/10.1016/1359-835X(95)00051-3.

[64]   Lin, H., J. Wang, A.C. Long, M.J. Clifford, and P. Harrison, *Predictive modelling for optimization of textile composite forming.* Composites Science and Technology, 2007. **67**(15-16): p. 3242-3252DOI: 10.1016/j.compscitech.2007.03.040.

[65]   Chen, S., L.T. Harper, A. Endruweit, and N.A. Warrior, *Formability optimisation of fabric preforms by controlling material draw-in through in-plane constraints.* Composites Part A: Applied Science and Manufacturing, 2015. **76**: p. 10-19DOI: 10.1016/j.compositesa.2015.05.006.

[66]   Chen, S., A. Endruweit, L.T. Harper, and N.A. Warrior, *Inter-ply stitching optimisation of highly drapeable multi-ply preforms.* Composites Part A: Applied Science and Manufacturing, 2015. **71**: p. 144-156DOI: 10.1016/j.compositesa.2015.01.016.

[67]   Harrison, P., F. Abdiwi, Z. Guo, P. Potluri, and W.R. Yu, *Characterising the shear–tension coupling and wrinkling behaviour of woven engineering fabrics.* Composites Part A: Applied Science and Manufacturing, 2012. **43**(6): p. 903-914DOI: 10.1016/j.compositesa.2012.01.024.

[68]   Hosseinia, A., M.H. Kashani, F. Sassani, A.S. Milani, and F.K. Ko, *Identifying the distinct shear wrinkling behavior of woven composite preforms under bias extension and picture frame tests.* Composite Structures, 2018. **185**: p. 764–773DOI: 10.1016/j.compstruct.2017.11.033.

[69]   Krishnappa, L., J.-H. Ohlendorf, M. Brink, and K.-D. Thoben, *Investigating the factors influencing the shear behaviour of 0/90∘ non-crimp fabrics to form a reference shear test.* Journal of Composite Materials, 2021: p. 0021998321991625DOI: 10.1177/0021998321991625.

[70]   Lomov, S.V., M. Barburski, T. Stoilova, I. Verpoest, R. Akkerman, R. Loendersloot, and R.H.W.t. Thije, *Carbon composites based on multiaxial multiply stitched preforms. Part 3: Biaxial tension, picture frame and compression tests of the preforms.* Composites Part A: Applied Science and Manufacturing, 2005. **36**(9): p. 1188-1206DOI: 10.1016/j.compositesa.2005.01.015.

[71]   Creech, G. and A.K. Pickett, *Meso-modelling of Non-Crimp Fabric composites for coupled drape and failure analysis.* Journal of Materials Science, 2006. **41**(20): p. 6725-6736DOI: 10.1007/s10853-006-0213-6.

[72]   Krieger, H., T. Gries, and S.E. Stapleton, *Shear and drape behavior of non-crimp fabrics based on stitching geometry.* International Journal of Material Forming, 2017DOI: 10.1007/s12289-017-1368-1.

[73]   Boisse, P., M. Borr, K. Buet, and A. Cherouat, *Finite element simulations of textile composite forming including the biaxial fabric behaviour.* Composites Part B-Engineering, 1997. **28**(4): p. 453-464DOI: Doi 10.1016/S1359-8368(96)00067-4.

[74]   Long, A.C. and M.J. Clifford, *1 - Composite forming mechanisms and materials characterisation*, in *Composites Forming Technologies*, A.C. Long, Editor. 2007, Woodhead Publishing. p. 1-21.

[75]   Boisse, P., A. Gasser, and G. Hivet, *Analyses of fabric tensile behaviour: determination of the biaxial tension–strain surfaces and their use in forming simulations.* Composites Part A: Applied Science and Manufacturing, 2001. **32**(10): p. 1395-1414DOI: https://doi.org/10.1016/S1359-835X(01)00039-2.

[76]   Ghosh, T.K., S.K. Batra, and R.L. Barker, *The Bending Behaviour of Plain-woven Fabrics Part I: A Critical Review.* Journal of the Textile Institute, 1990. **81**(3): p. 245-254DOI: 10.1080/00405009008658708.

[77]   Yu, W.R., M. Zampaloni, F. Pourboghrat, K. Chung, and T.J. Kang, *Analysis of flexible bending behavior of woven preform using non-orthogonal constitutive equation.*

Composites Part A: Applied Science and Manufacturing, 2005. **36**(6): p. 839-850DOI: 10.1016/j.compositesa.2004.10.026.

[78]   Jiang, Y., J. Hu, and F. Ko, *Characterizing and Modeling Bending Properties of Multiaxial Warp Knitted Fabrics.* Textile Research Journal, 1999. **69**(9): p. 691-697DOI: 10.1177/004051759906900910.

[79]   Cooper, D.N.E., *24—the Stiffness of Woven Textiles.* Journal of the Textile Institute Transactions, 1960. **51**(8): p. T317-T335DOI: 10.1080/19447026008659775.

[80]   Harrison, P., M.F. Alvarez, and D. Anderson, *Towards comprehensive characterisation and modelling of the forming and wrinkling mechanics of engineering fabrics.* International Journal of Solids and Structures, 2017DOI: 10.1016/j.ijsolstr.2016.11.008.

[81]   Döbrich, O., T. Gereke, O. Diestel, S. Krzywinski, and C. Cherif, *Decoupling the bending behavior and the membrane properties of finite shell elements for a correct description of the mechanical behavior of textiles with a laminate formulation.* Journal of Industrial Textiles, 2013. **44**(1): p. 70-84DOI: 10.1177/1528083713477442.

[82]   de Bilbao, E., D. Soulat, G. Hivet, and A. Gasser, *Experimental Study of Bending Behaviour of Reinforcements.* Experimental Mechanics, 2009. **50**(3): p. 333-351DOI: 10.1007/s11340-009-9234-9.

[83]   Liang, B., N. Hamila, M. Peillon, and P. Boisse, *Analysis of thermoplastic prepreg bending stiffness during manufacturing and of its influence on wrinkling simulations.* Composites Part A: Applied Science and Manufacturing, 2014. **67**: p. 111-122DOI: 10.1016/j.compositesa.2014.08.020.

[84]   Alshahrani, H. and M. Hojjati, *A new test method for the characterization of the bending behavior of textile prepregs.* Composites Part A: Applied Science and Manufacturing, 2017. **97**: p. 128-140DOI: 10.1016/j.compositesa.2017.02.027.

[85]   Potluri, P. and J. Atkinson, *Automated manufacture of composites: handling, measurement of properties and lay-up simulations.* Composites Part A: Applied Science and Manufacturing, 2003. **34**(6): p. 493-501DOI: 10.1016/s1359-835x(03)00056-3.

[86]   Lomov, S.V., I. Verpoest, M. Barburski, and J. Laperre, *Carbon composites based on multiaxial multiply stitched preforms. Part 2. KES-F characterisation of the deformability of the preforms at low loads.* Composites Part A: Applied Science and Manufacturing, 2003. **34**(4): p. 359-370DOI: 10.1016/s1359-835x(03)00025-3.

[87]   Syerko, E., S. Comas-Cardona, and C. Binetruy, *Models of mechanical properties/behavior of dry fibrous materials at various scales in bending and tension: A review.* Composites Part A: Applied Science and Manufacturing, 2012. **43**(8): p. 1365-1388DOI: 10.1016/j.compositesa.2012.03.012.

[88]   NgoNgoc, C., P. Bruniaux, and J.M. Castelain. *Modelling friction for yarn/fabric simulation: Application to bending hysteresis.* in *14th European simulation symposium*. 2002. Dresden, Germany.

[89]   Abdul Ghafour, T., J. Colmars, and P. Boisse, *The importance of taking into account behavior irreversibilities when simulating the forming of textile composite reinforcements.* Composites Part A: Applied Science and Manufacturing, 2019. **127**DOI: 10.1016/j.compositesa.2019.105641.

[90]   Nosrat Nezami, F., T. Gereke, and C. Cherif, *Analyses of interaction mechanisms during forming of multilayer carbon woven fabrics for composite applications.* Composites Part A: Applied Science and Manufacturing, 2016. **84**: p. 406-416DOI: 10.1016/j.compositesa.2016.02.023.

[91]   Avgoulas, E.I., D.M. Mulvihill, A. Endruweit, M.P.F. Sutcliffe, N.A. Warrior, D.S.A. De Focatiis, and A.C. Long, *Frictional behaviour of non-crimp fabrics (NCFs) in contact*

with a forming tool. Tribology International, 2018. **121**: p. 71-77DOI: 10.1016/j.triboint.2018.01.026.

[92]　Allaoui, S., C. Cellard, and G. Hivet, *Effect of inter-ply sliding on the quality of multilayer interlock dry fabric preforms.* Composites Part A: Applied Science and Manufacturing, 2015. **68**: p. 336-345DOI: 10.1016/j.compositesa.2014.10.017.

[93]　Zhao, Y., T. Zhang, H. Li, and B. Zhang, *Characterization of prepreg-prepreg and prepreg-tool friction for unidirectional carbon fiber/epoxy prepreg during hot diaphragm forming process.* Polymer Testing, 2020. **84**: p. 106440DOI: 10.1016/j.polymertesting.2020.106440.

[94]　Sjölander, J., P. Hallander, and M. Åkermo, *Forming induced wrinkling of composite laminates: A numerical study on wrinkling mechanisms.* Composites Part A: Applied Science and Manufacturing, 2016. **81**: p. 41-51DOI: 10.1016/j.compositesa.2015.10.012.

[95]　Potter, K., B. Khan, M. Wisnom, T. Bell, and J. Stevens, *Variability, fibre waviness and misalignment in the determination of the properties of composite materials and structures.* Composites Part A: Applied Science and Manufacturing, 2008. **39**(9): p. 1343-1354DOI: 10.1016/j.compositesa.2008.04.016.

[96]　Bloom, L.D., J. Wang, and K.D. Potter, *Damage progression and defect sensitivity: An experimental study of representative wrinkles in tension.* Composites Part B: Engineering, 2013. **45**(1): p. 449-458DOI: 10.1016/j.compositesb.2012.05.021.

[97]　Boisse, P., N. Hamila, E. Vidal-Sallé, and F. Dumont, *Simulation of wrinkling during textile composite reinforcement forming. Influence of tensile, in-plane shear and bending stiffnesses.* Composites Science and Technology, 2011. **71**(5): p. 683-692DOI: 10.1016/j.compscitech.2011.01.011.

[98]　Viisainen, J.V., A. Hosseini, and M.P.F. Sutcliffe, *Experimental investigation, using 3D digital image correlation, into the effect of component geometry on the wrinkling behaviour and the wrinkling mechanisms of a biaxial NCF during preforming.* Composites Part A: Applied Science and Manufacturing, 2021. **142**: p. 106248DOI: 10.1016/j.compositesa.2020.106248.

[99]　Alshahrani, H. and M. Hojjati, *Optimum processing parameters for hot drape forming of out-of-autoclave prepreg over complex shape using a double diaphragm technique*, in *20th International Conference on Composite Materials*. 2015: Copenhagen.

[100]　Alshahrani, H. and M. Hojjati, *Experimental and numerical investigations on formability of out-of-autoclave thermoset prepreg using a double diaphragm process.* Composites Part A: Applied Science and Manufacturing, 2017. **101**: p. 199-214DOI: 10.1016/j.compositesa.2017.06.021.

[101]　Chen, S., O.P.L. McGregor, L.T. Harper, A. Endruweit, and N.A. Warrior, *Optimisation of local in-plane constraining forces in double diaphragm forming.* Composite Structures, 2018. **201**: p. 570-581DOI: 10.1016/j.compstruct.2018.06.062.

[102]　Harrison, P., E. Taylor, and J. Alsayednoor, *Improving the accuracy of the uniaxial bias extension test on engineering fabrics using a simple wrinkle mitigation technique.* Composites Part A: Applied Science and Manufacturing, 2018. **108**: p. 53-61DOI: 10.1016/j.compositesa.2018.02.025.

[103]　HEXAGON. *https://www.hexagonmi.com/products/profile-and-surface-measurement/apodius-vision-system-3d*. 2021 [cited 2021 23 March].

[104]　Cao, J., R. Akkerman, P. Boisse, J. Chen, H.S. Cheng, E.F. de Graaf, J.L. Gorczyca, P. Harrison, G. Hivet, J. Launay, W. Lee, L. Liu, S.V. Lomov, A. Long, E. de Luycker, F. Morestin, J. Padvoiskis, X.Q. Peng, J. Sherwood, T. Stoilova, X.M. Tao, I. Verpoest, A. Willems, J. Wiggers, T.X. Yu, and B. Zhu, *Characterization of mechanical behavior of woven fabrics: Experimental methods and benchmark results.* Composites Part A:

Applied Science and Manufacturing, 2008. **39**(6): p. 1037-1053DOI: 10.1016/j.compositesa.2008.02.016.

[105]   Gong, Y., Z. Song, H. Ning, N. Hu, X. Peng, X. Wu, R. Zou, F. Liu, S. Weng, and Q. Liu, *A comprehensive review of characterization and simulation methods for thermo-stamping of 2D woven fabric reinforced thermoplastics.* Composites Part B: Engineering, 2020. **203**: p. 108462DOI: 10.1016/j.compositesb.2020.108462.

[106]   Badel, P., S. Gauthier, E. Vidal-Sallé, and P. Boisse, *Rate constitutive equations for computational analyses of textile composite reinforcement mechanical behaviour during forming.* Composites Part A: Applied Science and Manufacturing, 2009. **40**(8): p. 997-1007DOI: 10.1016/j.compositesa.2008.04.015.

[107]   Han, M.-G. and S.-H. Chang, *Draping simulation of carbon/epoxy plain weave fabrics with non-orthogonal constitutive model and material behavior analysis of the cured structure.* Composites Part A: Applied Science and Manufacturing, 2018. **110**: p. 172-182DOI: 10.1016/j.compositesa.2018.04.022.

[108]   Harrison, P., *Modelling the forming mechanics of engineering fabrics using a mutually constrained pantographic beam and membrane mesh.* Composites Part A: Applied Science and Manufacturing, 2016. **81**: p. 145-157DOI: 10.1016/j.compositesa.2015.11.005.

[109]   Yu, W.-R., P. Harrison, and A. Long, *Finite element forming simulation for non-crimp fabrics using a non-orthogonal constitutive equation.* Composites Part A: Applied Science and Manufacturing, 2005. **36**(8): p. 1079-1093DOI: 10.1016/j.compositesa.2005.01.007.

[110]   *Abaqus 2018. Abaqus analysis user's manual.*

[111]   Khan, M.A., *Numerical and experimental forming analyses of textile composite reiforcements based on a hypoelastic behaviour*, in *LaMCoS - Laboratoire de Mécanique des Contacts et des Structures*. 2010, Institut national des sciences appliquées, Lyon: France.

[112]   Harrison, P., M.J. Clifford, and A.C. Long, *Shear characterisation of viscous woven textile composites: a comparison between picture frame and bias extension experiments.* Composites Science and Technology, 2004. **64**(10-11): p. 1453-1465DOI: 10.1016/j.compscitech.2003.10.015.

[113]   Peng, X.Q., J. Cao, J. Chen, P. Xue, D.S. Lussier, and L. Liu, *Experimental and numerical analysis on normalization of picture frame tests for composite materials.* Composites Science and Technology, 2004. **64**(1): p. 11-21DOI: 10.1016/s0266-3538(03)00202-1.

[114]   Lebrun, G., M.N. Bureau, and J. Denault, *Evaluation of bias-extension and picture-frame test methods for the measurement of intraply shear properties of PP/glass commingled fabrics.* Composite Structures, 2003. **61**(4): p. 341-352DOI: https://doi.org/10.1016/S0263-8223(03)00057-6.

[115]   Harrison, P., J. Wiggers, and A.C. Long, *Normalization of Shear Test Data for Rate-independent Compressible Fabrics.* Journal of Composite Materials, 2008. **42**(22): p. 2315-2344DOI: 10.1177/0021998308095367.

[116]   Boisse, P., N. Hamila, E. Guzman-Maldonado, A. Madeo, G. Hivet, and F. dell'Isola, *The bias-extension test for the analysis of in-plane shear properties of textile composite reinforcements and prepregs: a review.* International Journal of Material Forming, 2016. **10**(4): p. 473-492DOI: 10.1007/s12289-016-1294-7.

[117]   Alsayednoor, J., F. Lennard, W.R. Yu, and P. Harrison, *Influence of specimen pre-shear and wrinkling on the accuracy of uniaxial bias extension test results.* Composites Part A: Applied Science and Manufacturing, 2017. **101**: p. 81-97DOI: 10.1016/j.compositesa.2017.06.006.

[118]   Pourtier, J., B. Duchamp, M. Kowalski, P. Wang, X. Legrand, and D. Soulat, *Two-way approach for deformation analysis of non-crimp fabrics in uniaxial bias extension*

tests based on pure and simple shear assumption. International Journal of Material Forming, 2019DOI: 10.1007/s12289-019-01481-8.

[119] Bel, S., P. Boisse, and F. Dumont, *Analyses of the Deformation Mechanisms of Non-Crimp Fabric Composite Reinforcements during Preforming.* Applied Composite Materials, 2011. **19**(3-4): p. 513-528DOI: 10.1007/s10443-011-9207-x.

[120] Margossian, A., S. Bel, and R. Hinterhoelzl, *Bending characterisation of a molten unidirectional carbon fibre reinforced thermoplastic composite using a Dynamic Mechanical Analysis system.* Composites Part A: Applied Science and Manufacturing, 2015. **77**: p. 154-163DOI: 10.1016/j.compositesa.2015.06.015.

[121] Charmetant, A., J.G. Orliac, E. Vidal-Salle, and P. Boisse, *Hyperelastic model for large deformation analyses of 3D interlock composite preforms.* Composites Science and Technology, 2012. **72**(12): p. 1352-1360DOI: 10.1016/j.compscitech.2012.05.006.

[122] Peirce, F.T., *The "Handle" of Cloth as a Measurable Quantity.* Journal of the Textile Institute Transactions, 1930. **21**(9): p. T377-T416DOI: 10.1080/19447023008661529.

[123] *British Standard. Textiles: test methods for nonwovens*, in *Part 7: Determination of bending length*. BS EN ISO 9073-7; 1998.

[124] ASTM, *Standard test method for stiffness of fabrics*, in *D1388–D1396*. 2002, Philadelphia: American Society for Testing and Materials.

[125] Clapp, T.G., H. Peng, T.K. Ghosh, and J.W. Eischen, *Indirect Measurement of the Moment-Curvature Relationship for Fabrics.* Textile Research Journal, 1990. **60**(9): p. 525-533DOI: 10.1177/004051759006000906.

[126] Liang, B., P. Chaudet, and P. Boisse, *Curvature determination in the bending test of continuous fibre reinforcements.* Strain, 2017. **53**(1): p. e12213DOI: 10.1111/str.12213.

[127] Soteropoulos, D., K. Fetfatsidis, J.A. Sherwood, and J. Langworthy, *Digital Method of Analyzing the Bending Stiffness of Non-Crimp Fabrics.* 2011: p. 913-917DOI: 10.1063/1.3589632.

[128] Dangora, L.M., C.J. Mitchell, and J.A. Sherwood, *Predictive model for the detection of out-of-plane defects formed during textile-composite manufacture.* Composites Part A: Applied Science and Manufacturing, 2015. **78**: p. 102-112DOI: 10.1016/j.compositesa.2015.07.011.

[129] Kawabata, S., N.S.i.K.G.H. Evaluation, and S. Committee, *The Standardization and Analysis of Hand Evaluation*. 1980: Textile Machinery Society of Japan.

[130] Sachs, U. and R. Akkerman, *Viscoelastic bending model for continuous fiber-reinforced thermoplastic composites in melt.* Composites Part A: Applied Science and Manufacturing, 2017. **100**: p. 333-341DOI: 10.1016/j.compositesa.2017.05.032.

[131] Cornelissen, B., U. Sachs, B. Rietman, and R. Akkerman, *Dry friction characterisation of carbon fibre tow and satin weave fabric for composite applications.* Composites Part A: Applied Science and Manufacturing, 2014. **56**: p. 127-135DOI: 10.1016/j.compositesa.2013.10.006.

[132] Sachs, U., R. Akkerman, K. Fetfatsidis, E. Vidal-Sallé, J. Schumacher, G. Ziegmann, S. Allaoui, G. Hivet, B. Maron, K. Vanclooster, and S.V. Lomov, *Characterization of the dynamic friction of woven fabrics: Experimental methods and benchmark results.* Composites Part A: Applied Science and Manufacturing, 2014. **67**: p. 289-298DOI: 10.1016/j.compositesa.2014.08.026.

[133] ten Thije, R.H.W. and R. Akkerman, *Design of an experimental setup to measure tool-ply and ply-ply friction in thermoplastic laminates.* International Journal of Material Forming, 2009. **2**(S1): p. 197-200DOI: 10.1007/s12289-009-0638-y.

[134] Gorczyca-Cole, J.L., J.A. Sherwood, and J. Chen, *A friction model for thermostamping commingled glass–polypropylene woven fabrics.* Composites Part A: Applied Science

and   Manufacturing,   2007.   **38**(2):   p.   393-406DOI:
10.1016/j.compositesa.2006.03.006.

[135]   Yu, W.R. and A.C. Long, *4 - Forming textile composites*, in *Design and Manufacture of Textile Composites*, A.C. Long, Editor. 2005, Woodhead Publishing. p. 149-180.

[136]   Haanappel, S.P., R.H.W. ten Thije, U. Sachs, B. Rietman, and R. Akkerman, *Formability analyses of uni-directional and textile reinforced thermoplastics.* Composites Part A: Applied   Science   and   Manufacturing,   2014.   **56**:   p.   80-92DOI:
10.1016/j.compositesa.2013.09.009.

[137]   Bussetta, P. and N. Correia, *Numerical forming of continuous fibre reinforced composite material: A review.* Composites Part A: Applied Science and Manufacturing, 2018. **113**: p. 12-31DOI: 10.1016/j.compositesa.2018.07.010.

[138]   Yu, W.R., F. Pourboghrat, K. Chung, M. Zampaloni, and T.J. Kang, *Non-orthogonal constitutive equation for woven fabric reinforced thermoplastic composites.* Composites Part A: Applied Science and Manufacturing, 2002. **33**(8): p. 1095-1105DOI: https://doi.org/10.1016/S1359-835X(02)00053-2.

[139]   Harrison, P., W.-R. Yu, J. Wang, A.C. Long, and M.J. Clifford, *A predictive approach to simulating the forming of viscous textile composite sheet.* Revue Européenne des Éléments Finis, 2005. **14**(6-7): p. 613-631DOI: 10.3166/reef.14.613-631.

[140]   Harrison, P., M.J. Clifford, A.C. Long, and C.D. Rudd, *A constituent-based predictive approach to modelling the rheology of viscous textile composites.* Composites Part A: Applied   Science   and   Manufacturing,   2004.   **35**(7-8):   p.   915-931DOI:
10.1016/j.compositesa.2004.01.005.

[141]   Xue, P., X. Peng, and J. Cao, *A non-orthogonal constitutive model for characterizing woven composites.* Composites Part A: Applied Science and Manufacturing, 2003. **34**(2): p. 183-193.

[142]   Peng, X.Q. and J. Cao, *A continuum mechanics-based non-orthogonal constitutive model for woven composite fabrics.* Composites Part A: Applied Science and Manufacturing,   2005.   **36**(6):   p.   859-874DOI:
https://doi.org/10.1016/j.compositesa.2004.08.008.

[143]   Peng, X. and F. Ding, *Validation of a non-orthogonal constitutive model for woven composite fabrics via hemispherical stamping simulation.* Composites Part A: Applied Science   and   Manufacturing,   2011.   **42**(4):   p.   400-407DOI:
10.1016/j.compositesa.2010.12.014.

[144]   Badel, P., E. Vidal-Sallé, and P. Boisse, *Large deformation analysis of fibrous materials using rate constitutive equations.* Computers & Structures, 2008. **86**(11-12): p. 1164-1175DOI: 10.1016/j.compstruc.2008.01.009.

[145]   Khan, M.A., T. Mabrouki, E. Vidal-Sallé, and P. Boisse, *Numerical and experimental analyses of woven composite reinforcement forming using a hypoelastic behaviour. Application to the double dome benchmark.* Journal of Materials Processing Technology, 2010. **210**(2): p. 378-388DOI: 10.1016/j.jmatprotec.2009.09.027.

[146]   Dörr, D., F.J. Schirmaier, F. Henning, and L. Kärger, *A viscoelastic approach for modeling bending behavior in finite element forming simulation of continuously fiber reinforced composites.* Composites Part A: Applied Science and Manufacturing, 2017. **94**: p. 113-123DOI: 10.1016/j.compositesa.2016.11.027.

[147]   Thompson, A.J., J.P.H. Belnoue, and S.R. Hallett, *Modelling defect formation in textiles during the double diaphragm forming process.* Composites Part B: Engineering, 2020. **202**: p. 108357DOI: 10.1016/j.compositesb.2020.108357.

[148]   Aimène, Y., E. Vidal-Sallé, B. Hagège, F. Sidoroff, and P. Boisse, *A Hyperelastic Approach for Composite Reinforcement Large Deformation Analysis.* Journal of Composite Materials, 2009. **44**(1): p. 5-26DOI: 10.1177/0021998309345348.

[149]   Peng, X., Z. Guo, T. Du, and W.-R. Yu, *A simple anisotropic hyperelastic constitutive model for textile fabrics with application to forming simulation.* Composites Part B: Engineering, 2013. **52**: p. 275-281DOI: 10.1016/j.compositesb.2013.04.014.

[150]   Guzman-Maldonado, E., N. Hamila, N. Naouar, G. Moulin, and P. Boisse, *Simulation of thermoplastic prepreg thermoforming based on a visco-hyperelastic model and a thermal homogenization.* Materials & Design, 2016. **93**: p. 431-442DOI: 10.1016/j.matdes.2015.12.166.

[151]   Sharma, S.B. and M.P.F. Sutcliffe, *A simplified finite element model for draping of woven material.* Composites Part A: Applied Science and Manufacturing, 2004. **35**(6): p. 637-643DOI: 10.1016/j.compositesa.2004.02.013.

[152]   Skordos, A.A., C. Monroy Aceves, and M.P.F. Sutcliffe, *A simplified rate dependent model of forming and wrinkling of pre-impregnated woven composites.* Composites Part A: Applied Science and Manufacturing, 2007. **38**(5): p. 1318-1330DOI: 10.1016/j.compositesa.2006.11.005.

[153]   Ben Boubaker, B., B. Haussy, and J.F. Ganghoffer, *Discrete models of woven structures. Macroscopic approach.* Composites Part B: Engineering, 2007. **38**(4): p. 498-505DOI: 10.1016/j.compositesb.2006.01.007.

[154]   Badel, P., E. Vidal-Sallé, E. Maire, and P. Boisse, *Simulation and tomography analysis of textile composite reinforcement deformation at the mesoscopic scale.* Composites Science and Technology, 2008. **68**(12): p. 2433-2440DOI: 10.1016/j.compscitech.2008.04.038.

[155]   Gatouillat, S., A. Bareggi, E. Vidal-Sallé, and P. Boisse, *Meso modelling for composite preform shaping – Simulation of the loss of cohesion of the woven fibre network.* Composites Part A: Applied Science and Manufacturing, 2013. **54**: p. 135-144DOI: 10.1016/j.compositesa.2013.07.010.

[156]   Gatouillat, S., E. Vidal-Sallé, and P. Boisse, *Advantages of the Meso/Macro Approach for the Simulation of Fibre Composite Reinforcements.* International Journal of Material Forming, 2010. **3**(S1): p. 643-646DOI: 10.1007/s12289-010-0852-7.

[157]   Tavana, R., S.S. Najar, M.T. Abadi, and M. Sedighi, *Meso/macro-scale finite element model for forming process of woven fabric reinforcements.* Journal of Composite Materials, 2012. **47**(17): p. 2075-2085DOI: 10.1177/0021998312454034.

[158]   P. Boisse, M.B., K. Buet, A. Cherouat *Finite element simulations of textile composite forming including the biaxial fabric behaviour.* Composites Part B: Engineering, 1997: p. 12.

[159]   Zouari, B., J.-L. Daniel, and P. Boisse, *A woven reinforcement forming simulation method. Influence of the shear stiffness.* Computers & Structures, 2006. **84**(5-6): p. 351-363DOI: 10.1016/j.compstruc.2005.09.031.

[160]   Hamila, N. and P. Boisse, *Simulations of textile composite reinforcement draping using a new semi-discrete three node finite element.* Composites Part B: Engineering, 2008. **39**(6): p. 999-1010DOI: 10.1016/j.compositesb.2007.11.008.

[161]   Hamila, N., P. Boisse, F. Sabourin, and M. Brunet, *A semi-discrete shell finite element for textile composite reinforcement forming simulation.* International Journal for Numerical Methods in Engineering, 2009. **79**(12): p. 1443-1466DOI: 10.1002/nme.2625.

[162]   Bel, S., N. Hamila, P. Boisse, and F. Dumont, *Finite element model for NCF composite reinforcement preforming: Importance of inter-ply sliding.* Composites Part A: Applied Science and Manufacturing, 2012. **43**(12): p. 2269-2277DOI: 10.1016/j.compositesa.2012.08.005.

[163]   Leong, M., C.F. Hvejsel, O.T. Thomsen, E. Lund, and I.M. Daniel, *Fatigue failure of sandwich beams with face sheet wrinkle defects.* Composites Science and Technology, 2012. **72**(13): p. 1539-1547DOI: 10.1016/j.compscitech.2012.06.001.

[164]　Mukhopadhyay, S., M.I. Jones, and S.R. Hallett, *Tensile failure of laminates containing an embedded wrinkle; numerical and experimental study.* Composites Part A: Applied Science and Manufacturing, 2015. **77**: p. 219-228DOI: 10.1016/j.compositesa.2015.07.007.

[165]　Mukhopadhyay, S., M.I. Jones, and S.R. Hallett, *Compressive failure of laminates containing an embedded wrinkle; experimental and numerical study.* Composites Part A: Applied Science and Manufacturing, 2015. **73**: p. 132-142DOI: 10.1016/j.compositesa.2015.03.012.

[166]　Boisse, P., B. Zouari, and A. Gasser, *A mesoscopic approach for the simulation of woven fibre composite forming.* Composites Science and Technology, 2005. **65**(3-4): p. 429-436DOI: 10.1016/j.compscitech.2004.09.024.

[167]　Iwata, A., T. Inoue, N. Naouar, P. Boisse, and S.V. Lomov, *Coupled meso-macro simulation of woven fabric local deformation during draping.* Composites Part A: Applied Science and Manufacturing, 2019. **118**: p. 267-280DOI: 10.1016/j.compositesa.2019.01.004.

[168]　Ropers, S., *Bending behavior of thermoplastic composite sheets*. 2017: Springer.

[169]　Giorgio, I., P. Harrison, F. dell'Isola, J. Alsayednoor, and E. Turco, *Wrinkling in engineering fabrics: a comparison between two different comprehensive modelling approaches.* Proc Math Phys Eng Sci, 2018. **474**(2216): p. 20180063DOI: 10.1098/rspa.2018.0063.

[170]　Shen, H., P. Wang, X. Legrand, and L. Liu, *Characterisation and optimisation of wrinkling during the forming of tufted three-dimensional composite preforms.* Composites Part A: Applied Science and Manufacturing, 2019. **127**: p. 105651DOI: 10.1016/j.compositesa.2019.105651.

[171]　Andersson, A., *Evaluation and visualisation of surface defects on auto-body panels.* Journal of Materials Processing Technology, 2009. **209**(2): p. 821-837DOI: 10.1016/j.jmatprotec.2008.02.078.

[172]　Dörr, D., T. Joppich, F. Schirmaier, T. Mosthaf, L. Kärger, and F. Henning, *A method for validation of finite element forming simulation on basis of a pointwise comparison of distance and curvature.* 2016. **1769**: p. 170011DOI: 10.1063/1.4963567.

[173]　Joppich, T., D. Doerr, L. van der Meulen, T. Link, B. Hangs, and F. Henning, *Layup and process dependent wrinkling behavior of PPS/CF UD tape-laminates during non-isothermal press forming into a complex component*. 2016.

[174]　Iwata, A., T. Inoue, N. Naouar, P. Boisse, and S.V. Lomov, *Meso-macro simulation of the woven fabric local deformation in draping.* 2018. **1960**: p. 020012DOI: 10.1063/1.5034813.

[175]　Wang, J., P. Wang, N. Hamila, and P. Boisse, *Mesoscopic analyses of the draping of 3D woven composite reinforcements based on macroscopic simulations.* Composite Structures, 2020. **250**: p. 112602DOI: 10.1016/j.compstruct.2020.112602.

[176]　Prior, A.M., *Applications of Implicit and Explicit Finite Element Techniques to Metal Forming.* Journal of Materials Processing Technology, 1994. **45**(1-4): p. 649-656.

[177]　Whitcomb, J.D., *Iterative global/local finite element analysis.* Computers & Structures, 1991. **40**(4): p. 1027-1031DOI: https://doi.org/10.1016/0045-7949(91)90334-I.

[178]　Mao, K.M. and C.T. Sun, *A refined global-local finite element analysis method.* International Journal for Numerical Methods in Engineering, 1991. **32**(1): p. 29-43DOI: 10.1002/nme.1620320103.

[179]　Hirai, I., Y. Uchiyama, Y. Mizuta, and W.D. Pilkey, *An exact zooming method.* Finite Elements in Analysis and Design, 1985. **1**(1): p. 61-69DOI: https://doi.org/10.1016/0168-874X(85)90008-3.

[180]   Tran, T., D. Kelly, B.G. Prusty, G. Pearce, and J. Gosse, *A micromechanical sub-modelling technique for implementing Onset Theory.* Composite Structures, 2013. **103**: p. 1-8DOI: 10.1016/j.compstruct.2013.03.016.

[181]   Mandal, N.K. and M. Dhanasekar, *Sub-modelling for the ratchetting failure of insulated rail joints.* International Journal of Mechanical Sciences, 2013. **75**: p. 110-122DOI: 10.1016/j.ijmecsci.2013.06.003.

[182]   Molnár, P., A. Ogale, R. Lahr, and P. Mitschang, *Influence of drapability by using stitching technology to reduce fabric deformation and shear during thermoforming.* Composites Science and Technology, 2007. **67**(15-16): p. 3386-3393DOI: 10.1016/j.compscitech.2007.03.022.

[183]   Coutandin, S., D. Brandt, P. Heinemann, P. Ruhland, and J. Fleischer, *Influence of punch sequence and prediction of wrinkling in textile forming with a multi-punch tool.* Production Engineering, 2018. **12**(6): p. 779-788DOI: 10.1007/s11740-018-0845-9.

[184]   Larberg, Y.R. and M. Åkermo, *On the interply friction of different generations of carbon/epoxy prepreg systems.* Composites Part A: Applied Science and Manufacturing, 2011. **42**(9): p. 1067-1074DOI: 10.1016/j.compositesa.2011.04.010.

[185]   Johnson, K.J., R. Butler, E.G. Loukaides, C. Scarth, and A.T. Rhead, *Stacking sequence selection for defect-free forming of uni-directional ply laminates.* Composites Science and Technology, 2019. **171**: p. 34-43DOI: 10.1016/j.compscitech.2018.11.048.

[186]   Pasco, C., M. Khan, J. Gupta, and K. Kendall, *Experimental investigation on interply friction properties of thermoset prepreg systems.* Journal of Composite Materials, 2018. **53**(2): p. 227-243DOI: 10.1177/0021998318781706.

[187]   Bouquerel, L., N. Moulin, S. Drapier, P. Boisse, and J.-M. Beraud, *Modelling and simulating the forming of new dry automated lay-up reinforcements for primary structures.* AIP Conference Proceedings, 2017. **1896**(1): p. 030008DOI: 10.1063/1.5007995.

[188]   Yu, F., S. Chen, J.V. Viisainen, M.P.F. Sutcliffe, L.T. Harper, and N.A. Warrior, *A macroscale finite element approach for simulating the bending behaviour of biaxial fabrics.* Composites Science and Technology, 2020. **191**DOI: 10.1016/j.compscitech.2020.108078.

[189]   Budiansky, B., J.L. Sanders, H.U.D.o. Engineering, A. Physics, and U.S.O.o.N. Research, *On the "best" First-order Linear Shell Theory*. 1962: Division of Engineering and Applied Physics, Harvard University.

[190]   *CloudCompare 2.11. Retrieved from* http://www.cloudcompare.org. 2016   [cited 2021 06/10].

[191]   Petitjean, S., *A survey of methods for recovering quadrics in triangle meshes.* ACM Computing Surveys, 2002. **34**(2): p. 211–262DOI: doi:10.1145/508352.508354

[192]   Garimella, R.V. and B.K. Swartz, *Curvature Estimation for Unstructured Triangulations of Surfaces*. 2003, Los Alamos Nat. Lab.: Los Alamos.

[193]   Marlow, R., *A general first-invariant hyperelastic constitutive model.* Constitutive Models for Rubber, 2003: p. 157-160.

[194]   Wang, W.-T., H. Yu, K. Potter, and B.C. Kim. *Improvement of composite drape forming quality by enhancing interply slip*. in *ECCM17-17th European Conference on Composite Materials*. 2016. European Society for Composite Materials.